University of Nottingham
UK | CHINA | MALAYSIA

Statistical Approaches to the Study of Self-Organised Nanostructures

Jo Everitt Alexander Hodgkinson

Submitted to the University of Nottingham

for the Degree of *Doctor of Philosophy*

January 2024

Abstract

Spin-casting solutions of colloidal nanoparticles onto solid substrates produces a diverse array of self-organised nanostructured patterns. Such patterns are regarded as far-from-equilibrium, relying on the complex dynamics of the solvent as the thin liquid film rapidly retracts from the surface. The observed ordering allows for varied statistical analysis upon atomic force microscopy images of the resulting patterns. An analytical toolbox utilising various statistical approaches is discussed and applied, supported by numerical simulations of the experiment, carried out using modified versions of the model developed by Rabani *et al.*[1].

A systematic study of the effects of both gold nanoparticle concentration in solution and introduced surface heterogeneities was carried out, scanning resulting patterned morphologies with atomic force microscopy and evaluating with relevant statistical analysis. Co-deposited fullerenes and atomic force microscopy probe-induced oxidation aimed to disrupt and mediate the typical dewetting process of the thin solvent film on a highly local level, enhancing our understanding of the dynamic properties of the solvent. A pathway from synthesis to ambient surface characterisation of nanostructured photoactive dyads was additionally studied.

A series of synchrotron x-ray experiments on fullerene-encapsulating molecules addressed the extent to which encapsulated molecules are electrostatically screened and decoupled from their external environment when deposited on a metal substrate. In the observed absence of temperature dependence of molecule height above the substrate surface, experimental NIXSW data across the temperature range is used to assess the mobility of caged molecules, as well as reconcile results within a two-adsorption site framework.

A case for being critical at the point of data entry is demonstrated by the data-mining and re-utilisation of historic dewetting pattern images previously produced within the group, to form data sets to confidently evaluate new statistical analysis software. This is presented with documented development of transparent automated mass image processing software, highly sensitive to images of multi-layered nanostructures and the inherent noise in scanning probe microscopy, by means of a statistical approach utilising modern data science methods.

Acknowledgements

I would like to thank the Low-Dimensional Materials and Interfaces Doctoral Training Program (LDMI DTP) run by the Nanoscale and Microscale Research Centre (nmRC) at the University of Nottingham. It has been a great way to gather together a diverse group of scientists exploring the field of nanoscience across multiple disciplines, sharing our successes and challenges throughout. The LDMI DTP also provided me the opportunity to work with Philip Moriarty, a bottomless well of nanoscience expertise and experimental know-how.

The scanning tunnelling microscopy squad, under Philip Moriarty and Alex Saywell, that is Oli, Matt, Ellie, Filipe, Chris, Alex and Abbie have been a great research cohort. I would especially like to thank Oli, a bright physicist who provided me with incredible insight in every meeting and conversation we shared. Peter Beton's regular atomic force microscopy team of James, James, Juan and Jonathan all played a huge role in getting me to a high level of competency with the kit.

I would like to pour out a mint tea for Stu, Chris, James, Max, Tyler and Juno. No matter how much I was catastrophising about my work for that morning or afternoon, a quick coffee break to discuss the finer things in life with you was always waiting at 11:30am and 4:30pm. My housemates throughout my PhD, Keir, Ryan and Nadhya, and furthermore Kira and Rei round out the support bubble that kept me sane through my studies and the COVID-19 pandemic.

An honourable mention should go to the Asylum Research MFP-3D AFM, a system that has provided me with a lot of ups, downs, and broken cantilevers. I only raised my voice with you once and regretted it for the next two years.

I would also like to thank the first-year undergraduate experimental physics module staff. My laboratory demonstrator role was a major highlight of my time as a post-graduate, and my efforts to improve the experience of those I taught were reciprocated with a teaching award. My four years in this role came with a lot of fond memories, and kept me involved with the school even in my darkest weeks.

And lastly and ultimately, thank you so much to my close family. My parents and brother got me through both a difficult and transformative time of my life that coincided with my studies, as well as providing the odd visit to provide food and washed bed sheets.

List of Publications

O Gordon, **J Hodgkinson**, S Farley, E Hunsicker, and P Moriarty. Automated Searching and Identification of Self-Organized Nanostructures. *Nano Letters*, 20(10):7688-7693, 2020.

S Farley, **J Hodgkinson**, O Gordon, E Hunsicker, and P Moriarty. Improving the Segmentation of Scanning Probe Microscope Images Using Convolutional Neural Networks. *Machine Learning: Science and Technology*, 2(1):015015, 2020.

S Jarvis, H Sang, F Junqueira, O Gordon, **J Hodgkinson**, A Saywell, P Rahe, S Mamone, S Taylor, A Sweetman, J Leaf, D Duncan, T. L Lee, P Thakur, G Hoffman, R Whitby, M Levitt, G Held, L Kantorovich, P Moriarty, and R Jones. Chemical shielding of H_2O and HF encapsulated inside a C_{60} cage. *Communications Chemistry*, 135, 2021.

Reuse of Materials Statement

Significant portions of the text and figures in this thesis are derived or reproduced from all of the publications listed above unless otherwise stated. All derived and reproduced material is licensed under a Creative Commons Attribution (CC BY) license, viewable at `https://creativecommons.org/licenses/by/4.0/`

For Stephen and Matt. Two people destined to be doctors, I hope I can fill that role.

Contents

1 Introduction

1.1 A different perspective

As the quantity and complexity of nanoscience data dramatically increases, our ability to analyse, visualise and interrogate the relationships between observed structure and physics needs to keep pace. Integrating data-driven methods that address structural diversity among samples is essential for broader adaptation, particularly when investigating structurally complex self-organised structures. Data science provides a variety of robust statistical methods, ideal for describing real nanoscale materials and conveying new sample properties numerically. Furthermore, automation and information technology in the field of data science aid in curating large-volume data sets.

Comprehensive applications of data science have high potential in the field of nanoscience. Modern material probing techniques for imaging nanoscale samples that facilitate high throughput experimentation, such as scanning probe microscopy (SPM)[2,3] and x-ray photoelectron spectroscopy (XPS)[4], are becoming increasingly widespread. Numerical models that attempt to simulate interactions at the nanoscale, such as molecular dynamics and Monte Carlo simulations (see Chapter 3 for an example of the latter), are constantly growing in popularity and act to provide data supplementary to experiments.

Recent work and collaborations within the Nottingham Nanoscience Group have focused on a data-driven approach, aiming to expand the nanoscientist's toolbox[5–8]. This commonly amounted to the collection, processing and evaluation of images produced by microscopes and simulations. Automation of scanning probe microscopy (SPM), by means of identifying what constitutes a "good" topograph, or surface image, on a scan-by-scan basis, then correcting scanning parameters in the SPM software until it produces a stable image, is an exciting concept explored by Gordon *et al.*[5–7]. Automated image classification and segmentation[8] were combined with image pre-processing tailored to high-precision images of nanostructures to produce an automated nanoscale far-from-equilibrium pattern categorisation model.[9]

Confidence in these applications comes from large data sets that fully explore the experimental and statistical parameter space. Consistent automated image processing facilitates the analysis of large data sets of images. Algorithmic image re-processing of raw image data also circumvents user biases at the time they were processed. Identification of the necessary processing steps with regard to the equipment's operation, common instrument noise signatures, and shortfalls of each processing technique with respect to the explored parameter space is essential. The application of more comprehensive data science methods to scanning probe image data of structurally similar systems of self-organising nanostructures, recently highlighted within the Group, is presented within this thesis.

1.2 Self-organising nanostructures

Traditionally, fabrication of nanostructures comes primarily in the form of "top-down" manufacture. Here, lithography is used to etch a larger piece of material, be it with chemicals, a probe, or a focused ion beam for example, much like carving a sculpture. The assembly and longevity of nanodevices constructed from etched components are met with challenges unique to the nanoscale. A "bottom-up" approach is a highly appealing alternative to the fabrication of nanoscale structures via lithographic and etching methods. Instead of a brute force removal of material, bottom-up methods – also known as self-assembly – harness and tune interatomic, intermolecular, and inter-nanoparticle interactions to form ordered lattices. The interactions, in this case, can arise from various sources: London dispersion forces, electrostatic forces, hydrogen bonding, coordination chemistry, and the Pauli exclusion principle. A self-assembled structure seeks to reach and maintain an ordered configuration that minimises the free energy in a stable or metastable state of equilibrium. Some scientists distinguish self-assembly and what is known as self-organisation, where the latter involves a far-from-equilibrium transfer of energy and matter not present for the former, which is a much closer-to-equilibrium phenomenon.

A "bottom-up" process of particular relevance to this thesis is the self-assembly (and self-organisation) of thiol-passivated gold nanoparticles deposited from a volatile solvent onto a solid substrate (typically native oxide-terminated silicon). This produces a vast variety of self-organised patterns[10,11], as discussed in Chapter 3. An extensive AFM data set (spanning tens of thousands of images of gold nanoparticle assemblies), acquired by the Nottingham Nanoscience Group over roughly a decade, was used as the foundation for the development of the automated analysis and classification protocols/algorithms described in Chapters 3, 4 and 6.

1.3 Thesis outline

A variety of self-assembled and self-organised nanostructured systems – spanning (endo)fullerenes, gold nanoparticles, and molecular dyads – form the focus of this thesis. An overarching theme throughout is the analysis and interpretation of the characteristic length-scales arising from the various assembly processes, from spinodal dewetting of nanoparticle suspensions in an ambient environment to the growth of a highly ordered endohedral fullerene monolayer under ultra-high vacuum conditions. Although scanning probe microscopy has been the primary experimental tool, synchrotron-based techniques, including photoelectron spectroscopy and x-ray standing wave analysis, have been used for the analysis of a nanostructured system for which SPM provides highly limited information, namely thin films and 2D overlayers of endofullerenes on metal substrates.

In parallel, several protocols have been developed for the automated analysis of scanning probe data, with a particular focus on pattern classification and the identification of spatial correlations. This thesis research component was carried out during the COVID-19 lockdown periods when access to experimental research instrumentation and facilities was, at best, severely limited.

Chapter 2 broadly introduces the materials, tools and techniques used in the experimental side of the presented work. This includes a discussion of various forms of scanning probe microscopy and the theory behind their operation, as well as steps for sample preparation in ambient and ultra-high vacuum conditions.

Chapter 3 introduces the concept of self-organisation, starting with the modes of far-from-equilibrium pattern formation mediating the dewetting of thin films. Standard techniques for producing self-organisation in thin films and typical parameterisation during systematic study are discussed. Monte Carlo modelling is also discussed within the context of dewetting, preceding the application of statistical analysis to well-understood dewetting patterns produced experimentally. The chapter concludes with the introduction of comparative statistical metrics to evaluate SPM of deposited self-organised nanostructures, and real-time simulations of dewetting produced by implementing a Monte Carlo simulation.

Chapter 4 is the first of four experimental chapters. This covers deposition studies using atomic force microscopy of functionalised gold nanoparticles, and co-deposition of nanoparticles and buckminsterfullerene upon silicon. This starts with a discussion of new applications of statistical analysis to real and simulated nanostructure AFM images, including Minkowski morphometry, Fourier-based evaluation of roughness, and simulated dewetting pattern coarsening. Types of gold nanoparticle dewetting patterns produced, control over the patterns exerted by selective tip oxidation methods, and co-deposition of buckminsterfullerene are demonstrated.

Chapter 5 describes synchrotron-based experiments on buckminsterfullerenes encapsulating H_2O and HF. Soft and hard x-rays, produced by the synchrotron at Diamond Light Source in Oxford, are utilised to address the extent to which encapsulated molecules are electrostatically screened and decoupled from their external environment. In particular, normal-incidence x-ray standing wave (NIXSW) measurements are performed on filled fullerenes adsorbed on a metal surface. NIXSW results quantify the displacement of the encapsulated molecules from their otherwise central position due to modification of the electrostatic potential within the C_{60} cage. X-ray photoemission spectroscopy (XPS) characterises the deposits and points towards substantial screening of the encapsulated molecules by the cage.

Chapter 6 describes the development of new protocols for the automated analysis of large SPM data sets using an extensive set of AFM images of self-organised nanopar-

ticle patterns. Particular attention is paid to intelligent automated segmentation and thresholding of SPM images, a perennially troublesome aspect of the analysis of probe microscope data.

This is followed by Chapter 7, covering a synthesis to surface probing pathway for a photoactive molecular dyad. Naphthalene diimide phenyl-phenothiazine (NDP), synthesised from naphthalene monoimide (NMI) and 4-aminophenyl-phenothiazine (Ph-PTZ), is deposited from toluene onto silicon using different deposition methods at a series of concentrations. The resulting far-from-equilibrium morphologies of NDP nanocrystals are evaluated using AFM. Ambient sample preparation techniques and AFM employed throughout the thesis are incipiently applied and calibrated in this chapter.

2 Experimental Techniques and Materials

2.1 Scanning probe microscopy

2.1.1 High precision surface imaging

It is hard to imagine the modern landscape of atomic-scale surface study without scanning probe microscopy (SPM). With the invention of the scanning tunnelling microscope in 1982[2] and the atomic force microscope a few years later[3], SPM since has revolutionised the acquisition of surface information for nanoscientists. The technique provides an unprecedented level of precision, with modern SPM under optimal conditions achieving sub-angstrom spatial resolution.

A scanning probe microscope operates on the design principle of a sharp probe rastering over a surface. The apex of the probe is held in close proximity (typically $<$1 nm) to the sample surface and scans over a predetermined region of surface, measuring physical parameters from the interaction at all possible positions. Each parameter measured at each position is incorporated into an image, built pixel by pixel, of that scanned area. The result is a map of the scanned region of the surface, describing features of the region, from topography to local work function.

The core SPM techniques used throughout this thesis are atomic force microscopy (AFM) and scanning tunnelling microscopy (STM). Other SPM techniques, such as kelvin probe force microscopy (KPFM), briefly discussed in Section 2.2, play a role, but a basic understanding of all SPM techniques can stem from an understanding of AFM and STM. While they often have the common goal of routine high-resolution imaging approaching atomic resolution using a sharp probe, the type of interaction between the probe and surface is specific to the type of SPM used. STM measures a tunnel current, while AFM directly measures a force response (or force gradient for NC-AFM). The theory behind measuring these interactions is explored in Sections 2.3 and 2.2.

While removing the inherent limits on resolving power placed by diffraction for optical microscopy, and by aberration and the need for sample coating for electron microscopy, SPM comes with its unique limitations. These include the state of the imaged surface and terminating point of the probe, the inherent sampling rate imposed by the minimum step width in digitally controlled systems, and the theoretical limits imposed by the technique. All SPM systems are designed to minimise sources of experimental noise or provide additional tools to do so. This can range from software for probe controls, to a cryostat surrounding the probe and surface.

The probe of the SPM instrument is attached to a piezoelectric transducer. The distortion of the piezoelectric materials, induced by appropriate voltages applied by the instrument's controller, allows for nanoscopic actuation of the transducer-mounted

probe, providing fine motion capabilities for the tip in 3D space. This is not only useful for xy scanning small selective regions and sensitive z responses to surface features, but in tandem with wider range transducers, this precision can be maintained with larger scan sizes and during the approach phase. This approach phase involves advancing the probe to bring the tip-surface separation to that of the interaction range. The precise transducers distort from the minimum to the maximum of their range before returning to their minimum while the larger transducer advances the same distance as that range. Once the larger transducer's maximum range is reached, both the small and large transducers retract and a stepper motor advances the whole assembly, repeating until a surface response is measured. This coordinated process allows for a safe and effective approach, with fine-tuned centring of the precise piezo range over the surface. The scanner in turn is attached to a series of servo motors or manual screws, allowing for coarse positioning of the probe, which would be held at a safe distance from the surface during coarse xy movement to avoid crashes, by using coarse z movement to retract. Using a mounted camera, the operator can coarsely approach the surface with the probe before the slow approach phase, avoiding observably damaged or contaminated surface regions, or relocate scanned regions of interest on the surface, often macroscopically-marked to be detected with the camera feed.

The described approach method was based on the atomic force microscopes used, specifically the Asylum Research Cypher and MFP-3D systems, and is highly common among AFM systems. STM systems similarly utilise a coarse approach followed by a highly sensitive walk-in method, monitoring for when the tip-sample separation reaches tunnelling range. However, a slipstick motor manages the coarse approach from a tip-sample separation on the order of millimetres into range. A voltage is applied to a piezoelectric plate, to which a piezoelectric scan-tube is mounted, in a sawtooth waveform. The linear increase in voltage causes a shear movement in the plate, the subsequent rapid decrease causes the plate to return to its original shape at the new position, progressing the assembly.[12,13]

Ideally, only the interaction with a single atom on the end of the probe and typical background interactions are measured. Probes are often initially manufactured with a microscopically sharp tip with low radii of curvature and are further sharpened with chemical etching and other techniques. While this can prepare a very sharp tip apex, atomic-scale asperities and protrusions local to the apex can introduce unwanted scan artefacts, such as double-tips. Further modification assures a surface response, like tunnel current during STM, is due to a single atom at the apex of the tip. The tip properties are inevitably altered during SPM sessions, with many *in situ* ways to modify the tip's shape actively. Unlike *ex situ*[14,15] methods of tip sharpening, such as ion beam lithography, *in situ* methods in STM are far more primitive. The operator is generally limited to controlled crashes of the STM tip and applying sudden voltage pulses to the tip. Terminating with an individual atom, or a highly conical tip, though optimal, is not necessary due to the short interaction range and the exponential re-

lationship with separation, unique for each SPM approach as discussed in Sections 2.2 and 2.3, a single atom protruding from the tip dominates any interactions over neighbouring atoms above it. Blunt tips with a large tip radius of curvature can, however, introduce convolution effects due to interactions between the surface and the micron-scale bulk of the tip. These long-range forces are detrimental to the spatial resolution. Though a blunt tip may be enough to resolve the nanostructures being investigated, a consistently sharp tip is preferable to maintain consistency across images.

As the signal measured at the probe dynamically affects data acquisition, via the feedback system, great care is taken in eliminating noise produced by the SPM instrument, while isolating it to reduce the effect of external noise sources. For example, a pre-amplifier in series with the tip-surface junction boosts the signal-to-noise ratio attainable. Vibrations place a hard limit on SPM resolution to the degree that even sub-angstrom amplitude vibrations must be avoided. SPM systems often have a specially-designed damping apparatus to attenuate mechanical vibrations. This often includes a series of low tension springs to suspend the platform that holds the tip and surface and the whole instrument resting on air legs. Electrical noise is limited with efficient electronics, often with low noise ratings, high-quality grounding, and cable shielding. Choice of location also matters, seeking a vibration-free environment outside the boundaries of the instrument often leads to placing them on lower floors of buildings to minimise the effects of structural vibrations. Even after relocating the SPM instrument to the basement, some inherent noise still is not tackled. Non-linearity of the piezoelectric material behind the probe and the curved trajectory of the scanner introduce inherent distortion to images that must be removed via image processing software. Subsection 6.1.4 discusses this further.

Scans at the atomic scale are susceptible to thermal drift, predominantly caused by the material's response to variations in local temperature. The scan is exposed to uncontrolled time-dependent distortions, by which the tip moves relative to the surface, horizontally or vertically, by gradients in local temperature. When the thermal drift velocity and scan time are of similar magnitude to the scan size, it can introduce uncharacteristic skewing to the resulting image. Thermal drift is a common threat to high-resolution imaging, especially prohibiting long-lasting data acquisition over small regions of interest, and hence, solutions are well-explored. Cooling the instrument with liquid helium or nitrogen on low-temperature systems with a cryostat to stabilise the temperature significantly reduces the impact of thermal drift. Drift compensation employing atom tracking and thermal analysis, modelling drift velocity with respect to temperature, to estimate drift behaviour on the software side aims to mitigate the effects of thermal drift.

2.1.2 Working in UHV conditions

SPM and preparation of materials for SPM took place in either ambient or ultra-high vacuum (UHV) conditions ($< 10^{-9}$ mbar though optimally held below 10^{-10} mbar). Achieving and maintaining UHV in a sealed stainless steel vacuum chamber keeps the sample and tip free from contaminants in air and fully isolates an experiment from the environment. This makes the system highly appealing for atomic resolution imaging and atomic manipulation experiments. These conditions are prerequisites for thermal sublimation and other *in situ* techniques used or considered throughout.

Maintenance of UHV conditions within the system is often a heavily involved process. Minority gases under atmospheric pressure can chemically react with the sample during sensitive processes like high-temperature annealing, while metallic surfaces, deposited materials and sensitive components within the chamber may oxidise. Maintaining low levels of impurities within the UHV chamber is hence crucial. At the minimal pressure within the UHV chamber, the major gas load present is hydrogen, a much more inert gas than oxygen and water vapour.

A series of pumps act to remove gas from the chambers of the two UHV systems used, the Scienta Omicron variable temperature scanning tunnelling microscope (VT-STM) and low-temperature scanning tunnelling microscope (LT-STM). Different pumps have different standard operating pressure ranges. Therefore, a variety of pumps are connected to the UHV chamber to take the system's pressure down from atmospheric to UHV levels. A roughing pump, such as a scroll pump, removes the gas from the chamber to bring the chamber to rough vacuum levels ($> 10^{-3}$ mbar). A combination of the roughing pump and a turbomolecular pump, as well as a bake-out process described later, reduce the pressure to the upper boundary of high vacuum levels ($> 10^{-8}$ mbar). The turbomolecular pump further reduces the pressure to UHV ($< 10^{-9}$ mbar). Two further pumps are operated at this pressure, the ion getter pump and the titanium sublimation pump (TSP). The ion getter pump works by applying a strong electric field across two plates, ionising the gas atoms and molecules between them, causing the ions to accelerate towards a cathode. Cathode materials sputtered by incoming high energy gas ions are deposited onto the anode or pump walls, and the resulting film acts as a getter to further evacuate gas by chemisorption and physisorption[16]. The pump material is often titanium due to its effectiveness at pumping hydrogen thanks to hydrogen's solubility and diffusion rate within titanium, hydrogen being the major gas load at low pressures[17]. The TSP is a titanium alloy filament that is electrically heated until titanium sublimates from the filament's surface into the UHV chamber. The sublimed titanium coats the surfaces and chemically captures any active gases within the chamber.[16]

Active user measures to maintain UHV include the use of a secondary sealed chamber, the load lock, to transfer samples from outside the chamber; a system bake-out,

enclosing the system in a tent and regulating to 100-150 °C for approximately 12 hours to desorb gases from system surfaces, to reduce the minimum chamber pressure; applying mechanical seals between fixtures, often in the form of copper gaskets, which are scored by the cutting edge between the flanges of connected fixtures.
UHV conditions are a powerful and unique tool for studying new surfaces unsuitable for preparation or probing under ambient conditions. Chapter 5 features the study of C_{60} on Ag(111) under UHV conditions, using deposition and probing techniques discussed in Sections 2.4 and 2.6 respectively.

2.1.3 Controlling SPM systems

For the time being[5,6], SPM instruments are controlled in real-time by a user, usually within the proprietary software of the instrument's manufacturer. These communicate with the control box of the instrument via their own coding language, manipulating parameters for image capture through a user interface (UI) of control panels. All atomic force microscopes used were controlled with Asylum Research 13, while all scanning tunnelling microscopes were controlled with MATRIX 4.3.5. These two programs, and most SPM-associated software, share some terminology for their user-definable scan parameters, in particular, their primary feedback parameters. One of the most important of these is setpoint, corresponding to a returned physical attribute generated by the interaction between probe and sample, such as tunnel current or deflection. The microscope will aim to keep this value constant during a scan with the degree of correction, generated by a feedback loop, which is reflected in the pixel value at that position in the scan. SPM instruments use a control loop feedback system purposely designed to maintain the defined setpoint value. This is slightly more complex, and generally smoother, than a simple negative feedback loop where, in the case of a z motion correction, the tip goes down when the strength is too low and goes up when it is too high.

A proportional-integral-derivative (PID) controller is the most commonly used feedback system. A PID controller for SPM makes adjustments to the tip-sample separation with respect to equation 2.1

$$\delta h(t) = K_p E(t) + K_i \int_0^t E(\tau) d\tau + K_d \frac{d}{dt} E(t) \qquad \{2.1\}$$

where $\delta h(t)$ is the time-dependent controller output, in this case, the correction to separation at time t, E is the difference between the defined setpoint and measured setpoint, the error term, and τ is a dummy integration variable. K_p, K_i and K_d are the proportional, integral and derivative system gains respectively. The user sets these gain parameters, each requiring systematic adjustment to reach a stable and damped configuration for the scanned surface. Incorrect setting of these parameters leads to imaging uncharacteristic of the surface and other undesirable effects.[18]

Increasing the proportional gain increases the direct corrective response to deviation from the setpoint. Still, it is liable to cause overshooting, which, when further rapidly re-corrected for, appears as high frequency oscillations in the scan. The integral gain acts upon the history of the error term, this stabilises the feedback response and hence reduces steady-state errors, by which the probe corrects to an offset from the setpoint while correcting for the dynamic signal, often caused by sample drift in the z direction or scanning sloped samples[19]. This term can still, however, lead to low frequency oscillations by overshooting. The derivative gain acts to reduce overshooting and is proportional to the rate of change of the error term. The derivative term's amplification of rapidly-oscillating noise renders it unsuitable for the majority of SPM systems, excluding those with high signal-to-noise ratios. It is hence common to see SPM feedback controllers referred to as PI controllers, which is effectively the same as a PID controller with $K_d = 0$.[19]

2.2 The atomic force microscope

AFM extends the principles of SPM to insulating substrates. A tunnel current cannot be used as a measure of the tip-sample interaction for an insulating sample, and thus STM is not possible. This is circumvented by measuring the force upon a cantilever instead of a tunnel current. This is conducted with a cantilever of known stiffness, quantified by its spring constant, held in close proximity to a surface. In a static mode, the cantilever will deflect from the surface towards a local minimum, in the potential well commonly defined by either the Lennard-Jones or Morse potential in equations 2.2 and 2.3 respectively, at an equilibrium position σ, bonding energy E_{bond} and characteristic inverse decay length κ in the Morse potential case. The tip, located at the apex of the cantilever, at displacement $z > \sigma$, is attracted by long-range London dispersion/van der Waals (vdW) forces, instantaneously-formed and induced dipoles. At $z < \sigma$, a repulsive tip-sample interaction arises from the Pauli exclusion principle, which states that fermions cannot occupy the same quantum state. Such forces are ubiquitous among atoms of any and all materials. Hence AFM places no limitations on the electronic nature of surfaces it can study.

Different modes exploit different sections of the typical force-distance profile shown in Figure 2.2.1, with contact modes occupying the repulsive regime, non-contact (NC) modes in the attractive regime (with some exceptions[20]), and intermittent contact utilising a combination of the two.

$$V_{LJ} = -E_{bond}(2\frac{\sigma^6}{z^6} - \frac{\sigma^{12}}{z^{12}}) \quad \{2.2\}$$

$$V_{Morse} = -E_{bond}(2e^{-\kappa(z-\sigma)} - e^{-2\kappa(z-\sigma)}) \quad \{2.3\}$$

Dynamic modes of AFM utilise a vibrating cantilever. Instead of a force measurement based on the deflection and effective spring constant of the cantilever, a force gradient

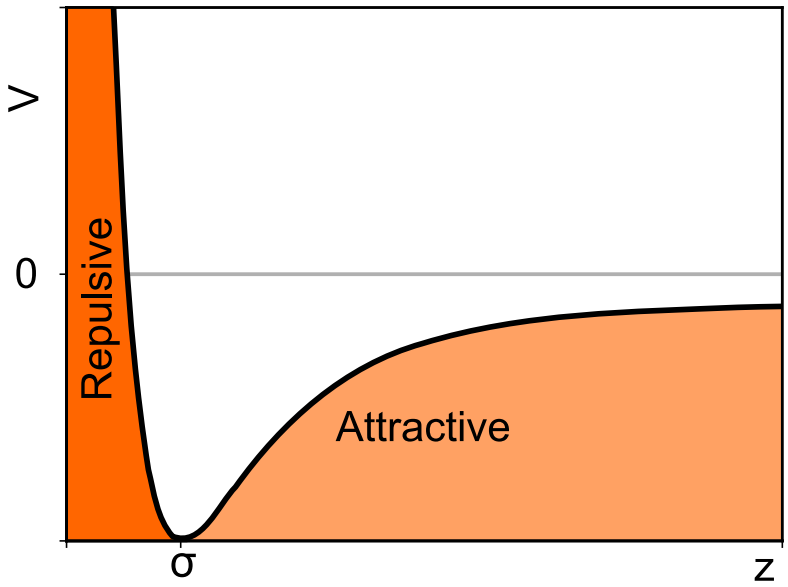

Figure 2.2.1: Appearance of the interaction potential in AFM, typically defined by the Lennard-Jones or Morse potential, with the regimes for dominant short-range repulsive (chemical) and dominant long-range attractive (vdW) forces labelled. σ represents an equilibrium position.

measurement is used to regulate the probe. It is at this point more properties of the cantilever matter. For one, a quality factor, Q, quantifies the decay in the amplitude of oscillations as frequency deviates from the resonance peak. Operation in air, liquid or vacuum will modify this factor accordingly. All dynamic modes deployed were resonant modes. Resonant modes operate at or near the resonant frequency of the cantilever. This is typically with the cantilever externally driven at its resonant frequency, or within $\pm$5% of it, with a piezo-actuator fed an alternating voltage, sometimes referred to as a shaker piezo. In all cases, the driven cantilever was oscillated near resonance with the tuning panel in software, most commonly set to oscillate the cantilever at -5% of the found resonant frequency. Occupying one side of the resonance curve during a scan guarantees a near-linear relationship between amplitude and frequency at little to no cost to resolution.

A high resonant frequency minimises the effects of vibrational noise. This, combined with the demand for a low stiffness, meant that a general-purpose silicon cantilever with a spring constant of 2 Nm^{-1} and a resonant frequency of 70 kHz was used throughout. The same cantilever with a 40 nm platinum coating was used for conductive measurements. Higher frequency driving oscillations, beyond the first harmonic, can render the AFM image more sensitive to the surface composition by introducing multiple degrees of freedom (eigenmodes) for excitation and detection of individual material properties.[21]

Modern AFM most often utilises a laser beam deflection configuration to detect the force-driven deflection, shown in Figure 2.2.2. The cantilever deflection is measured by

a laser focused on the tip-end of the probe, enabled by a reflective coating, which reflects into a photodiode. During operation, the position of the reflected laser changes and is detected by the position-sensitive photodiode as a signal.

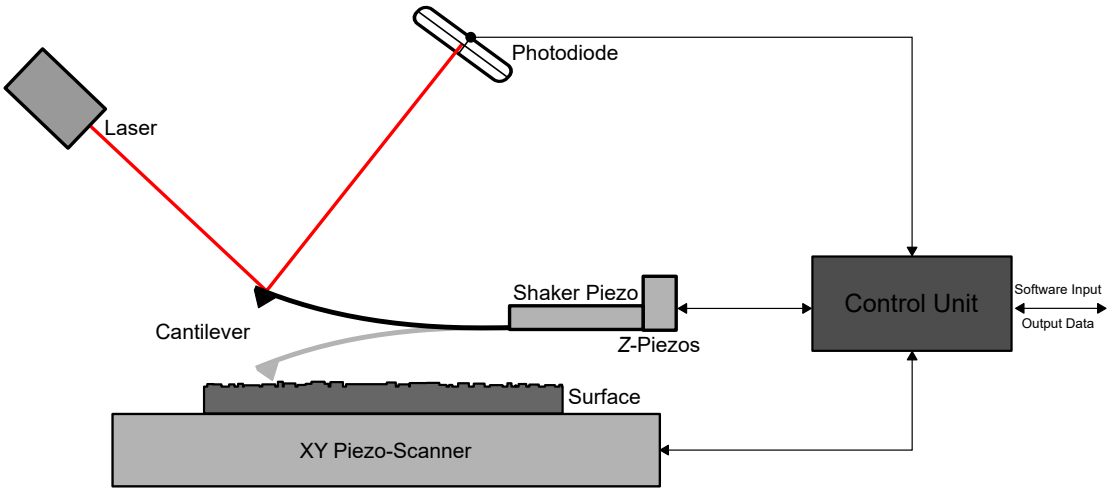

Figure 2.2.2: The conventional setup of an AFM instrument using a laser beam deflection configuration.

There are several modes in which one can operate an atomic force microscope. Those discussed below are conventional modes available with most software and instruments utilised for material characterisation throughout the thesis research.

Contact mode is the simplest implementation of AFM. This static mode involves the undriven cantilever being effectively dragged over the surface, with deflection directly measured. In this case, the setpoint governs the degree to which the cantilever pushes into the surface. Contact mode boasts rapid scan speeds at greater resolutions than most other imaging modes, as the gradient of the repulsive regime the cantilever is pushed into is relatively steep, which provides a highly contrasting image as the probe directly traces the surface topography. The high interaction strength and probe proximity of the mode come at the cost of damage to the probe and surface. The invasive nature means contact mode can damage weakly bound molecular layers, with the lateral forces often causing rapid blunting of the tip and any material interacting weakly with the surface to be swept away during scans. While this can be a useful feature for characterising structures and their surface adhesion, contact mode is only typically used for high-resolution scans of bare substrate or small scans upon nanostructures to limit damage to a small vicinity. Though contact mode is the definitive use of static mode AFM, the mode is not limited to measuring surface topography and other material properties. A static mode was utilised for additive nanolithography on silicon over square regions using parameterisation in the software's contact mode, discussed further in Subsection 4.3.2.

The first dynamic modes to discuss are those operated in the non-contact regime. Non-contact atomic force microscopy (NC-AFM), as the name suggests, is operated with no contact between the surface and tip within the attractive regime of Figure 2.2.1. During NC-AFM, the amplitude of oscillations of the vibrated cantilever is controlled such that the energy of the cantilever at the closest point of approach to the surface is sufficient to avoid a "jump to contact" within the repulsive regime of tip-surface interaction. Short-range forces can be probed without risk of permanent deformation of the tip and surface without coming into full contact with the surface.

The tip-sample interaction modifies the cantilever's effective spring constant, modifying its resonant frequency. Considering the resonance curve in Figure 2.2.3 by which a force gradient experienced by the probe translates the curve along the horizontal axis. Operating on the attractive side of the potential minimum results in negative frequency shifts with a reduction in amplitude and the appropriate phase difference.

Two NC-AFM modes were deployed for surface scanning. **Amplitude Modulation mode** (AM) AFM is analogous to that in the original AFM design by Binnig *et al.*[3], while **Frequency Modulation mode** (FM) AFM was later developed by Albrecht *et al.*[22]. AM mode measures the change in amplitude of the cantilever oscillation and adjusts the tip-sample separation using the PID controller to maintain a fixed amplitude value. FM mode utilises a phase-locked loop and PID controller to track the shift in resonant frequency induced by the tip-surface interaction, Δf, relative to that of the cantilever oscillated at a suitable distance from the surface[23].

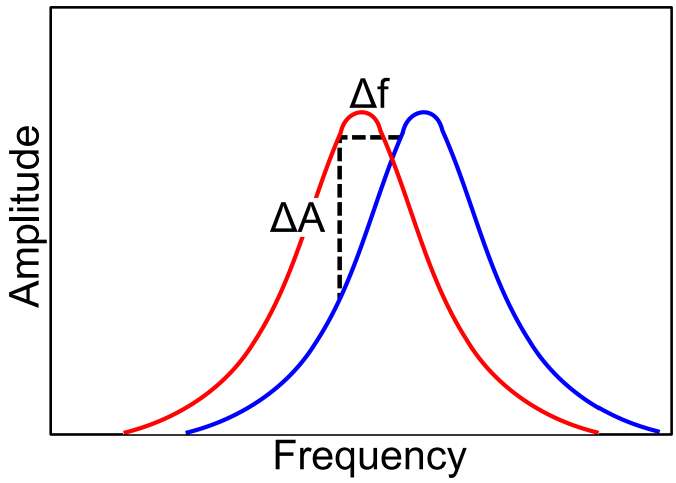

Figure 2.2.3: Resonance curve shift induced during NC-AFM. Δf and ΔA are tracked in frequency modulation AFM and amplitude modulation AFM respectively to build an image.

When AFM was implemented under UHV conditions[24], standard silicon or silicon nitride cantilevers exhibited very high Q. The fast response times of the instrument scaled proportional to Q, this often renders AM-AFM and tapping mode AFM too sluggish in UHV conditions. This makes FM-AFM preferable, as response times of the

instrument in FM mode do not scale with Q[25].

Tapping mode provides an alternative height imaging approach and acts as the primary probing method for the work presented in this thesis. This dynamic mode is referred to as intermittent contact mode, as the probe is positioned such that the tip taps the probed surface at the bottom of each swing of the oscillating cantilever. The cantilever's amplitude is dampened due to intermittent tip-sample contact during a scan.
The feedback loop maintains the tapping regime at the probe setpoint amplitude with respect to the topography of the surface, modifying z accordingly. The adjustments to z required to maintain the constant amplitude of the probe during a scan are presented in the height image[26]. Short-term contact with the surface maintains the high lateral resolution of contact mode, without the invasive nature.

Phase contrast imaging is another common AFM imaging option, deployed simultaneously with tapping mode with no drawback. The change in probe amplitude near its resonant frequency, which is used for feedback in tapping mode, does not fully define the tip-sample force interactions. Monitoring the probe's phase lag between the signal that drives the cantilever oscillation and its output signal, performed alongside amplitude control, provides a deeper understanding of the tip-sample interaction. Such shifts are recorded in a phase image, relative to the driving signal. Excited cantilever oscillations exhibit a phase shift $\Delta\phi$ between the drive and response. At resonance, $\Delta\phi$ is 90° compared to the phase well below resonance. During a dynamic mode scan, a phase lag between the driving signal and recorded signal will be detected due to a change between the tip-surface interaction. This lag is correlated to the energy dissipated while tapping the tip on the surface. This can differentiate areas on the sample of differing properties, beyond differences in height. A problem emerges in the measurement often being a convolution of multiple material properties, most often the adhesion, stiffness and viscoelasticity. Isolating such properties is best explored with single-point AFM force spectroscopy. While not useful at pinpointing the exact material source of the contrast, phase contrast mode provides a source of image contrast in cases of a lack of visible features in the height image. This feature was exploited to help identify or relocate nanostructures or nanolithography patterns over large, topographically flat regions.[26]

Kelvin probe force microscopy (KPFM) is an NC electrical characterisation method available with the atomic force microscope grounding platform and software. KPFM provides another source of contrast in surfaces, this time by measuring the contact potential or work function, defined as the energy required to remove an electron from the Fermi level in a solid into vacuum at 0 K, of the probed surface using a conductive probe. A dual-pass setup is used, by which the cantilever passes over the same row of scanned region twice, recording surface topography using AM-AFM on the first pass, and then KPFM on the second. During this pass, voltage dithering is applied

to the scanning cantilever, typically at a high harmonic of the cantilever. Shifts in resonant frequency by electrostatic forces from the surface are monitored, and a potential feedback system supplies a suitable DC voltage offset to minimise the shift. The voltage value is recorded for all positions as the interaction parameter, similar to that of all forms of SPM. Though this dual recording method has a long acquisition time, based upon the combined scan rate of the AM and KPFM measurements, the ability to strongly correlate topography to electrical properties is exceedingly useful. Though the work function was uncalibrated in the use cases presented in Appendix D, and often calibrated by use of a control surface such as silver, a clear understanding of the tip-surface electrostatic interaction allows for relative quantitative KPFM measurements of variations in the sample's local work function[27,28]. Additionally, the constructed "Kelvin" image maps spatially inhomogeneous surfaces (for example, due to areas of different materials, orientations, or due to surface defects) where the force profile between the tip and surface is liable to vary across different regions of the image. Hence, a constant force gradient profile from such a surface may not generally be the same as a purely topographic profile[29,30].

2.3 Scanning tunnelling microscopy

Scanning tunnelling microscopy (STM) was the secondary SPM technique used. The principles remain consistent with those discussed for SPM in general, a sharp probe is brought into close proximity to a surface to measure the magnitude of the specific interaction. This time however, the tip-sample separation, z, is within the order of a few angstrom. At this distance, the phenomenon of quantum tunnelling takes place, such that the interaction measured is the transmission of electrons between the tip and sample. Notably, an image produced by STM, though capable of atomic resolution, does not directly return atomic positions. Instead, the local density of electronic states (LDOS) is measured. The two modes of operation are constant height and constant current mode. The former measures the tunnel current by rastering the tip over the surface at a constant height, while the latter uses a PI(D) feedback response to maintain the tunnel current. In constant height mode, the current between the tip held at the same z displacement and surface is recorded as a function of xy tip position to build an image. In constant current mode, the tip height necessary to maintain a setpoint current is recorded as a function of xy tip position to build an image.

Due to the quantum mechanical basis of STM, the essential physics for operation is captured by the simple problem of tunnelling through a 1D barrier[31]. The rectangular barrier of height V_0 and width z_t represents a metallic tip separated in vacuum from the sample by a distance z_t, an electronic wavefunction of energy E would need to overcome an apparent barrier height of (V_0-E). This is shown visually in Figure 2.3.1. The resulting wavefunction, ψ, at the barrier can be described at each region by equation 2.4

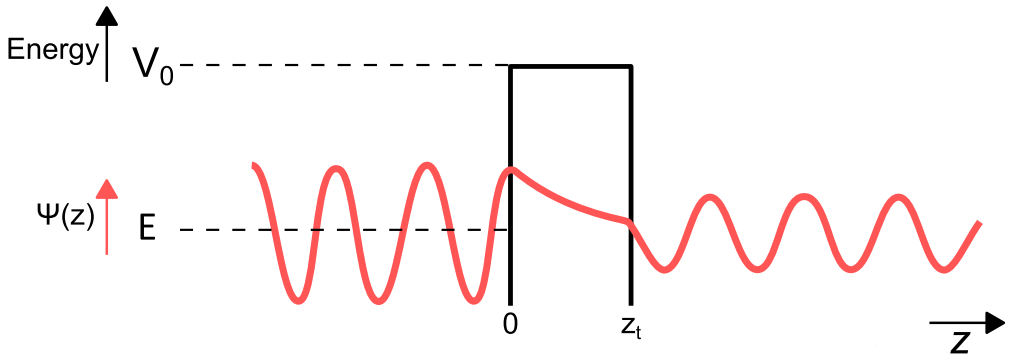

Figure 2.3.1: Demonstration of quantum tunnelling through a 1D potential barrier.

$$\psi(z) = \begin{cases} Ae^{ikz} + Be^{-ikz} & z < 0 \\ Ce^{\mu z} + De^{-\mu z} & 0 < z < z_t \\ Fe^{ikz} & z > z_t \end{cases} \quad \{2.4\}$$

where k is the wave number, $k = \sqrt{\frac{2mE}{\hbar^2}}$, μ is the inverse decay length of the electron at the surface, $\mu = \sqrt{\frac{2m}{\hbar^2}(V_0 - E)}$, while A, B, and F are constants that govern transmission, and C and D the reflection.

Relating 1D tunnelling to measurements during an STM scan is accomplished through a transmission coefficient, $T(E)$. This defines the ratio between the probability flux of the transmitted wave after the barrier and the incident wave as it arrives at the barrier. By ensuring continuity of the wavefunction and its first derivatives at the boundaries, $z = 0$ and $z = z_t$ in equation 2.4,

$$T(E) \propto I \propto e^{-2\mu z_t} \quad \{2.5\}$$

The derived exponential dependence of current upon tip-sample separation results in STM's sub-atomic resolution. Even a single angstrom shift in separation, and hence barrier width, can vary I by nearly an order of magnitude.[32,33]

2.3.1 Tersoff-Hamann approach

Interpretation of STM images requires a more complex theoretical description than that of just the 1D tunnelling model. Though the 1D approach captures the essential physics of the problem, a more realistic model was proposed by Tersoff and Hamann in 1985[31]. At large tip-sample distances, the tip-sample interaction can be modelled as a small perturbation[34]. The tunnel current, I, as such can be represented by equation 2.6

$$I = \frac{2\pi e}{\hbar} \sum_{t,s} f(E_t)[1 - f(E_s + eV)]|M_{ts}|^2 \delta(E_t - E_s). \quad \{2.6\}$$

The equation sums over all tip (t) and sample (s) states. The $f(E_t)$ and $(1 - f(E_s + eV))$ terms ensure tunnelling is between filled and empty states by giving the probability for an electron to occupy a filled energy level in the tip, where $f(E)$ is the Fermi function, the probability of occupying an available energy level. The δ term ensures the conservation of energy for elastic tunnelling. The matrix element, M_{ts}, is the tunnelling matrix between the tip and sample, and is given by equation 2.7

$$M_{ts} = \frac{\hbar^2}{2m} \int_S (\psi_s^* \nabla \psi_t - \psi_t \nabla \psi_s^*) d\mathbf{S} \qquad \{2.7\}$$

ψ_s and ψ_t are the wavefunctions of the sample surface and tip respectively, while also serving as eigenfunctions of the isolated system to be solved independently. $\int_S d\mathbf{S}$ represents an integral over any surface S, lying entirely within the tunnelling gap into respective tip and sample regions. Overall, the tunnelling matrix evaluates the probability of the tip and sample wavefunctions overlapping, which is necessary for any tunnelling to occur.

The tunnelling matrix can be fully evaluated by knowledge of the precise structure of the tip and, hence its wavefunction. Tersoff and Hamann suggested a simplified spherical STM tip model. The apex approximated a sphere with a radius of curvature R and centre of the globe, r_0, illustrated in Figure 2.3.2.

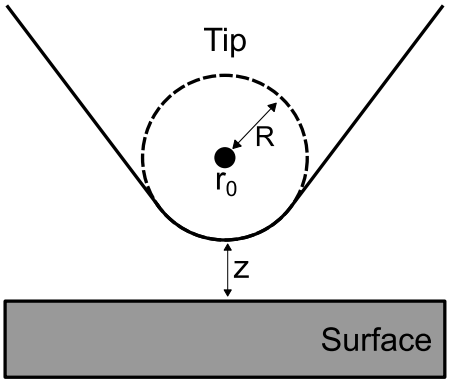

Figure 2.3.2: Schematic of the Tersoff-Hamann s-wave tip model.

The idealised tip wavefunction is given by equation 2.8

$$\psi_t = \Omega_t^{-1/2} c_t \kappa R e^{\kappa R} e^{-\kappa |r - r_0|} (\kappa |r - r_0|)^{-1}, \qquad \{2.8\}$$

where Ω_t is the volume of the tip, c_t is a normalisation term, and $\kappa = \hbar^{-1}(2m\phi)^{1/2}$, the minimum inverse decay length for the wavefunctions in vacuum, where ϕ is the work function of the surface. The tunnelling matrix is hence given by equation 2.9

$$M_{ts} = \frac{4\pi\hbar^2}{2m\kappa} \Omega_t^{-1/2} \kappa R e^{\kappa R} \psi_s(r_0). \qquad \{2.9\}$$

In the limit of zero temperature, such that the Fermi functions can be approximated by a unit step function, V is small, and the tip and sample are only weakly coupled, equation 2.6 simplifies to equation 2.10

$$I = \frac{2\pi e^2 V}{\hbar} \sum_{t,s} |M_{ts}|^2 \delta(E_t - E_F)\delta(E_s - E_F). \quad \{2.10\}$$

Implementing the s-wave state for the tip wavefunction[31] from equation 2.8 into equation 2.10 further simplifies it to equation 2.11

$$I \propto \sum_{s} |\psi_s(\mathbf{r}_0)|^2 \delta(E_t - E_F). \quad \{2.11\}$$

$|\psi_s(\mathbf{r}_0)|^2$ is the probability density of the surface wavefunction at the position of the tip. Given equation 2.11, I is directly proportional to the surface's local density of states (LDOS). However, this only reasonably holds for metallic surfaces. In actual experiments, the electronic and chemical interaction between the tip and sample is much stronger, and the voltage can be significantly higher than assumed in the Tersoff-Hamann model.

For semiconducting samples and molecular adsorbates, given that only electron states between E_F and $E_F + eV$ contribute to tunnelling, equation 2.11 can be modified to equation 2.12 for finite voltages

$$I \propto \int_{E_F}^{E_F+eV} |\psi_s(\mathbf{r}_0)|^2 \delta(E - E_F) T dE, \quad \{2.12\}$$

where $T(E)$ is the aforementioned transmission coefficient.

The Tersoff-Hamann model, as presented, does not provide a full picture. The s-wave approximation is much too simple to describe the apex of a tip during experiments. Previous works expand the model to different tip shapes by deriving their respective tunnelling matrix element[35,36], or conduct expansive analytical modelling of tip shape and its effect on surface interaction[37]. Regardless, beyond thermal fluctuations at the Fermi level, applying a voltage bias between the tip and surface is required to measure a tunnel current, during which all electron states between E_F and $E_F + eV$ are assessed. Varying the bias allows for direct measurement of the LDOS.

2.3.2 Voltage bias

Transmittance is not just reliant on the distance between the probe and the surface; there is also dependence on the density of empty states that electrons can tunnel into, and the density of filled states that electrons can tunnel from. Tip bias when probing semiconducting materials of often complex band structure plays a key role in the observed LDOS in STM images. It would be beneficial to first consider a purely

metallic tunnel junction, depicted in Figure 2.3.3. In an ideal case, E will be close to the Fermi energy, hence $V_0 - E = \phi$, where ϕ is the work function of the material. Figure 2.3.3(a) shows an unconnected tunnel junction, just two metals separated by a vacuum. The Fermi levels of each material, E_{F1} and E_{F2}, are defined by a displacement of ϕ_1 and ϕ_2 from the common vacuum level, E_{vac}, respectively. Once electrically connected, in the case of Figure 2.3.3(b) where $\phi_1 < \phi_2$, a transfer of charge from the first to the second material occurs, aligning the Fermi levels at E_F. There is no net flow of electrons in either direction; hence no tunnel current is measured. When a negative bias V is applied, a shift in Fermi level by eV results in a tunnel current from the second to the first metal, depicted in Figure 2.3.3(c).

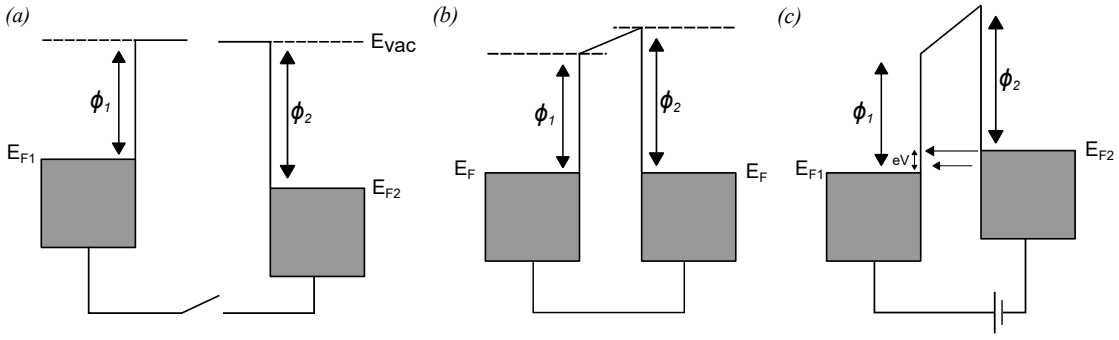

Figure 2.3.3: Energy level diagrams at a purely metallic tip-sample junction for STM. **(a)** The tip and sample are electrically isolated, the common reference is E_{vac}, the vacuum level. **(b)** The tip and sample are electrically connected with zero bias, the Fermi levels align and no net tunnelling is observed. **(c)** A negative bias V is applied across the connection (right to left), shifting the energy level by eV, the transmission of electrons from occupied states on the right into empty states on the left.

When considering a semiconducting material, the relative positions of the Fermi levels driven by the bias affect whether electrons tunnel from the valence band or into the conduction band, shown in Figure 2.3.4. The tunnel current is hence described by equation 2.12, proportional to the convolution of the density of states of the tip and sample within the energy window defined by the sample bias.

This does not, however, describe the entire picture while probing a semiconducting material, as the tip is not necessarily terminated by metal atoms. More often, the apex is coated in the surface materials during the scan, including possible deposited adsorbates, contaminants, or substrate.

STM was used for early material characterisation of silicon and HOPG, as well as test deposition methods under UHV conditions. However, changes in the project's scope caused the technique to be underutilised. The work presented primarily focuses on AFM, particularly the analysis of images returned by tapping mode.

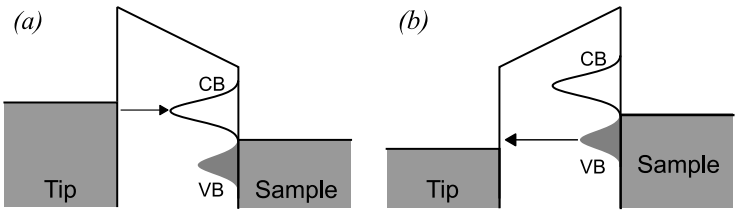

Figure 2.3.4: Energy level diagrams at a tip-sample junction with a semiconducting adsorbate for STM. **(a)** A negative tip bias is applied, causing electrons to tunnel from the tip to the sample's conduction band (CB). **(b)** A positive tip bias is applied, causing electrons to tunnel from the valence band (VB) to empty states in the tip.

2.4 Vacuum deposition techniques

2.4.1 Thermal sublimation

Thermal sublimation via a sublimation cell was the primary deposition approach for x-ray experiments on surface-bound molecules. The cell allows for deposition directly into the UHV chamber, assuming the solid angle projected has a line of sight with the sample, by a molecule flux diffusing into the chamber. The cell's internal design follows that of M. Schunack[38], presented in Figure 2.4.1. The heating wire acts as a filament that heats the glass crucible containing the molecules through resistive heating using a power supply attached to external wires outside the chamber. A K-type thermocouple embedded in the base of the crucible monitors the temperature using a multimeter attached to the external wires.

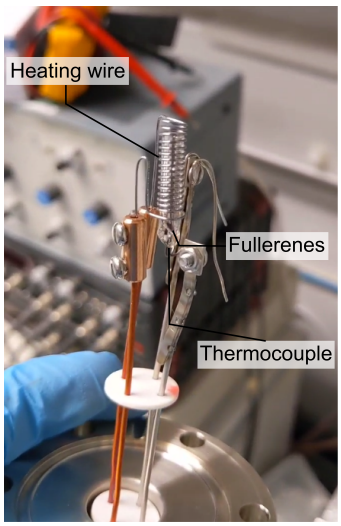

Figure 2.4.1: Photo of the end of the sublimation cell mounted into the UHV chamber of the LT-STM.

Cross-contamination when changing the contents of the crucible was avoided by a thorough clean, the glass crucible and other loose components were submerged in acetone then left for a 20 minute cycle in an ultrasonic bath, then resubmerged in isopropyl alcohol for a second 20 minute cycle. The inserted material is thoroughly

degassed in UHV at high temperatures - for several hours at 400 °C for a crucible containing C_{60} - before sublimation. Endofullerenes were prepared for deposition via this standardised method. Endofullerenes are discussed further as a material and experimentally in Chapter 5.

2.5 Materials

This section describes the key materials used throughout the thesis research, namely graphite, silicon, hexagonal boron nitride and fullerenes. SPM is carried out to examine these materials during preparation, and their chemical interactions with molecules deposited upon them, as a substrate. Graphite, silicon and silicon modified *in* and *ex situ* with dopants, passivations, or a deposited different substrate are reviewed below, as well the C_{60} fullerene molecule. Gold nanoparticles are central to their own chapters. They are discussed as materials later on in context, in Subsection 3.1.2.

2.5.1 HOPG

Graphite is a crystalline form of the element carbon, consisting of hexagonally arranged layers of carbon atoms, stacked parallel to provide a three-dimensional crystal of long-range order. Carbon atoms in each sheet, effectively a graphene layer, are covalently bonded with sp^2 hybridisation with a C-C distance of 141.7pm. Weak van der Waals forces hold the layers together[39]. Pyrolytic graphite is described as highly oriented when the mosaic spread is sufficiently low. The mosaic spread is typically given as an angle, defined as 0° when all layers of graphite sheets in the material are parallel. A mosaic spread angle below 1° is achieved with high temperature and stress treatment.

Highly oriented pyrolytic graphite's (HOPG) well-understood surface morphology makes it a useful calibration standard for atomic resolution imaging. The step edges create a consistent step height of 3.4 Å, the effective spacing between two layers of carbon atom sheets measured when a profile is taken in SPM, scanning an incomplete layer atop another. The layered nature allows for robust substrate modelling due to the relatively low complexity of the delocalised π orbitals. The material is also easily renewable under ambient conditions. Cleaving with tape removes an unclean layer off the HOPG, providing an atomically flat polycrystalline surface with minimal residue. HOPG was used in Appendix D as a substrate for *in situ* vapour deposition for sub-monolayer coverage of C_{60}, and as a manner of calibrating an STM operating under ambient conditions, discussed below.

Surface level defects significantly affect the observed superlattice when probing with STM. Bulk HOPG exhibits Bernal stacking, ABAB, to form a crystal, with the offset between A and B planes being one atomic spacing. There are two atomic sites: α-sites, where carbon atoms in adjacent layers are directly above and below each other, and β-sites, where carbon atoms in adjacent layers are directly above or below hole

sites. This leads to a primitive unit cell consisting of four carbon atoms, 2 α and 2 β, of unit cell length 2.46 Å. STM upon HOPG theoretically returns a trigonal pattern of bright spots with the same spacing, observed experimentally in Figure 2.5.1(a), but this is not always the case. The second image's appearance is potentially due to a misalignment, 2.5.1(b), a local deformation of graphite due to a very short tip-sample distance, attractive forces decouple the top layer of graphite from the surface[40]. This returns an image of the hexagonal lattice, effectively the standard atomic resolution of HOPG, using only α-sites occurring at the surface.

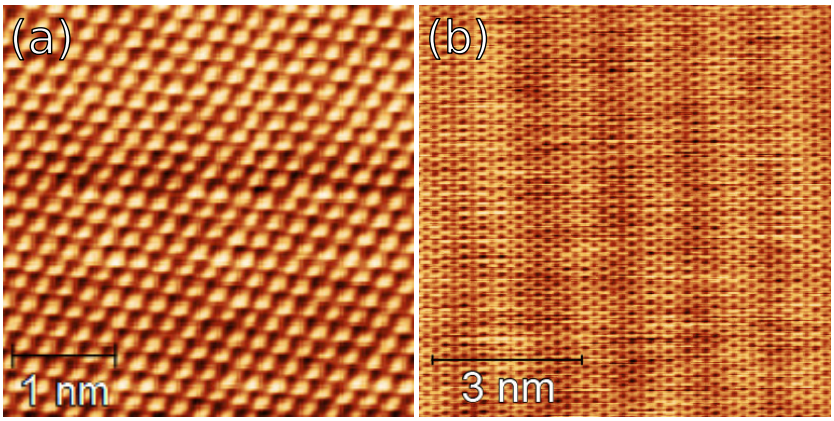

Figure 2.5.1: STM images of HOPG taken under ambient conditions using a hand-cut Pt-Ir wire as a probe. **(a)** Trigonal pattern with ∼2.4 Å spacing; **(b)** hexagonal pattern with side length ∼1.4 Å. The differences in appearance are accredited to different tunnelling and tip conditions, or a misalignment in the outermost layer of graphite.

2.5.2 Silicon

Silicon is a mainstay of the semiconductor industry, with silicon components present in a staggering number of electronic devices. The material is similarly a mainstay of surface study, being one of the most widely studied surfaces in the field. Silicon here acts as a benchmark substrate for SPM. Mono-crystalline silicon cut at two specific atomic planes, Si(100) and Si(111), were used. Illustrated in Figure 2.5.2, the Miller indices are indicative of the angle of cleaving of the bulk crystal. Cleaving the diamond-lattice structure exposes the $3s^2$ $3p^2$ valence electrons, forming covalent tetrahedral bonds with four neighbouring silicon atoms in a process called surface reconstruction.

Uncontaminated Si(111) reconstructs into a complex 7 x 7 surface, formed by dangling bonds among the outermost three layers, shown in Figure 2.5.3. Si(100) reconstructs to form dimers, which buckle to reduce the free energy. Depending on the relative orientation of buckling of adjacent dimers, various surface reconstructions form, ideally p(2 x 1) symmetric, p(2 x 1) asymmetric, p(2 x 2), and c(4 x 2), shown in Figure 2.5.4.[41,42]

The silicon wafer used was thermally oxidised and polished commercially, but scored and cut into rectangular wafers of suitable size for SPM with a diamond scribe. Thermal oxidation grows a uniform oxide layer 10 - 100s of nanometres thick, often within

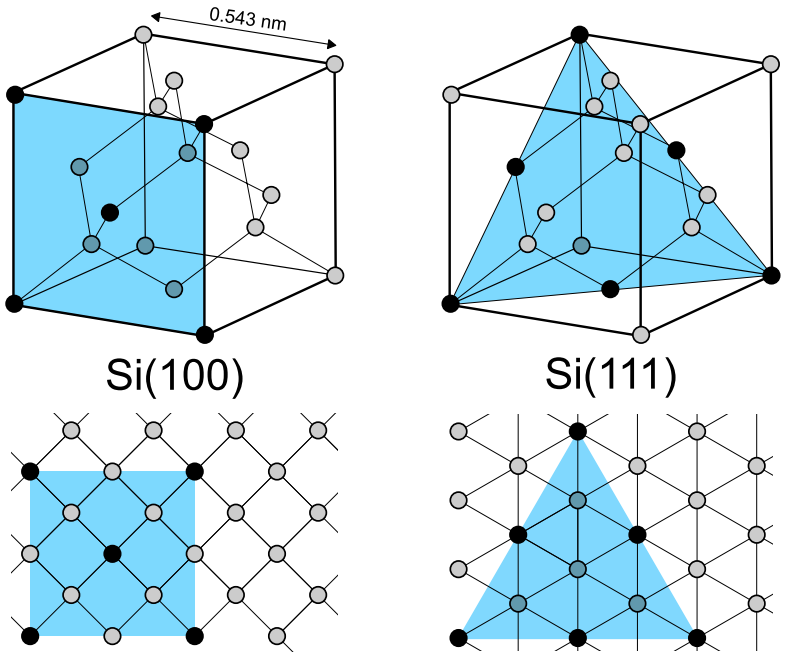

Figure 2.5.2: Atomic structure of the ideal bulk-terminated Si(100) and Si(111) crystal planes. Reconstruction in each case leads to dramatic repositioning of the surface, and near-surface, atoms.

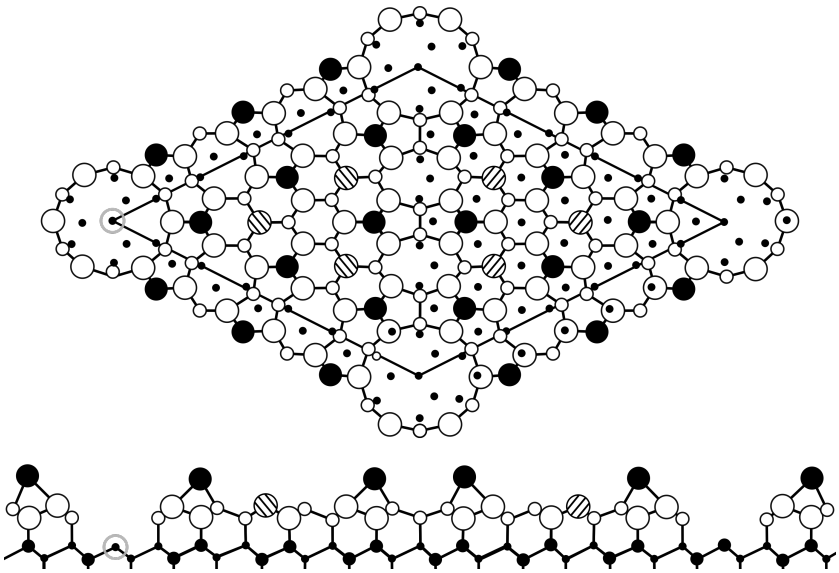

Figure 2.5.3: Top view and side view of a Si(111) 7 x 7 reconstruction. From Gomoyunova *et al.*, Technical Physics 49(10):1249-1279, 2004 [43]

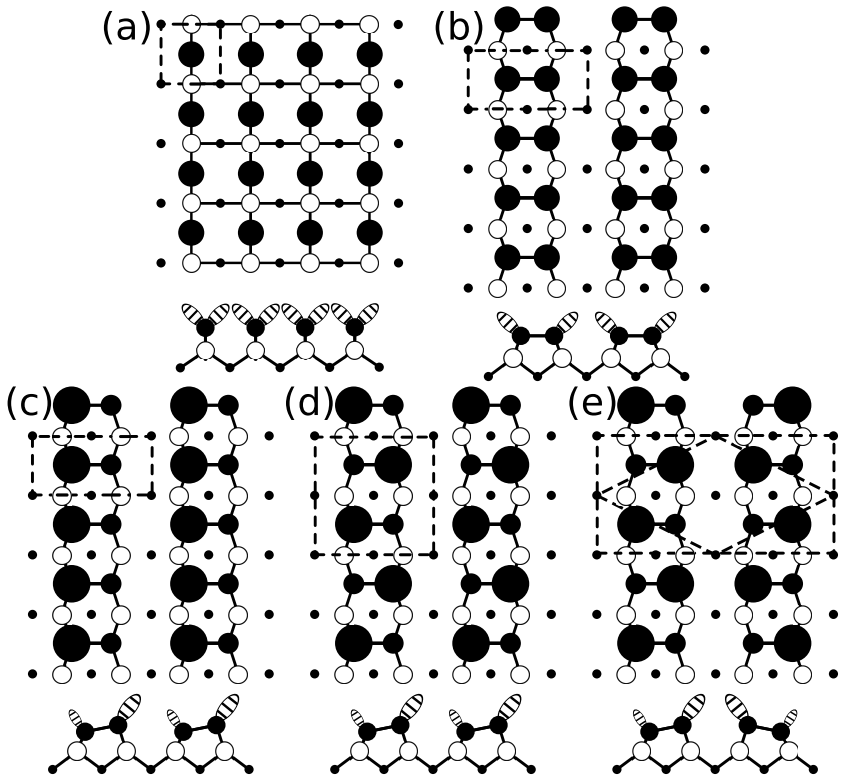

Figure 2.5.4: Si(100) reconstruction and phases of dimer rows. **(a)** Top view and side view of the polished unreconstructed 1 x 1 surface, surface atoms have 2 dangling bonds. **(b)** The p(2 x 1) symmetric reconstruction of paired dimers, surface atoms have a single dangling bond. **(Bottom row)** Lower energy configurations with asymmetric dimers; **(c)** p(2 x 1) asymmetric, **(d)** p(2 x 2), and **(e)** c(4 x 2),

a 10% boundary of error, providing a sufficiently flat surface for numerous AFM deposition studies with NDP, C_{60} and thiol-passivated gold nanoparticles from solvent. Silicon with this grown oxide layer (often amorphous with crystalline defects[44,45]) is denoted as SiO_2/Si.

Cleaning silicon *ex situ* for SPM uses a simple, well-established procedure. The cut pieces of a wafer are solvent cleaned, pieces are submerged in acetone, then left for a 20 minute cycle in an ultrasonic bath, and then resubmerged in isopropyl alcohol for a second 20 minute cycle. Excess solvent is removed by a nitrogen gas stream. This process removed oil and organic residue for deposition and dewetting studies, and sample entry into the UHV chamber.

Preparation of silicon for atomic resolution UHV STM requires an even higher standard of cleanliness. Even short-term exposure of the surface to atmosphere oxidises the surface and picks up multiple contaminants such as airborne carbon. The silicon is typically cleaned *ex situ* with solvents as before, alongside the disassembled sample holder components. Upon entry to UHV, the surface is degassed. The sample and holder are heated to 650 °C for several hours in the UHV chamber's manipulator arm via resistive heating, with temperature measured by a pyrometer aimed at the hottest part of the surface through a viewing window. Chamber pressure and temperature are highly monitored, with spikes in pressure and changes in surface resistivity indicative of desorption events, and long-term reductions in pressure indicative of the majority of contaminants being removed from the sample and holder, such as water and residual solvent from cleaning. Degassing was also conducted for HOPG after cleaving and then entry to UHV, at a similar temperature of 600 °C.

Degassing is subsequently followed by flash annealing. The flash annealing process aims to rapidly increase the temperature to 1200 °C for short periods to remove the native oxide layer, drive residual carbon contaminants into the bulk, and expose the bare silicon underneath. The manual temperature ramping is termed "flashing". Monitored using a pyrometer, the surface is returned to the degassing temperature, flashed to the flashing temperature, then returned to the degassing temperature, and then repeated. A series of flashes is conducted to remove further contaminants exposed during the removal of the native oxide layer. Instead of returning to the intermediate degassing temperature, the final flash is followed by a short anneal at a secondary intermediate temperature of 800 °C. This cooling temperature allows the silicon surface to reconstruct, during which surface atoms rearrange to minimise the free energy. The surfaces of Si(111) and Si(100) would reconstruct in UHV in the previously discussed ideal manner, a 7 x 7 reconstruction or a c(4 x 2) (low temperature)/(2 x 1) (room temperature) reconstruction, respectively.

More specialised preparations of silicon are discussed in their respective chapters. This includes wet chemical etching and selective re-oxidation of silicon in Chapter 4, and

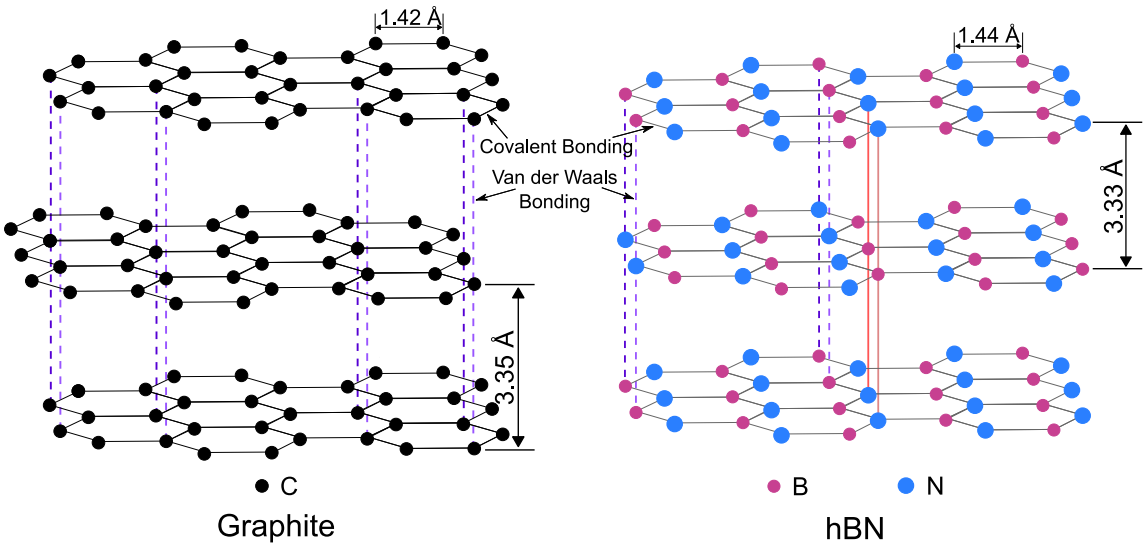

Figure 2.5.5: Structural comparison of highly oriented pyrolytic graphite (HOPG) to hexagonal boron nitride (hBN).

considerations of modelled silicon substrate via Monte Carlo simulations between Chapters 3 and 6.

2.5.3 Hexagonal boron nitride

Thermally-oxidised silicon wafers were chosen for the deposition of layers of a second substrate. Hexagonal boron nitride (hBN) sees persistent usage as a well-defined atomically flat dielectric substrate for the growth of organic thin films, with ease of preparation *ex situ* to return a flat appearance for AFM. Graphene and hBN are isostructural, shown in Figure 2.5.5, forming a honeycomb network. Compared to graphene's unit cell of length 2.46 Å, hBN sheets form a unit cell of two boron and two nitrogen atoms of unit cell length 2.51 Å. There is similarly a lack of dangling bonds, limiting interactions with functional groups of molecular adsorbates. The dielectric properties of the material arise from a 6.0 eV bandgap[46], rendering the material weakly interactive during thin film depositions for AFM and spectroscopy. For these reasons, the substrate was deployed in a photoactive dyad-substrate systematic study in Chapter 7.

Growing an expansive, flat, organic thin film first requires a flat, uncontaminated hBN film, for which the group has a consistent standard operating procedure. The hBN substrate is prepared by mechanically exfoliating flakes from single crystals using Scotch^{TM} tape. Repeatedly adhering and peeling away the tape to and from the hBN crystallites causes mechanical cleavage, returning a thin layer of hBN upon the tape. The tape is then applied to a series of silicon wafers upon their polished face, and slowly peeled away, with the resulting substrate checked under an optical microscope. Low hBN coverage could be fixed by plasma and heat treatment of the silicon substrate before transfer.

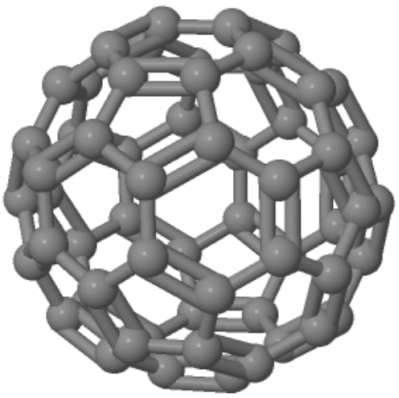

Figure 2.5.6: 3D rendering of buckminsterfullerene (C_{60}) made in JSmol.

Using tape returns a significant amount of polymer residue, beginning a long and rigorous cleaning process, involving flame-annealing and subsequent furnace-cleaning. Normally one of these methods is used and enough to remove all residue, but both were deployed due to persistent nucleation in the deposited organic thin films. The cleaning process began with a minimum 12 hour toluene submersion, with excess solvent removed by a nitrogen gas stream. Subsequent flame-annealing involved exposure to a butane gas torch upon the non-polished side of the wafers. This was followed by furnace cleaning, the samples were heated in a tube furnace at 350 - 400 °C for 8 hours in an atmosphere of 5% hydrogen 95% argon. The cleanliness and roughness of the resulting substrate are checked with AFM. The resulting cleaned and exfoliated hBN flakes have typical lateral dimensions of 20 - 100 µm and thicknesses 25-75 nm.[47,48]

2.5.4 Buckminsterfullerene

Fullerenes are a well-known group of carbon allotropes, with the most renowned member being C_{60}, buckminsterfullerene. The C_{60} molecule takes the appearance of a quasi-spherical net of carbon atoms, made of twenty hexagons and twelve pentagons with a carbon atom at each vertex, shown in Figure 2.5.6. Since its discovery in 1985[49], the study of the molecule deposited onto solid surfaces has remained a consistent and fruitful field of research, stimulating and underpinning advances in numerous sub-fields of condensed matter physics and surface science. Aspects of fullerenes, and functionalised fullerenes, have been interpreted by a broad range of techniques, from SPM to synchrotron-based methods.

All of the presented fullerene studies were conducted in the context of recent work with endofullerenes, fullerenes encapsulating molecules, discussed in Chapter 5. AFM studies on unfilled fullerenes, co-deposited from solution onto silicon or via thermal sublimation onto HOPG, are covered in Subsection 4.3.1 and Appendix D.

2.6 X-ray techniques

2.6.1 X-ray photoelectron spectroscopy

X-ray photoelectron spectroscopy (XPS) is a non-destructive surface analysis technique used to determine a material's elemental and chemical composition, using the photoelectric effect. In the XPS technique, a sample surface is irradiated with x-rays, typically from a monochromatic light source of energy hv. This excites core-level electrons of atoms in the sample, which meet the condition $hv > E_b + \phi$, where E_b is the binding energy and ϕ is the spectrometer's work function. These electrons are then ejected from the parent atoms as photoelectrons. The energy and number of the ejected electrons are detected and used to determine the elemental and chemical composition of the surface. Ejected electrons at shallow enough depths, determined by Beer's law[50], can escape and be detected by an electron energy analyser, returning the distribution of kinetic energies. Consequently, XPS can determine how the composition varies in the topmost surface layers, as well as the nature of adsorbates.

XPS can provide information on the valence state of elements and the presence of impurities or contaminants on the surface of a material. XPS analysis focuses on the spectrum of the intensity of the photoemission against the binding energy, over either the typical binding energy range of an element or over the full binding energy range, a survey. A range of kinetic energies of photoelectrons observed experimentally correspond to a series of binding energy peaks. For a constant energy monochromatic source, the kinetic energy of the photoelectron increases as the binding energy decreases. Each element has a unique set of core electron levels, acting as a fingerprint to identify them in the spectrum. The intensity of the photoemission is proportional to the intensity of the irradiating photons.

Changes to the chemical environment induce a chemical shift, a change in binding energy for a given core-level peak. Bonding, for example, can cause core-level electrons to be held more strongly to the atom, consequently making electrons more difficult to remove and, hence, have a greater binding energy. A series of core-level peaks in spectra, associated with atoms in different chemical bonds or states, can overlap, requiring additional interpretation during XPS analysis. Fitting, typically with software or bespoke code, using known peak position data is used to estimate the presence and relative abundance of elements in each chemical environment.

High-resolution XPS analysis, centred on the O 1s and F 1s core levels, is used to characterise H_2O and HF, respectively, incarcerated in deposited C_{60} in Chapter 5. This is paired with photoemission spectroscopy of the valence band and normal-incidence x-ray standing wave (NIXSW) analysis. The following section describes the NIXSW technique.

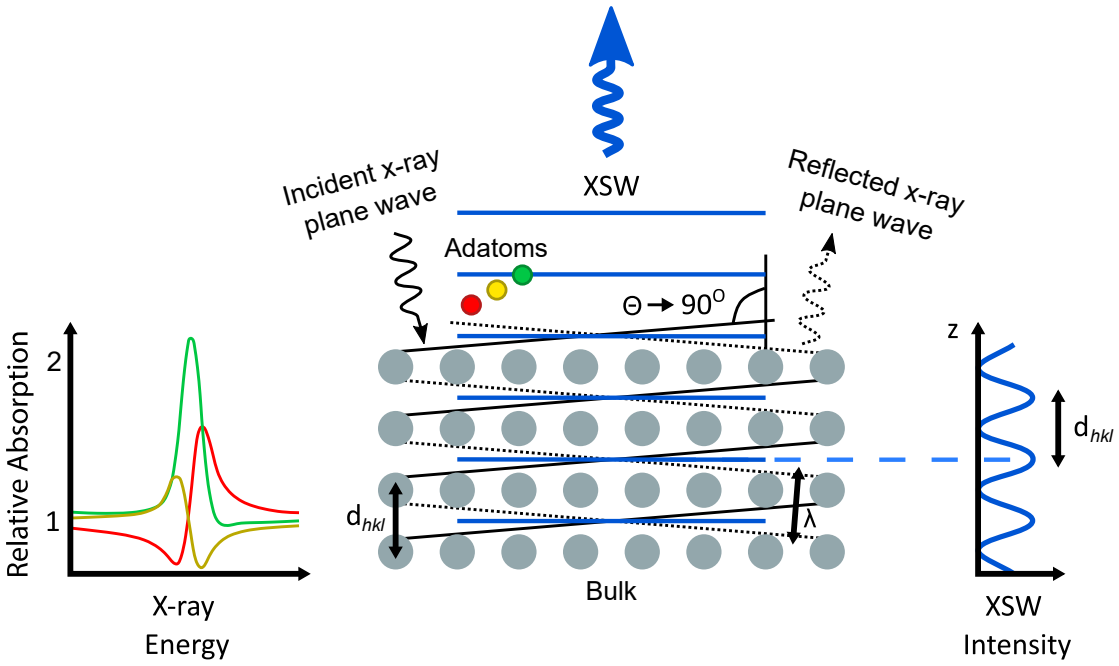

Figure 2.6.1: Production of an x-ray standing wave (XSW). An x-ray beam source directed into the bulk of a surface causes the incident and reflected waves with a constant phase difference to produce a stationary wave, with position-dependent intensity characteristic of the surface.

2.6.2 Standing wave production

Normal-incidence x-ray standing wave analysis (NIXSW, often simplified to XSW[4]) provides a primary source of quantitative structural data for the positions of adsorbed atoms and molecules, primarily on metal surfaces[51]. The method induces an interference pattern with x-ray photons between incident photons and those reflected from the crystal structure, depicted in Figure 2.6.1. The method exploits the x-ray standing wavefield that is created above the surface (and in the bulk) of a sample due to the interference of incident and Bragg-reflected photons; the photon energy is tuned to match the Bragg diffraction condition for the particular crystal planes of interest (see Figure 2.6.1). The resulting emission of photoelectrons allows one to identify the position of adsorbates on the surfaces with respect to the spacing of crystal planes, absorbing x-rays strongly when positioned at the anti-nodes and weakly when positioned at the nodes, with repetition at multiple planes ultimately triangulating their position in 3D space.

The desired XSW effect is realised experimentally by first aligning a crystal in a particular crystallographic direction, then directing an x-ray beam from a synchrotron source at the surface. The energy of the incident x-ray beam, E_0, is tuned to meet the Bragg condition, shown in equation 2.13, of the x-ray scatterer plane of the bulk material.

$$n\lambda = 2d_{hkl}sin(\theta) \qquad \{2.13\}$$

where n is the diffraction order, λ is the x-ray wavelength, d_{hkl} is the layer spacing of the x-ray scatterer planes in the crystal with Miller indices hkl and an angle θ between the plane and x-ray beam[52]. By aligning the crystal such that the incoming beam is at normal incidence to the scatterer planes, $\theta = 90°$, both the incident and back-scattered beam are normal to the plane. Hence, due to a constant phase difference, ϕ, the incident and reflected wave interfere, producing a standing wave. At the perpendicular distance from the atomic scattering planes z, the intensity of the standing wave, I, is given by equation 2.14.

$$I = \left|1 + \frac{E_{hkl}}{E_0} \exp\left(\frac{-2\pi i z}{d_{hkl}}\right)\right|^2 \qquad \{2.14\}$$

E_{hkl}/E_0 is a ratio between the energy of the incident and reflected beam.[52–54]

X-ray adsorption leads to the ejection of photoelectrons, Auger electrons, x-ray fluorescence photons, and other inelastic scattering events[53,55,56], by the photoelectric effect. Emission also depends on position with respect to the intensity maxima of the x-ray standing wavefield. Atoms centred at anti-nodes in the standing wave will radiate strongly. Conversely, atoms at nodes will not radiate and will be "invisible" experimentally[56]. As the incident x-ray is scattered multiple times, much like ϕ, the reflectivity of the crystal, R, is a function of E_0. This dependency, much like diffraction from defects or non-parallel planes, in crystals returns a flat-topped reflectivity curve (otherwise known as the Darwin or rocking curve[53,55,56]).

Measuring the reflectivity curve experimentally returns a very low reflectivity curve width, $\Delta\theta$. This places a significant limit on experimental sensitivity, and strict requirements on crystal quality and angular spread of the x-ray source. By consideration of equation 2.15,

$$\Delta\theta = \frac{\Gamma F_0}{sin(2\theta)} \qquad \{2.15\}$$

normal incidence ($\theta = 90°$) results in $sin(2\theta) \to 0$, and thus $\Delta\theta \to \infty$, rendering the reflectivity curve much wider. Γ is a constant dependent on the x-ray wavelength and volume of the unit cell, while F_0 is the structure factor for forward scattering[53]. Varying E while maintaining a fixed Bragg angle of normal incidence to the crystal's scatterer plane is typical in modern XSW experiments.

2.6.3 Characterisation with NIXSW

Detecting the emission of photoelectrons is integral to XSW measurements. Photoelectrons are amplified by a microchannel plate, with an integrated high pass filter, and detected using a digital camera-like CCD. Monitoring the intensity and position of photons hitting the CCD over a distinct timeframe enables photoemission (and Auger)

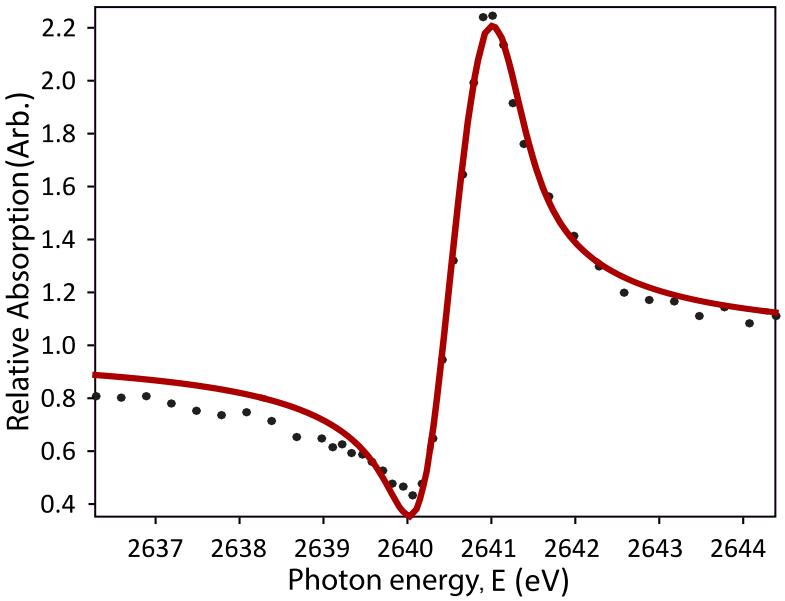

Figure 2.6.2: Example graph of XSW intensity against the Bragg energy for water-encapsulating C_{60} ($H_2O@C_{60}$) deposited on a Ag(111) substrate for the O 1s peak. The fit to the graph (red), combined with the reflectivity curve fit, returns a coherent position $P_c = 0.28 \pm 0.01$ and coherent fraction $F_c = 0.46 \pm 0.02$.

spectra to be acquired.

Taking the relationship,

$$\frac{E_{hkl}}{E_0} = \sqrt{R}\, e^{i\phi} \qquad \{2.16\}$$

and substituting into equation 2.14 yields the following relationship

$$I = 1 + R + 2\sqrt{R}\,\cos\left(\phi - \frac{2\pi z}{d_{hkl}}\right) \qquad \{2.17\}$$

Distance z is best treated as distribution dz over a periodic range d_{hkl}, due to thermal fluctuations and disorder at the crystal surface[53,55,56]. Hence equation 2.17 becomes equation 2.18.

$$I = 1 + R + 2F_c\sqrt{R}\,\cos\left(\phi - \frac{2\pi P_c}{d_{hkl}}\right) \qquad \{2.18\}$$

The new parameters here are the coherent position, P_c and the coherent fraction, F_c. Mathematically, these are the phase and amplitude of the first Fourier component of the real-space structures respectively[51]. The coherent position relates to the average height of absorber atoms above the Bragg planes, while the coherent fraction tracks the order of absorbing sites with respect to the plane[51]. $F_c = 1$ in a perfectly ordered system. All sites are in the same position relative to the projection of the bulk crystallographic planes.

Determination of the position of an adsorbate relative to the crystallographic plane normal to the beam requires a plot of I against E_0. An example XSW spectrum of water-encapsulating C_{60} ($H_2O@C_{60}$) deposited on Ag(111) for the O 1s peak is shown in Figure 2.6.2. A fitting algorithm[57] is deployed to determine the coherent position and fraction.

NIXSW lends spatial resolution to x-ray spectroscopy techniques, identifying the position of adsorbates on a surface relative to the extended crystallographic planes of the bulk crystal. In Section 5.3, NIXSW is used to track the sensitivity of C_{60}-encapsulated molecules to surface adsorption[58], utilising soft and hard x-rays produced by the synchrotron at Diamond Light Source in Oxford.

3 Far-From-Equilibrium Pattern Formation

3.1 Self-organisation

3.1.1 Dewetting thin films

A thin film is defined as a layer of material with thickness ranging from a few microns down to fractions of a nanometre. Thin liquid films on solid substrates appear everywhere in everyday life, from lubricant films on the cornea of our eyes or pistons in car motors, to decorative or protective coatings on our belongings. Unlike thick simple films, the stability and dynamics of thin films are complex due to the coupling of the many processes involved at these scales, including wettability, capillarity, diffusion, adsorption and excess intermolecular energy. Understanding the unique physics of thin films is essential for understanding the properties of materials of these thicknesses.

Dewetting is the term given to the spatial retraction of liquid from a non-wettable solid boundary over time. The simplest interpretation of the process is that of liquid adapting to the closest local equilibrium. The creation of an interface between materials has an associated energetic cost. A free-falling raindrop will try to minimise its surface area, and thus free energy, by forming a sphere. A droplet deposited on a solid surface balances three interfacial energies, between the solid-liquid, solid-gas and liquid-gas interfaces. The relationship between the three determines the macroscopic contact angle, and hence whether the liquid wets the surface or "beads up" and dewets[59]. While desirable for your raincoat to not become sodden during the rain, the oil lubricating a piston in the combustion engine of your car dewetting is suboptimal, to say the least.

Expansion of this concept to thin film brings numerous complications. The micro and nanoscale behaviour of liquid on a surface depends on long-range van der Waals forces and short-range polar and electronic interaction[60]. Dewetting in an unstable thin film proceeds by the rupturing of the thin film, and the formation of holes that expose the underlying surface, which then grow and coalesce, until the remaining threads of liquid break up by Rayleigh instabilities into individual droplets much like the raindrop example[61,62]. Rayleigh instabilities, however, do not fully describe the initial often nanoscale portion of the dewetting process. The complexities of the rupture event are described by a combination of nucleation, spinodal and hydrodynamic processes that mediate transition states in the film.

The physics of dewetting thin films is best characterised by a series of potentials coinciding with three different energetic states of the film: stable, unstable and metastable. These potentials are known as interface potentials, $\phi(h_z)$, functions which describe the free energy per unit area of two surfaces at a separation h_z. In this case, h_z represents the distance between the solid-liquid interface and liquid-air interface, the effective thickness of the film. The shape of the interface potential for each film state,

with generalised shapes shown in Figure 3.1.1, determines the stability of the film.

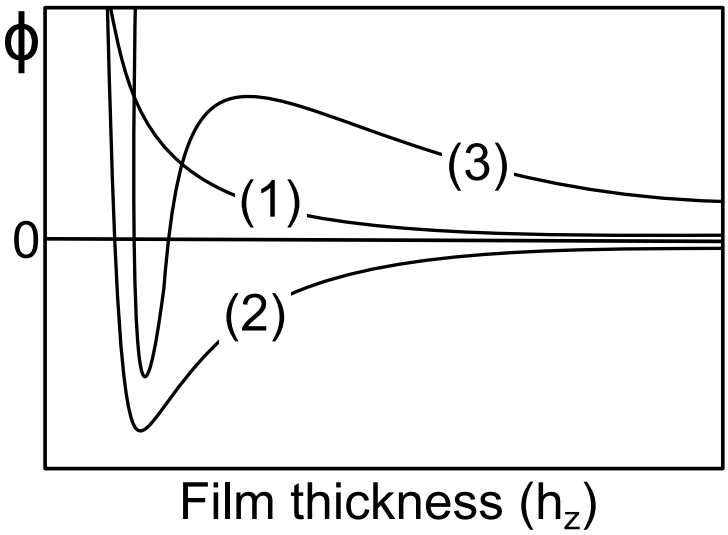

Figure 3.1.1: The shape of the effective interface potential $\phi(h_z)$ as a function of film thickness h_z for **(1)** stable, **(2)** unstable and **(3)** metastable films[63].

Curve (1) displays a monotonic relationship between the potential and film thickness. The film is considered to be in a stable state, as the thinning of the film always has an associated energy cost at any film thickness, and is hence not energetically favourable. Curve (2) represents an unstable state except at the minimum in the potential at h_z. The unstable film seeks to reduce its energy by thinning and spontaneously dewetting. Curve (3) is similarly unstable for small thicknesses where $\phi''(h_z) < 0$, whereas for larger film thicknesses, the film is stable. This describes a metastable state, characterised by a potential barrier the system must overcome to reduce its potential energy. A nucleation event by thermal activation in the film or at a local defect or impurity causes holes to nucleate, driving the system towards becoming unstable and dewetting, given the energy required for nucleation, represented by the local maximum in (3).[63]

The interface potential provides the surface excess free energy associated with the growth of a fluid film from a surface. By extension, there is a force the fluid exerts on the surface at a given film thickness, $\phi'(h_z)$, referred to as the disjoining pressure, Π. The disjoining pressure can conveniently be expressed in terms of aforementioned forces, a linear combination of three structural components, shown in equation 3.1,

$$\Pi = \Pi_w + \Pi_e + \Pi_s \qquad \{3.1\}$$

where Π_w arises from van der Waals forces between the film and substrate, Π_e accounts for short-range polar or electronic interactions, and Π_s accounts for variations in the structure of molecules in the thin film and the bulk liquid[60]. Modelling is an integral part of understanding interactions in a thinning film. Simulating forces exerted by

the fluid at a series of film thicknesses in kinetic Monte Carlo[64] and dynamic density functional theory simulations[65] provide an interesting means to construct the effective interface potential of a thin film.

3.1.2 The role of gold nanoparticles

Nanoparticles are crystalline pieces of matter with dimensions below 100 nm. A gold nanoparticle has vastly different physical properties from its bulk material counterpart, from minimised capacitance to quantum effects due to their size. Their usage as a dye predates the field of nanoscience by thousands of years[66,67], the origin of their red colour being that of blueshifted plasmon resonance in metallic nanoparticles of dimensions in the common nanoparticle range[68,69]. The synthesis of colloidal gold - gold sub-micron particles suspended in fluid - has grown easier and more consistent over the last few decades, cultivating interest from contrasting fields of scientific study.

Gold nanoparticles are initially stabilised to prevent aggregation and precipitation from the solution. Covalently or ionically bonding molecules, known as ligands, are commonly used to stabilise nanoparticles. Ligands passivate the gold core to lower the surface free energy of the nanoparticle as well as introduce a steric hindrance to nanoparticle coalescence. One of the more popular ligands for gold nanoparticles is thiol due to the strong affinity of the sulphur atom to gold, as initially observed with bulk gold surfaces[70,71]. This results in a highly chemically stable thiol-functionalised nanoparticle both in and out of solution, while still soluble in a wide array of organic solvents. Additionally, alkane chain lengths of the thiols can be modified at this synthesis stage to vary the resulting nanoparticle radii. Unlike charge-stabilisation[72,73], which has been shown to affect the packing of structures deposited on the surface due to repulsion of like-charged nanoparticles[74], ligand-stabilised nanoparticles are charge neutral.

Thiol-passivated gold nanoparticles, see Figure 3.1.2, particularly octanethiol ($C_8H_{17}S$)-passivated gold nanoparticles, were the primary solute for studies of self-organising nanostructures described in Chapter 4. Gold nanoparticles benefit dewetting experiments threefold: as a tracker and mediator of the solvent dewetting process, and as a potential means of electron transport[75–79]. Non-volatile nanoparticles suspended in a volatile organic, or inorganic, solvent, sometimes referred to as a nanofluid, cast on an ideally flat, smooth and homogeneous solid surface is a perfect system for the study of pattern formation under non-equilibrium conditions[80–83]. A static surface-bound nanofluid droplet of finite contact angle with a pinned contact line leaves behind a solute drying line around its perimeter as the solvent evaporates. The nanoparticles accumulated at the contact line self-pin the droplet by adhering to and modifying the surface at the perimeter, after the solute was deposited there via a compensating flow from the droplet centre during evaporation[84,85], as shown in Figure 3.1.3. The resulting "stain" acts as a history of solvent dewetting before complete solvent evaporation.

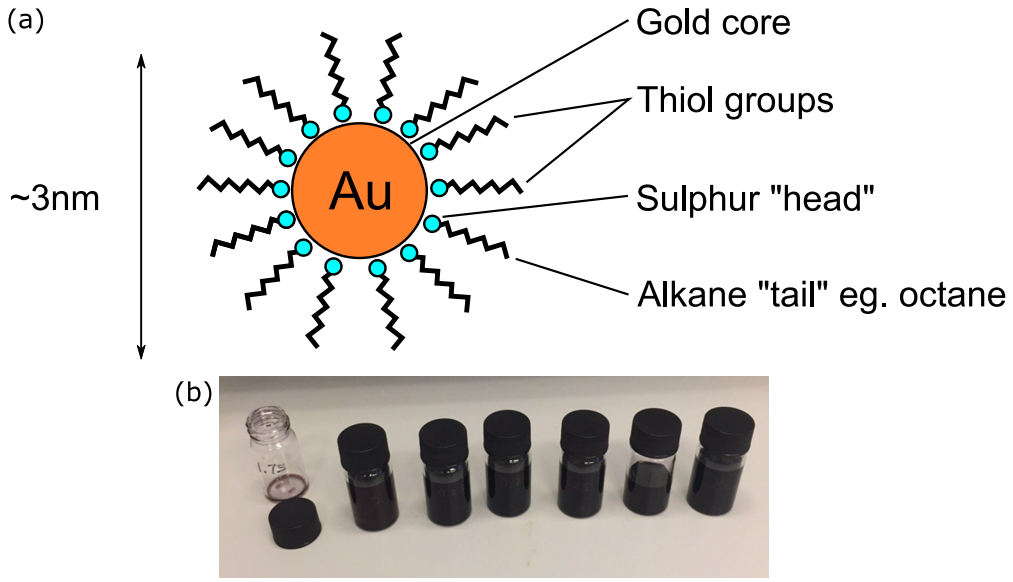

Figure 3.1.2: (a) The schematic structure of a thiol-passivated gold nanoparticle; **(b)** dilute solutions of octanethiol ($C_8H_{17}S$)-passivated gold nanoparticles of particle sizes 2-4 nm suspended in toluene, taking on a dark violet appearance in solution.

This concept naturally extends to a thin film, but with much more visually stunning results.

In thin films, nano and microscale patterning induced by dewetting colloidal gold solutions from the substrate results in a fascinating and diverse array of self-organised patterns[11]. Interactions at the interface and between constituents of the nanofluid lead to the formation of different aggregated structures. The non-equilibrium structures observed after dewetting are the result of drying-mediated self-organisation. Nanoparticle patterns broadly do not evolve in the absence of the solvent because the nanoparticles are kinetically trapped far away from their equilibrium state; the structure formed following evaporation is "frozen" in place[10]. Contrary to equilibrium structures, induced by the timescales necessary for self-assembly, far-from-equilibrium patterns are inherently indeterministic in their formation, and lead to interesting patterning and emergent properties, ripe for adaptive statistical analysis. Equilibrium structures exhibit limited adaptability, while non-equilibrium structures track the intricacies of the entire film breakdown process by a combination of real time[87–89] and real space[90,91] measurements. Stannard provides an excellent review of these patterns[11], including their extensive simulation with Monte Carlo methods, which will be covered later in Subsection 3.3.2.

Tables 3.1.1 and 3.1.2 provide examples of the foundational morphologies observed in colloidal nanoparticle assemblies formed in a far-from-equilibrium regime via rapid solvent evaporation, as observed by tapping mode AFM. Alkylthiol-passivated gold nanoparticles of diameter between 2 and 6 nm self-organise as the volatile solvent

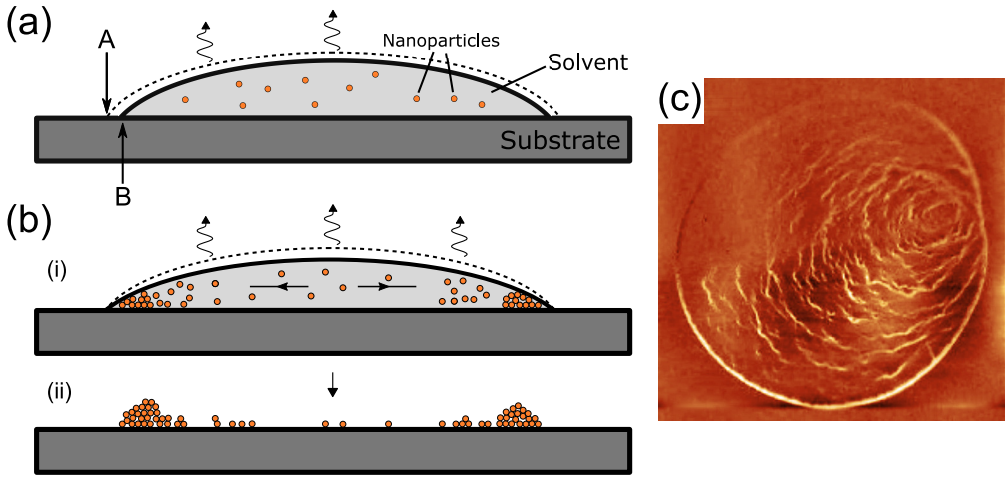

Figure 3.1.3: Schematic illustration of self-organisation in nanofluid droplets on a surface. **(a)** In an unpinned system, the contact line at point A withdraws to point B as the droplet evaporates, resulting in uniform evaporation. **(b)** In a self-pinned system, *(i)* nanoparticles accumulate at the perimeter of the droplet, preventing the retreat of the contact line from A to B. *(ii)* An advective current acts to replenish the lost fluid at the boundary, resulting in a ring-like "stain" on the surface as the solvent fully evaporates.[85]. **(c)** A 10 µL droplet of dodecanethiol-passivated gold nanoparticle solution left to evaporate in open air[86].

dewets from the flat surface, in this case, the native oxide layer (SiO_2) of a Si(111) substrate. The wide range of patterns arises due to variations in nanoparticle concentration, solvent, and deposition method. This, however, only explores a small portion of the available parameter space, with further parameterisation discussed in Subsection 3.3.1. Other nanoparticles, such as CdSe[92] and PbSe[1], similarly produce a wide variety of complex patterns upon a substrate.

The nanoparticle patterns observed in the literature typically fall into several broad classes including isolated islands[1,92,93], worm-like domains[1,92], spinodal and labryinthine structures[1,92,94,95], interconnected cellular networks[95–99], branching and viscous fingering-like fractal structures[95,100–102], rings, stripes and concentric circles[98,101,103–106]. These different structures have been found to co-exist on the scales of AFM scans at different nanoscopic length-scales, providing unique and striking multi-level patterns[10]. Automated classification of the most common morphologies into a broad number of categories is one of the core aspects of the machine learning protocols developed by the Nottingham Nanoscience Group[5–7] and described later in this thesis.

The strong spatial ordering of patterning and reproducibility of morphologies are owed to the dewetting mechanisms governing the solvent. The mechanisms and their capacity to create long-range ordering are evaluated in the next section.

Pattern type	Example AFM images	Distinguishing features
Islands	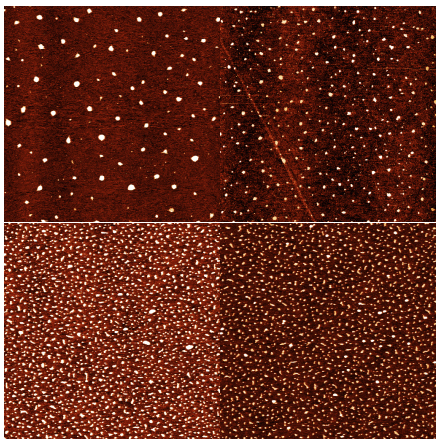	• Isolated mostly-circular islands • Typically uniformly distributed across the surface
Worm-like	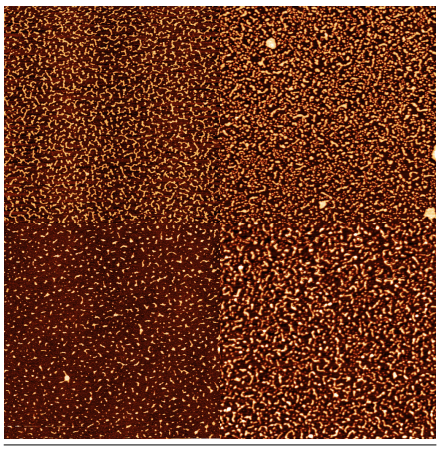	• Longer islands with a wide distribution of lengths • Appears like an intermediary phase between islands and spinodal/labyrinthine
Spinodal	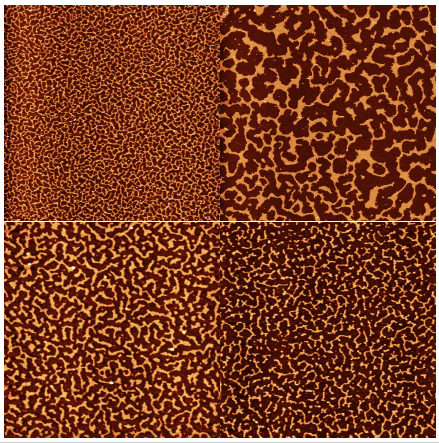	• Intertwined snake-like structures of modal thickness • Resembles that of patterns observed in spinodal decomposition

Table 3.1.1: Diverse patterns observed in colloidal nanoparticle assemblies formed in a far-from-equilibrium regime.

Pattern type	Example AFM images	Distinguishing features
Cellular	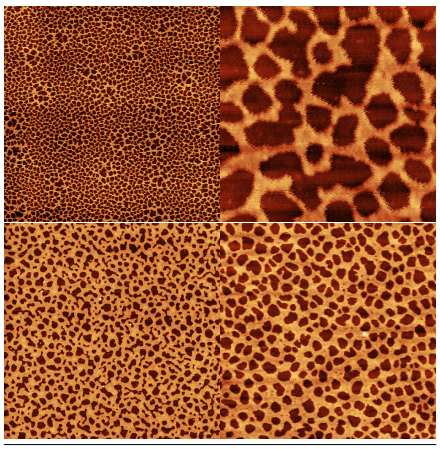	• Interconnected web-like arrays • Continuous walls between cells • Modal or bimodal cell sizes
Holes	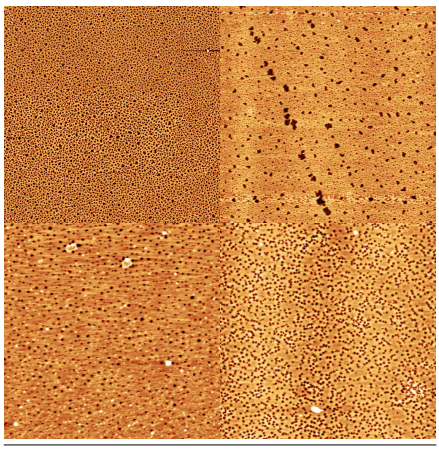	• A much denser cellular pattern with thick walls • Majority-circular holes in the nanoparticle film • Foam-like appearance
Fingering	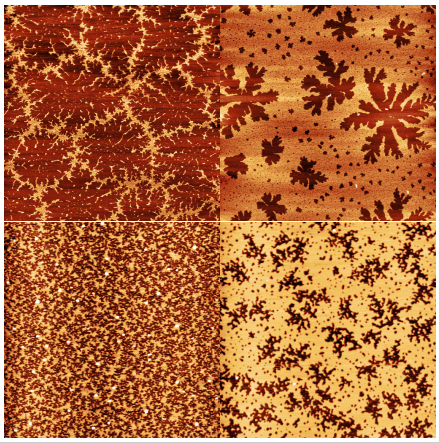	• Branching fractal-like pattern • Spanning microns in size • Non-periodic structure

Table 3.1.2: Further diverse patterns observed in colloidal nanoparticle assemblies.

3.2 Non-equilibrium pattern formation

3.2.1 Dewetting modes

We now turn to the prominent dynamics governing the drying and mixtures of liquids. This includes how they initiate and moderate the dewetting of the thin film upon a substrate, and their current understanding regarding how they are characterised in non-equilibrium pattern formation, both visually and statistically. Assessment and identification in both real experiments and simulations is essential for evaluating the capacity of a given parameter space. Spinodal dewetting, heterogeneous and homogeneous nucleation, and Marangoni convection account for many of our observations. However, these processes are by no means entirely distinct, processes coexist on length-scales observable by SPM, and often converge or diverge throughout the dewetting process. Each mechanism's reliance on different factors, such as film thickness and solvent stability, can mean conditions met by domination or nucleation of different processes that can initialise or diminish another, evidenced by multi-level dewetting patterns. Each mode's unique impact on the solvent and nanoparticle distribution is addressed here.

3.2.2 Spinodal dewetting

Similar pattern formations are apparent across wildly different natural systems, and are typically governed by local and simple interactions between components. For example, the morphogenesis that leads to complex patterns in mammal hides is of great evolutionary importance for communication, concealment or even thermoregulation[107], yet genetically coding the formation of such patterns runs against the economic nature of evolution. Evolution, however, stumbled upon reaction-diffusion systems, a means to let physics form patterns for it. Such a system would only require a few genes to set the gestational conditions for pattern formation.

Some of the most famous morphologies in reaction-diffusion systems are Turing patterns, named after Alan Turing. The activator-inhibitor principle, introduced in his 1952 paper, describes how dynamically-maintained yet stationary patterns emerged from a chemical reaction[108]. In a reaction with two products, one that catalyses the reaction and one that inhibits the rate of reaction, the products will spatially separate. This assumes both products are allowed to diffuse freely, and both products are removed from the system to maintain the concentration that stabilises the resulting pattern. Two potential Turing patterns, spots and labyrinthine, are shown in Figure 3.2.1. Figure 3.2.1 also depicts functionalised gold nanoparticles in toluene dewetting patterns imaged in AFM reminiscent of the presented Turing patterns. Though similar, the systems are driven by different self-organisation mechanisms, with the dewetting pattern predominantly driven by a process similar to "demixing" binary fluids.

Spinodal decomposition is the general label for spontaneous phase-separating processes

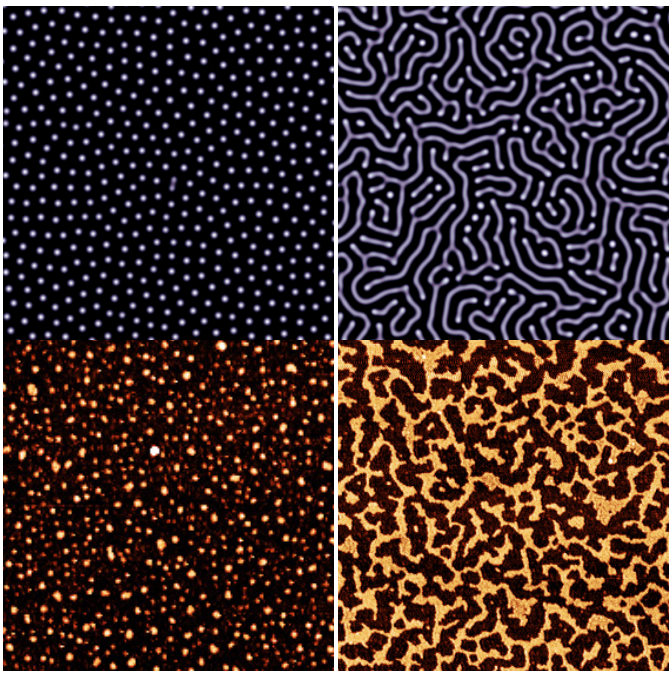

Figure 3.2.1: (**Top row**) Two different morphologies, spots and labyrinthine, in a simulated reaction-diffusion system based upon the activator-inhibitor principle, known as "Turing patterns"; **(bottom row)** comparable instances of island and labyrinthine gold nanoparticles in toluene dewetting patterns, primarily formed by spinodal decomposition between the solvent and substrate.

in mixtures of two materials, such as metals or polymers, initiated by amplifying local fluctuations in material density or composition. The conditions for this form of "demixing" phenomenon are met when it is more energetically favourable for a system to decompose into two phases. This is best described as a result of the shape of the free energy curve (or phase diagram) of a given system. The free energy curve, more specifically a plot of the free energy as a function of composition, ϕ, represents a quantifiable measure of the proportion of a material in the system, such as density or concentration. When completely concave, it represents a stable mixture at any value of ϕ, as there is an energetic cost to separation. However, in the case of a convex region being present in the free energy curve, like in Figure 3.2.2(a), the free energy of mixing in this region (F_0, ϕ_1) is higher than the free energy of a separation into two phases ϕ_2 and ϕ_3, F_0'. The mixture at this local maximum is hence unstable, sensitive to small local fluctuations, and liable to spontaneously decompose into these two phases.

The phase diagram for such a system is shown in Figure 3.2.2(b). Below the spinodal line, the system spontaneously separates, while above the coexistence curve, also known as the binodal line, the mixture is stable. Between these lines is a metastable state, a phase transition will occur if an activation energy is received. Quenching down from a temperature above critical temperature T_c through the critical point where the two lines meet, at composition ϕ_c, induces spinodal decomposition.

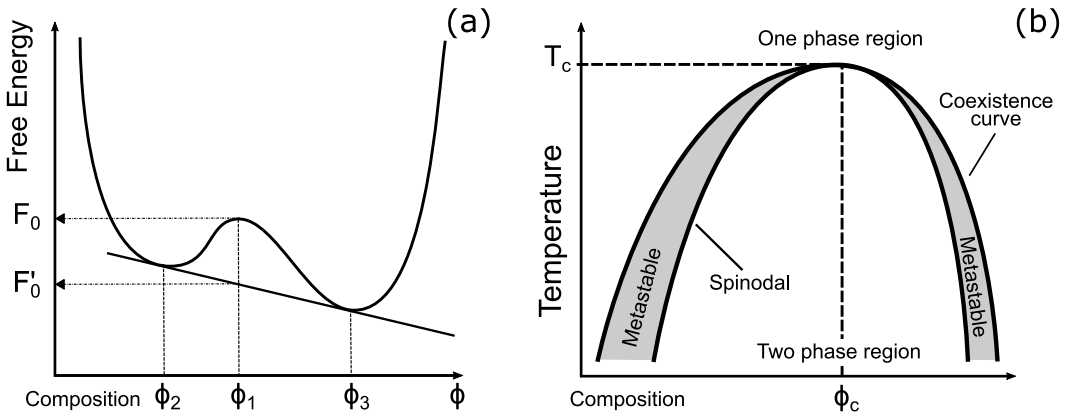

Figure 3.2.2: Graphs of mixtures of two materials in the case of demixing by spinodal decomposition. **(a)** The shape of a hypothetical free energy curve as a function of the composition; **(b)** a schematic phase diagram showing the interception of the coexistence curve and spinodal line, with spontaneous phase separation occurring below the spinodal line.

Spinodal dewetting is the equivalent of spinodal decomposition in unstable and metastable films, and is highly cited as a reason for patterns observed in a wide variety of dewetting thin film systems, from metals[109] to polymers[110]. The wetting transition, by which a stable film wetting a surface becomes unstable and dewets from the surface, shares many characteristics with phase separation in liquid-liquid systems. The first studies of extremely thin films ($\leq$10 nm) led to reproducible spinodal dewetting patterns coexisting with nucleated growth[111], with further studies suggesting a crossover film thickness for which both processes occurred before diverging to one or the other[110]. Spinodal dewetting is a far faster process than heterogeneous nucleation. This is due to the exponential growth of the fluctuations in the early stages of spinodal dewetting, combined with the film rupture event occurring when the amplitude of the undulation has a similar magnitude to the film thickness.

A defining feature of spinodal dewetting, like spinodal decomposition, is the resulting morphologies exhibiting a preferred length-scale. Fluctuations in an unstable film are a convolution of a large spectrum of wavelengths. These do not all grow at the same rate, short wavelengths have a prohibitively high energetic cost due to surface tension from the large surface area they create, while long wavelengths necessitate the transport of large amounts of matter, slowing the growth process significantly. Wavelengths that balance the consequent limitations lead to a local maximised growth rate and hence a preferred length-scale associated with a wavelength[112]. The perturbation of this wavelength leads to a process analogous to spinodal decomposition, with features in the phase separation correlated in size and shape to the wavelength as the film ruptures homogeneously in space and time. Preferred scales, however, are not exclusive to spinodal dewetting, previously noted convergences and divergences from nucleation-induced dewetting are expanded upon below. This characteristic preferred feature length is later used and extracted using Fourier analysis.

3.2.3 Nucleation events and growth

Nucleated dewetting places dependencies on the thickness of the thin film by means of an energy barrier. An unstable film dewets due to spontaneous amplification of a range of perturbation wavelengths - this is spinodal dewetting. Meanwhile, a metastable film will remain stable above a critical film thickness, hence, a nucleation event needs to occur that locally drops the film thickness below that threshold, rendering that area of film unstable and initiating dewetting. Once the nucleation event has occurred, this dewetted area will grow laterally in size and, assuming a local isotropic interface energy, symmetrically in all directions, as shown in Figure 3.2.3.

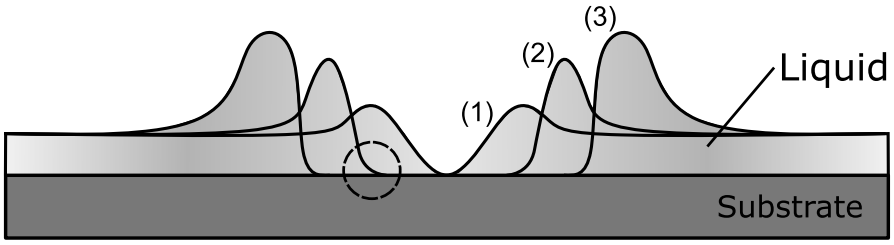

Figure 3.2.3: The evolution of a nucleated dewetting event in thin film. **(1)** A fluctuation in film thickness to below the critical thickness destabilises a small area of the film, causing it to dewet. **(2)** The (circled) contact region between the film and dewetted area of the substrate is similarly unstable, and hence dewets, forcing isotropic outward growth of the dewetted area. **(3)** The dewetting front continues to retract, and fluid accumulates at the ridge [113].

For systems with a low energy barrier for nucleation, such as when the thickness is close to the local maximum of the interface potential curve, or when the temperature is sufficiently high, the amplification of random thermal fluctuations in the surface of the thin film is enough the alter the film stability and induce the nucleation of a hole. This is referred to as thermal nucleation. The characteristic visual element of thermal nucleation is the nucleation event occurs randomly in space and time, with minimal correlation in location or size.

While the driving forces behind both nucleated and spinodal dewetting are the same, the true difference between these processes is how dewetting initiates. Spinodal dewetting begins spontaneously when the excess in intermolecular interaction energy per surface area of the film displays a positive curvature with respect to thickness. This results in fluid flow from thinner to thicker regions, eventually leading to film rupture. Much like thermal nucleation, the process can occur on chemically homogeneous substrates. However, in the case of a spinodally stable system in all areas of the surface, with insufficient thermal energy to surpass the local energy barrier, another source of rupture is required. Heterogeneous nucleation commonly fills this gap caused by defects or impurities on or in the surface, such as dust or cavities. A chemically heterogeneous substrate exhibits a contrast in wettability between chemically heterogeneous

areas of the substrate. The wettability gradient creates a fluid flow from less wettable to more wettable regions, which can induce rupture of the film along boundaries between the regions. Rupture at these boundaries induces characteristic "castle-moat" morphologies[106] around heterogenous patches on the surface.

On a region of homogeneous surface, the dewetting front will grow outwards isotropically from the site of the nucleation event. The rapid forced movement of fluid at the dewetting front can result in the accumulation of fluid, and hence nanoparticles, in a raised rim, with thickness dependent on fluid viscosity. Circular holes with a raised rim are a common signature of the involvement of nucleated dewetting processes.[109,114]

In real experiments, it is highly challenging to separate dewetting patterns into those caused solely by spinodal or nucleated processes by AFM imaging alone. Countless different factors affect the divergence and convergence of these two processes in a dewetting film, such as the evaporation rate and density of defects and surfactants. Plus, the transition from a stable to a metastable state commonly may be obfuscated by a low energy barrier for nucleation. A combination of the two processes is used to describe observations for the experiments described in this thesis.

3.2.4 Marangoni effect

The third candidate for pattern formation is a convective process. A thin film of volatile solvent on a solid surface produces an effective temperature gradient across the surface as it evaporates. A small disparity between the temperature of the surface of the substrate and the surface of the liquid will be dependent on film thickness, hence small fluctuations in the thickness of the film create hot and cool regions across the liquid surface. This results in a gradient in interfacial tension γ, which is dependent upon temperature, between these two types of region, with colder regions of the film surface having a higher interfacial tension. This, in turn, causes the movement of liquid from hot to cool regions to maintain the surface energy minimum. Surface tension acts to maintain the thickness of the film during this flow, hence, a convective flow is established. This self-stabilisation process for tackling instabilities in the liquid flow is called the Marangoni effect.[98,115]

The Marangoni effect has been shown to form a hexagonal pattern parallel to the film's surface, as observed by Bénard in 1900[116] and described theoretically in the 1950s[117,118]. The hexagons, sometimes referred to as Bénard cells, exhibit a fluid flow up from the cell centres and back down, tracing the liquid surface and the cell boundary as shown in Figure 3.2.4.

The physical parameters controlling the Marangoni effect in a system undergoing the described perturbations can be consolidated into an equation, equation 3.2, returning a quantitative parameter known as the Marangoni number M_a.

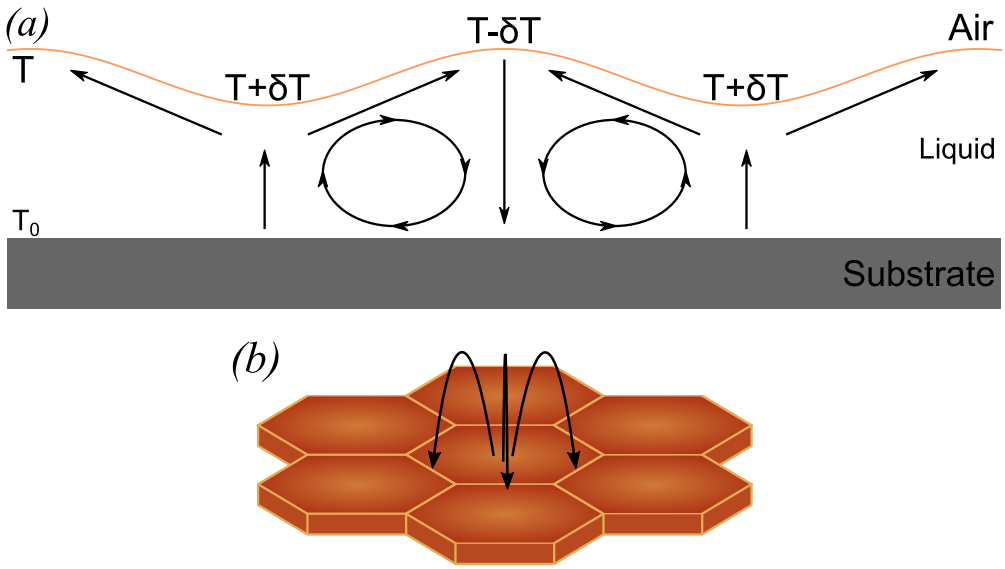

Figure 3.2.4: Schematic of Marangoni convection in thin fluid films.

$$M_a = \frac{Bh\delta T}{\rho\nu\kappa} \quad \{3.2\}$$

B represents variation in interfacial tension with respect to temperature ($-d\gamma/dT$), h is the film thickness, ρ is the liquid density, ν is the liquid dynamic viscosity, and κ the liquid thermal diffusivity, placing multiple strong dependencies on the properties of the solvent.

A critical value of the Marangoni number, below which a convective flow does not occur was found to be $M_c = 80$ for thermally-induced convection[118]. Hence, the characteristic wavelength of the instability λ is given by equation 3.3[115]

$$\lambda = 4\pi h\sqrt{\frac{2}{M}}. \quad \{3.3\}$$

A combination of equations 3.2 and 3.3 asserts that increasing the density and viscosity decreases the Marangoni number, which in turn increases the characteristic length-scale of convection cells. Density and viscosity depend primarily on the physical properties of the solvent and the concentration of nanoparticles within the solvent.

The experimental manifestation of the Marangoni effect in nanoparticle dewetting patterns is a characteristic polygonal pattern. Early evidence in the formation of nanoparticle nanostructured networks reported polygonal patterns with convincing links to Bénard-Marangoni convection[92] with reinforcement of findings of dependence upon temperature and nanoparticle concentration shortly after[99]. Nanoparticles were carried by the convective flow, the rings in Figure 3.2.4(a), self-organising primarily at the boundaries of the convection cells. While fairly promising as a descriptor of cellular

patterns, the equations describing the Marangoni effect cannot quantifiably describe all observed correlation lengths at that scale. Large scale structure with previously-observed dependence on this surface tension-driven effect is observed in the early stages of thiol-passivated gold nanoparticle experiments, using the above equations to aid characterisation, are discussed in Section 4.2.

3.3 Analysis methods

While it is useful to visually categorise and scrutinise the myriad of patterns generated by thin film experiments, the ever-growing assortment of historic data, simulated data and new experimental data of growing complexity demands a substantially more rigorous, quantitative approach. Fourier transforms, Voronoi tessellations, and Minkowski morphometry are three key analytic methods for feature extraction from images containing nanostructures. In this thesis, these methods saw new exploration in Python, R and Matlab to develop new tools for extracting statistics from real or simulated AFM images containing semi-ordered nanostructures. Application of the right tools to the right system is critical. While Voronoi tessellations provide insight into the physics of island and cellular gold nanoparticle dewetting patterns, their use in their current form does not expand to other pattern types. Similarly, current Fourier analysis tools do not respond positively to nanostructure ordering beyond two configurations in the same image, such as images containing premeditated heterogeneities. Developing new or adapted versions of tools, or even data treatments to images such that they work with older tools, is essential for the perception of these far-from-equilibrium processes. Subtle variations in surface patterning that are impossible to interpolate with the naked eye provide important clues as to the roles of different mechanisms at play during self-organisation.

3.3.1 Systematic experimentation

Observations before, during, and after the evaporation of colloidal solutions of nanoparticles from solid surfaces continue to be a mainstay of the field after more than twenty-five years[119]. The ease of synthesis of near mono-disperse metal nanoparticles functionalised by diverse ligands, and the availability of modern microscopy and analysis techniques, leads to a highly tailorable experiment. The core dewetting experiment of preparing a suspension of non-volatile nanoparticles in a volatile solvent, preparing a flat substrate, depositing the solution onto the substrate, and then probing the resulting surface has been systematically explored, probed and modified at all stages throughout the literature.

Pre-Deposition

A volatile solvent such as toluene, dichloromethane, hexane or chloroform is preferred for far-from-equilibrium conditions, while less volatile fluids are preferable for droplet contact angle study. Solution additives such as salts[120] and excess ligands[121] could

also be used to modify the solution without alterations to the synthesis of the functionalised nanoparticles or choice of solvent. Toluene was the primary solvent in this thesis, as it was known to take on nearly all morphologies of dewetting patterns identified and categorised in modelling, exclusively by systematic adjustment of nanoparticle concentration. The molecular dyad deposition experiments also used toluene, as they required a non-polar solvent to prevent the dyad from precipitating out of the solution. All performed experiments here involving gold nanoparticles used octanethiol ($C_8H_{17}S$)-passivated gold nanoparticles of particle sizes 2-4 nm suspended in toluene purchased from Sigma-Aldrich, diluted in further HPLC-grade toluene. Similar solution additives were not explored, but co-deposition with suspended buckminsterfullerene was studied in Subsection 4.3.1.

The choice of ideally homogeneous, flat and smooth surface being coated is of critical importance to dewetting, particularly in the form of the aforementioned interface potential. Choice of substrate and its preparation dictate surface roughness, the hydrophilic/phobic qualities of the substrate, and the density of defects or heterogeneous sites, all of which cause significant changes in pattern formation and the contact angle of deposited droplets or retracting fluid[63,120,122]. Experiments using non-equilibrium conditions for evaporation often use substances such as native oxide terminated silicon[100,123], highly-oriented pyrolytic graphite[92], silicon nitride[124], or carbonaceous film[125] as a substrate. Substrates chosen for presented dewetting experiments are covered in Section 2.5.

While the wetting properties of free surfaces and laterally homogeneous substrates remain a significant area of study, recent work has focused on patterned substrates. Previous modelling has suggested the involvement of heterogeneous sites, such as dust, microcavities, chemical contaminants, variations in oxide layer thickness in silicon surfaces, variable chain adsorption, etc., generate local patches of surface properties different from the surrounding substrate[126]. The interplay between the preferred length-scales of dewetting patterns and these local variations in surface properties became an area of intensive study[127]. Patterned substrates have more apparent heterogeneities designed to act as a mediator of dewetting, induced by a variety of methods throughout literature.

5 mm internal diameter teflon rings placed on a prepared surface, then a droplet of solution placed at the centre, causes a dewetting process similar to droplet deposition but with liquid thinning starting at the centre. This meniscus-mediated deposition allowed for simultaneous far-from and close-to equilibrium structure formation, which would appear in the resulting dewetting pattern dependent on radius within the ring[86]. A breath figure approach, by which water droplets condensed on the surface at oxidation-induced adsorption sites act as a template, produced nanoparticle ring perimeters around a denuded area focused on these sites[106]. Electron beam patterning[128,129], and deposited chemical quantum dots[130] and nanorods[131] similarly act as

distinct sites of sizes similar to the length-scales of dewetting patterns to disrupt regular dewetting. Localised oxidation has been shown to create microscale regions of heterogeneous surface, which support dewetting patterns on top that are quantifiably different to that of the surrounding surface, with high precision using an AFM tip[132]. New surface properties and the effects upon dewetting by the tip-induced oxidation approach are further explored in Subsection 4.3.3.

Deposition

The method of nanoparticle deposition of a solution onto a prepared substrate is equally critical in determining the key self-organisation processes and final morphology. Once deposited, the evaporation process begins immediately for a volatile solvent, with remnant nanoparticles spontaneously forming assemblies by self-organisation. Two popular methods for solution deposition are discussed below.

Droplet deposition is a common approach to enable slow localised solvent evaporation. A droplet of solution is left to evaporate from the surface in the open air. The appearance of the droplet is dictated by the contact angle, determined by the solvent-substrate, substrate-air and solvent-air interface potentials. A non-finite contact angle means the droplet has no structural integrity on the surface, and the solution wets the surface. The solute accumulates at the edge of the droplet, giving a thick drying line of particles. As the droplet evaporates, a series of pinning events, where the radius of the droplet has competing shear forces from liquid surface tension and retraction of liquid from a hydrophilic to hydrophobic region of the surface, result in concentric rings of solute. Such formation is often compared to coffee stains[104,133,134]. While a slow and controlled evaporation approach provides a diversity of macro and micro scale patterns, often with multiple layers, long-range ordering similar to that found in thin film is difficult to emulate. While solution additives can modify the contact angle to a point where such ordering is present[124,135], the dewetting pattern is incomparable to those produced by the dewetting of a true thin film.

Spin-casting, or spin-coating, is the most widely-used technique for the deposition of solution onto solid substrates, and the primary deposition method for performed experiments. The technique is particularly popular in the electronic device fabrication industry, primarily for coating photo and electron resist layers prior to lithography. Here, thin film is achieved during the deposition stage, prompting forced evaporation resulting in the desired far-from-equilibrium morphologies. The substrate, typically a 1 x 1 cm^2 sample, is held by a vacuum chuck in a shielded chamber, and then tens of microlitres of solution are pipetted onto the sample, such to make a meniscus over the entire substrate. The sample is sealed in the chamber and made to rapidly spin up to a target speed, typically a few thousand revolutions per minute (rpm) at a target acceleration, held at the target speed for a few seconds, and then returned to a standstill. While speeds and durations significantly affect the final film thickness, beyond

a trivially met threshold spin speed and duration, they are largely irrelevant[136]. The process is split into stages outlined in Figure 3.3.1, providing a consistent process to produce thin films.

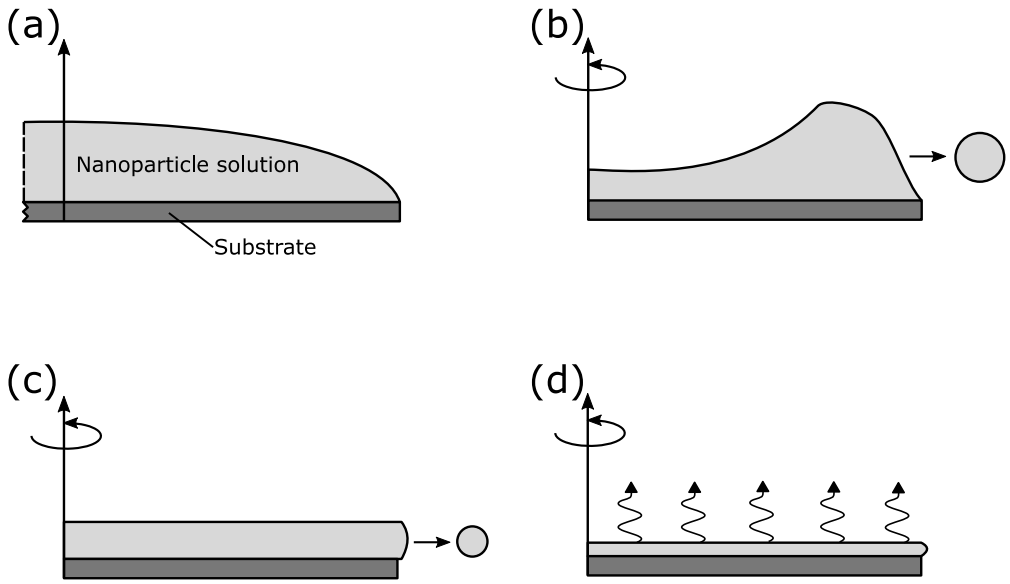

Figure 3.3.1: The different stages in the spin-casting process. **(a)** Nanoparticle solution is pipetted onto the substrate; **(b)** the substrate spins up to the target spin speed, during which the majority of solution is thrown off due to acceleration forces; **(c)** at a steady angular velocity, fluid thinning is dominated by a viscous outward flow; **(d)** as the coating further thins, solvent evaporation dominates the thinning process[113].

Observation during deposition, and short and long-term thereafter, provide unique insights. The spin-casting process has previously been monitored using an optospinometer, by which laser light is reflected from a spinning sample[137,138]. Observation of the reflected rays, in conjunction with the known refractive index of the solvent and wavelength of the laser, extracts a time dependence on film thickness. Such apparatus has previously identified a dependence on the chain length of passivating thiols, with solutions of suspended octanethiol-functionalised gold nanoparticles taking approximately 0.74 ms for the last nanometre of solvent to evaporate fully. Identifying this time frame is significant in evaluating a relative time frame in modelled dewetting.

Post-Deposition

AFM and electron microscopy remain popular tools to probe the resulting surface, with tapping mode AFM used almost exclusively as the probing tool in performed experiments. The typical scan size limits for both are adequate for fully evaluating known pattern morphologies. Experimental image data produced by these tools are processed in external processing and analysis software, such as Gwyddion[139], WSxM[140] and ImageJ[141], or via bespoke code. Charge transfer properties evaluated with $I(V)$ curves[76] and small-angle x-ray scattering to evaluate aggregate sizes serve as further

post-deposition analysis techniques[93]. While temperature and humidity strongly influence pattern formation during deposition, they can also assess post-deposition pattern stability. Further stability tests include annealing, exposure to solvent, and AFM probes in tapping mode.[91,93]

Systematic experimentation with controllable characteristics provides room for countless matched pairs experiments, even with AFM upon the final surface as the exclusive probing method. External pattern manipulation has proven to be a substantial field, providing physicists with fabrication routes without modifying the underlying solution or substrate chemistry. Quantification of the AFM images converts the visual data into comparable statistics, with key methods for doing such for dewetting patterns discussed later in this section.

3.3.2 Modelled dewetting

Modern simulation physics can highly accurately reproduce the appearance of AFM images, including those of self-organised nanoparticle assemblies[11,95]. By the time a single experiment based upon the previous section was finished, including AFM image processing with segmentation to give a binary image of nanoparticles and surface, a model has produced over 10^5 simulated images exhibiting similar dewetting patterns. Such simulations replicate all the structures in Tables 3.1.1 and 3.1.2 across multiple length-scales. The sheer volume of images produced renders it a potent medium to test current analysis techniques or develop new ones, such as powerful new machine learning-based categorisation tools, all of which can then be applied to real data with higher confidence. Such simulation work continues to develop within the Group, and acts as a substantial backdrop for performed experiments in Chapter 4, and software developed in Chapter 6. Below the underlying principles for such work are laid out, starting with the basic model and then moving to the relevant surface science application.

The Monte Carlo model is a foundation of simulation methods in modern physics, with applications in any system with a probabilistic interpretation[142]. Surface science particularly utilises an adapted 2D solution to the Ising model using Monte Carlo methods to investigate time-dependent dynamics upon a surface. The 1925 formalisation of the model describes a ferromagnetic system consisting of discrete variables that represent magnetic dipole moments of atomic spins[142]. On a square lattice of size L x L, each site, i, has spin $\sigma = \pm 1$, "up" or "down". The total energy of a lattice configuration is given by the summation of all interaction energies between the ith and the adjacent jth sites, giving the Hamiltonian shown;

$$E = -\frac{J}{2}\sum_{i,j}\sigma_i\sigma_j, \qquad \{3.4\}$$

where J represents the energetic favourability of the interaction between the sites, with

the same units as energy. The spin-aligned case ($\sigma_i = \sigma_j$) is energetically favourable, energy $-J$, while the opposed-spin case ($\sigma_i = -\sigma_j$) has an associated energy cost of $+J$. Such a system is affected by an effective temperature, T, meaning the Maxwell-Boltzmann probability distribution defines energy at each site. The energetic cost for a spin state to switch at each site is given by an energy barrier, ΔE, hence, the probability of of any lattice configuration of spins at equilibrium is given by equation 3.5

$$P = \frac{e^{-\Delta E/k_B T}}{\sum_\sigma e^{-\Delta E/k_B T}}, \qquad \{3.5\}$$

where k_B is the Boltzmann constant.

The lattice configuration will not entirely evolve in perpetuity. The system will generally tend to a steady equilibrium state based upon T, with the lattice dominated primarily by one of the two spin states. An unstable yet equal presence of both states in the lattice is met at a critical temperature T_C, representing a discrete phase boundary. While a highly complex analytical solution exists[143], the spatially unstable yet statistically stable nature of the system lends itself to a simple solution using the Monte Carlo model. The evolution to reach the equilibrium state is dictated by the Metropolis-Hastings algorithm, developed in 1953 and generalised in 1970[144]. The algorithm is portrayed in Figure 3.3.2, at each lattice site, the opposite state to the current state is trialled in turn, determining whenever it is energetically favourable to switch.

Algorithm: Metropolis-Hastings Acceptance

Result: System in equilibrium

Generate initial lattice grid with random σ;

while *not in equilibrium* **do**
  Select random grid site;
  Invert $J_0 \rightarrow J_1$;
  $\Delta E = E_1 - E_0$;
  if $\Delta E < 0$ **then**
    Accept J_1;
  else
    Generate random number, η;
    if $\eta < \exp(-\Delta E / k_B T)$ **then**
      Accept J_1;
    else
      Reject J_1 and restore J_0;
    end
  end
end

Figure 3.3.2: The Metropolis-Hastings Accept/Reject algorithm, in terms of the Ising model[145].

Equilibrium states from the Metropolis-Hastings algorithm of the 2D Ising model are shown in Figure 3.3.3. The algorithm's limited complexity as a series of logic statements applied to individual sites renders it highly suitable for parallel computing. The thermal energy component means this naturally expands to thin films evaporating.

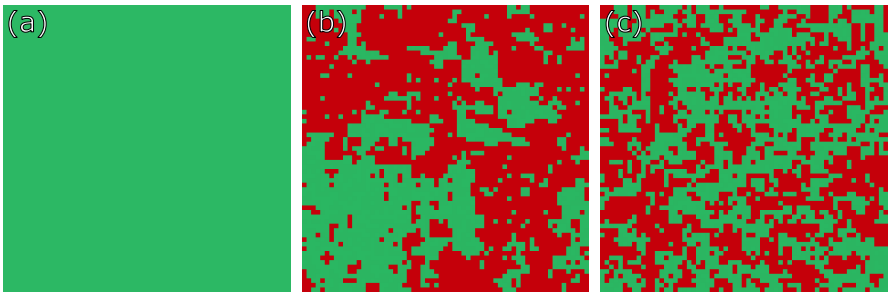

Figure 3.3.3: Three different Ising model simulations in their equilibrium states. **(a)** $T << T_C$; **(b)** $T \approx T_C$; **(c)** $T >> T_C$.

A computational approach proposed by Ge and Brus in 2000[92], and developed by Rabani *et al.* in 2003[1], generated real-time dewetting models using Monte Carlo methods, with moderate success[93,95,97]. While the Ising model's titular purpose was to describe the spin in 2D ferromagnetic systems, the Rabani *et al.* model expanded the possible cell states from "up" and "down", to "liquid", "nanoparticle" and "substrate". The

spin system effectively illustrates the "evaporation" of a liquid state. A controlled fraction parameter, C, dictates the initial coverage of nanoparticles in a circular boundary condition 2D grid, deposited from a thin film solvent, a liquid state on the grid liable to dewet from a site due to spatial-correlations and thermal energy, leaving behind a bare substrate state. Interaction between grid sites can be represented by the modified Hamiltonian in equation 3.6,[146]

$$E = -\epsilon_l \sum_{i,j} l_i l_j - \epsilon_n \sum_{i,j} n_i n_j - \epsilon_{nl} \sum_{i,j} n_i l_j - \mu \sum_i l_i \qquad \{3.6\}$$

where μ is the chemical potential responsible for determining the mean density of solvent at equilibrium, and ϵ_n, ϵ_l and ϵ_{nl} are the interaction energies between nanoparticles, liquid, and nanoparticles and liquid at neighbouring sites i and j respectively.

The liquid states operate on a similar principle to the aforementioned Ising model example. Each liquid state evaluates the state of surrounding sites in an attempt to convert the solvent phase from liquid to vapour via the Metropolis-Hastings acceptance algorithm. Nanoparticle states exhibit a random walk, moving up, down, left or right, provided the new position is surrounded by liquid states (a "wet" site). This is analogous to the diffusion of nanoparticles suspended in the solvent, where they have little agency otherwise. Diffusing nanoparticle states displace liquid states to be positioned in the wake of the nanoparticle, such to preserve solvent density[95]. Much like the dewetting of the liquid state, this walk is governed by an independent Metropolis-Hastings acceptance algorithm. Each Monte Carlo step, as in each full loop in the Metropolis-Hastings algorithm ran upon each liquid state, represents MR steps of the loop governing the nanoparticle random walk, where MR is a user-set 'mobility ratio'. The progression from the initial grid to an ordered structure, in this case labyrinthine, is shown in Figure 3.3.4.

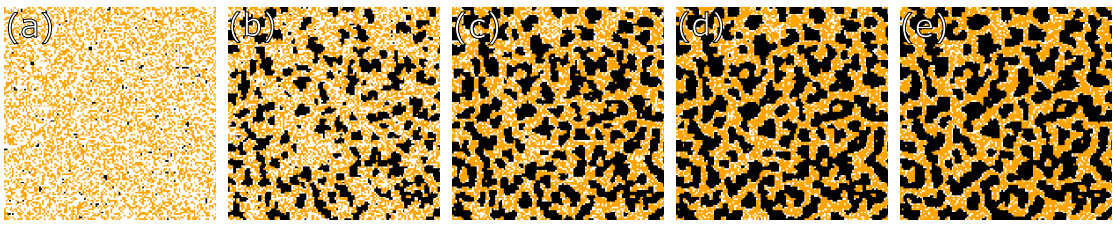

Figure 3.3.4: The evolution of a single Rabani *et al.* Monte Carlo simulation as it progresses from an initial grid of states; substrate (black), liquid (white) and nanoparticles (orange). The starting parameters are given as $k_BT = 0.35$, $\mu = 3$, $MR = 1$, $C = 0.4$, $\epsilon_{nl} = 1.5$, $\epsilon_n = 2$ & $L = 128$. **(a)** 0 steps; **(b)** 25 steps; **(c)** 50 steps; **(d)** 75 steps; **(e)** 100 steps. From Gordon *et al.*, Nano Letters 20(10), 2020[9]

The evolving system often settles into the pattern morphologies observed experimentally, with the liquid state dissipating from the grid. By tuning a handful of factors in the software, commonly μ and k_BT[95], the model returns a continuum of these morphologies indistinguishable from real data, shown in Figure 3.3.5. Such simulated data

is exploited throughout as a means to test a handful of analysis tools newly adapted to nanostructures, as discussed in Subsections 3.3.3 to 3.3.5 below and applied in Section 4.1.

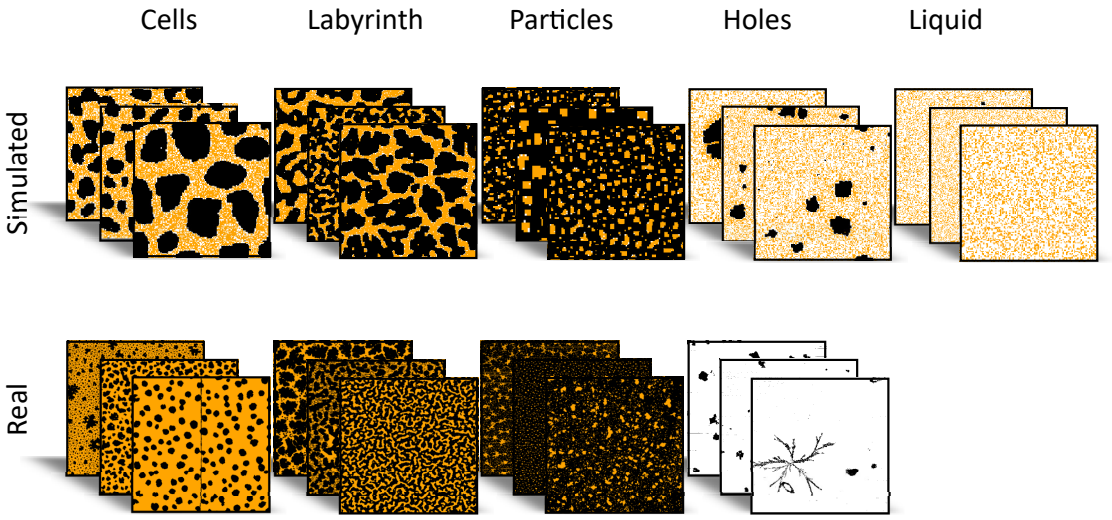

Figure 3.3.5: Examples of the distinct structures attainable from simulation as compared to observed AFM images of dewetting patterns. The colour scheme for states in simulated data (top row), substrate (black), liquid (white) and nanoparticles (orange) are applied to the real data (bottom row) using segmentation, producing binary images that integrate seamlessly into analysis and categorisation software tested upon simulated images. As such, the columns represent automated categorisation of the real images, using manual labelling of the simulated images as training data for a convolutional neural network (CNN) designed for this purpose. From Gordon *et al.*, Nano Letters 20(10), 2020[9]

3.3.3 Voronoi tessellation

A problem-solver across countless scientific fields, Voronoi diagrams provide a concise way to generalise polygonal systems, and hence quantify both cellular and isolated island patterns. A 2D Voronoi diagram takes the appearance of a series of tessellating irregular convex polygons, often coined Voronoi tessellations, generated by a series of seeding sites from which a perpendicular bisector is drawn between their nearest neighbours. These polygons, or cells, hence define regions that are closest to their encapsulating site than any other site[147]. The simple premise and construction of Voronoi diagrams allow for mapping of them to a multitude of systems in neighbouring fields, such as the Wigner-Seitz unit cell, with similarly uncomplicated acquisition of useful statistical information.

The Voronoi tessellation, and associated graphs, were plotted for viable systems containing island, hole or cellular morphologies, using protocols developed within the Group[96,97]. Island and hole patterns were mapped by treating the centre of each island or hole as a seeding site, while cellular patterns were mapped with the centroid of each cell, such that the cell edges line up both physically and in the resulting Voronoi diagram. The results for each case are shown in Figure 3.3.6.

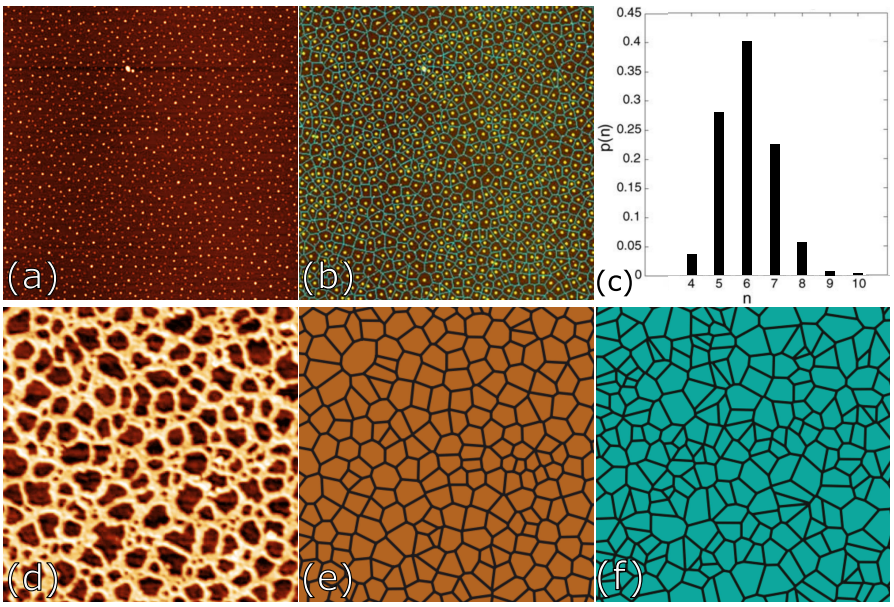

Figure 3.3.6: **(a)** 30 x 30 μm^2 tapping mode AFM image of spin-cast dendrimer-functionalised gold nanoparticles from toluene onto a native oxide-terminated Si(111) substrate exhibiting an island pattern; **(b)** A Voronoi tessellation constructed using islands as seeding sites; **(c)** Histogram of the probability, $p(n)$, of finding an n-sided cell in (b), giving $\bar{n} = 6.01$, $\mu_2 = 0.92$ and $S = 1.37$. **(d)** 1.5 x 1.5 μm^2 tapping mode AFM image of spin-cast functionalised gold nanoparticles from toluene onto a native oxide-terminated Si(111) substrate exhibiting a cellular pattern; **(e)** The Voronoi tesselation of (d), returning $\bar{n} = 5.94$, $\mu_2 = 1.19$ and $S = 1.48$; **(f)** The Voronoi tesselation generated with a completely random (Poisson) set of points[10,11].

While a skeleton-like format of existing images may be partially useful for the visualisation and length measurements of the morphology, they can also be used to measure order or disorder in structure. Previous reports of deviation from Poisson statistics by Voronoi diagram mapping over nanoparticle assemblies were interpreted as indicative of spatial order[96,97]. Voronoi tessellations generated with a completely random (Poisson) set of points, $p(n)$, the probability distribution for finding a cell of n sides, will empirically take on an asymmetric shape. $p(n)$ here peaks at the mean sidedness, $\bar{n}$, with variance μ_2, which is followed by a tail into greater values of n. The orderliness of the distribution of points is measured with the so-called Voronoi entropy. Entropy, S, here is defined by equation 3.7.

$$S = -\sum p(n) \ln p(n) \qquad \{3.7\}$$

Elucidation of the degree of spatial correlation in nanoparticle assemblies is by comparison of their tessellation's μ_2 and entropy, S, to those of the Poisson-generated tessellation. $S = 1.71$ and $\mu_2 = 1.78$ for the Poisson-generated tessellation[148]. As the archetypal disordered system, these values act as the lower boundary, and hence, values lower than these for Voronoi diagrams based on experimental data suggest an underlying source of correlation.

3.3.4 Minkowski morphometry

Mecke demonstrated the effectiveness of morphological measures in systems driven far from equilibrium undergoing spinodal decomposition in the aforementioned Turing patterns[149,150]. The measure in question was Minkowski functionals, which provide a small range of easily extracted parameters to characterise irregular structures. The Minkowski functionals in a 2D domain are the area, A, perimeter, P, and Euler characteristic, χ. The latter is the most prominent member of this family, defining the connectivity of spatial patterns.

All three measures are calculated through a simple algorithm[151]. Conveniently, images produced by simulations are quantised, and the two potential states, "nanoparticle" and "substrate", are assembled on a grid, so the algorithm effectively counts pixels. A is the number of pixels containing particles, P is the number of pixel edges shared by particles and particle-free substrate, while χ identifies and counts all connected and disconnected regions pixels in the particle state, and subtracts the frequencies of holes in those regions, containing the substrate state. Real images must be binarised first, defining each pixel in the image as either the particle-free substrate or as containing nanostructures by a process called segmentation. Techniques for segmentation of images viable for Minkowski measurements are discussed in Chapter 6.

Comparative measures highlighted the necessity of a scale-invariant version of these measures, essential for subsampled images, comparing real to simulated images, and comparing AFM images of different scan sizes. These scale-invariant measures are given in equations 3.8

$$\tilde{A} = \frac{A}{L^2} \qquad \tilde{P} = \frac{P}{2N\sqrt{\pi \bar{A}_p}} \qquad \tilde{\chi} = \frac{N_0 + N_1}{2N_0} \qquad \{3.8\}$$

where L is the physical length of the image, N is the larger number between the number of particles or holes, $\bar{A}_p$ is the average particle area, N_0 and N_1 are the number of particles and holes present respectively. The equation for $\tilde{P}$ assumes the particles are circular. The denominator can be replaced with $LN^{1/2}$ in the case of square particles, a common alteration in modelled data to prevent distortions with scaling. The modification to the Euler characteristic is to calculate a ratio between particles and holes.

The intersection of the three parameters for binary images of nanostructures provides a unique means of distinguishing and labelling pattern morphologies in a purely statistical manner[152]. Minkowski morphometry in the form modified for scale-invariant metrics aimed to enhance this purpose, demonstrated using principal component analysis (PCA) in Subsection 4.1.1 and explained in Subsection 3.3.6. New numeric classification of data-mined and simulated images of gold nanoparticle dewetting patterns, namely convolutional neural networks (CNNs)[9], aimed to replace Minkowski metrics as a labelling system. This was prompted by instabilities first observed by Stannard

et al.[95], by which the manual labelling of a continuum of morphologies in simulated nanoparticle dewetting data did not match that of scaling of the scale-invariant Euler characteristic. Data mining for that CNN, as well as for preceding machine learning-based segmentation, is covered in Chapter 6.

3.3.5 2D Fourier transforms

The correlation length is a universal parameter gleaned from various surface features. The distance between features within a nanoparticle dewetting pattern AFM image can correspond to the spacing of islands of deposits, distances between worm-like domains, the width of the labyrinthine pattern, or the density of holes or pores in the nanoparticle film, rendering it a transferable measurement across all morphologies. These distances, in turn, correspond to a convolution of spatial frequencies, these spatial frequencies can be presented in a reciprocal space in the form of a discrete Fourier transform. This could be obtained directly from processed AFM images within Python using a two-dimensional fast Fourier transform (2DFFT).

Periodic structures upon a surface, be it evenly-distributed islands, cells of similar radii, or a preferred length-scale of spinodal patterns, can be envisioned as a bell-curve distribution of spatial frequencies, with a peak or dominant wavelength and hence frequency. This distribution appears as a ring in the 2DFFT, with a radius to the peak at wave vector q. This typically corresponds to a modal distance in the pattern in real space ($2\pi/q$). The shape of the 2DFFT also provides useful information. An inversely proportional relationship means a wider radius coincides with the shortening of distances between surface features.
The most convenient representation of the 2DFFT inspecting this shape is the radially-averaged 2DFFT, one such is shown in Figure 3.3.7. Plotting the average intensity against the radius from the centre of the 2DFFT was highly effective for identifying the dominant wavelength, or correlation length, the presence of multimodal lengths, and the approximate standard deviation of each within AFM images of periodic surface patterns. The peak in the spectrum, and as such a bright ring in the 2DFFT, has been shown to correspond to primary (and secondary) surface patterning, often cited as evidence for long-range ordering.[110,153–156]

The Python process for calculating the radially-averaged 2DFFT of an AFM image is shown in Figure 3.3.8. (a) shows an AFM image with a typical cellular pattern of long-range ordering, the displayed image was previously processed using software developed in Chapter 6. This PNG file is converted to a single-channel grayscale array before being forwarded to a three-step process using the Python library `fftpack`. The 2DFFT of the array is computed, the quadrants of the returned 2D array are shifted such that the low spatial frequencies are in the centre of the transform, and then the power spectrum is calculated from the square modulus of the result. The resulting array is displayed as an image in (b), using logarithmic scaling to display all features.

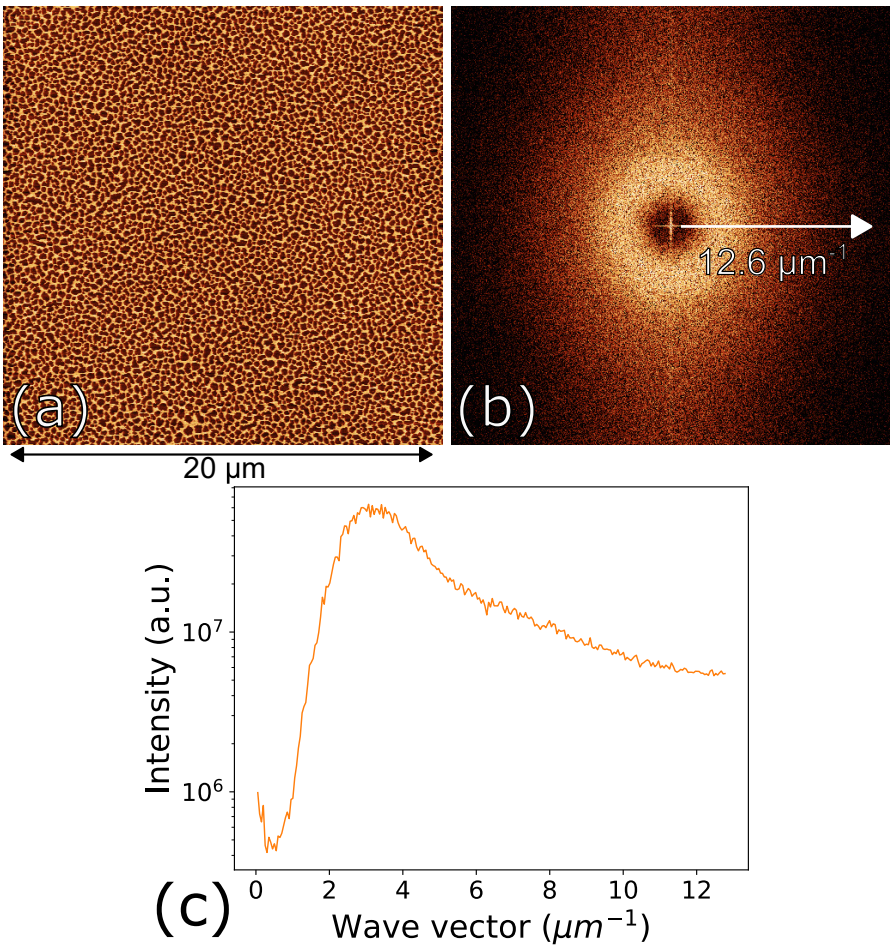

Figure 3.3.7: Example application of a 2DFFT to a tapping mode AFM image of spin-cast gold nanoparticles from toluene onto native oxide-terminated Si(111). **(a)** 20 x 20 μm^2 tapping mode AFM image of spin-cast gold nanoparticles from toluene onto a native oxide-terminated Si(111) substrate; **(b)** 2DFFT of (a). **(c)** The radially-averaged 2DFFT of (a), which is calculated by taking radial bins from the centre of (b) and plotting the mean value of intensity on a semilogarithmic plot against radius. The central bright spot and surrounding dark ring in (b), and hence the peak at 0 and subsequent trough in (c), are an example of spectral leakage caused by the discontinuous nature of scanning a finite region, rendering edges of nanostructures an effective square wave.

The physical size of the 2DFFT is determined by the sampling rate, defined by the Nyquist-Shannon sampling theorem[157]. The maximum visible frequency is that sampled between two neighbouring pixels in the image. The image in (a) is 5 x 5 μm^2 with 512 x 512 pixels, hence the size of (b) is 102.4 x 102.4 μm^{-2}. Plot (c) is obtained from a binned radial sum of the (b), a radial profile of the 2DFFT. The final few radial bins, highlighted in (c), correspond to bins beyond the centre-to-edge radius of the 2DFFT. Due to contributions from radii between this radius and the centre-to-vertex radius, there is no clean cut-off index, so it is cropped out for the final presentation of the radially-averaged (d). Notably, the returned radially-averaged 2DFFT is a form of power spectral density (PSD), the capacity of which to derive surface properties is assessed in Subsection 4.1.2.

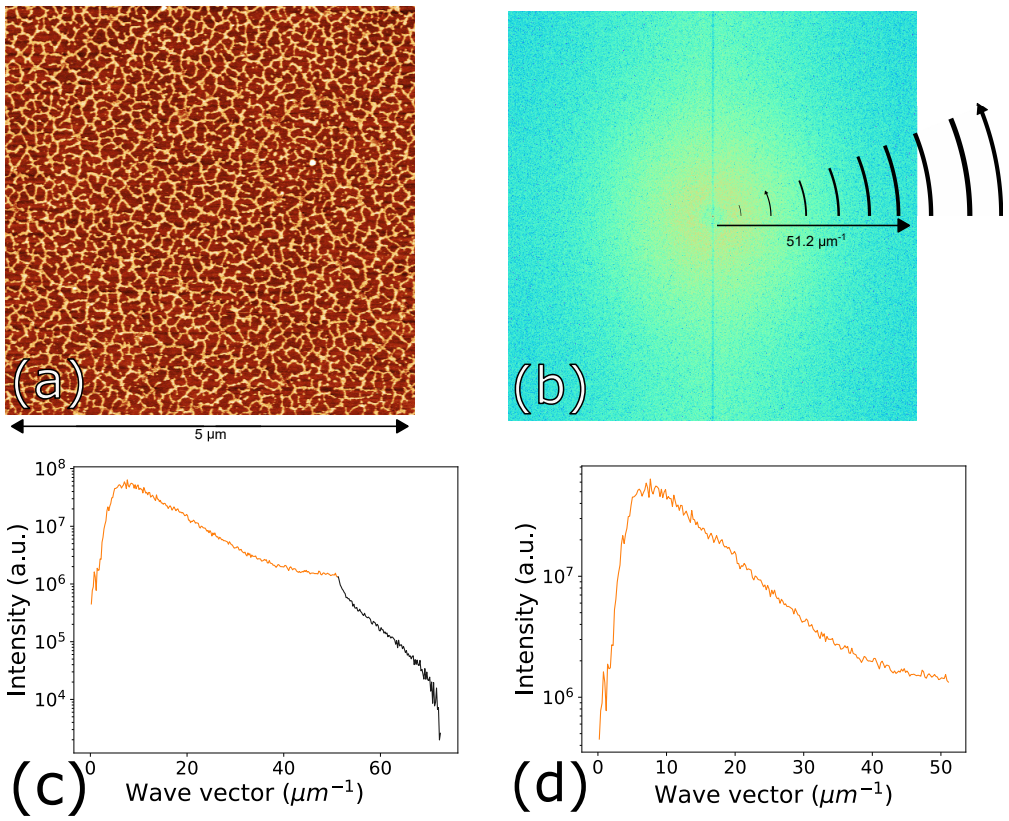

Figure 3.3.8: The process for calculating the radially-averaged 2DFFT of an AFM image. **(a)** 5 x 5 µm^2 tapping mode AFM image of spin-cast gold nanoparticles from toluene onto a native oxide-terminated Si(111) substrate with a spinodal pattern exhibiting spatial ordering. **(b)** 2DFFT of (a), the image radius by definition is the number of pixels, 512, divided by the real scan size. **(c)** The radial average of (b) taken using radial bins from the centre. **(d)** The radially-averaged 2DFFT of (a), (c) but with the highlighted degenerate data in (c) corresponding to data between the radius between the centre and vertex and that drawn to the corner removed.

Spectral leakage was a liability from the edges of the real images, and real segmented and simulated binary images, potentially suppressing the prominence of frequency peaks or even shifting the peak indices in the PSD. Windowing[158,159] is commonly used to improve the appearance, by convolving the image with a 2D sinusoidal function before application of the FFT algorithm. Figure 3.3.9 shows the results of the application of eight of the most common windowing functions to the stable cellular pattern image result from a simulation in (a), with 1D versions of the rotationally-symmetric 2D windowing functions applied shown in (c). The appearance of the windowed radially-averaged 2DFFTs in (b) was common, the same ordering was present with minor changes to the shape of the peak. In the few cases with bimodal peaks of close peak wave vector, windowing helped distinguish this visually in the spectrum.
New tools discussed and applied in Chapter 4 were tested with a modified rendition of the Rabani *et al.* model. The original form does not feature coexisting patterns that could occur in real experiments due to film thickness-dependent disjoining pressure[111,114]. Reproduction of coexisting patterns was achieved with a dynamic chemical potential value, by coupling an initial chemical potential[100,132], μ_0, with a sigmoidal

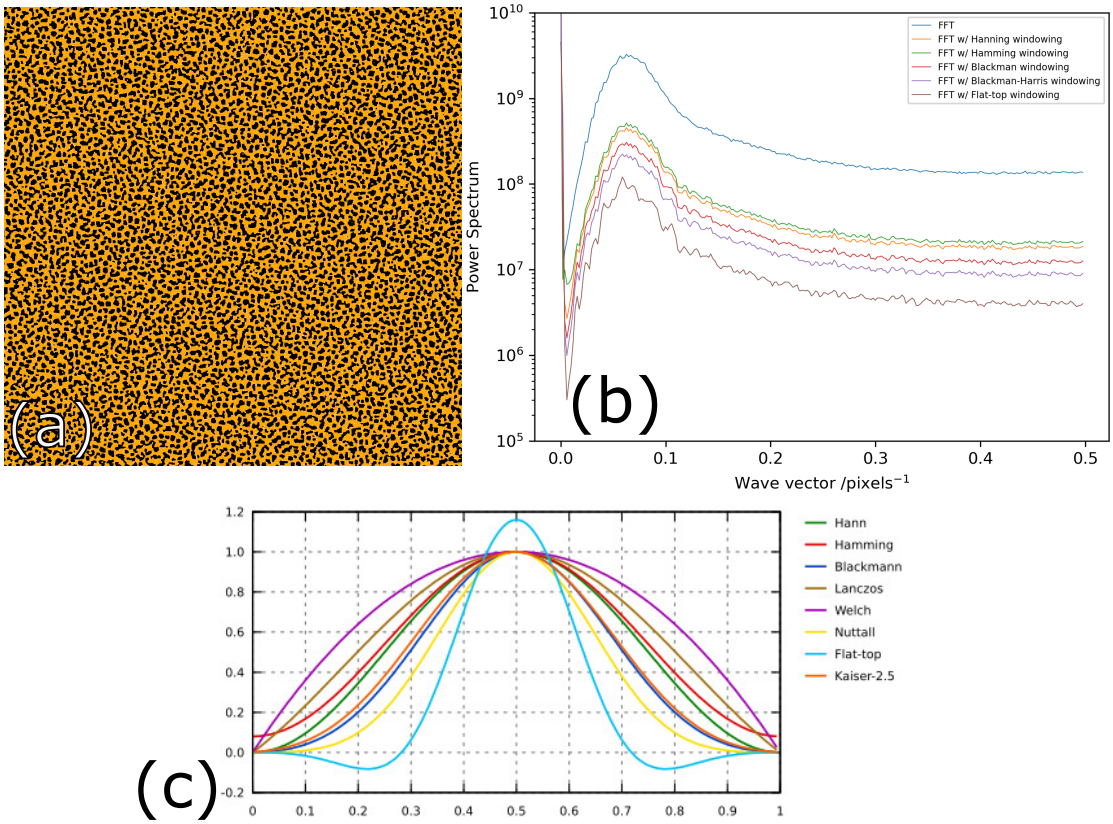

Figure 3.3.9: Demonstration of the application of 2D windowing functions to simulated data. **(a)** Equilibrium state from the modified Rabani *et al.* model, using $C = 0.55$, $k_BT = 375$, $MR = 1$, $\Delta\mu_f = 0.15$, $\mu_0 = 3.05$, $\nu_s = 0.75$, $\epsilon_{nl} = 1.5$, $\epsilon_n = 2$, $L = 1024$ & $\sigma = 0.1$. **(b)** Radially-averaged 2DFFT of (a) with four of the most common windowing functions applied. **(c)** The 1D appearance of eight of the most common windowing functions[139].

function, shown in equation 3.9

$$\mu(\nu) = \mu_0(1 + \frac{\Delta\mu_f}{1 + e^{-(\nu-\nu_s)/\sigma}}) \qquad \{3.9\}$$

where $\Delta\mu_f$ is the fractional increase in chemical potential past a critical vapour fraction ν_s with sharpness σ. The vapour fraction, ν, is defined as the ratio between the sum of the sites in the "liquid" and "nanoparticle" states and the total available states, L^2, in the current Monte Carlo step[95]. 3.3.9(a) implements this modification, though much like real experiments, coexistence does not occur under most experimental conditions or, in this case, user parameters.

3.3.6 Principal component analysis

The core of principal component analysis (PCA) is best understood graphically. This starts with the standardisation of the initial variables, such that each of them contributes equally to the analysis. This is done mathematically by subtracting the mean and dividing it by the standard deviation for each value of each variable. Consider

a data set of N observations and K variables, fitted into a matrix of N rows and K columns. For example, the initial variables in Subsection 4.1.1 were N segmented images, each with K Minkowski numbers. Identifying the correlations in this set requires the computation of a K x K covariance matrix. For K=3, the covariance matrix is:

$$\begin{bmatrix} Cov(x,x) & Cov(x,y) & Cov(x,z) \\ Cov(y,x) & Cov(y,y) & Cov(y,z) \\ Cov(z,x) & Cov(z,y) & Cov(z,z) \end{bmatrix}$$

As covariance of a variable with itself is its variance ($Cov(a,a)=Var(a)$), and covariance is commutative ($Cov(a,b)=Cov(b,a)$), each matrix entry is symmetric along the diagonal. A positive covariance indicates that the two variables are correlated, while a negative covariance means those variables are inversely correlated.[160]

The geometric approach to PCA finds lines, planes and hyper-planes in the K-dimensional space that approximate the data set as effectively as possible using a least squares method[161]. The least squares method fits a line, plane and hyper-plane, which minimises the sum of the square of the residuals of all data points from the fit. A line that provides the least squares approximation for a set of data points maximises the variance of the coordinates on the line or plane. The line accounting for the largest possible variance through the standardised data points is the first principal component (PC1). The second best, which is also orthogonal to the first, is the second principal component (PC2). Figure 3.3.10 demonstrates PCA for K=3. Here, the first two principal components express the orientation of a plane, with which all data points are now projected onto.[162]

The eigenvectors of the covariance matrix define the vectors of all principal components. The eigenvectors and eigenvalues of the covariance matrix are computed by eigendecomposition. Despite there being K principal components, the information among each principal component is weighted towards a single component, often named the first principal component (PC1), followed by the new highest weighting, the second principal component (PC2). The eigenvalues, the coefficients of the eigenvectors, give the amount of variance carried in each principal component. The percentage of variance (information) accounted for in each component by dividing each eigenvalue by the sum of all eigenvalues.

A feature vector is a matrix that has, as columns, a limited select number of eigenvectors. The construction of the feature vector from the most meaningful components is the step in PCA that reduces the dimensionality of the data set. PC1 and PC2 typically explain over two-thirds of the variance in the data set[163]. The N projected scores, effectively reorienting the data from the original data from their original axes to that of the principal components, make up a final data set (of size N x the number of selected principal components).[160]

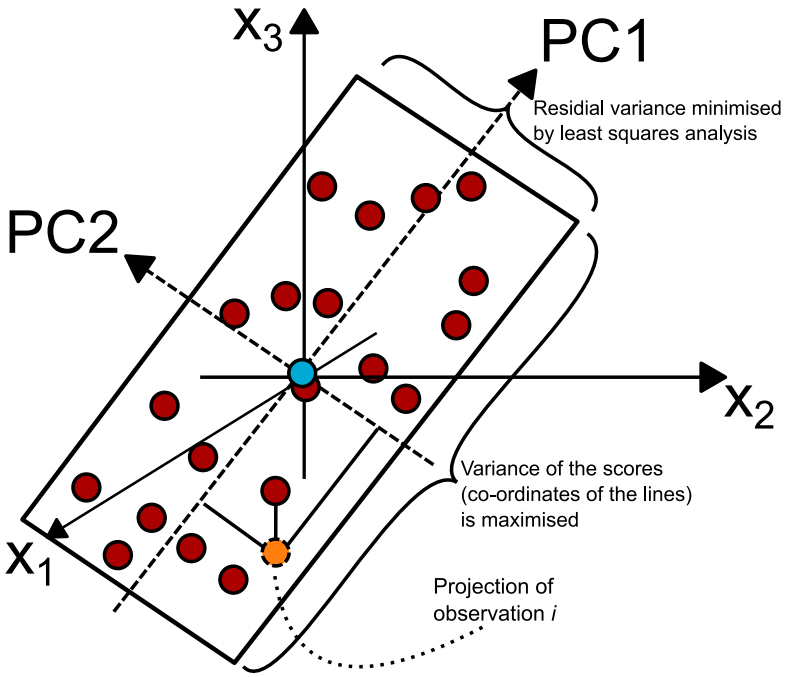

Figure 3.3.10: Visual approach to PCA in the case of 3-dimensional variable space. A set of data points for a group of observations (red dots), with variables x_1,x_2 and x_3, are standardised to centralise the mean (blue dot) and divided by the standard deviation, and plotted on a 3D graph. The vector that both minimises residual variance but maximises the variance in the data is calculated, this is the first principal component (PC1). A second vector orthogonal to the first, and similarly minimises residual variance but maximises the variance in the data, is calculated, the second principal component (PC2). The first two principal components define a plane, of which each observation may be projected onto the low-dimensional sub-space (orange dot). Plotting the projected coordinates (t_1,t_2) in this configuration is known as a score plot. The resulting score plot is a 2D plot of observables with three variables. [161]

Interpreting a 2D score plot produced by principal component analysis was highly appealing as a way to address more than two variables per image when evaluating the relationships between extracted image statistics. Clustering of labelled data in such a score plot could provide a means of categorisation of unlabelled dewetting pattern images, using the proximity of the score of new images from the clusters associated with pattern types as a metric of confidence. PCA is deployed on Minkowski metrics of a multi-class data set of real and simulated images in Subsection 4.1.1, as well as on frequency space peak information on a different simulated data set in Subsection 4.1.2.

4 AFM Investigations of Self-Organised Nanostructures

This chapter focuses primarily on new systematic studies of passivated gold nanoparticles deposited from a solvent thin film, evaluating the resulting patterned surfaces with atomic force microscopy (AFM) and statistical methods. The use of images produced by Rabani *et al.*'s model alongside real AFM data aims to enhance the development of statistical tools and their application to similar nanostructured systems imaged with SPM. Beyond systematic study into the influence of nanoparticle concentration on the formation of nano- and microstructured patterns, the extent to which dewetting can be influenced via mediators – specifically buckminsterfullerene and lithographically patterned silicon oxide – is explored in some detail.

4.1 Applied statistical analysis using nanostructure image data

4.1.1 Automating nanostructure analysis via principal component analysis

Comparative evaluation of the performance of the AFM image feature extraction methods deployed in this thesis, namely Fourier analysis, Minkowski morphometry, and Voronoi tessellation, is limited throughout the literature. The multivariate data sets produced by these methods can be difficult to present compellingly and to detect and compare underlying trends between observations and variables. Principal component analysis (as discussed in Subsection 3.3.6) is a well-known statistical procedure for accomplishing this, yet is rarely applied to the analysis of AFM data. The application of PCA to self-organised gold nanoparticle assemblies is supported by both the Rabani *et al.* model and the rapid automated image processing routines written in Chapter 6.

Chowdhury *et al.*[164] explores automated recognition of dendrital microstructures, formed during alloy solidification, in scanning electron microscope (SEM) images. The classification accuracies of machine learning and statistical methods of feature extraction were tested with feature selection algorithms, including PCA. PCA was uniquely placed among the dimensionality reduction approaches. PCA functions in the absence of prior classification by only looking at the variability between data in the provided matrix, and then later evaluated by cross-validation with previous classifications. The technique maintained the ability to extract information for the classification of images with high accuracy. This would prove useful for investigating clustering among extracted nanostructure features attributed to dewetting modes of unknown origin or unassigned dewetting pattern type. Chowdhury *et al.*[164] only considers binary-class classifications, identifying the presence of dendrites and their orientation (transverse or longitudinal). There were also no further categories of images to help evaluate the robustness and generalisation of the feature extraction and selection methods. New research below expands this for a multi-class problem.

Pierpaoli *et al.*[165] conducts relationship mining through multivariate analysis with PCA. Minkowski morphometry is used as a method of feature extraction from segmented SEM images of self-assembling graphene nanostructures, particularly Euler's characteristic[166,167]. These are then related to the chemical vapour deposition parameters to identify which factors maximised dissimilarity among the data sets for sample morphology and electrochemical behaviour. Similar PCA-based relationship mining is carried out by Farkas *et al.*[168]. A 9-variable (K=9) data set of technological and geometric parameters describing droplet-epitaxially grown point-like GaAs nanostructures was collected. The geometric parameters are direct measurements from AFM images, such as structure depth, height, and diameter. The results of PCA are a score plot between the first two principal components, exhibiting clustering into the pre-defined categories of quantum dots, single and double quantum rings, and nano-holes. The use of score plot clustering to reinforce morphological categorisation of nanostructures was compelling, and could be generalised for segmented images of nanoparticle assemblies using Minkowski functionals[165]. Classification of images of nanoparticle assemblies spanning the probed surface using solely the clustering observed in a score plot of the first two principal components was a promising concept, especially when supplemented with model data from accurate Monte Carlo simulations.

PCA was used to evaluate Minkowski morphometry-based labelling of both real experimental data and simulated data of gold nanoparticle dewetting patterns. The degree of clustering in a score plot between real and simulated data manually labelled with the same pattern type was of greatest interest. A small data set was prepared. 255 images from Monte Carlo modelling of solvent dewetting and 60 AFM images from dewetting experiments were manually labelled as either cellular, labyrinthine, porous/-holes, islands, fingering or worm-like. The experimental images were processed using the code discussed in Chapter 6, and segmented into binary images of nanoparticles and bare substrate, then denoised by morphological processes[9]. This made the images have the same appearance as the simulated images and viable for Minkowski measurements. The scale-invariant area, $\tilde{A}$, perimeter, $\tilde{P}$, and Euler characteristic, $\tilde{\chi}$ (as defined in Subsection 3.3.4) were calculated for every binary image in the data set. The scale-invariant Minkowski metrics were prepared for PCA using the method from Subsection 3.3.6, returning the first two principal components, PC1 and PC2. The resulting score plot of PC1 against PC2 is shown in Figure 4.1.1(b).

Although the Minkowski numbers (i.e. area, perimeter, and Euler characteristic) for the experimental and simulated nanoparticle patterns occupy similar regions of the PCA plot, all pattern types exhibit a high degree of clustering among simulated data. The adjacency of score clusters for each pattern type is in agreement with the physical observations of continuity between those patterns. The porous/holes and islands clusters being opposite each other on the PC1 axis similarly agree with the pattern types' physical contrast. Simulated data labelled as labyrinthine exhibited high variance along a different axis to the rest of the data set, being the only pattern to significantly stray

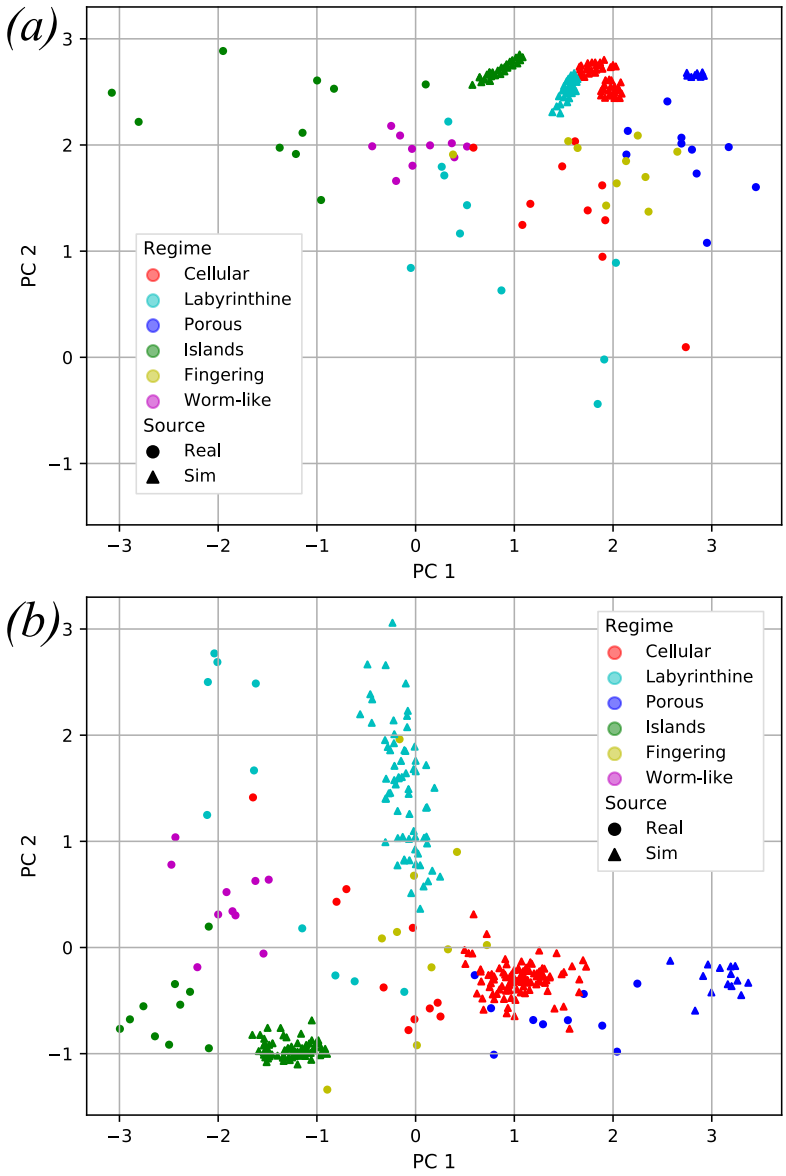

Figure 4.1.1: Principal component analysis of a set of simulated images (filled triangles) and experimental AFM images (filled circles) of gold nanoparticle assemblies labelled manually, using Minkowski functionals as the metric. **(a)** A plot of the first two principal components of the area, perimeter and Euler characteristic; **(b)** A plot of the first two principal components of the scale-invariant area, perimeter and Euler characteristic.

from the PC2 axis. Inspecting the dataframe reveals this is due to high variance in $\tilde{\chi}$ among labyrinthine pattern images.

PCA using both the scale-variant and scale-invariant Minkowski metrics was implemented to evaluate the effect of scale-invariance on labelling. Figure 4.1.1 shows this change having the most effect upon images produced by the Rabani *et al.* model (as described in Subsection 3.3.2). Simulated cellular and labyrinthine pattern populations no longer intersect, and elliptical clustering is far more prominent. A significant im-

provement in the appearance and clustering of populations is shown in the PCA once scale-invariance was implemented.

AFM data was further categorised into worm-like and fingering pattern types before PCA. The two regimes were not identified in simulations, as fingering did not occur in the current Rabani *et al.* model, and worm-like patterns were not highly distinguished from other patterns. The scores for images labelled as fingering are highly dispersed, Minkowski morphometry is less useful for quantifying fingering patterns, due to the diversity in fingering pattern sizes, frequency and degree of branching. A highly-branched hole in a fingering pattern has the same Euler characteristic as a single circular hole or cell, making them difficult to distinguish by Minkowski metrics alone. The overlapping of clusters among the labelled AFM data means purely Minkowski morphometry-based labelling routine would exhibit a misclassification rate when provided real unlabelled data, particularly for highly similar pattern types.

Observed clustering in the score plot shows Minkowski morphometry is a promising feature extraction method for the purpose of categorising images produced by the Rabani *et al.* model. More confident classification of unlabelled images of nanoparticle assemblies could come from addressing the observed minor discrepancy between the clustering of experimental and modelled data. Scale-variance may be poorly accounted for by equations 3.8, which could be tested by a wider range of grid sizes in the model, or by suitable image compression or scaling of existing images to observe the effects on score plot clustering. The Rabani *et al.* model-generated portion of the data set may not provide a full representation of final states observed in experiments, possibly fixed by an expansion of the generative parameter space. Images in the data set were labelled manually, and hence susceptible to being mislabelled or objectively labelled. PCA upon Minkowski metrics also assumes a consistent and accurate segmentation algorithm for the real data, as well as the denoising by morphological processes and the proposed autoencoder.[9]

4.1.2 Fourier analysis of real and simulated AFM data

Roughness estimation

Radially-averaged 2D Fourier transforms in principle provide another mechanism whereby different image classes may be distinguished. Calculating the roughness of a relocatable region of the particle-free surface enables insights into the impact of substrate roughness on the self-assembly and self-organisation processes giving rise to nanoparticle patterns. Ideally, the surface topography is given as a continuous map of heights $h(x, y)$ along a xy plane, with a mean of zero. Surface roughness is given by root mean square height, h_{rms}, calculated by taking the square root of the average of the squared heights of the surface profile. In this ideal case, h_{rms} could be computed directly from the real-space topography. However, we can only experimentally measure heights at discrete points, in this case, limited by the finite resolution of the AFM,

defined by the tip radius of curvature. 2DFFTs enable a quantitative prediction of the surface roughness in AFM images.[169]

The roughness of the un-patterned surface was characterised by the root mean square height, h_{rms}. The area underneath the PSD is proportional to h_{rms}^2[169], so taking the 2DFFT of an AFM image provides a direct route to estimating the roughness parameter of the scanned region. Experimentally, the PSD is computed from a single and hence incomplete measurement of the surface, a measurement highly prone to surface and scanning artefacts of finite size. As previously discussed, the AFM has fundamental resolution limits placed by tip shape and sampling rate. While the limit is insignificant when detecting nanoparticle patterns, probing to measure surface roughness is limited by an inability to detect sub-pixel roughness, translating to a cut-off wave vector in the PSD utilising the Nyquist-Shannon sampling theorem. AFM on un-coated surfaces, followed by a roughness calculation, could shed light on dewetting's dependencies of contact area and adhesion at the smallest observable scales of roughness[63,122,170]. Jacobs' thorough review also shows other directions to take to improve the roughness results as derived from the FFT.[169]

Subsampling by sectioning off and calculating the 2DFFT of portions of an image, or across same-sized images from the same scanning session, provided a pathway to calculating spatial changes in roughness. A percentage change, $\Delta\%h_{rms}$, could be quoted between images by taking the roughness of sections while avoiding sections containing artefacts. This was particularly useful for comparing the roughness of induced surface-spanning heterogeneities to that of the rest of the surface. When combined with the shift in reciprocal correlation length, Δq, between those two regions when patterned, a purely quantitative dependence of the density of patterns upon the underlying surface parameters could be derived entirely by Fourier analysis, as realised in Subsection 4.3.4.

Modelled dewetting analysis

A few open-source tools for enhancing measurements of q and h_{rms}, provided in Appendices A and B, were developed[171] and integrated into new readings. The automated indexing and segmentation tools were adapted from Chapter 6 to be applied to processed real AFM data or simulated data.

Automated extraction of the wave vector peak q's height, variance and position was conducted with more tools extrapolated from Chapter 6. The spike in intensity at 0 is suppressed and a smoothed version of the PSD is acquired by a moving average function. The `find_peaks` function returns the index of q along the x-axis, as well as any other peaks in the PSD, which can, in turn, be used to calculate its height and variance. Figure 4.1.2 depicts the automated process upon simulated data.

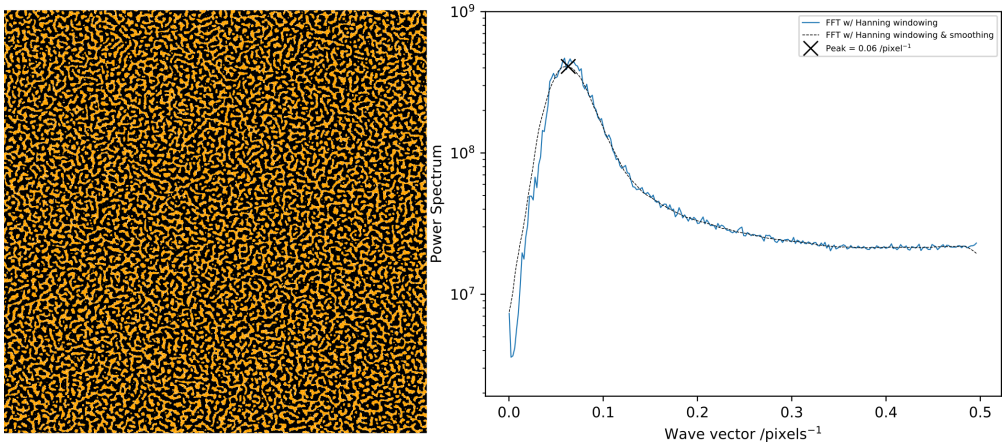

Figure 4.1.2: Final spinodal-like Monte Carlo state on a 1024 x 1024 grid alongside its windowed radially-averaged 2DFFT annotated with moving average over 15 data points in the spectrum.

A simple UI for selecting multiple square portions of images to calculate a local 2DFFT, that would plot the spectra upon the same axis, was also developed. Assuming these boundaries are the same size, a comparative value for h_{rms} is returned, otherwise q is returned. The foundational version of this code is presented in Appendix B, while realised as an analysis tool in Subsection 4.3.4. Two animation tools, applications of which are presented below and in Subsection 4.3.1, are also available. The first was a sweeping subsampling window to replace the portion selection UI, which was useful for larger images of shifting nanostructure patterns upon coated surfaces, often caused by convective processes or local wettability gradients. The second was designed specifically for simulated data, showing the temporal evolution of the radially-averaged 2D FFT with each step in the Monte Carlo process. For both cases, all frames are saved as images, as well as a final video file.

Two applications of the new Fourier-based tools utilising simulated data were proposed. The first was to use 2DFFTs upon a data set of simulated images from the Rabani *et al.* model, to assess for a relationship between the model parameters and the appearance of the PSD. A set of 1629 unlabelled images, with a range of C, k_BT and μ_0 values and fixed $\Delta\mu_f$, ν_s and σ values with over 1000 Monte Carlo steps modelled in each, were collected into a data set. The 2D FFT software extracted the wave vector peak's height, variance and position from the PSD of each image. Scatter plots of model starting parameters against statistics of the peak in the radially-averaged 2D FFT of the final images and a score plot are presented in Figure 4.1.3. Little direct correlation between the individual simulation parameters for the Rabani *et al.* model and PSD peak intensity and prominence is observed in the explored parameter space through scatter plots. Studies relating pattern morphology to the same Rabani *et al.* model parameters have previously shown certain combinations of simulation parameters promote faster evaporation times and pattern coarsening[95]. Sufficiently low values of C, k_BT and μ_0 would cause simulations to remain metastable after 1000 Monte

Carlo steps, "liquid" states would still be present until upwards of 4000 steps. This is attributed to a phase boundary in the system. Experimentally, the solvent thin would rupture due to external nucleating factors, but the isolated simulation instead remains 'wetted'. Different growth modes and nucleation dominate over the full range of C, k_BT and μ_0 values, evidenced by potential bifurcation in Figure 4.1.3.

PCA exhibited stronger clustering with Minkowski morphometry than with Fourier analysis. Cross-validation with the same image data set categorised by dewetting pattern type, either manually or by a CNN[6], could help identify underlying trends in the FFT score plot. Beyond comparison with PCA is the capacity of a feature extraction method to extract information that best fits predictive models of properties or generative models of materials. Fourier analysis as a means to track the morphological evolution in the Rabani *et al.* model is explored below.

Coarsening

The second application of Fourier analysis was an attempt to observe the onset of coarsening in simulated data purely from frequency space[1,93]. After reaching a metastable yet dewetted state, exhibiting a known dewetting morphology (as defined in Tables 3.1.1 and 3.1.2), further Monte Carlo steps have shown that smaller nanoparticle structures begin to coalesce to form larger structures, while maintaining the same assigned pattern type. This decay of smaller features to larger features, known as coarsening, would theoretically be detectable at very low magnitudes by calculation of the PSD at each iteration of the model. Every 20 steps of simulations were collected into videos that simultaneously tracked the model and the PSD for numerous simulations of each morphology. The adapted version of the animation code for data processing is presented in Appendix A.

Some key frames of three of the videos were adapted into Figure 4.1.4. In each case, the PSD starts by resembling a logarithmic function, as it is a semi-logarithmic plot. The broad peak encompassing the whole PSD, peaking at the right side of the graph, represents the wave vector of single nanoparticle states spaced apart by single surface states, single mobile nanoparticles moving between "wet" sites. The random walk of these particles rapidly becomes limited by the decaying of liquid states to surface states, limiting the occurrence of periodic pixel spacing and dropping the intensity of this broad peak. By this point, the thin film has ruptured, and liquid is retracting from these ruptures, carrying "nanoparticle" states – as defined by the Rabani *et al.* model discussed in Subsection 3.3.2 – with them. This causes a small initial peak in the left of the PSD, associated with the spacing of these initial ruptures, as shown in 4.1.4(a)'s PSD in (e). The initial peak grows into a broader primary peak, as more rupture events occur that more closely adhere to the inherent modal feature length of the evolving nanostructures. At this point in the first of the three simulations, (b), the simulation more closely resembled a labyrinthine pattern and this is reflected in the

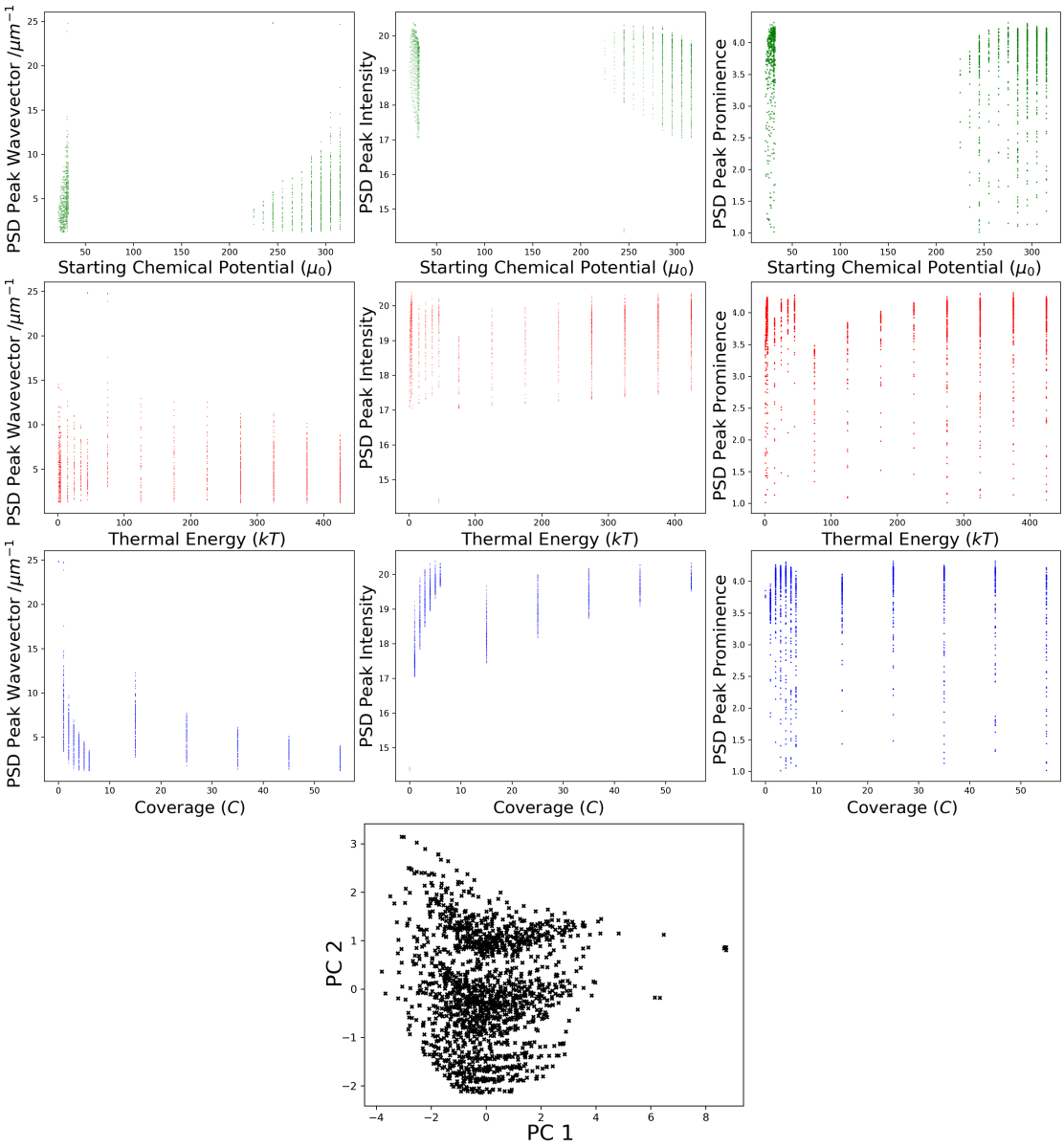

Figure 4.1.3: Scatter plots and a PCA score plot of a range of starting parameters for Monte Carlo models of gold nanoparticle dewetting against various statistics for the peak in the radially-averaged 2D FFT of the final model state.

broader PSD. This is to be expected at this point, as the liquid states form capillary bridges between the island domains. The morphology rapidly shifts to an island phase, which is reflected by a significant change in the shape of the PSD between (b) and (c). Between (c) and (d) there is little significant difference between the PSDs The peak has increased in intensity, shifted left and partially narrowed over the 420 steps. Physically this represents a wider and more uniform spacing between isolated regions of nanoparticle states as the system evolves.

A stronger case for coarsening is shown in the second of the three examples. 4.1.4(f-i)

displays a labyrinthine dewetting pattern in a metastable state. (f) shows the end of a relatively short evaporation phase, followed by a long coarsening process into (i). The process takes a large number of iterations and is difficult to track with the naked eye, but the PSD in (j) displays a trend of the primary peak increasing in intensity, narrowing and shifting to the left, with the background data to the right of the peak reducing in intensity. The peak shift is indicative of the growing population of structures with larger spacing, with the drop in background intensity and narrowing indicative of a diminishing population of mobile nanoparticles and periodic smaller structures.

Running the simulation further, the peak wave vector tends towards a maximum at a rate inversely proportional to the peak's displacement from the maximum peak coordinate. This is in agreement with similar analysis on simulations with island domain coarsening, where the diffusion of nanoparticles at this stage is inversely proportional to cluster size[172]. Diffusion resulting in net transfer from smaller to larger structures is referred to as Ostwald ripening[173]. The time evolution of coarsening of these structures is described by a dynamical power law, $L(t) \sim t^{\gamma}$, where $L(t)$ is an increasing characteristic length-scale of the nanoparticle domains, and γ is the coarsening exponent. $L(t)$ here was defined as the wave vector at the primary peak of the PSD of the simulation at a given Monte Carlo step. The scaling of this metric is considered highly sensitive to the simulation parameters, and often related to the average island sizes. Fitting Monte Carlo steps against peak wave vector, using automated peak-finding code, returned $\gamma = 0.25$ for 4.1.4(a-e) and $\gamma = 0.30$ for 4.1.4(f-j). Rabani *et al.*, when measuring coarsening in island deposits from PbSe in octane nanoparticle solutions on HOPG, and models, attributed values of γ in this range to thermally-driven coarsening[1]. Blunt expanded these observations with mechanically-induced coarsening[93] with tapping mode AFM upon colloidal gold on silicon substrates, which similarly utilised FFTs for analysis, returning $\gamma = 0.25$ for labyrinthine and $\gamma = 0.49$ for island morphologies. The rapid decay of liquid states and behaviours in the PSD suggest a degree of coarsening via Ostwald ripening, and provides evidence of the sensitivity of Fourier analysis for observation of coarsening.

4.1.4(o) is the only case shown that exhibits broadening of the primary peak in the PSD in the final state, after 5500 steps. This broadening feature is indicative of the secondary cellular pattern formation towards the end of the simulation in (n), with the liquid states in (m) (white) withdrawing from the region by Metropolis-Hasting acceptance. This agrees with the conclusion of only cases of rapid evaporation resulting in pattern coarsening. All videos show the PSD closely tracks the first film rupture events, and secondary pattern formation if present.

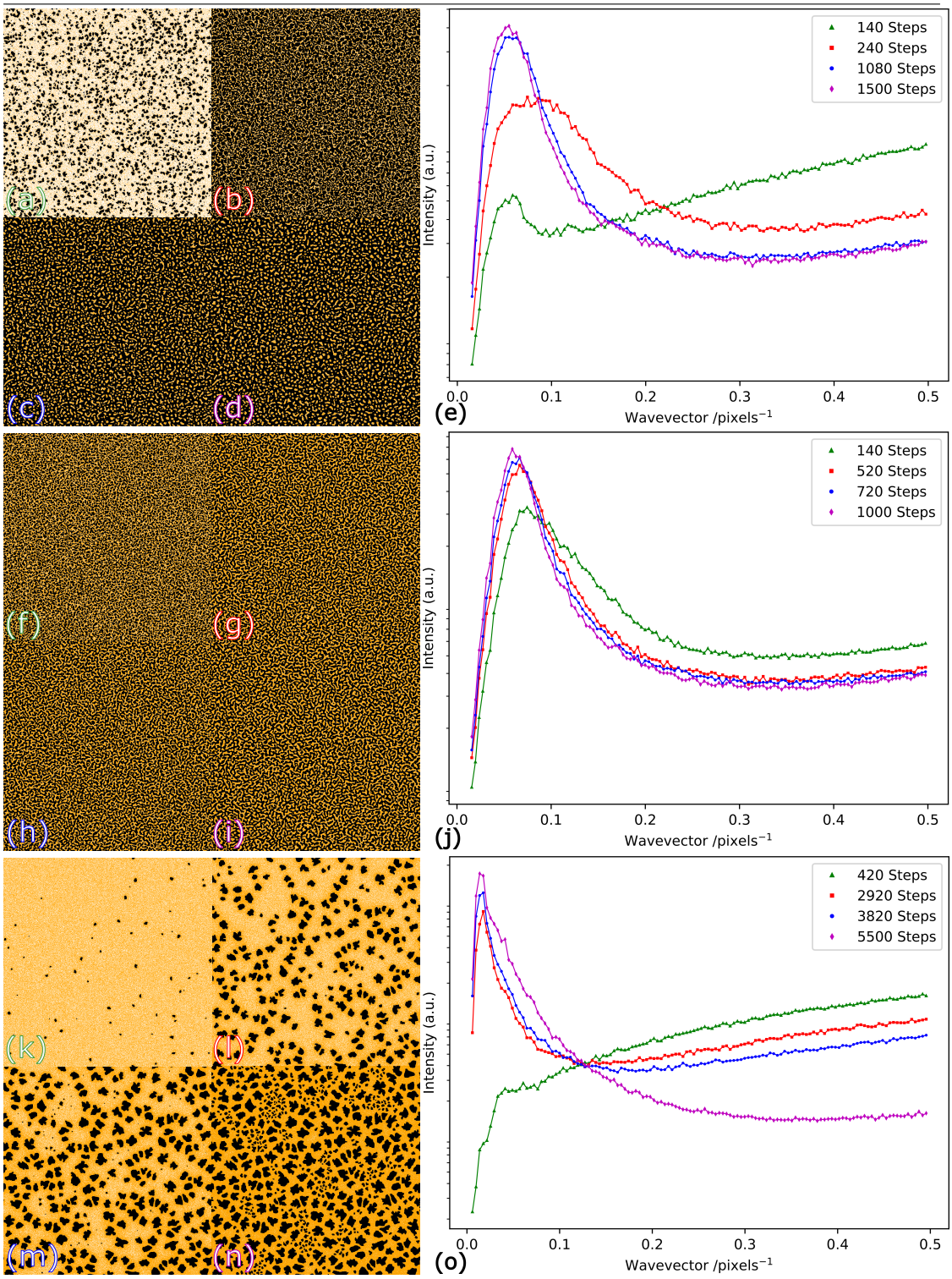

Figure 4.1.4: Fourier analysis as a tool to monitor coarsening in the dual-scale modified Rabani *et al.* model. Three different simulations of formation are displayed, with the power spectral density, the radially-averaged 2DFFT, upon the nanoparticles and substrate states in the grid for the four stages plotted. The step count for each image (going across the top row, then across the bottom row) is displayed in the graph legends with colour-coding.

4.2 Effects of concentration on gold nanoparticle dewetting patterns

The deposition method for planned directed dewetting experiments was taken as an opportunity to perform a short matched pairs study upon the appearance of dewetting patterns on SiO_2 with respect to the gold nanoparticle concentration in the toluene solution. 2-4 nm average diameter octanethiol-functionalised gold nanoparticles suspended in toluene were purchased from Sigma-Aldrich and diluted in HPLC-grade toluene to concentrations ranging from 0.1 to 2.25 g/l. Previous studies on the same nanoparticles explored a range of 0.025 to 1.0 g/l in order to produce submonolayer coverages[10,91,96,132]. 1 x 1 cm^2 SiO_2/Si(111) tiles were prepared from a large wafer using a diamond scribe to cut into squares suitable for the spin-coater and AFM chamber, then thoroughly cleaned in a series of solvent washes and exposure to oxygen/argon plasma, detailed in Section 7.2. Each tile had 75 µl of each nanoparticle solution pipetted then spin-cast onto them. Over 11 seconds, the rotary spin-caster accelerates up to 4000 rpm at 1000 rpm/s, stays at 4000 rpm for 3 seconds, and then returns to a stationary position. All newly spin-cast samples were probed with two atomic force microscopes, the MFP-3D and Cypher systems, within a week of deposition.

Figure 4.2.1 shows a selection of tapping mode AFM images from samples between 0.1 g/l and 1.75 g/l. Every concentration tested exhibited a sub-monolayer coverage of a fully connected network morphology with a consistent height of 3.0$\pm$0.4 nm, as shown in (f). Lack of multi-layer networks is typical in systems with a lack of relatively strong interparticle forces compared to particle-substrate forces, such as those for nanoparticles with shorter functionalising alkyl chains[10,174], solutions with solvents with a higher dielectric constant[175], or complex near-planar molecules similar to NDP. A purely spinodal dewetting mechanism would similarly entail multi-layer pattern formation, this is hence supplemented with a viscoelastic phase separation model[176], by which the final steps of dewetting takes into consideration an effective increase in solvent viscosity, or by a contribution from a subsequent heterogeneous nucleation route in the dewetting process[177].

Spatial information was quantified with a radially-averaged 2DFFT upon all images presented in Figure 4.2.1, in (e). The peak in all spectra suggests a preferred correlation length in the system[110,178], included in Table 4.2.1. The wave vector of the peak, q, is within error of the mean physical distances between cellular pattern cell centres, the Voronoi site distances as defined by Voronoi tessellation mapping onto 4.2.1(a-d), in all cases. The FFT identifies and effectively quantifies the periodicity of the cellular structures in each AFM image. The high variation in cell spacing in single images results in a significant overlap in correlation length between concentrations of 0.1, 0.75 and 1.25 g/l. This makes it difficult to distinguish the concentration of gold nanoparticle solution solely by calculating the correlation length.

Despite the common association, there are however cases where the connection of spinodal processes to preferred correlation lengths does not hold. Small scale cellular holes may coalesce with larger holes, in the same way large islands of material may capture smaller islands within a specific distance[179], giving the illusion of a higher degree of order. Coalescence and hence its generated non-Poisson ordering of feature sizes is not unique to the spinodal dewetting regime. This emphasises the requirements for dynamic simulation, and particularly the analysis of later steps. On the other end, ordering of larger scale than the scan sizes can play a role, hence large scan sizes were also explored.

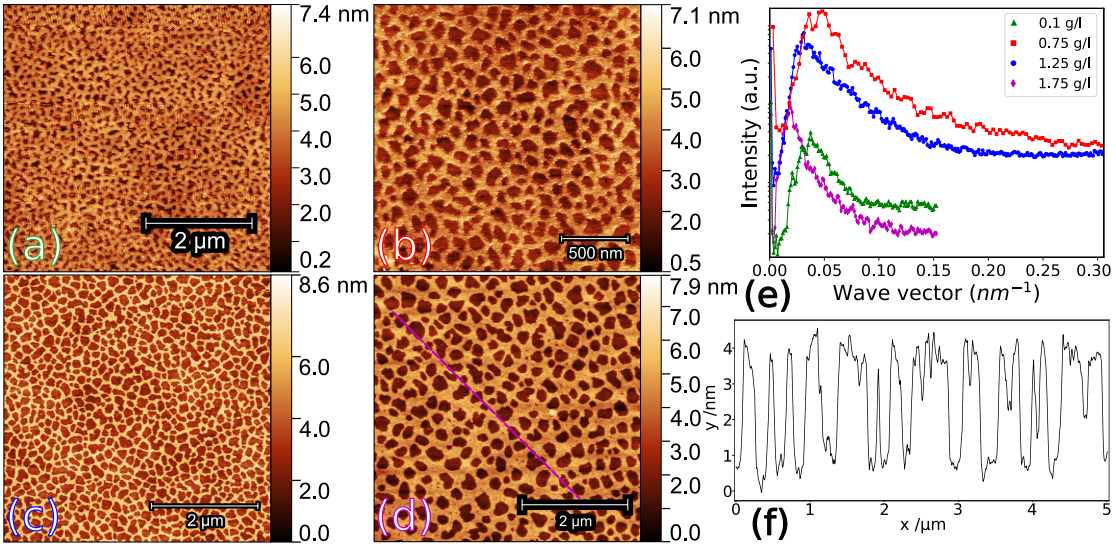

Figure 4.2.1: Tapping mode AFM images of spin-cast gold nanoparticle assemblies from toluene onto 1 x 1 cm^2 wafers of plasma- and solvent-cleaned SiO_2/Si(111). **(a)** 5 x 5 μm^2 0.1 g/l; **(b)** 2 x 2 μm^2 0.75 g/l; **(c)** 5 x 5 μm^2 1.25 g/l; **(d)** 5 x 5 μm^2 1.75 g/l. **(e)** Radially-averaged 2DFFT of Hann-windowed binary images of (a-d); **(f)** line profile across (d).

		Concentration (g/l)			
	Analysis Type	0.10	0.75	1.25	1.75
λ (nm)	Voronoi	169 ± 30	133 ± 20	187 ± 30	334 ± 40
	Fourier	170 ± 50	133 ± 30	202 ± 30	319 ± 30

Table 4.2.1: Gold nanoparticle dewetting pattern correlation length, λ, against gold nanoparticle concentration in solution. The Voronoi correlation lengths are derived from the average Voronoi site distances, as mapped onto the AFM images in Figure 4.2.1. The Fourier correlation lengths are derived from the peak indices, q, in 4.2.1(e), using $\lambda = 2\pi/q$.

Despite the heavy emphasis on discrete categorisation, it is important to note each category is not entirely distinct, but instead lies along a continuum. Categorisation, be it via a CNN, PCA, or manual labelling with criteria established by Tables 3.1.1 and 3.1.2, of the images in Figure 4.2.1 as exhibiting cellular patterns ignores that visually

(a) appears more closely related to spinodal patterns than the rest of the displayed images, while (d) is closer to pore-like patterns. This is in line with common observations of a transition from spinodal to cellular to pore-like patterns as nanoparticle concentration increases. It is important for analysis software to confidently recognise the truest cellular patterning presented in real data, such as that in 4.2.1(c).

Large scale AFM images produced by the same spin-casting method reveal unusual patterns left by the gold nanoparticles. The Asylum Research MFP-3D system allowed for stable scans at up to 90 x 90 μm^2 scan sizes, returning clear visualisation of these previously unobserved patterns in tapping mode AFM in Figure 4.2.2. While an underlying cellular network of correlation lengths of nanometre scale is present, a much larger cellular network is present. The much more distinctive white rings at some of these nodes suggest a rapid nucleation event[109,114]. Additionally, the larger network's height is seemingly tied to nanoparticle concentration, ranging from 1 - 2 µm high in the 0.75 - 2.25 g/l cases.

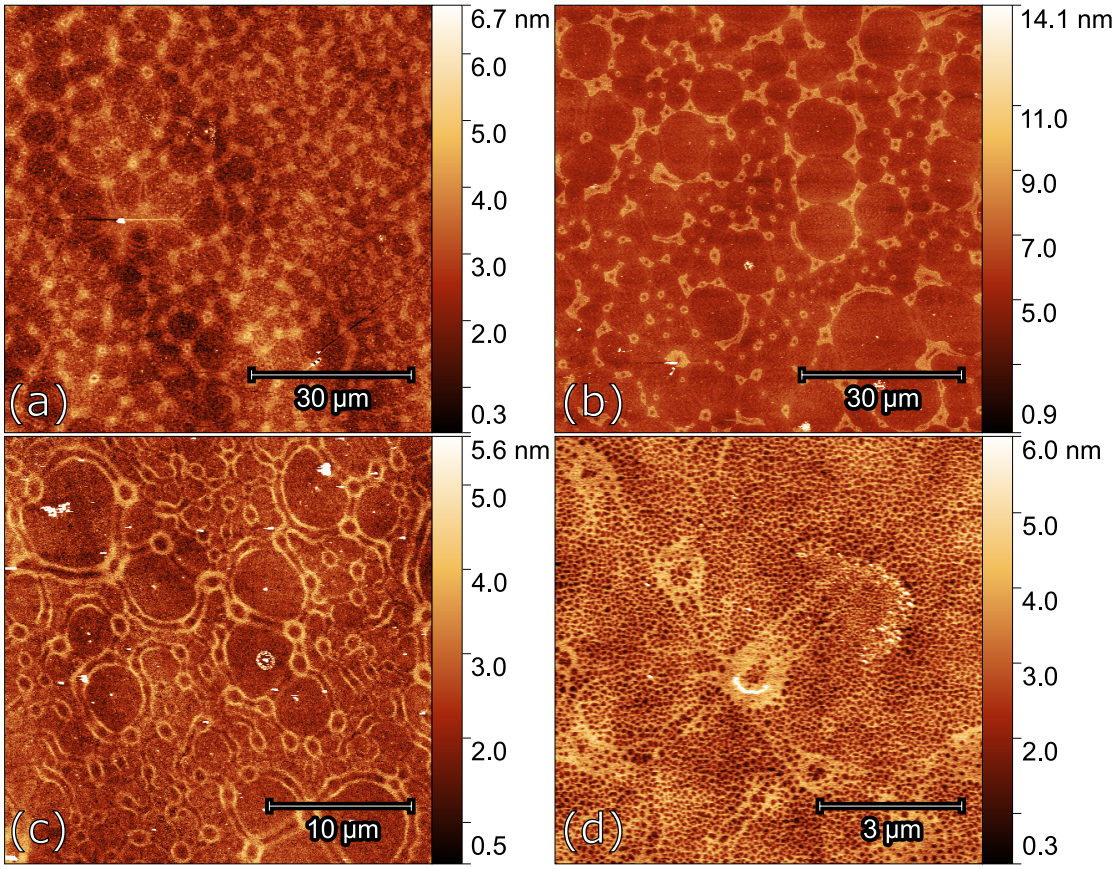

Figure 4.2.2: Large scale tapping mode AFM images of spin-cast gold nanoparticle assemblies from toluene onto 1 x 1 cm^2 wafers of plasma- and solvent-cleaned SiO_2/Si(111) taken with the MFP-3D system. **(a)** 80 x 80 μm^2 1.75 g/l; **(b)** 80 x 80 μm^2 2.25g/l; **(c)** 30 x 30 μm^2 0.75 g/l; **(d)** zoom upon (c) to 9 x 9 μm^2.

The correlation wavelength, λ, for all large scale structures was quantified with a

radially-averaged 2DFFT and by mapping to a Voronoi tesselation. Figure 4.2.3 shows that analysis for Figure 4.2.2(a). The Voronoi diagram, 4.2.3(a), is mapped such that the white rings were at the Voronoi cell vertices. Two measurements were extracted from the diagram, the distribution of polygon sidedness, 4.2.3(b), and the separation of Voronoi sites for cells sharing an edge, an approximation of λ. A bimodal λ was identified, 3.67$\pm$0.10 μm and 5.70$\pm$0.10 μm.

The radially-averaged 2D FFT for 4.2.2(a) is shown in Figure 4.2.3(c). The highlighted major peak at wave vector 0.21 μm^{-1} does not coincide with the dewetting pattern length-scales, but instead coincides with an identified periodic feature across the image. Taking a line profile across the entire image shows the feature is image curvature with a periodicity of 30 μm. While in numerical agreement with the location of the peak, $2\pi/0.21$=30 μm, the sensitivity of the FFT to surface curvature was confirmed by performing Fourier filtering. Removing the ring in the 2DFFT responsible for the peak at 0.21 μm^{-1} inverse Fourier transforming the result returns Figure 4.2.3(d). The image is fully detrended. The two highlighted auxiliary peaks in 4.2.3(c) at 1.12 and 1.66 μm^{-1} agree upon the two correlation lengths returned by the Voronoi approach, $2\pi/1.66$=3.79 μm and $2\pi/1.12$=5.61 μm. The Fourier and Voronoi analyses are coherent.

Multiple pieces of evidence suggest the long-range pattern being a manifestation of the Marangoni effect. The first piece of evidence stems from the Voronoi diagram, 4.2.3(b) shows the preferable formation of hexagonal cells across all concentrations, in a non-Poisson distribution. This is in agreement with the most commonly observed hexagonal patterns of Bénard cells. Large-scale cellular assemblies formed at nanoparticle concentrations at or below 0.75 g/l, become less pronounced. For the pattern in 4.2.3(c), it is more difficult to define convex polygons for a Voronoi tessellation approach as the line edges are no longer straight. Further below this concentration, the height begins to match that of the rest of the first layer of nanoparticles, while disrupting the local nanometre scale cellular pattern correlation length less and less.

Previous studies have shown the Marangoni number for nanoparticle solutions scaling inversely with the nanoparticle concentration c[99]. Combined with equations 3.2 and 3.3, this suggests $\lambda \propto \sqrt{c}$. The graph in Figure 4.2.4 does not support this for the entire studied concentration range. However, there is a critical value of Marangoni number for Marangoni dewetting to occur, given by equation 3.2. The proportional relationship hypothesised for Marangoni-induced long wavelength instabilities of $\lambda \propto \sqrt{c}$ holds in the case of the critical value being met between concentrations of 0.75 and 1 g/l. This relationship however does not hold true for the patterns present in Figure 4.2.1, implying two distinct combinations of dewetting mechanisms for large-scale and small-scale pattern formation.

It is possible that the Marangoni effect plays a role in film rupture by the creation of

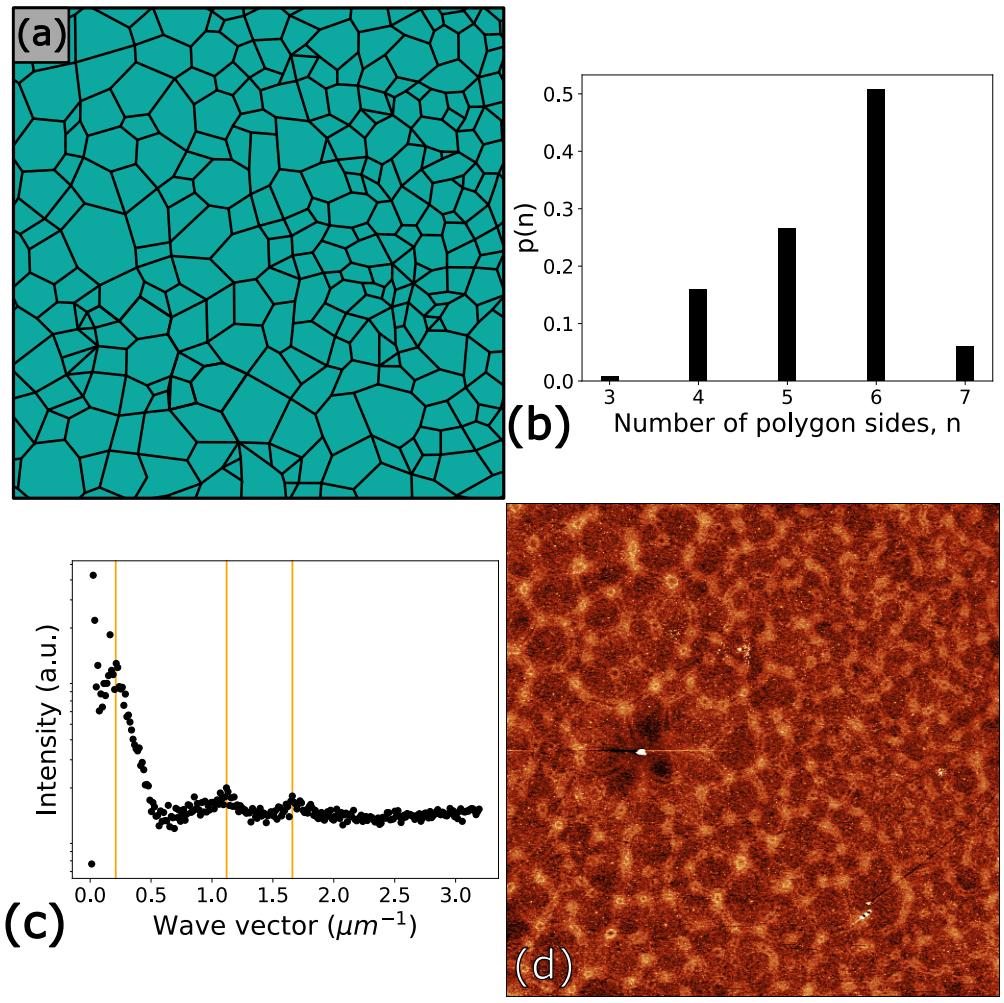

Figure 4.2.3: Image analysis upon Figure 4.2.2(a). **(a)** Voronoi diagram of 4.2.2(a) constructed by defining the white rings as vertices **(b)** Histogram of polygon side distribution of Voronoi diagram shown in (a). **(c)** Radially-averaged 2DFFT of 4.2.2(a). 3 points are highlighted along the spectrum; the first (0.21 μm^{-1}) corresponds to a perceived surface curvature (30 µm), while the second and third points are similar to the found bimodal distances between Voronoi centres sharing an edge in the Voronoi diagram in (a), 3.67 µm and 5.70 µm. The alignment of the two minor peaks in the spectrum with these points (at 1.12 and 1.66 μm^{-1}) show the Voronoi and Fourier analyses are in agreement. **(d)** Fourier-filtered version of 4.2.2(a) that effectively removes the first highlighted major peak in (c) then inverse transforms the result.

nucleation sites, as thin films exhibiting the effect will have a thickness of the order of the amplitude of the convective waves, atop Figure 3.2.4(a). This is evidenced by the common occurrence of a nucleation site centred in every single polygon, located much like sites in a Voronoi diagram. Though not highly visible in Figure 4.2.2, Asylum Research Cypher AFM images of a second deposition using the 1.75 g/l solution at higher resolution Figure 4.2.5 makes this clearer. The centre is where one would expect the liquid film to be the most thin and hence most susceptible to initiating rupturing, rendering the Marangoni-induced nucleation centres similar to that of Voronoi seeding sites. These sites have a spacing of 4.8$\pm$1.0 µm, which maintains consistent with the correlation length approximated for the same concentration toluene-based nanoparticle

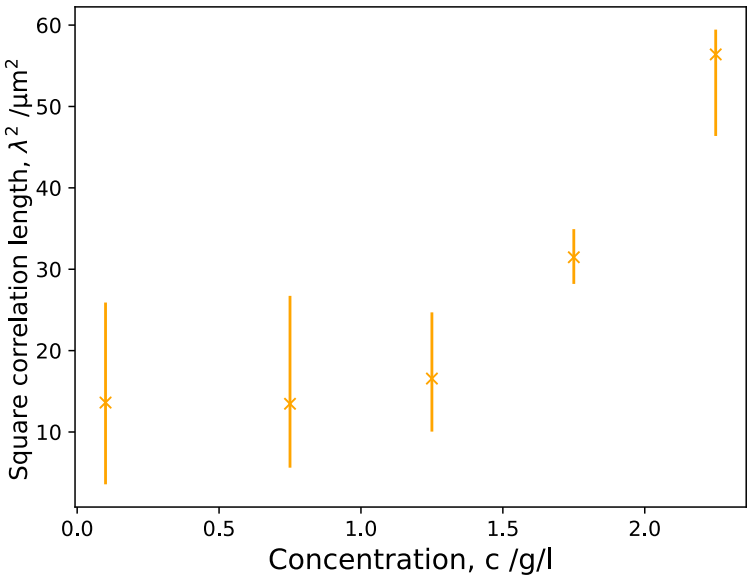

Figure 4.2.4: Plot of the observed square correlation lengths, extracted from the most prominent peak wave vector position q in the radially-averaged 2DFFT of large scale dewetting patterns in AFM images using $\lambda = 2\pi/q$, against the concentration of the deposited and spin-cast gold nanoparticles in toluene solution.

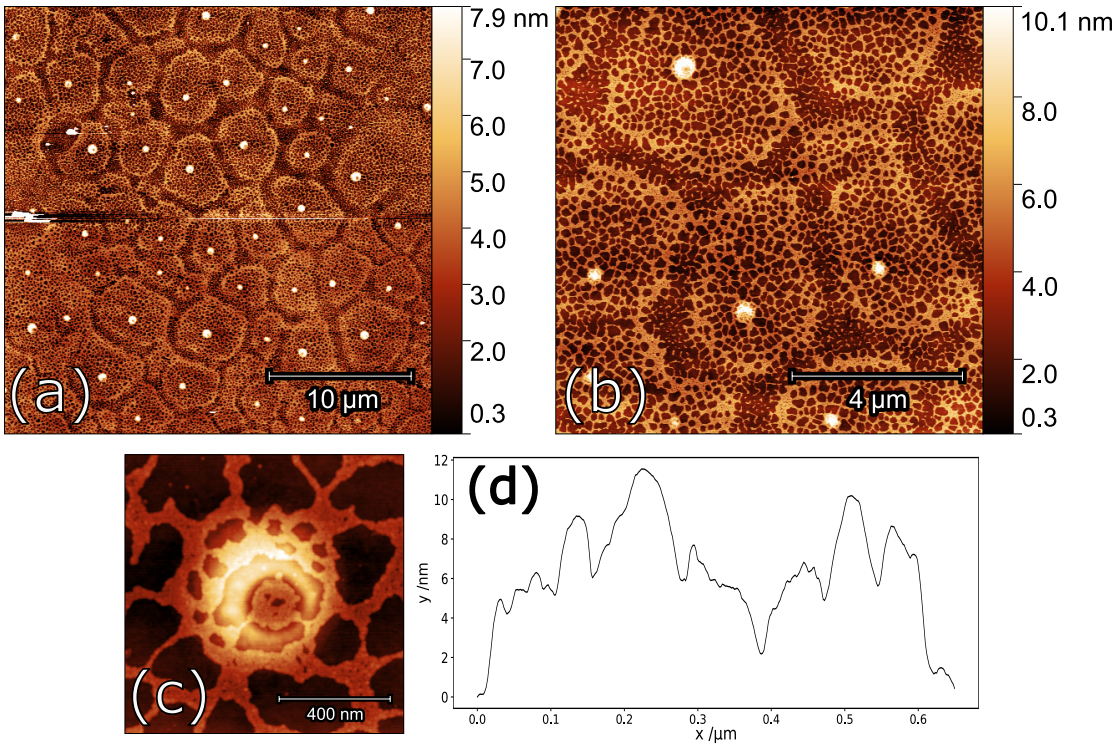

Figure 4.2.5: Tapping mode AFM images of spin-cast gold nanoparticle assemblies from toluene at a concentration of 1.75 g/l onto 1 x 1 cm^2 wafers of plasma- and solvent-cleaned SiO_2/Si(111) taken with the Asylum Research Cypher system. **(a)** 30 x 30 µm^2; **(b)** 10 x 10 µm^2 **(c)** 1 x 1 µm^2 zoom upon (b), highlighting appearance inside a nucleation site; **(d)** 1D line profile of (c) from the top-left to bottom-right.

solution.

The Marangoni effect's role in rupturing the thin film speaks to the stability of these thin films on the manufacturer-prepared thermally oxidised surface prepared in this manner and the effectiveness of the spin-casting technique, as an internal convective flow drives the initial phase instead of defects, or other thermal processes. AFM scans taken at the maximum scale allowed by the MFP-3D system identify an alternative route to nucleation in metastable thin films. Both Fourier and Voronoi analysis can be applied effectively at the larger scales at which Marangoni convection and subsequent nucleation conceivably occurs. The effects of a convective dewetting mechanism upon all levels of the resulting dewetting pattern are profound, introducing periodicity at correlation lengths of 4-15 µm.

4.3 Nanoscale directed dewetting

4.3.1 Fullerene co-deposition

While disruption of dewetting upon homogeneous substrates with tip-grown topographical structures is conducted in Subsection 4.3.3, mixed C_{60}-AuNP films formed by co-deposition from a single solution provides a simple, single-step method to create chemical and topographical heterogeneities for mediating dewetting patterns. While co-deposition of polymer films is common, deliberate simultaneous deposition from solutions of C_{60} and metallic nanoparticles is only previously explored in the context of thick nanocomposite films.[180]

The co-deposition experiment uses the same parameters and systematic approach as Section 4.2. Toluene-based solutions of a combination of octanethiol-functionalised gold nanoparticles and C_{60} (from powder) of varying concentrations were spin-cast, using the parameters from Section 4.2, H:Si(111), produced in Subsection 4.3.2, from a 75 µl pipetted meniscus. 12 different combinations of concentrations of nanoparticles and fullerenes were tested, with nanoparticle concentrations in the range 0.1 - 2.25 g/l, and buckminsterfullerene concentrations of 4 - 28 g/l. Resulting patterns were probed with the MFP-3D system within two weeks of deposition.

All cases in Figure 4.3.1 show a phase separation. Complex dewetting patterns continue to form, but are sensitive to their proximity to deposited aggregates. The full continuum of nanoparticle dewetting patterns, islands to pores, can be observed across the same scanned region, with islands forming closer to aggregates and pores forming at the furthest distance from aggregates. The aggregates appear as flat white features with dark halos around them in the AFM images, the former is due to the necessary masking of the relatively high aggregates in order to observe the dewetting patterns. The dark halos are uncharacteristic of the surface, caused by a flattening artefact induced by the substantial height difference between the silicon surface and aggregate

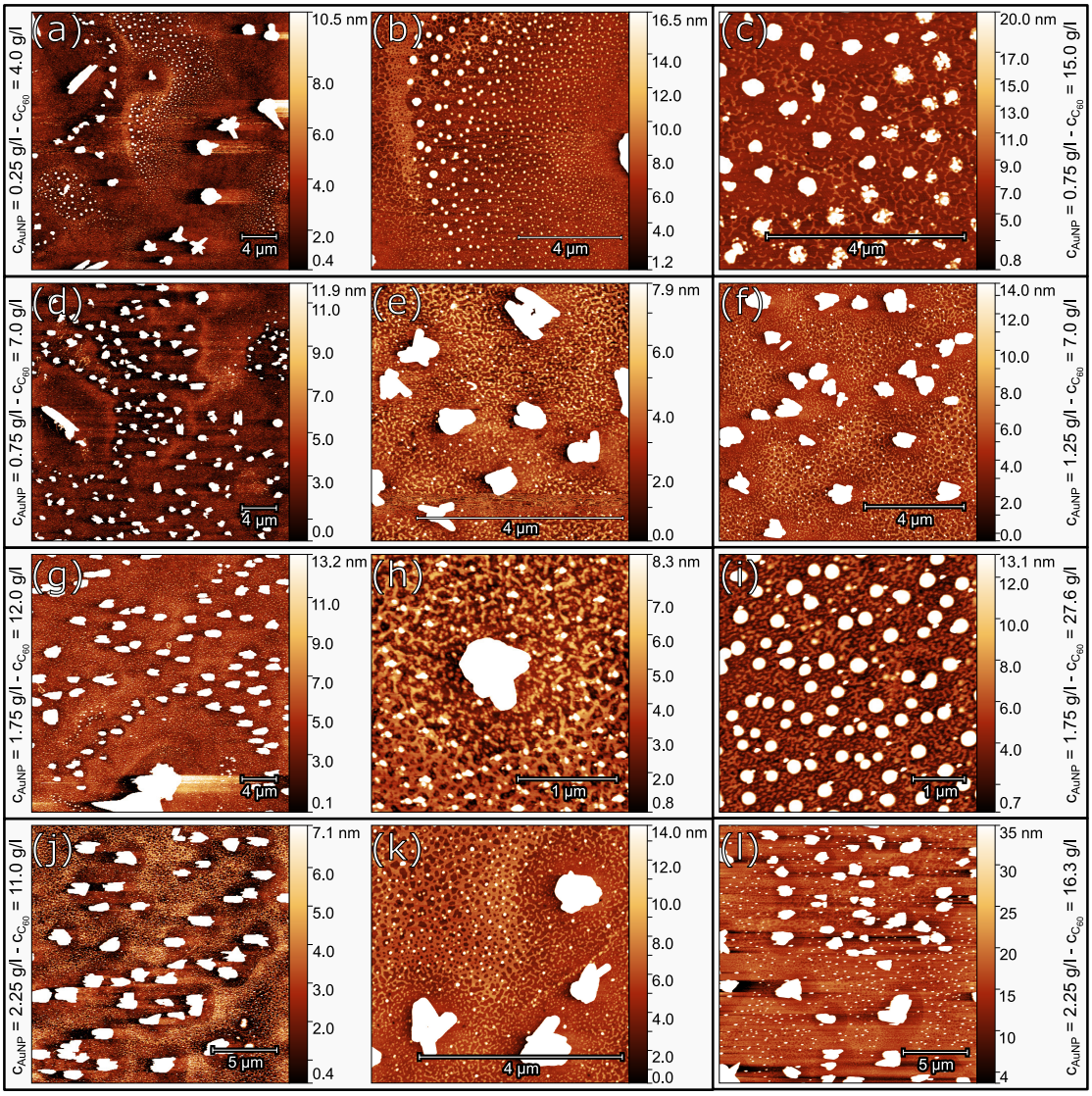

Figure 4.3.1: Tapping mode AFM images of spin-cast gold nanoparticle assemblies and buckminsterfullerene (C_{60}) co-deposited from toluene at various concentrations of both onto 1 x 1 cm^2 wafers of H:Si(111) taken with the Asylum Research MFP-3D system. Concentrations of gold nanoparticles (c_{AuNP}) and concentrations of buckminsterfullerene ($c_{C_{60}}$) in toluene solution used are listed next to the appropriate image(s).

islands.

The aggregate phase in all images demonstrates two phases of aggregation, a "fractal" phase spanning up to 2.2 µm parallel to the surface, and a quasispherical cluster phase of up to 90 nm in diameter. This agrees with previous high-resolution TEM observations of C_{60} in toluene[181], during which the cluster phase is a close-packed monomolecular dispersion. The larger "fractal" aggregate phase meanwhile is characterised as an unstable, porous phase with a $\approx$ 3 nm spatial gap between structural units of the "fractal", observed in solutions prepared under non-equilibrium conditions.

It was unclear whether the aggregate and pattern phases were the result of the phase separation of the fullerenes and gold nanoparticles in solution. Analysis of the relative interaction strengths between particles in the solvent were be used to make predictions about the phase behaviour of the composite nanofluid[59,182]. For the octanethiol-functionalised gold nanoparticles, the Hamaker constant, A, in toluene for the AuNP-AuNP interaction was approximated as 1.1 eV[183,184]. The C_{60}-C_{60} interaction was approximated using A=0.1 eV[185], while the gold nanoparticle-fullerene interaction can be approximated using $A_{12} \approx \sqrt{A_1 A_2}$[59]. Computing an estimate interaction potential[182] returns relative interaction strengths of 10:18:1 for AuNP-AuNP:C_{60}-C_{60}:Au-NP-C_{60}.

Scaling of the coverage of the "fractal" aggregates shown in Figure 4.3.2 agrees with the observed high abundance of the pattern when the solution is prepared under non-equilibrium conditions. While the ratio between average "fractal" diameter and height remains consistent for all concentrations and sizes, experiments could not identify a linear relationship between concentration and size of "fractal" aggregates, also shown in Figure 4.3.2. This is due to "fractal" aggregates rapidly decaying in solution, as their size overwhelmingly exceeds that of stable aggregates[186]. Both phases have drastically different effects and influences during dewetting in the thin film regime. Gold nanoparticle concentration in the same toluene solutions had little effect on the size and stability of the aggregate phase observed during AFM. Deposition of fullerene in toluene without nanoparticles present yielded similar results, suggesting nanoparticles were not binding to either phase.

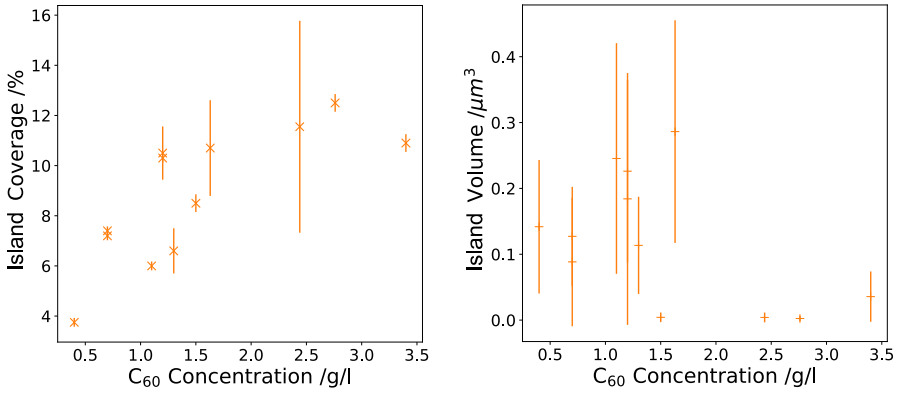

Figure 4.3.2: Graphs showing scaling of observables from AFM of the aggregate "fractal" phase with concentration in toluene solution when deposited onto H:Si(111).

The relationships between correlation lengths and concentration that previously provided evidence of the Marangoni effect initialising dewetting do not hold for all cases in Figure 4.3.1.

Though the AFM images presented appear highly disordered, 2DFFTs sampled from portions of the image suggest local ordering by means of dominant correlation lengths among different pattern types, a case for a combination of spinodal dewetting and strong coalescence phenomena induced by a significant wettability gradient, this is

particularly clear in (b), (f) and (k). (b) has a pore-like region on the left, radially tracking the aggregate on the right of the scan, with a strict correlation length. In the case of (k), where the nanoparticle concentration is relatively high, the cellular pattern outside of transitional regions around the aggregates similarly maintains a correlation length. The transitional boundaries between pattern types are highly abrupt and maintain a critical length for each, all while maintaining dependence on the locations of deposited large "fractal" aggregates.

These observations were quantified by adaptation of the aforementioned sweeping subsampling window tool from Subsection 4.1.2. The chosen side length of the subsampling window was a compromise between being small enough to provide a suitable resolution to the FFT maps, particularly when subsampling in close proximity to the aggregate phase, but large enough to detect a prominent peak in the PSD from the pattern phase. A window size of 128 x 128 pixels was used throughout, which would span between 0.3 and 1.25 µm. The window sweeps over all possible positions on each AFM image, performing the 2D FFT of the enclosed region at each position, fitting a curve to the radially-averaged 2D FFT, then calculating the underlying correlation length of the gold nanoparticle dewetting pattern λ from the peak wave vector q using $\lambda = 2\pi/q$[187]. This builds a series of maps that track the pattern spacing changing across the image, shown in Figure 4.3.3. The maps shown make the transitional boundaries and tracking of dewetting patterns with respect to deposited aggregates far more apparent, particularly in the leftmost images associated with 4.3.1(b).

The tallest "fractal" phase aggregate seemingly nucleates the dewetting process, with clear dewetting fronts originating from them, in some cases, such as (d), creating a pronounced rim of transitioning nanoparticle patterns. The rim is not as pronounced as the "castle moat"-like appearance seen in breath figure experiments using oxide nanorings[106], potentially due to disruption by the smaller aggregates, including the cluster phase. All aggregates should act like quasi-1D defects that spur heterogeneous nucleation. Previous simulations of mixed heterogeneities[126,188] suggest a series of rupture events could be caused by different heterogeneities. The low width of aggregates would mean these events happen near simultaneously, quoted in previous simulations as 0.021 s apart[188]. This however only holds for heterogeneities of the same height and width, with early instability induced by local changes in the critical thickness in the metastable film comes different dewetting mechanisms and rates, resulting in film variation similar to that of altering external factors like ambient humidity on a very local level[114]. The timescale often exceeds that of spinodal dewetting, resulting in non-standard pattern formation, (h) displays a multi-layer nanoparticle pattern centred on an aggregate, attributed purely to a flow of material as fluid retreats from thinner areas of film to thicker areas.

The rapidly retracting front around that of the tallest "fractal" aggregate also drags the other aggregates on the surface. (b) even displays a cluster size dependence on

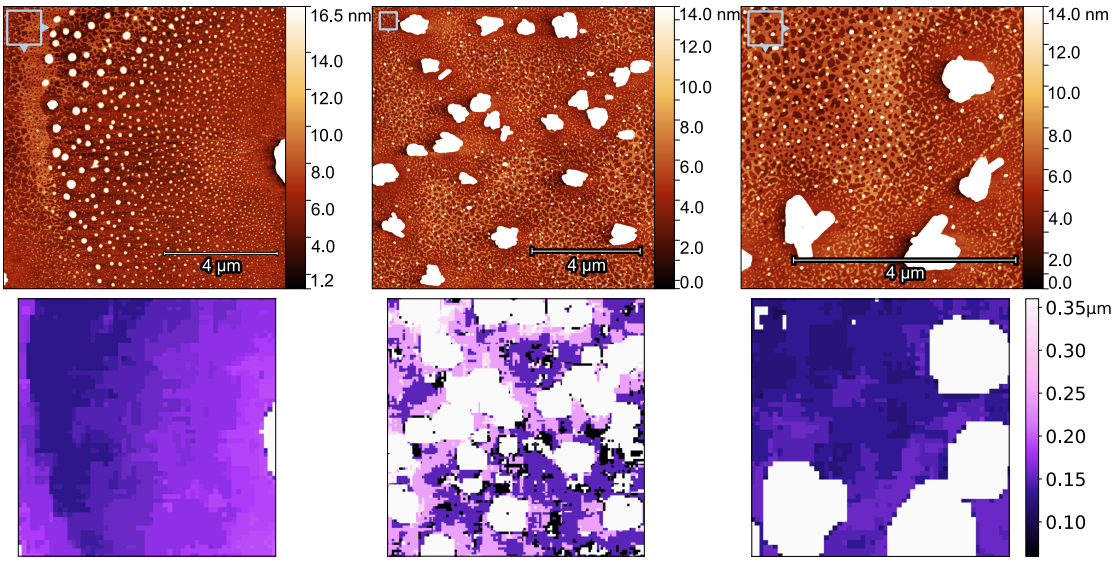

Figure 4.3.3: Quantification of observed shifts in dewetting pattern type and correlation length with respect to co-deposited C_{60} by use of a sweeping subsampling window using Fourier analysis. **(Top row)** Images (b), (f) and (k) from Figure 4.3.1 annotated with the chosen size of the scanning window; from left to right: c_{AuNP}=0.25 g/l, $c_{C_{60}}$=4.0 g/l, c_{AuNP}=1.25 g/l, $c_{C_{60}}$=7.0 g/l, c_{AuNP}=2.25 g/l, $c_{C_{60}}$=11.0 g/l. **(Bottom row)** Map of correlation lengths of the underlying dewetting patterns obtained from the peak wave vector q from a radially-averaged 2D FFT of the region enclosed by the local subsampling window centred on each position on the image directly above. The scale bar represents the local correlation length from $\lambda = 2\pi/q$ for all maps.

distance from the tall aggregates. Some of these aggregates, relocated or not, have little to no influence on the dewetting patterns on the gold nanoparticles, (i) and (l) illustrate this well. This is also observed in simulations[188] and experiments[111] in terms of late-onset from the instance of dewetting in mixed morphologies, in this case, multiple different surface defects of varying wettabilities. Figure 4.3.4 shows the process by which structures form around the central heterogeneity, separated by a rim, the rim becomes more circular and binding to the heterogeneity, until any evidence of dewetting from the later onset is eliminated. This tight rim is observed in 4.3.1(g), where smaller and lower height aggregates in proximity to the larger aggregate at the bottom of the image.

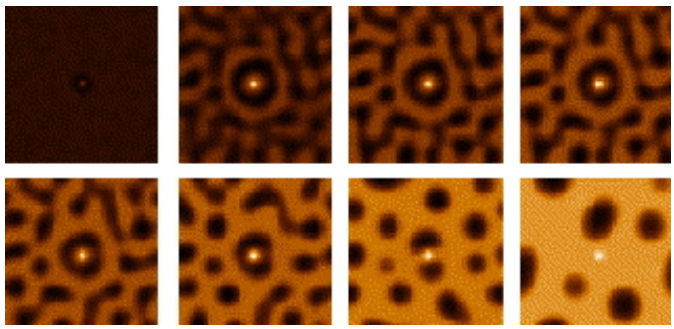

Figure 4.3.4: Morphological evolution of a 40 nm thin film on a 500 x 500 µm^2 heterogeneous substrate dewetting from a smaller and less wettable 25 x 25 µm^2 heterogeneity over time T; from top left to bottom right T=0.43, 19, 25.5, 28.8, 33.7, 52.4, 94.8 and 365.7. From Sharma *et al.*, Physica A 1-2, 2003[188]

In summary, buckminsterfullerene and octanethiol-functionalised gold nanoparticles co-deposited from toluene at a series of concentrations onto a H:Si(111) surface produce an aggregate phase and dewetting pattern phase. Aggregates create strong wettability gradients across a H:Si(111) surface by providing both topographical and chemical heterogeneities, causing an effective shift in the local interface potential $\Phi(h, x, y)$. The resulting shift in observed correlation lengths of the patterning phase is quantified effectively by Fourier analysis, which locally maps the AFM image.

While aggregates provide a point-like microscale dewetting mediator, the disordered nature of the resulting AFM images provides little room for statistical applications beyond the presented Fourier analysis. Revisiting C_{60}-AuNP co-deposition would necessitate strong modification of the experimental method. A mechanical mixing process[181], deposited grids[131], or the teflon ring and breath figure approaches described in Subsection 3.3.1 could be used to improve the aggregate phase's size uniformity, and induce more uniform spacing of the phase on the surface. Monte Carlo method-based simulations with tall circular aggregates with seeded locations and local chemical potential[126,188] could happen in conjunction with experiments. Though supported theoretically by Hamaker analysis, it would be necessary to experimentally establish whether the aggregate and patterning phases consist of a single molecule in order to assert phase separation of the co-deposits.

Nanoscale directed dewetting by means of a co-adsorbate demonstrated the effectiveness of gold nanoparticles as a far-from-equilibrium tracer for mediated shifts in the local interface potential. Subsection 4.3.3 continues the exploration of mediated dewetting with highly localised modification of the underlying surface. Lithographically patterning the silicon oxide substrate could direct the self-organisation of gold nanoparticles by controlling nanoparticle adsorption and dewetting pattern formation.

4.3.2 AFM-induced local oxidation

Scanning probe techniques go beyond imaging, providing readily available routes to modify the surface upon similar length-scales to deposited nanostructures. This includes exerting a physical force from the tip, such to scribe patterns on the surface below[189], or a "dip-pen" method, by which the tip is coated from a reservoir of molecules prior to scanning, such to precisely deposit them onto the surface[190]. Another established technique is highly-localised induced oxidation of hydrogen-terminated silicon using an electrically biased probe[191], exploited below as a means to direct dewetting on top and around oxidised regions.

The selective oxidation process begins with a hydrogen-terminated silicon surface. Replacement of the oxide layer on a silicon surface with terminating hydrogen atoms, known as hydrogen passivation, can be prepared with atomic-level cleanliness in UHV, via deposition onto highly reactive bare silicon from a hydrogen source, a thermal gas

cracker. The resulting surface is preferable to an oxide layer in many cases, providing an inert, low-defect density substrate with differing electronic properties.[192]

An alternative for preparation under ambient conditions is deployed here. The silicon's oxide layer was chemically etched with a combination of hydrofluoric acid (HF) and ammonium fluoride (NH_4F)[193]. The etch both removes the oxide layer and provides the hydrogen passivation of the surface, returning an atomically-flat hydrogen-terminated surface[194,195]. The presence of HF submersion in the method meant a highly controlled workflow was planned and tested before each etch. The workflow that returned the cleanest and most homogeneous surface, when inspected with optical microscopy and tapping mode AFM, was a sequential 15 minute submersion of a Si(111) wafer in HF, followed by a 15 minute submersion in HF buffered with ammonium fluoride in a 1:7 ratio. The etched Si(111) wafer was cut into 1 x 1 cm^2 square chips, ready for insertion onto the conductive platform in the atomic force microscope.

The immediate exposure to ambient conditions causes the chemically-etched silicon to partially re-oxidise[196–198]. After removal from the buffered HF solution, the silicon surface is near-saturated with H-Si bonds, with a few Si-F defects. Fluorine atoms are quickly substituted by OH^- ions from water in the atmosphere, while hydrogen is also substituted in a similar manner at a much slower rate. The Si-OH^- bond rapidly polarises due to the highly electronegative OH^- group, this in turn polarises the Si-Si bonds in the sub-surface layer, exposing them to atmospheric water, resulting in an initial oxide layer. The oxide layer continues to grow by a diffusive process. Electrons from the Si conduction band may tunnel through the oxide layer into surface-adsorbed species, inducing ionic oxygen species. Diffusion of oxygen ions across the growing film is promoted by an electronegativity gradient between Si and SiO_x that results in an interfacial charge double layer. This oxidation process is self-limiting, the increasing tunnelling and diffusion barrier of the growing oxide layer limits the thickness to around 0.7 nm under ambient conditions.[198]

The diffusive stage of the oxidation process is further encouraged with an electrically-biased probe. Electrons from the probe supplement the ionisation of surface species and the enhanced electric field in proximity to the probe promotes the mobility of oxygen ions on the surface. Reports showed an exposure to an AFM probe held at -10 V increased the local oxide height up to 4 nm[132]. The rapid decay of the electric field strength away from the tip-substrate cavity causes the process to locally self-terminate beyond the critical strength, resulting in the technique's localised nature.[199]

The original process[191] utilised an STM probe and was later expanded to conductive AFM probes in non-contact mode. The process was deemed to place high emphasis on surface-adsorbed water, with a water bridge forming between the probe and surface[200], shown in Figure 4.3.5, providing a source of O^- and OH^- for oxidation. The water bridge sets a resolution limit for structures grown by this process. The signifi-

cant difference between the dielectric constant of the water compared to air, 81 to 1, renders it an effective "lens" for the electric field between the apex of the tip and the substrate. The area enclosing the neck of the water bridge confines the field and hence the oxidation process, and hence controls the resolution of the process[200]. Control of the tip-sample distance and volume of adsorbed water meant structures as small as 10 nm have been achieved.[132]

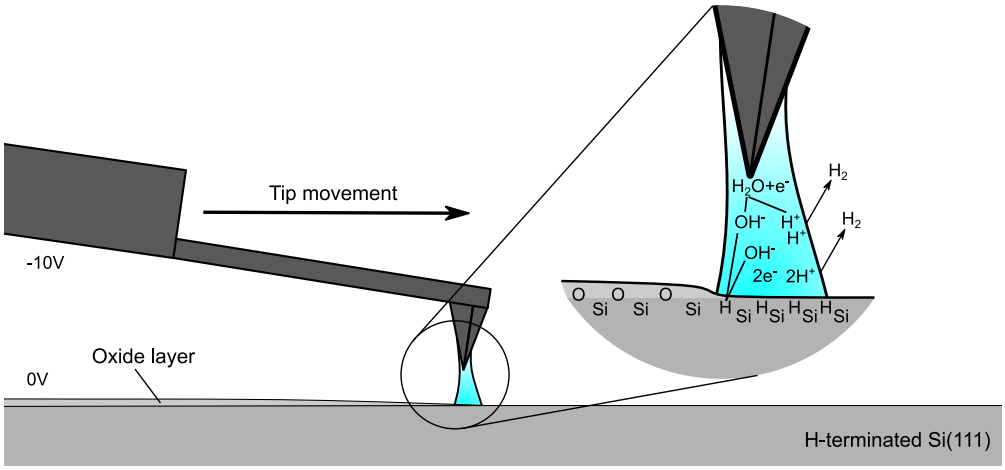

Figure 4.3.5: AFM tip-induced oxidation of H-terminated silicon.

The lithography was performed upon etched 1 x 1 cm^2 Si(111) chips using a standardised method that produced oxide layers of consistent desired characteristics. Localised oxidation was carried out using a silicon tip held at a bias of -10 V and moving at a speed of 0.75 $\mu m/s$. This yields the majority of oxidised surface as square blocks, of 4 - 36 μm^2 (from 1 x 4 μm^2 to 6 x 6 μm^2) surface areas with a consistent height across the entire oxidised region.

The microscale blocks shown in Figure 4.3.6 of one of the three oxidised wafers remained stable during spin-coating and solvent cleaning. There were no significant signs of erosion during the nine month period of systematic study under ambient conditions, with the method causing minimal disruption to the surrounding H:Si(111) substrate. Oxide layer thicknesses ranged from 1.4 to 3.1 nm in vertical height relative to the surrounding HF-etched surface. FFT measurements showed roughness was not necessarily correlated to final height. The new oxide layer had the capacity to either increase or reduce h_{rms} by up to 50% compared to the local un-patterned silicon. Qualities of the tip-induced oxide layer were determined by a combination of the scan speed, the quantity of water adsorbed on the surface (essentially the humidity within the atmosphere around the microscope), the true tip apex-substrate separation, tip sharpness and the underlying etched silicon quality[201]. While most of these factors were controlled during experiments, a wide range of height and roughness were observed.

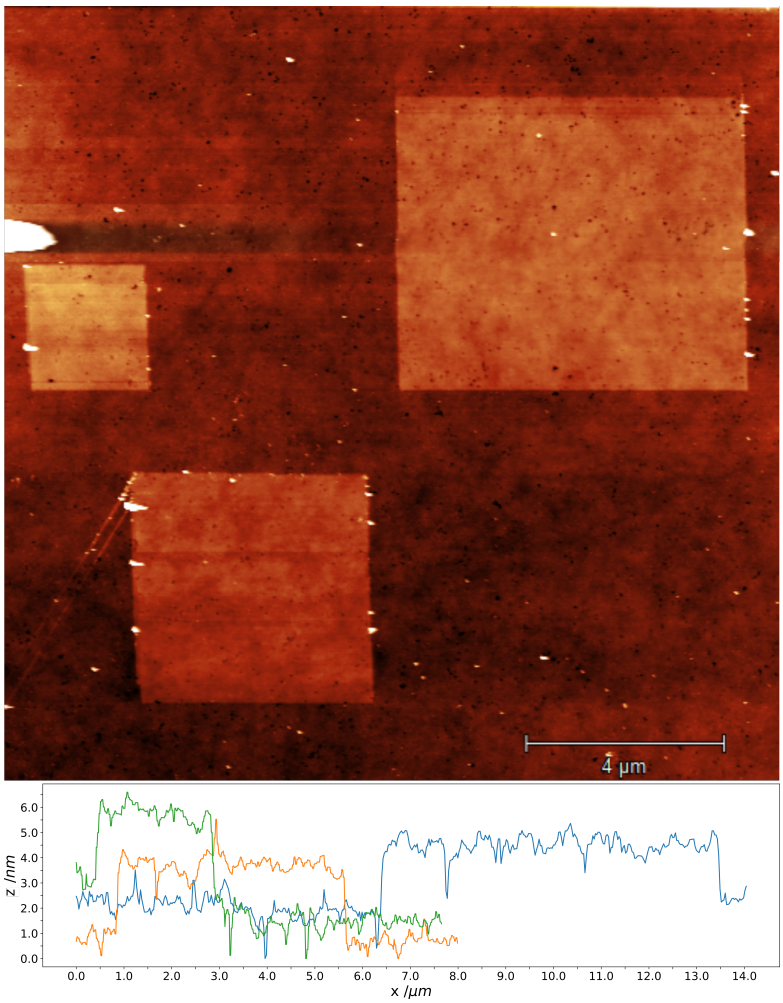

Figure 4.3.6: AFM image of SiO_2:Si(111) with tip-induced heterogeneities. Thick AFM tip-grown oxidised regions on a Si(111) substrate that has been etched in hydrofluoric acid and ammonium fluoride then exposed to air to induce a thin oxide layer growth upon the resulting surface. Neighbouring grown regions of sizes 2 x 2, 4 x 4 and 6 x 6 μm^2 are shown, including horizontal line profiles of each tip-grown region and surrounding un-patterned area.

4.3.3 Locally mediated dewetting

Octanethiol ($C_8H_{17}S$)-passivated gold nanoparticles of particle sizes 2-4 nm were prepared in toluene and diluted to nanoparticle concentrations between 0.1 and 17.5 g/l. 75 µL of each nanoparticle solution was spin-coated, using the parameters from Section 4.2, onto the selectively-oxidised 1 x 1 cm^2 square Si(111) chips. Tapping mode AFM for the purpose of imaging was carried out using the Asylum Research MFP-3D and Cypher. Prior to further spin-coating, wafers were submerged in toluene for 4 hours to remove the previous gold nanoparticle coating.

Figure 4.3.7 shows the variety of patterns formed for changes in concentration across the oxide regions shown in Figure 4.3.6. Nanoparticle patterns in 4.3.7(a-c) show dewetting at low nanoparticle coverage, 1.75 g/l of gold nanoparticles in toluene. The

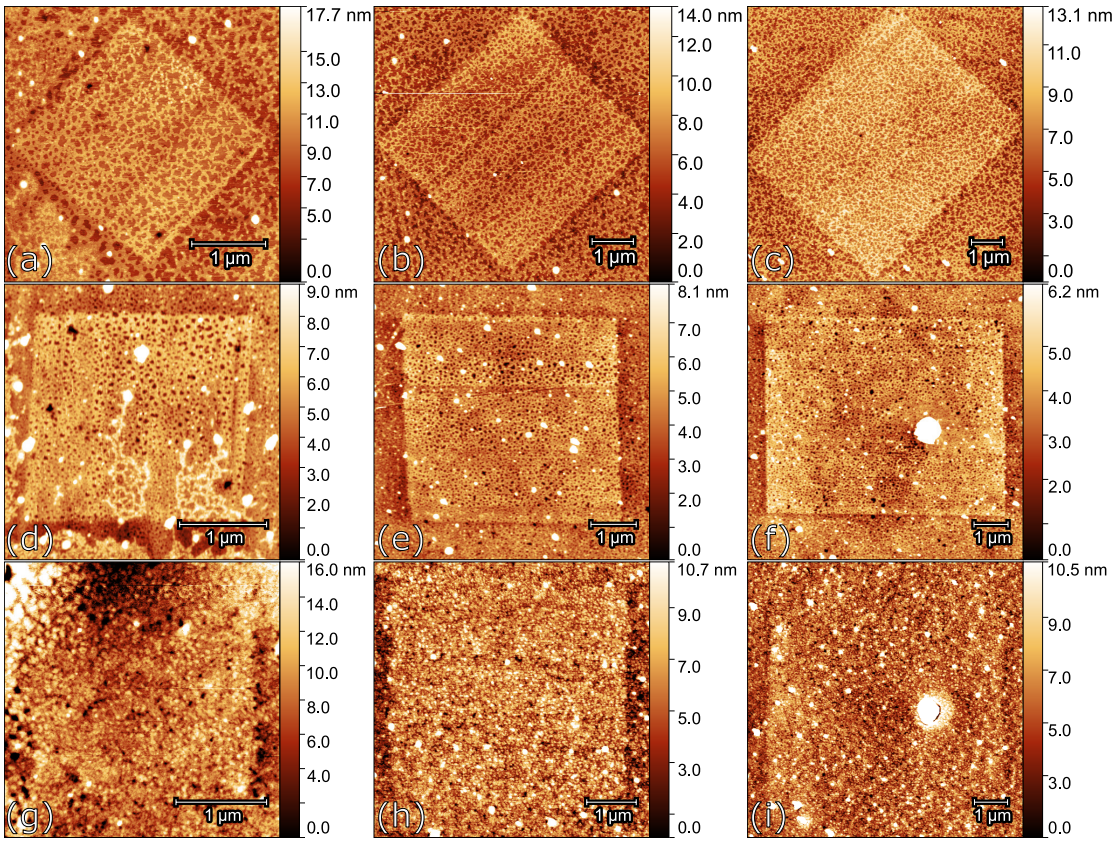

Figure 4.3.7: AFM images of gold nanoparticles spun from toluene onto Si(111) chips acid-etched to remove the native oxide layer in hydrofluoric acid and ammonium fluoride to encourage H:Si(111) growth, exposed to air to re-oxidise a thin layer on the surface, then subsequently selectively re-oxidised with thick AFM tip-grown SiO_2:Si(111) square regions. **(first row)** 1.75 g/l concentration; **(second row)** 5 g/l concentration; **(third row)** 17.5 g/l; **(first column)** 2 x 2 μm^2 region of oxide; **(second columnn)** 4 x 4 μm^2; **(third column)** 6 x 6 μm^2. As nanoparticle concentration increases, down the figure, a transition in type of dewetting pattern morphology is observed from cellular networks (a-c), pore-like holes (d-f), to surface-independent self-organisation(g-i).

cellular pattern continues nearly seamlessly between the tip-oxidised region and surrounding area.

No sharp transition in the type or types of dewetting pattern was observed between the tip-oxidised and surrounding regions in the tested range of concentrations with AFM. Previously, both experimentally and computationally, lower concentrations of thin film provide a striking contrast of labyrinthine on the surrounding thin oxide region and cellular on the thick square oxide region, similar to that in Figure 4.3.8. Simulations suggest high coverage affects the mobility of the nanoparticles, and reduces the solvent evaporation rate from thin film[59,202]. Labyrinthine patterns form during faster evaporation rates than those of cellular patterns, this suggests at the concentrations explored that the shift in surface properties between the two regions was not significant enough to induce a transition in pattern type.

Dewetting nucleated by defects in the surface proved to have a key role in the be-

haviour of the solvent. Substantial point-like imperfections act as persistent nucleation sites across all concentrations. This is particularly visible in 4.3.7(f) and (i), showing the same white dot between concentrations for the same tip-oxidised layer, showing significant nucleation at the same location between multiple different concentrations. Cavities that appear as black spots in AFM images, particularly visible in Figure 4.3.7(a) and (d), are crater defects caused by the HF reacting with defects in the silicon wafer during etching. Cavities consistently create a small nanoparticle-free perimeter on the tip-oxidised region of radius similar to the nanoparticle feature length, even at higher concentration spin coats. Feature length is shown to play a fundamental role in dewetting, as it is shown to be unfavourable to form patterns of lower length around these cavities. This lends itself to a confinement effect mediated by the surface, without the need for further chemical modifications.

The Si(111) substrate patterned with spin-casted gold nanoparticle solutions with concentrations between 2.5 and 7.5 g/l exhibited larger micron length-scale dewetting patterns that induced shifts in the height of the nanoparticle monolayer of up to 2 nm high. These were similar to the cellular patterns observed in Section 4.2. Micron length-scale patterns have previously been tentatively accredited to secondary dewetting processes acting within the thin film, Marangoni convection being a probable source[10].

Multi-layer dewetting patterns were found to be prominent at the higher concentration ranges studied. Discounting island-like patterns, only 4.3.7(d) exhibits complex multi-layer patterns. This effect is promoted by a reduction in nanoparticle mobility caused by the volume of nanoparticles in the nanoparticle-solvent film. This becomes a less likely occurrence in the presence of surface imperfections, which causes heterogeneous nucleation to become the dominant dewetting mechanism. At a critical concentration, the immobility caused by the sheer volume of nanoparticles in the film causes them to not establish a coherent surface to self-assemble onto, resulting in the appearances of Figure 4.3.7(g-i), where nucleation independent of surface and its defects dominate.

4.3.4 Quantification with Fourier analysis

Initial modelled studies previously conducted in the Group suggested the shifts in pattern properties were due to a shift in interaction strength between the solvent and surface. This was tested by adding spatial dependence to Rabani *et al.* model's Hamiltonian, by spatially varying the value of the chemical potential term, μ, in equation 3.6. Figure 4.3.8 shows how even slightly (6%) lowering the term inside the square causes a striking difference in pattern type between the square and surrounding area. This was enough to cause a transition from cellular networks "on" the square, to worm-like domains "off" the square. The physical interpretation is a greater wettability upon the tip-oxidised square region.[132]

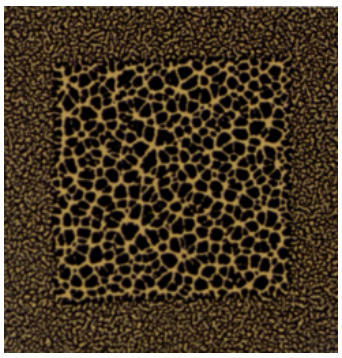

Figure 4.3.8: Previous result for a Rabani *et al.* model simulation modified to include a spatially-dependent variable, the central square in given a chemical potential term, μ, that is 6% lower than that of the surrounding area. From Martin *et al.* Phys. Rev. Lett. 99, 116103, 2007[132]

Investigation of the underlying source of the wettability shift by systematic experiment is of interest. At a chemical level, the Hamaker constants for H:Si(111) and SiO_2:Si(111)[59] as estimates for the solely etched and tip-oxidised regions respectively could explain the distinction between the two regions. However, previous experiments show an expected contact angle difference from this hypothesis is not observed[132]. A more appropriate system would be that of SiO-Si against SiO-Si, which explains the near-identical contact angle but discounts changes at the chemical level as a sole driver of the shift in wettability[63].

The origin of the transition in solvent-surface interaction was also loosely traced to roughness, with the hypothesis of increased surface roughness acting to slow the evaporation of the solvent. This operates in tandem with the hypothesis of solvent evaporation rate being responsible for differences in pattern morphology[132]. The existence of oxidation that smooths the surface allows for an extension of this hypothesis for a reduction in roughness. This is explored using Fourier analysis, using the methods discussed in Subsection 4.1.2, as a means to track both RMS roughness on the tip-oxidised region and surrounding surface before depositions, and feature length post-deposition.[169]

A series of AFM surface images that had both a consistent RMS roughness and exhibited cellular patterns across both regions of their images were collected for Fourier analysis using code in Appendix B. Figure 4.3.9 shows a portion of the process of Fourier analysis to determine a relationship between roughness and cellular pattern assembly. (a) and (c) show the extremities of shifts in feature length between the tip-oxidised silicon and etched silicon solely exposed to air (and hence primarily H:Si(111)). Visually the cellular pattern on the tip-oxidised silicon in (a) appears less dense than that on the surrounding silicon, and vice versa for (c). This is backed up statistically by the FFT, by which the peak wave vectors diverge in different directions returning negative and positive Δq for (a) and (c) respectively.

(i) suggests the shift in feature length between tip-oxidised and surrounding silicon for all observed cellular patterns track a loose trend with the detectable oxidation-induced roughness. (e) and (g) notably deviate from this trend. (e-f) displaying a significant shift in feature length both visually and statistically, despite very little difference in roughness between the two regions. (g-h) exhibits limited shift in feature length, despite the FFT upon the pre-deposition 2 x 2 μm^2 square and surrounding surface in Figure 4.3.6 returning a $\Delta\%h_{rms}$ of $+35\%$. This is potentially due to higher order heterogeneous nucleation, evidenced by the large stalagmite-like aggregate upon the oxide region in (e) and multiple circular aggregates in the H:Si(111) region and denuded areas around defects in the tip-oxidised region in (g). This may be driving rapid dewetting in those regions independently of surface roughness.

Previous modelling, as well as the C_{60} co-depositions experiments, suggests a rupture event that initialises heterogeneous dewetting induced by a larger local defect will reduce the impact of smaller defects on the resulting nanoparticle pattern, and by extension the roughness of the tip-induced oxide layer[126,188]. There are other potentially significant factors outside of detected roughness impacting cellular pattern feature lengths, with more emphasis being placed on larger defects or nanoscale roughness/porosity of the grown layer below the size of pixels captured by the microscope. Additionally, the height difference between the two surface regions may become significant during dewetting. Taller regions are likely to be the first to reach critical thickness for the disjoining pressure to cause the nucleation of a hole in the film. The correlation between the shift in percentage RMS and wave vector, both calculated by Fourier analysis, plotted in Figure 4.3.9(i) is not significant enough to propose the total surface roughness observed by AFM, or is an unsuitable metric for evaluating surface roughness induced by the charged tip, as the underlying source of the wettability shift.

4.4 Final remarks

Self-organisation and self-assembly play a substantial role in nature all the way down to the nanoscale. Identifying dynamic behaviour at this scale has the capacity to expand to similar or even higher scale analogues. Far-from-equilibrium nanoparticle assemblies demonstrate the striking and diverse appearance of self-organisation phenomena throughout nature. Near mono-diperse metal nanoparticles functionalised by diverse ligands see continued interest for applications in nanoelectric devices, as a unique form of bottom-up assembly via spontaneous pattern formation in a thin solvent film.

Convective, nucleated and spinodal dewetting were all observed inseparably by means of AFM upon gold nanoparticles kinetically "trapped" on a silicon surface, long after the volatile solvent they were suspended in had rapidly retracted and evaporated from the surface. Suspended gold nanoparticles proved to be an effective history of the volatile solvent as it dewets from a surface. Their unique far-from-equilibrium pattern formation was readily observed by AFM, and quantified with specialised appli-

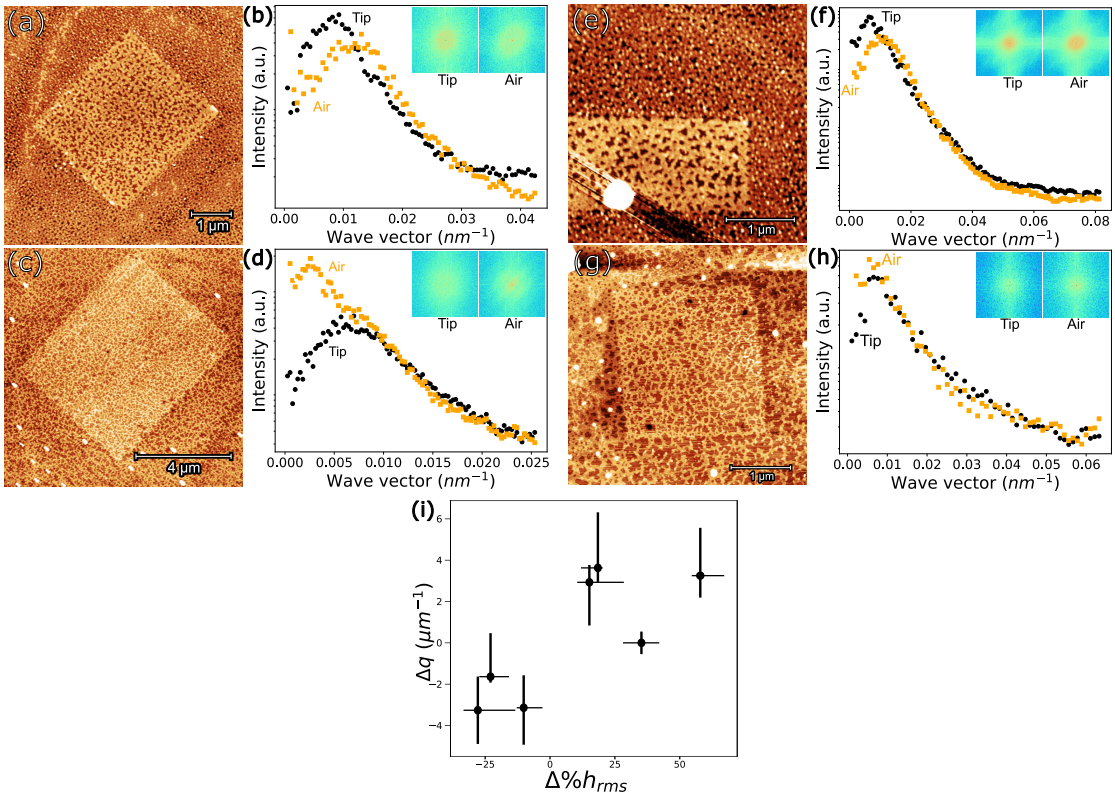

Figure 4.3.9: Fourier analysis of AFM images of a silicon wafer containing cellular-type nanoparticle patterns from Figure 4.3.7 and other surfaces. **(a)** 3 x 3 µm^2 @ 2.25 g/l; **(c)** 6 x 6µm^2 @ 1.75 g/l from 4.3.7(c) expanded; **(e)** 1 x 4 µm^2 @ 2.25 g/l; **(g)** 2 x 2 µm^2 from 4.3.7(a) expanded. **(b,d,f,h)** Semi-logarithmic plot of the radially-averaged 2DFFT of the raised tip-oxidised region compared to the HF-etched silicon, that is solely exposed to air, of their respective AFM images, with the 2D FFTs of each region inset; **(i)** plot of the percentage change in root mean square roughness against the change in effective feature length between the pre-deposition tip-oxidised and air-exposed regions among cellular-type nanoparticle pattern AFM images. The roughness of the tip-oxidised region is shown to either increase (a) or decrease (c) the cellular pattern's feature length, or maintain the feature length in the face of dewetting-nucleating surface defects on (e) or off (g) the region.

cations of common statistical methods. The system benefits from rich literature, and a large range of tunable laboratory conditions, from the alterations to the synthesis of nanoparticles to AFM-induced pattern coarsening. Such an expansive parameter space will continue to be explored, aided by modern computational tools.

High-accuracy numerical simulations of the self-assembly of nanoparticle superlattices based on modified versions of the Rabani *et al.* model support experimental observations. High volume data sets of simulated image tested analytical software using Fourier and principal component analysis. Pattern recognition and automated labelling based on modified Minkowski metrics were evaluated by using a manually-labelled Rabani data set and real AFM data with PCA. Clustering in the score plots for real and simulated images among identified dewetting pattern morphologies was highly promising for automating classification of images of nanoparticle assemblies. Rabani *et al.* model images were utilised in Fourier-based feature extraction software at all stages, first in testing wave vector peak fitting to attain the correlation length. PCA upon Ra-

bani *et al.* model generative parameters and reciprocal space feature metrics gathered from the radially-averaged 2D FFTs of final states of the model for a large data set returned weaker clustering than Minkowski morphometry. Relationship mining between the generative parameters and the shape of the PSD returned a little direct correlation between individual parameters across the whole range, attributed to a phase boundary in the system. However, the strength of Fourier analysis came from tracking the evolving Monte Carlo model in reciprocal space for numerous resulting dewetting pattern types, aiding the observation of nanostructure coarsening in simulation. A comparable coarsening exponent in simulated coarsening island and worm-like domains suggested thermally-driven Ostwald ripening as the primary cause of coarsening in both real and simulated data.

While set parameters in a simulated space produce consistent pattern types, reproducibility of patterns in experiments, as well as mapping of simulated onto experimental parameters, remains a challenge. Consistent workflows for silicon cleaning, hydrogen-passivation, tip-induced oxidation and spin-coating were recorded in great detail. Studies of nanoparticle concentration beyond that of common concentration ranges utilised in literature, combined with high scan stability at wide scan sizes in AFM, led to uncommon observations of secondary long-range microscopic ordering. Evidence is presented, particularly Voronoi cell mapping and a characteristic relationship between concentration and correlation length acquired from Fourier analysis, for the involvement of Marangoni convection in its formation. The physical lengths observed in AFM images of cellular patterning, specifically the effective Voronoi site distances, corresponded to correlation lengths calculated from the peak wave vectors using Fourier analysis.

Control over far-from-equilibrium pattern formation by means of direct surface modification before deposition was quantified by Fourier analysis. A sharp AFM probe boasts the capacity to create stable microscale oxidised patches on a chemically-etched Si(111) surface. Much like the untreated substrate, the tip-oxidised squares support far-from-equilibrium pattern formation, assuming lateral dimensions are greater than the characteristic feature lengths of nanoparticle patterns produced in the experimental parameter space, dictated by concentration, interface potential and further conditions during deposition. Below this limit, be it by smaller tip patterns, defects like cavities, or other surface heterogeneities, it was more energetically favourable for nanoparticles to form a denuded perimeter and maintain the local pattern feature length. Tip oxidation had the capacity to roughen or smoothen a continuous region of substrate, compared to the local hydrofluoric acid-etched regions, in terms of the RMS roughness measured in reciprocal space. In the absence of larger aggregation sites, roughness was a potential primary driver of feature length in cellular patterns in self-organising deposits, displaying a limited positive trend between the percentage change in RMS roughness and the percentage change in peak wave vector. In real space, this translates to the density of cellular patterns increasing with underlying surface roughness.

Future work that explored pattern development upon a wider range of tip-oxidised layers of differing RMS roughness, and aims to generate non-transient values of RMS roughness via Fourier analysis, could be explored. The methodology, observations, and quantification with Fourier analysis form the in-preparation paper.

Far below the aforementioned denuding limit was observed during co-deposition, during which an aggregate phase created a local wettability gradient, from rapid evaporation times to slower evaporation times, originating from the centres of the larger fractal-like clusters. This gradient was marked by the presence of transitioning nanoparticle pattern morphologies, from islands to holes. Coalescence phenomena along this gradient resulted in sharp transitions between observed morphologies, quantified with the application of unique Fourier analysis code to segment images. Final AFM images produced by co-deposition were highly complex, larger aggregates impacted the arrangement of smaller aggregates upon the surface. A manner of limiting aggregate sizes, or spatially guiding the deposition of aggregates that do not compromise pattern formation in the co-deposited patterning phase could reduce image complexity to enable rigorous statistical image analysis.

Key directors of the dynamic behaviour of thin films of solvent have been identified. The self-organisation of nanostructures in a series of new and modified solvent deposition experiments in a far-from-equilibrium regime is explored. Open-source statistical analysis tools, tested on simulated data using a modified form of the Rabani *et al.* model, and then real experimental data, are devised to be applicable to similar nanostructured systems and beyond. Chapter 6 explores further image-focused tools for experimental nanoscientists, to convert large data sets of raw scanning probe microscopy images into statistically-robust images for analysis explored in this chapter and beyond.

5 Locating Caged Molecules with NIXSW

Author Contribution Statement

Some of the data discussed in this chapter is published in Jarvis *et al.*, Communications Chemistry 4(1), 2021[58]. This chapter also describes additional data analysis that is not included in the Communications Chemistry paper cited above and which is entirely JH's own work.

5.1 Endofullerenes

Endohedral fullerenes, often abbreviated to endofullerenes, represent a complex form of functionalisation of the molecule by the addition of specific groups inside the carbon cage. The established nomenclature for a fullerene of Y carbon atoms encapsulating a group X is X@C_Y. Water confined by buckminsterfullerene, $H_2O@C_{60}$, and HF confined by buckminsterfullerene, HF@C_{60}, are central to this chapter.

Endofullerenes encapsulating a wide variety of species have been synthesised in the past, though the concept of "molecular surgery" [203] provided new opportunities in the form of a wider array of containable species. Carbon cages of different sizes have been synthesised to include lanthanides, group 1, 2, 3 and 5 elements, and noble gases, as well as poly-encapsulations of up to 4 groups[204–209]. The processes for these often involve physical methods under harsh conditions, such as arc discharge of metal-doped carbon rods, ion implantation or high pressure/temperature treatment with rare gases[210]. Such processes were unsuitable for producing a high yield of endofullerenes encapsulating molecules. The surgical approach is a short synthetic route that creates a wide opening in the fullerene for guest molecules, followed by a chemical "suturing" technique to reform the cage.[211,212]

The encapsulation of molecules within the C_{60} cage provides a unique opportunity to study their properties unperturbed by interactions with the environment. High yields of $H_2O@C_{60}$ and HF@C_{60} allowed for physical and spectroscopic study of the near-isolated molecule and new system as a whole, free from the complications of dimerisation and hydrogen bonding. Weak interactions with the cage meant nuclear spin isomerism and ortho-para conversion has been observed from confined H_2O[213], as well as quantisation of translational and rotational degrees of freedom of both confined HF and H_2O.[214,215]

SPM of fullerenes deposited on metallic[217,218], semiconducting[219–221], and semiconductor substrates[222] has remained a powerful tool to study the resultant morphology. STM/NC-AFM investigations of sub-monolayer and multilayer coverage of $H_2O@C_{60}$ revealed filled and empty cages had a very similar appearance, shown in Figure 5.1.1. Characterisation using imaging methods aiming to evaluate the short-range response

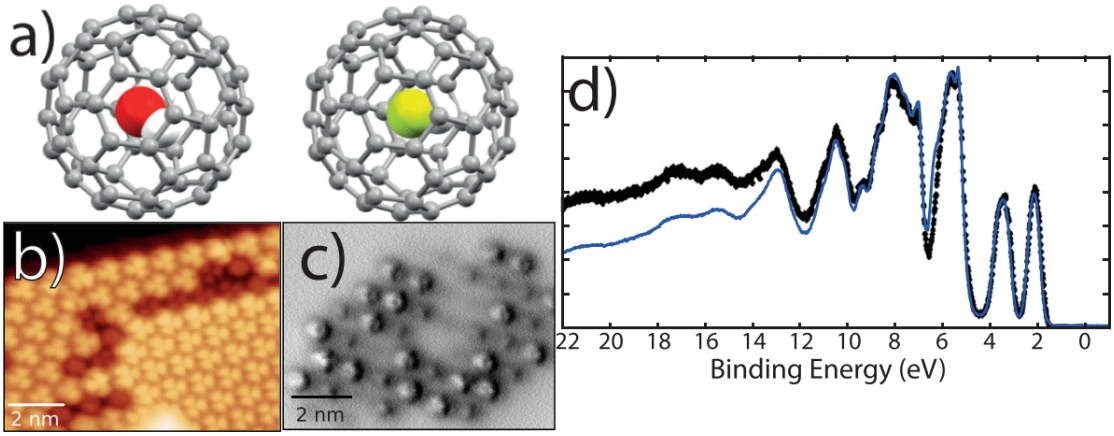

Figure 5.1.1: Scanning probe and photoemission data as evidence for substantial screening of encapsulated molecules. **(a)** Ball-and-stick models of water encapsulated in C_{60} ($H_2O@C_{60}$) and hydrogen fluoride encapsulated in C_{60} ($HF@C_{60}$). **(b)** STM image of a mixed (70:30) $H_2O@C_{60}$:C_{60} sub-monolayer film on Cu(111) deposited at room temperature, light and dark molecules are the result of a 200 pm height difference caused solely by the Cu(111) surface reconstruction. Taken at 5K, 1.5 V voltage bias and 10 pA setpoint. **(c)** Constant height NC-AFM image of a single mixed composition island atop a reconstructed Cu(111) surface. Taken at 5K, -2.1 mV setpoint and 300 pm oscillation amplitude. **(d)** Valence band photoemission (synchrotron-based with $h\nu$=110 eV) of a thick film of 95% pure sample of $H_2O@C_{60}$ (blue), alongside reference data[216] for empty C_{60} (black). From Jarvis *et al.*, Communications Chemistry 4(1), 2021[58]

of a single fullerene to a probe was another consideration. The force response of a molecule-molecule or molecule-substrate system involving fullerenes takes a similar form to the Lennard-Jones potential, exhibiting a global minimum. The mathematical form of this potential has been widely discussed through modelling[223–226]. Analytical work often compares experimental measurements to the Girifalco potential[227]. The Girifalco potential is a pair potential which computes the interaction between two C_{60} molecules. The molecules are treated as spherical surfaces of uniformly distributed carbon atoms[224,228]. The Girifalco potential has a stiffer repulsive part, and its attractive well is much shorter-ranged and deeper, when compared to the Lennard-Jones interaction.

5.2 Endofullerene deposition on Ag(111) for NIXSW

Figure 5.1.1 suggests the electrostatic shielding of encapsulated molecules prevents the traditional probing with STM, AFM and valence band photoemission spectroscopy. Each method fails to distinguish between filled and unfilled C_{60} molecules, despite, for example, STM's exceptional capacity to detect changes in electronic structure. New research turned to the normal-incidence x-ray standing wave (NIXSW) technique, performed on adsorbed endofullerenes. Positions of encapsulated molecules, relative to the x-ray scatterer plane of the substrate's bulk material towards the surface, could shed light on the extent to which they interact with their C_{60} cage. Encapsulated H_2O could be probed via the O 1s core-level photoelectron peak, excited at the Ag(111) Bragg energy, while HF could be located via F 1s emission. Silver was prepared as the substrate, chosen to exploit the $(2\sqrt{3}$ x $2\sqrt{3})$R30° molecular superlattice formed on the Ag(111) surface.[229,230]

95% pure samples of endofullerenes encapsulating either water or HF molecules, $H_2O/HF@C_{60}$, were deposited onto Ag(111) via thermal sublimation in UHV conditions, covered in Subsection 2.4.1. Following a sputter-anneal cycle of the Ag(111) sample, endofullerenes were sublimed at 370 °C for 15 minutes, with the Ag(111) sample directly facing the endofullerene source.

A combination of LEED and XPS characterised each sample and confirmed (sub)monolayer coverage prior to NIXSW measurements. X-ray photoelectron spectroscopy (XPS) using the aforementioned core-level photoelectron peaks on the deposited endofullerenes is shown in Figure 5.2.1. The relatively intense peak in the C 1s region reflects the presence of C_{60} sp^3 single carbon bonds and sp^2 carbon double bonds, and match across the $H_2O@C_{60}$ and $HF@C_{60}$ samples[231]. The fitted peaks at 3 and 6 eV higher binding energies relative to the intense peak are attributed to electron shake-up, when an ejected photoelectron promotes a valence band electron to an unoccupied level at the expense of kinetic energy. The kinetic energy loss of the photoelectron appears as a chemical shift in the XPS spectrum[232,233]. The O 1s and F 1s peaks were interpreted as indicative of the presence of H_2O and HF inside deposited fullerenes.

LEED patterns, shown in Figure 5.2.2, confirmed the $(2\sqrt{3}$ x $2\sqrt{3})$R30° ordering typically formed on silver surfaces.[229,235]

Charge redistribution of C_{60} adsorbed to the Ag(111) was predicted to displace encapsulated H_2O and HF from their approximate central position[238,239]. Photoelectron spectra taken at the relevant core-level energy range can be used to support this experimentally. 5.2.3(c) compares the O 1s peak associated with the encapsulated water molecule for the monolayer to that in a bulk film. Using the fitted Gaussians, the full width at half maximum increases by 0.3 eV and the peak position shifts by 0.2 eV for monolayer coverage of $H_2O@C_{60}$. The 0.2 eV shift, given the lack of chemical interaction between the encapsulated molecule and the C_{60} cage, could be explained by a difference in screening of the photogenerated core-hole due to a modification of the intra-cage electrostatic environment[58]. DFT calculations, by which an O 1s core level shift is approximately calculated as the energy required to excite a caged H_2O's O 1s core electron, find a similar binding energy shift and peak broadening[58,217]. The calculations overestimate the shift, by over double, and underestimate the peak broadening, by a third, but agree on the direction of the shift and broadening of the core-level peak for a chemisorbed monolayer of endofullerenes. XPS combined with previous calculations qualitatively support the presence and influence of the intra-cage electric field on encapsulated molecules. NIXSW measurements in Section 5.3 aim to provide a direct experimental measurement of the position of the caged molecules.

Further x-ray photoemission spectroscopy recorded at the Diamond beamline, before taking NIXSW, shown in Figure 5.2.4, points towards substantial screening of the en-

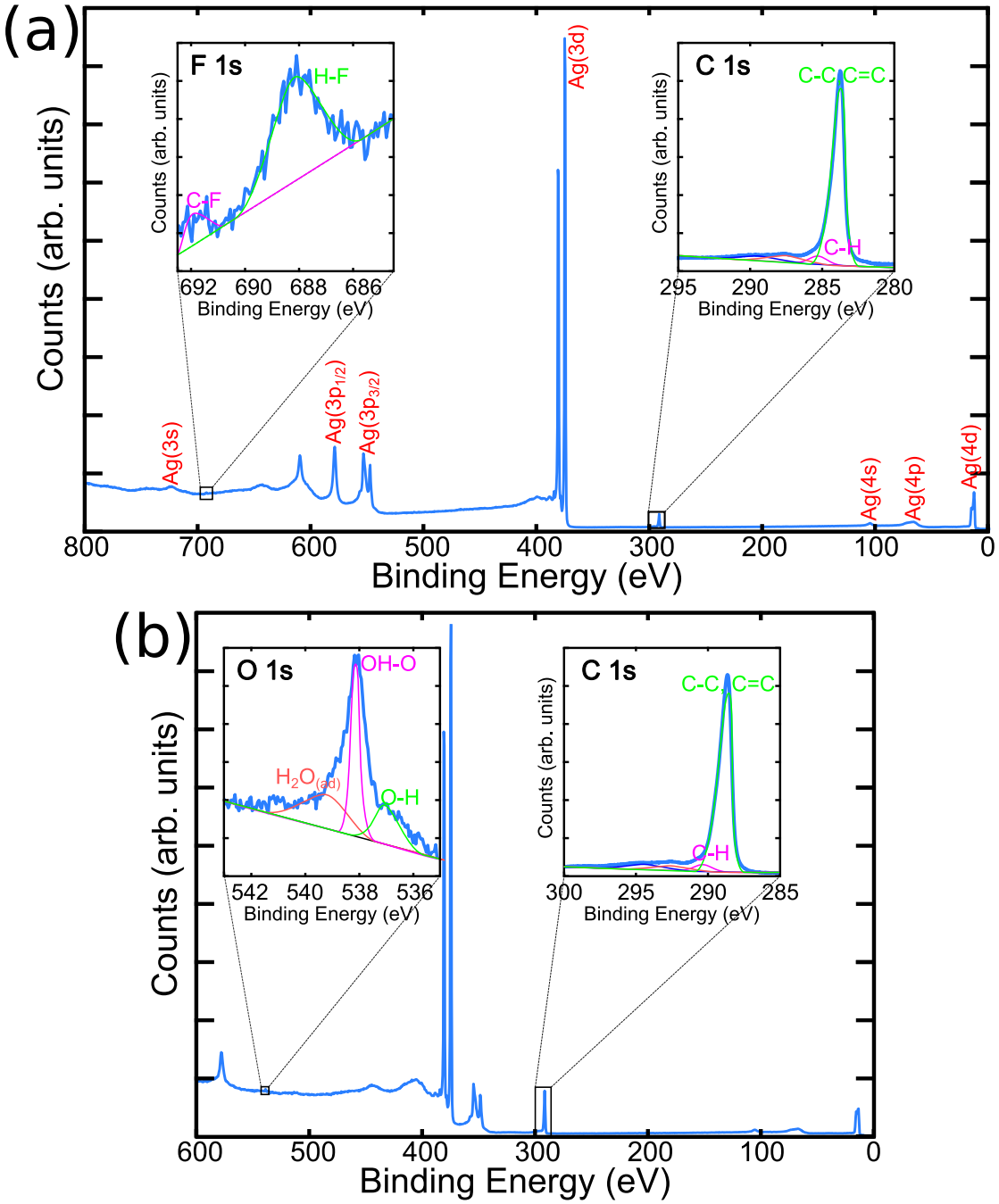

Figure 5.2.1: XPS survey spectra of the silver surface post-deposition of endofullerenes via thermal sublimation, with peak-fitting referenced to the Ag 3d core level binding energy. **(a)** Spectrum after sputter-annealing off the $H_2O@C_{60}$, and deposition of $HF@C_{60}$, photon energy $h\nu$=900 eV. **(Embedded)** Peak-fitting of XPS spectra at the F 1s and C 1s regions, using a linear background and binding energy data from NIST [234]. **(b)** Spectrum after the initial sputter-annealing cycles of Ag(111), and deposition of $H_2O@C_{60}$, photon energy $h\nu$=700 eV. **(Embedded)** Peak-fitting of XPS spectra at the O 1s and C 1s regions, using a linear background and binding energy data from NIST. [234]

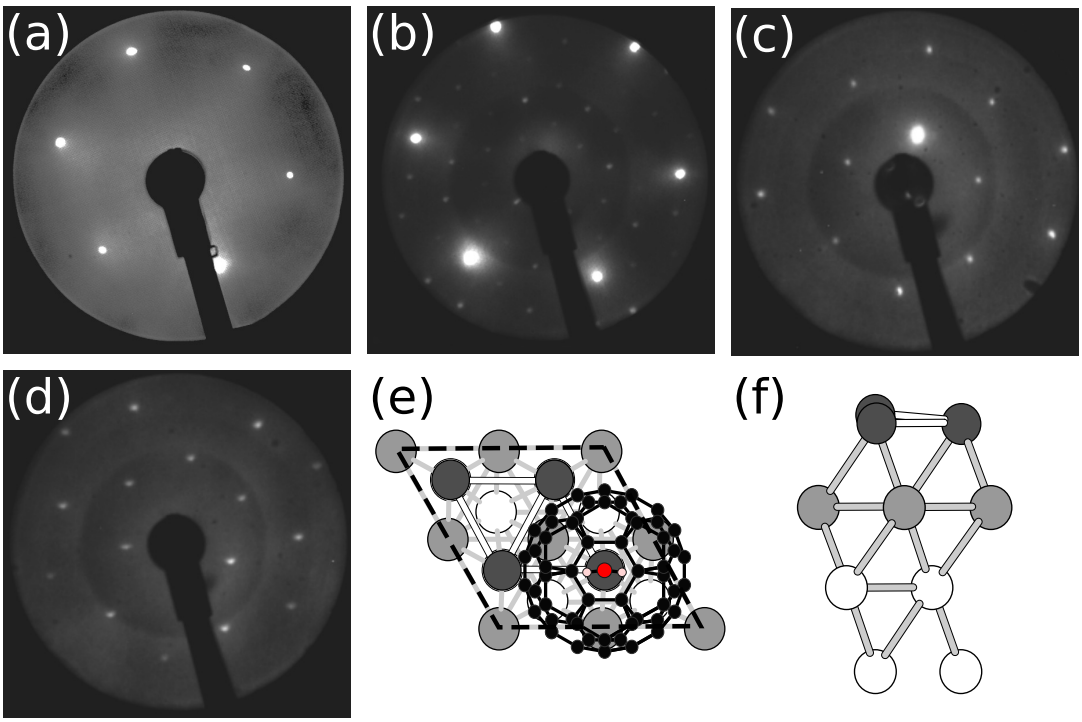

Figure 5.2.2: LEED for endofullerenes prepared as a single layer ($2\sqrt{3} \times 2\sqrt{3}$)R30° molecular superlattice on Ag(111). **(a)** Pattern for clean Ag(111) annealed at 450 °C (E = 119.2 eV); **(b)** pattern for the same surface after HF@C_{60} deposition (E = 111.8 eV). **(c)** Pattern for H_2O@C_{60} (E = 46.5 eV); **(d)** pattern for HF@C_{60} (E = 50.5 eV). **(e)** Top-down view of the modelled ($2\sqrt{3} \times 2\sqrt{3}$)R30° molecular superlattice for H_2O@C_{60} on Ag(111) (adapted from Gatica *et al.*, Phys. Rev. B 77, 045414 (2008)[235]) alongside a side view of Ag(111) **(f)** (adapted from Huo *et al.*, J Mol Model 27, 38 (2021)[236]).

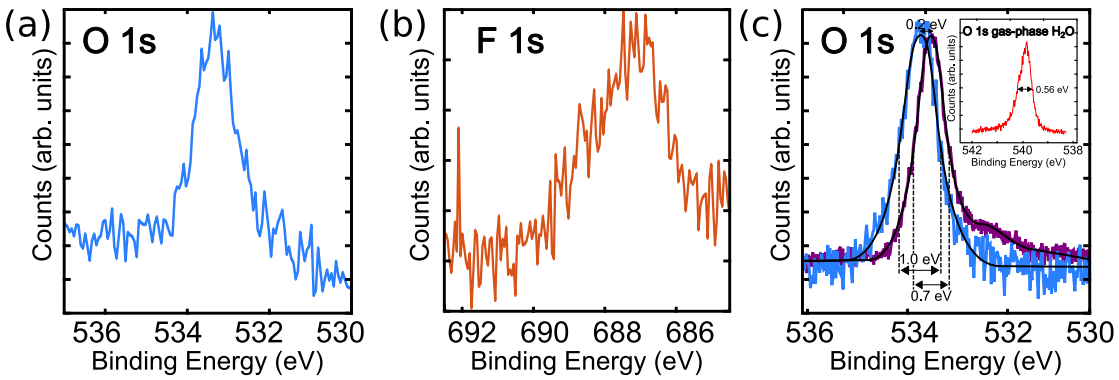

Figure 5.2.3: XPS spectra for deposited H_2O@C_{60} and HF@C_{60} on Ag(111). **(a)** O 1s core-level photoemission spectrum acquired with photon energy $h\nu$=700 eV for a H_2O@C_{60} monolayer at 200K. **(b)** F 1s core-level photoemission spectrum for photon energy $h\nu$=900 eV for a HF@C_{60} monolayer at 200K. **(c)** Detrended and normalised O 1s core-level photoemission spectra acquired with photon energy $h\nu$=700 eV for a H_2O@C_{60} monolayer (blue) and a bulk endofullerene film (purple). Inset is the O 1s spectrum for free H_2O, $h\nu$=600 eV, from Fransson *et al.*, Chem Rev. 13;116(13), 2016[237]. The relevant H_2O peaks are annotated with the full-width-at-half-maximum value of the fitted Gaussian curve.

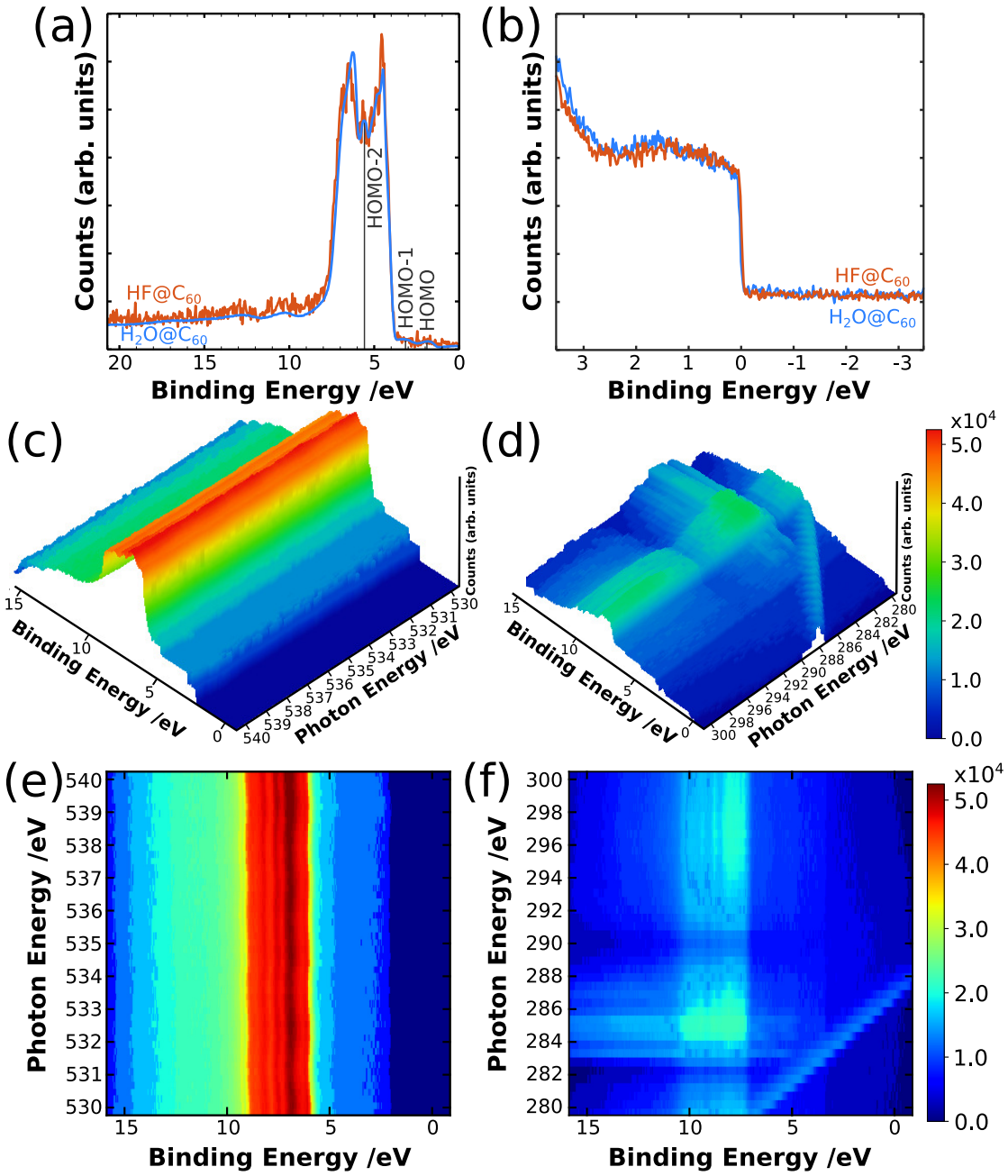

Figure 5.2.4: (Top) Valence band photoemission spectroscopy results. **(a)** Valence band spectra of $H_2O@C_{60}$:Ag(111) and $HF@C_{60}$:Ag(111) taken at the same photon energy (110 eV), calibrated to the Fermi level **(b)**. **(Middle)** 3D intensity plots of resonant valence band photoemission spectra for $H_2O@C_{60}$:Ag(111). **(c)** oxygen K-absorption edge map; **(d)** carbon K-absorption edge map. **(Bottom)** 2D intensity plots of resonant valence band photoemission spectra for $H_2O@C_{60}$:Ag(111). **(e)** oxygen K-absorption edge map; **(f)** carbon K-absorption edge map.

capsulated molecules by the C_{60} cage. The peak position and relative heights in the valence band spectra, in 5.2.4(a), is in agreement with monolayer coverage on unfilled C_{60} on Ag(111)[217]. The $H_2O@C_{60}$:Ag(111) and $HF@C_{60}$:Ag(111) spectra taken at the same energy are identical, up to and including the Fermi edge, 5.2.4(b).

Resonant photoemission spectroscopy (RPES) was attempted for $H_2O@C_{60}$:Ag(111), by which the photon energy was swept through the O 1s and C 1s binding energies. The carbon map, 5.2.4(d), shows a variation in intensity when sweeping the K-absorption edge. The diagonal feature, particularly visible in the bottom right corner of 5.2.4(f), arises from the second-order excitation of the C 1s core level[217]. No change in intensity is observed in the oxygen map, 5.2.4(c), confirming the lack of oxygen contribution to the HOMO and neighbouring occupied orbitals.

5.3 NIXSW results

Normal-incidence x-ray standing wave (NIXSW)[52,53,55] measurements aimed to assess the sensitivity of encapsulated molecules to surface adsorption by locating their positions within their fullerene cage, by tuning the x-ray energy to the Bragg condition of the silver crystal structure[58]. The technique is discussed in detail in Subsection 2.6.3.

The intensity against energy relationships in Figures 5.3.2(a) and 5.3.3 were fitted using a Matlab script, originally provided by David Duncan, Senior Beamline Scientist (BL I09), Diamond Light Source[51]. The algorithm is illustrated in Figure 5.3.1. The core script functions by first fitting and normalising the relevant element peak (O 1s and F 1s) of XPS spectra along the rocking curve, yz in the figure. The XPS spectrum at each energy was typically an average over multiple scans. The fitting program uses a convolution of a Gaussian and a Doniach-Sunjic with a step function, to fit each peak. While the program can fit up to six peaks to a given profile, the intensity of the prevalent central peak was used as an estimate intensity of the relevant molecular peak. The peak intensities are plotted against energy, xy, then fitted by equation 2.18 for coherent position and coherent fraction, with an associated fitting error.

Beam damage was a significant concern. Damage was limited and managed by several means. The incident beam's undulator was detuned to reduce x-ray intensity. XPS spectra were collected between XSW measurements to monitor for changes in the sample, similar to those shown in Figure 5.2.3, with the x-ray spot regularly moved across the crystal. The sample temperature range was kept low, and periodically warmed to 180K to desorb any extrinsic water. Water is a typical contaminant in these conditions. Water adsorbed on the silver surface was given by its O 1s photoemission peak. In the case of the $HF@C_{60}$ sample, the O 1s peak was used to detect the contamination signal during preparation. Exposing the $H_2O@C_{60}$ sample to full beam conditions would cause significant damage to the encapsulated water, resulting in the broad $H_2O_{(ad)}$ peak in 5.2.1(b). XPS measurements of the $H_2O@C_{60}$-Ag(111) sample showed

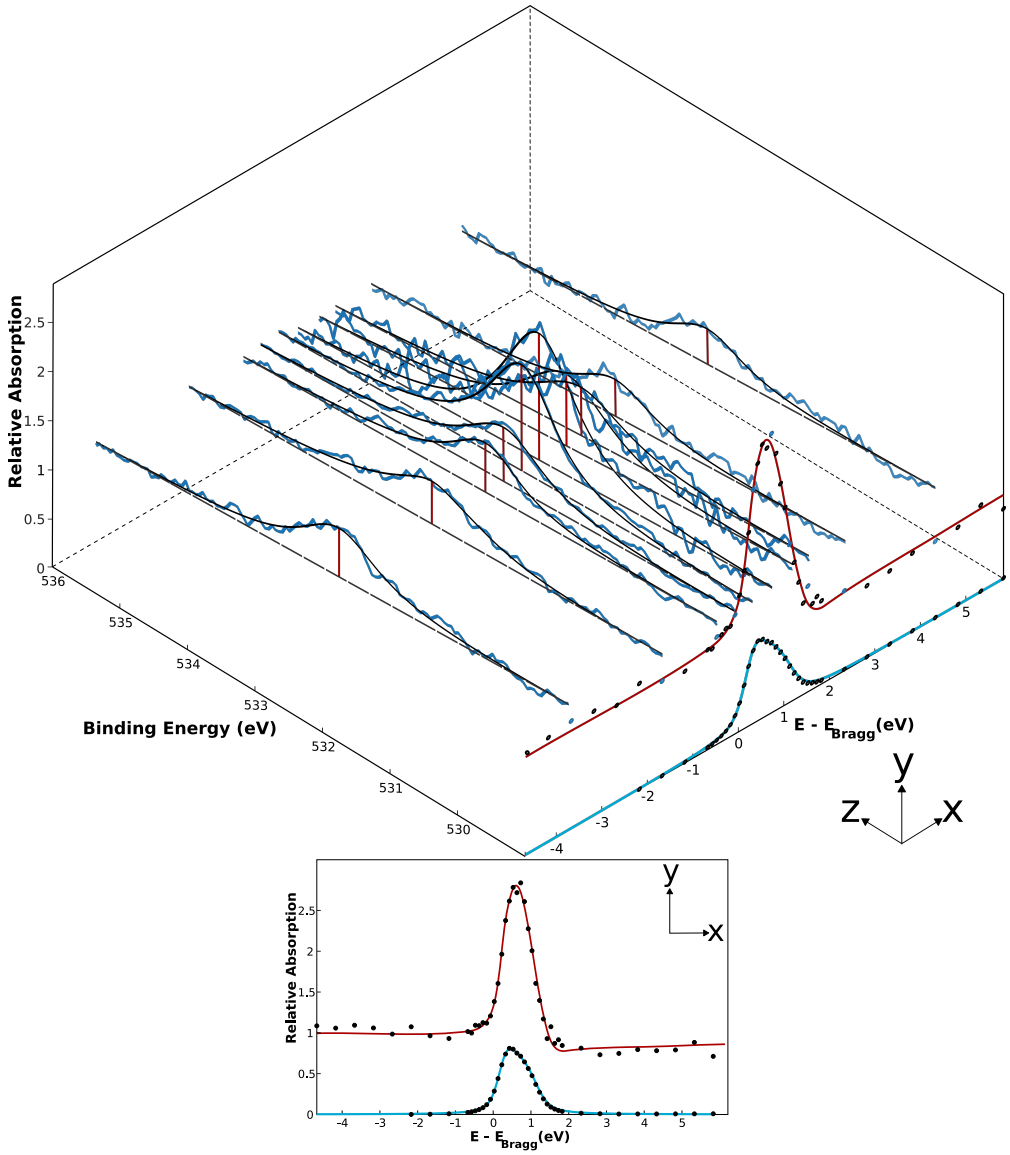

Figure 5.3.1: From raw XPS data to encapsulated molecule position. **(Top)** 3D graph showing the relationship between the normalised intensity of the fitted XPS spectra, averaged over readings from $H_2O@C_{60}$:Ag(111) at 50±4K, at the O 1s region (yz), and the XSW spectrum (xy). **(Bottom)** Resultant XSW spectrum for $H_2O@C_{60}$ on Ag(111) at 50K, XSW intensity vs energy (red) and fits to reflectivity (blue). The fit is based on the Ag(111) Bragg energy (2631 eV), coherent position $P_c = 0.367 \pm 0.070$ and coherent fraction $F_c = 0.517 \pm 0.100$. The position of the oxygen atom relative to the silver surface for these values is z_{111}(O)=5.59±0.40 Å.

the ratio between the intensities of the C 1s and O 1s photoemission peaks remained constant throughout.

Figure 5.3.2(a) shows the NIXSW data for $H_2O@C_{60}$:Ag(111) collected at 200K. The fit is weighted towards the sharp peak, returning a coherent position $P_c = 0.378 \pm 0.060$ and coherent fraction $F_c = 0.645 \pm 0.100$. The error is derived from confidence of the fit of the XSW curves in Matlab, given by the local gradient of the contour map in

5.3.2(a). The coherent position and coherent fraction, as defined in Subsection 2.6.3, provide an approximate position of the oxygen atom relative to the silver surface using

$$z_{111} = (n + P_c)d_{111}(Ag). \quad \{5.1\}$$

d_{111}(Ag) is the Ag(111) layer spacing, 2.361 Å, while n is the diffraction order. The coherent position, P_c, represents the adsorbate distance between the nth and $n+1$th Bragg planes above the crystal's surface, in the units of the spacing between the Bragg planes. $n = 2$ is used in line with observed adsorption heights of C_{60} on Ag(111) with STM, and with DFT calculations. The uncertainty on z_{111}, δz_{111}, is typically calculated as the upper limit from repeat measurements across the temperature range and between sample preparations. This returns z_{111}(O)=5.61±0.30 Å as calculated in Figure 5.3.2(b).[51,240]

Sample temperature was varied throughout the experiment, between 20 and 200K for the HF@C_{60} sample, and between 20 K and room temperature for the H_2O@C_{60} sample. For Figure 5.3.3, temperatures were categorised into 20K, 50K, 100K, 200K and room temperature, with allowed thermal drift up to 7K. No appreciable shifts in Bragg energy were observed within the selected bounds. Figures 5.3.3 and 5.3.4 show, within error, no evidence of temperature dependence on the fitted spectra. Intensity for both the O 1s and F 1s peaks, in Figure 5.2.3, remained relatively constant, indicative of results presented not being due to the sample damage caused by the x-ray beam in both cases.

Due to little observed change in coherent position and coherent fraction as a function of temperature, as shown in Figure 5.3.3, the height of encapsulated molecules above the surface is calculated as an average over the temperature range. The H_2O@C_{60} data over the temperature range (20K - room temperature) across multiple sample preparations, returns coherent position and fraction $P_c = 0.36 \pm 0.05$ and $F_c = 0.72 \pm 0.10$. These translate to a z displacement above the (111) plane[53] for the oxygen, z_{111}(O)=5.57±0.30 Å. In comparison, the HF@C_{60} depositions returned $P_c = 0.40 \pm 0.07$ and $F_c = 0.62 \pm 0.10$, with a fluorine atom height of z_{111}(F)=5.67±0.30 Å.

The NIXSW data shows the mobility of encapsulated molecules. Molecular dynamics simulations of intra-cage H_2O (T=180K) suggest that the height varied within the range of 4.6 and 5.7 Å, with a mean of 5.2 Å and a standard deviation of 0.2 Å[58]. The coherent position values obtained from each individual NIXSW measurement provide limits on z_{111} of 5.28 and 5.68 Å for H_2O, with a mean of 5.46 Å and a standard deviation of 0.10 Å, and between 5.41 and 5.74 Å for HF, with a mean of 5.41 Å and a standard deviation of 0.12 Å. While both are less than half of the molecular dynamics simulation's predicted height range and change, Figure 5.3.4 addresses the individual NIXSW data further, using the fitted coherent fraction values. The calculated uncertainty on z_{111} for each reading, provided by the XSW curve fitting error,

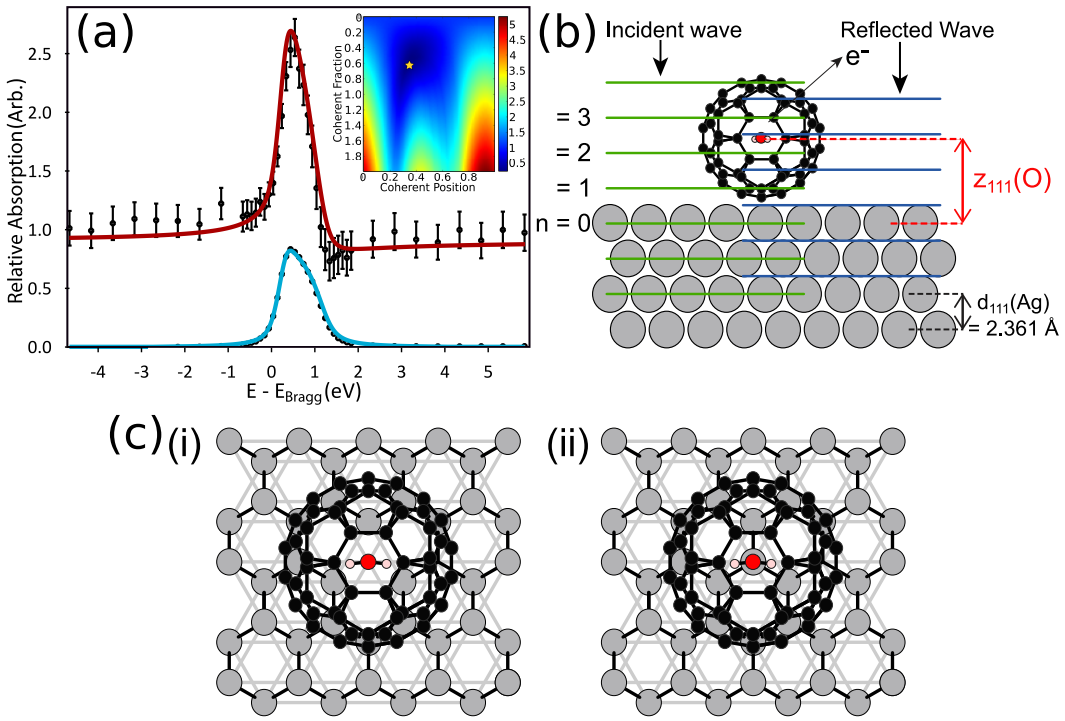

Figure 5.3.2: Locating water in a cage; **(a)** XSW spectrum for $H_2O@C_{60}$ on Ag(111) at 200K, XSW intensity vs energy (red) and fits to reflectivity (blue). The fit is based on the Ag(111) Bragg energy (2631 eV), coherent position $P_c = 0.378 \pm 0.060$ and coherent fraction $F_c = 0.645 \pm 0.100$. The inset shows a contour map of the sum of squared residuals from the fit, versus the coherent position and coherent fraction, with a yellow star indicating the best fit. **(b)** Diagram of the NIXSW technique on $H_2O@C_{60}$:Ag(111)[58]. The position of the oxygen atom relative to the silver surface is given by $z_{111}(O)=(n+P_c)d_{111}(Ag)=5.61\pm0.30$ Å. **(c)** Top-down view of modelled $H_2O@C_{60}$:Ag(111) in (i) a vacancy and (ii) atom-top adsorption sites.

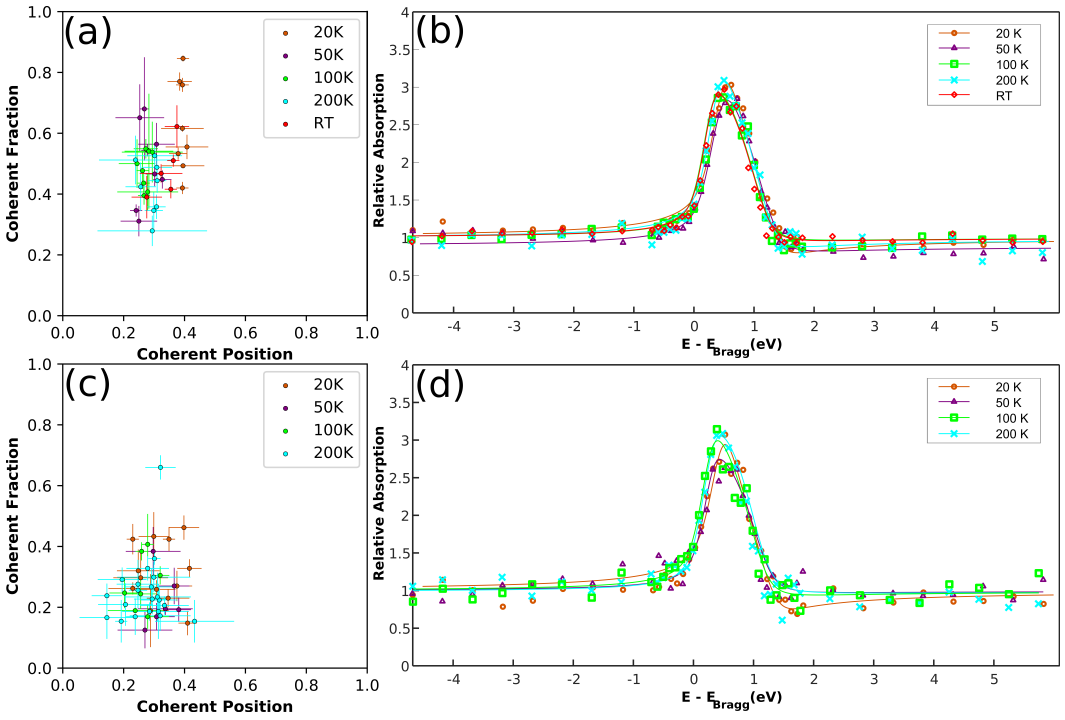

Figure 5.3.3: (Left side) Coherent position and coherent fraction fitted for all individual XSW readings. The error bars are a 1σ error from the confidence of the XSW curve fit in Matlab, given by the local gradient of the contour map. **(a)** $H_2O@C_{60}$; **(c)** $HF@C_{60}$. **(Right side)** Fitted XSW spectra for endofullerenes on Ag(111); **(b)** $H_2O@C_{60}$; **(d)** $HF@C_{60}$.

returns an upper limit, z_{ub}, and lower limit, z_{lb}, for each molecule. The data spread in experimental findings is in good agreement with molecular dynamics simulations.

Molecule height distribution calculations are complicated by a hypothesised mixture of discrete heights[241] of endofullerenes on the metal substrate. Experimental values of $z_{111}(O)$ and $z_{111}(F)$ are significantly different from the modelled result[58], with a discrepancy averaging 0.2 Å in either direction. This is addressed by consideration of previous observations of multiple adsorption sites in SPM[218,242] and further low energy electron diffraction (LEED) analysis[229,230,243]. Experimental XSW data could also provide insight via Argand diagram analysis[241]. XSW readings can be represented as a resultant vector of polar coordinates (F_c, 360° x P_c). The induced adsorbate height distribution, such as by thermal vibrations, can be treated qualitatively as associated component vectors, with their own set of coherent positions and coherent fractions[241]. Beyond single site occupancy, contributions from different adsorption sites can be examined quantitatively by decomposition of the XSW experimental data's representative vectors. Argand diagram analysis aimed to find the best fit for component vectors associated with each C_{60}:Ag(111) site.

Previous observations, LEED and DFT calculations suggest two possible adsorption sites for C_{60} on Ag(111), a lower vacancy site and a higher atop site, shown in Figure

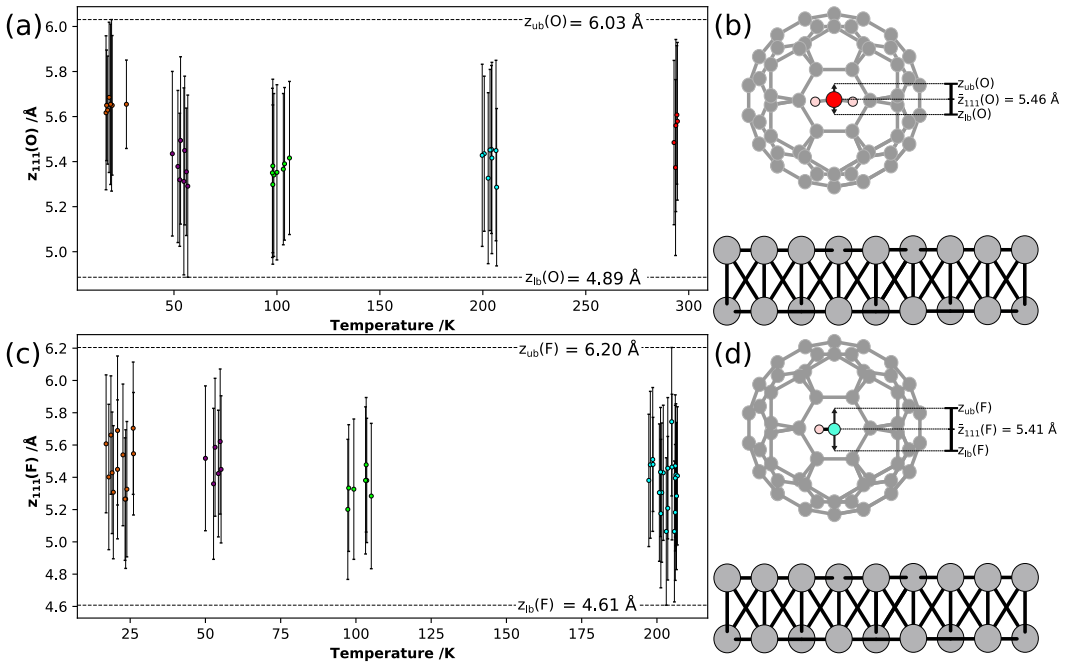

Figure 5.3.4: Discerning the outermost limits on intra-cage position. **(Left side)** Plot of temperature against the z displacement above the (111) plane, using the coherent position and coherent fraction derived from the fitted XSW curves for individual measurements. The lower bound of the probed atom above the outermost (111) plane, z_{lb}, and upper bound, z_{ub}, are derived from the lowest and highest possible value of $z_{111}\pm\delta z_{111}$, with δz_{111} derived from the XSW curve fitting. **(a)** $H_2O@C_{60}$; **(c)** $HF@C_{60}$. **(Right side)** Modelled side-view of deposited endofullerenes, annotated with the mean z displacement of the encapsulated molecule, $\bar{z}$. **(b)** $H_2O@C_{60}$:Ag(111); **(d)** $HF@C_{60}$:Ag(111).

5.3.2(c)(i) and (ii) respectively. The sites have a height difference of $\Delta z_{111} = 0.4$ Å and, assuming the fullerenes and molecules move as one, would address the 0.2 Å discrepancy in either direction. Hence, the two component vectors on the Argand diagram needed to be $\Delta z_{111}/d_{111}(Ag) \equiv 60.99°$ apart. The experimental coherent position and coherent fraction for $H_2O@C_{60}$, $P_c = 0.36 \pm 0.05$ and $F_c = 0.72 \pm 0.10$, is represented by the vector (0.72±0.10, 129.6±2.0°), plotted in Figure 5.3.5. A program, written by Prof. Robert Jones, from the School of Chemistry, Nottingham, and described in greater detail in the supporting information of Jarvis *et al.*[58], decomposes the vector into two component vectors. The vectors, at θ and $\theta + 61°$ are rotated through 360°, in steps of 1°, with the radii systematically varied from 0 to 1, in steps of 0.04. For every combination, the resultant vector is calculated by vector summation, and all resultants that fall within the uncertainty range of the experimental vector are assigned a quality of fit parameter. The parameter is defined as the normalised distance from the experimental value, with 0 being outside and at the edge of the box enclosing the experimental error, and 1 at the experimental value. A threshold of 5-15% is added to the radial error, to account for imperfections and thermal vibrations in the substrate scatterers, which reduce the maximum observable coherent fraction.[241]

Figure 5.3.5 plots the most probable solutions for both H_2O and HF, prepared using the experimental values and error on the coherent position and coherent fraction acquired

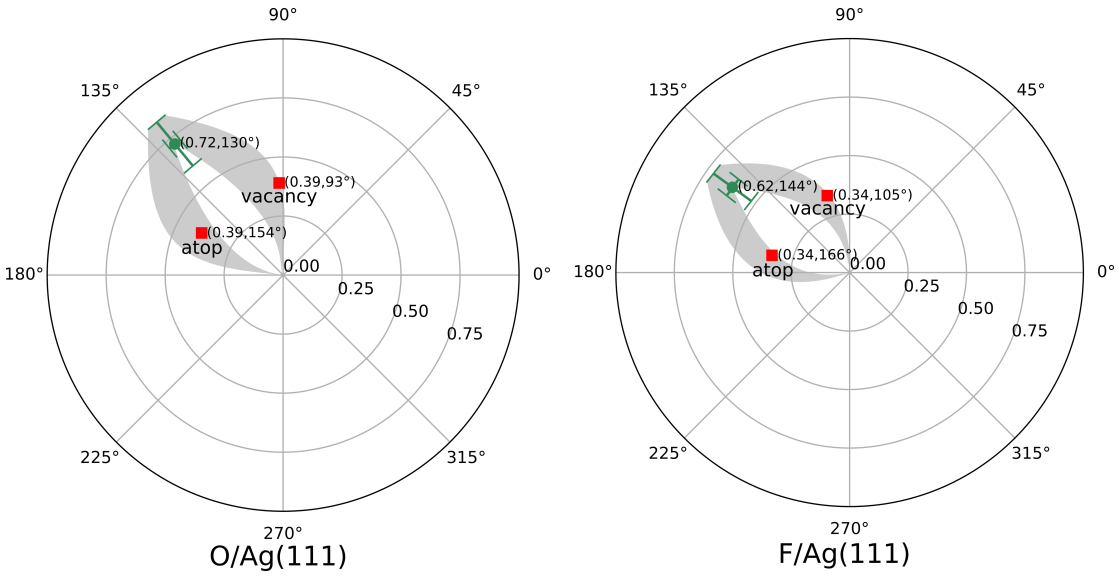

Figure 5.3.5: Argand diagram analysis for NIXSW data on endofullerenes. The experimental vector (green) is fitted directly from the XSW data, at (F_c, 360° x P_c). The gray area highlights the locations of all possible vector pair angles and lengths by which the resultant vector is enclosed by the error bars on the experimental value. The component vectors (red) are the most likely pair which give the resultant vector (green), which correspond to the two positions of the encapsulated molecule relative to the extended crystallographic planes of the bulk silver crystal, annotated with the adsorption sites of the endofullerenes.

by averaging over the temperature range in Figure 5.3.3. The quality of fit parameter is maximised in both cases when the populations are equal, which suggests adsorption at the vacancy or atop sites occurs in equal abundance. To summarise, when modelled with equal populations (0.5:0.5) and a 5% threshold, the two water molecule positions are z_{111}(O)=5.37±0.10 Å (vacancy site) and 5.77±0.10 Å (atop site). The error on each z_{111}(O) value corresponds to changes in population from 0.2:0.8 to 0.8:0.2. For HF, z_{111}(F)=5.46±0.20 Å (vacancy site) and 5.86±0.20 Å (atop site) when modelled for a 10% threshold with equal populations. The errors correspond to changes in population from 0.13:0.87 to 0.87:0.13. Argand analysis shows the XSW data is broadly consistent with the two-site adsorption model.

5.4 Conclusion

The results of a series of x-ray synchrotron-based experiments on endofullerenes address the extent to which encapsulated molecules are electrostatically screened and decoupled from their external environment. NIXSW upon $H_2O@C_{60}$ and $HF@C_{60}$ deposited on Ag(111) suggests adsorption to a metal surface causes a strong modification of the electrostatic potential within the cage, resulting in a displacement of the encapsulated molecules from their otherwise central position.

No systematic change in coherent position or coherent fraction was observed in the observed temperature range. Data across the whole temperature range was instead used to examine the disorder in the position of the molecular encapsulate. Experimen-

tal NIXSW measurements could be reconciled within a two adsorption site framework, with a height difference of 0.4 Å. The experimental findings were carried forward for published work.[58]

Rotating the Ag(111) crystal along the azimuthal, polar, and linear directions to perform XSW measurements in different crystal orientations was planned. A combination of (111), (11$\bar{1}$) and (200) would allow for triangulation of molecule positions, which could aid in drawing further experimental conclusions on adsorption sites and temperature dependency, though little success was had with early attempts at NIXSW measurements at (11$\bar{1}$). Future atomic resolution SPM was planned, beginning with AFM and KPFM in Appendix D. The aim would be identifying single molecules of water and HF within C_{60}, H_2O/HF@C_{60}, in a deposition of known percentage abundance of filled and empty fullerenes.

6 Automating Nanostructure Discovery in SPM Data

Author Contribution Statement

Gordon *et al.*, *Nano Letters*, 20(10):7688-7693, 2020.[9]: P.M., O.G. and J.H. devised the project. O.G. and J.H. wrote the Monte Carlo script. O.G. wrote the CNN script. O.G. wrote the paper, with revisions to the final manuscript provided by all authors. J.H. wrote the pre-processing script (Appendix C) which provided all input data. P.M. and E.H. supervised the project.

Farley *et al.*, *Machine Learning: Science and Technology*, 2(1):015015, 2020.[8]: P.M., E.H. and S.F. devised the project. S.F. wrote the U-Net script, with feedback provided by all authors. J.H. wrote the pre-processing script (Appendix C). S.F. and J.H. wrote the paper, with revisions to the final manuscript provided by all authors. P.M. and E.H. supervised the project.

6.1 Goals of algorithmic image processing

6.1.1 Tools of the trade

The recent prominence of machine learning within science, and by extension nanoscience, as well as new exploration of modelled data, has caused demand for a high volume of processed image data. Manually processing large data sets is not only impractical, but places significance on finding a consistent workflow, a set of sequentially applied processing techniques with the same parameters, that processes the most amount of images to a satisfactory level. Standardised and well-documented solutions to data pre-processing, contextualised by the physics and objective of the project, are crucial.

Within popular software, the user interface (UI) may not make it transparent to the user the most optimal methods to process all their similar images, from both a visual and statistical standpoint. Popular readily available image processing software is easy to treat as a black box, often uncritical of image statistics and placing more emphasis on the visual appeal of the finalised image. Automation replaces the judgement of a nanoscientist with the principles of statistics and attempts to remove the user from the equation, and any visualisation biases they bring.

Critical probing of image statistics and meeting the individual needs of different research sooner or later leads to the integration of image processing into the data preparation steps of machine learning, within the coded script. Said methods remove the component of user visual feedback entirely, putting the code in control of all image processing algorithms. Creating a generic code that automates the entire image processing for all image data inputted presents some challenges. The strengths and weaknesses of various image processing approaches have been previously studied, but there is no clear theoretical combination of these techniques to provide optimised images. Much

like traditional image processing software, a toolbox of image-manipulating scripted functions, callable in sequence, is essential to creating versatile scripts.

This chapter explores the experimentation with bespoke code written in Python and R for automated mass image processing tailored to the study of nanostructures. The aim is to create a new toolbox for image processing of nanostructures, alongside that of statistical tools developed in Chapter 4, similarly using gold nanoparticle AFM imaging as the primary lens. This includes the exploration of common data science techniques, beyond those available in popular image processing software, that particularly enhance the processing and study of images containing nanostructures.

The development of an algorithm essential for published work[8,9] is also presented. This extracts raw image files from a large data set of historic AFM data, and outputs pre-processed image files, using a combination of optimal functions from the toolbox. Seamless integration of the pre-processed data set with images produced by Rabani *et al.*'s model[1] was achievable. Algorithms aim to minimise the information lost from imaging the nanostructures and enhance the performance of feature extraction methods that characterise the geometry of nanostructures[164]. Statistical and machine learning tools for predictive modelling and relationship mining[165], trained on modelled data and readily applied to the pre-processed real data, had the potential to solve the problem of fitting observed dewetting behaviour to initial generative parameters, and ultimately the problem of inverse mapping of experimental images back to their starting experimental parameters.

6.1.2 User bias in visualisation

Images returned from SPM presented in other chapters were processed individually and manually using popular image analysis tools, most commonly Gwyddion[139]. Gwyddion provides a wide selection of individual algorithms available to the user to be applied to loaded SPM images. Figure 6.1.1 shows the appearance of Gwyddion's UI, including typically called software features for image processing. Once the user is satisfied, the final image is saved, and either the image itself or data extrapolated from it, such as line profiles, are presented elsewhere. The priority while processing these images is normally results-oriented, often treating the processed image as the final product. The processed image may be used as a scientific communication tool in publications, presentations, and similar visual media. This places emphasis on the visual component of image processing, bringing attention to the physics at play at sub-micron length-scales relies heavily on visual observations. This goal involves a few broad steps, achievable within Gwyddion.

The first of these is the removal of undesirable features such as noise and discontinuities introduced during SPM scans. Kernel-based image filtering and data alignment algorithms can be applied in individual menus with a variety of options for what image

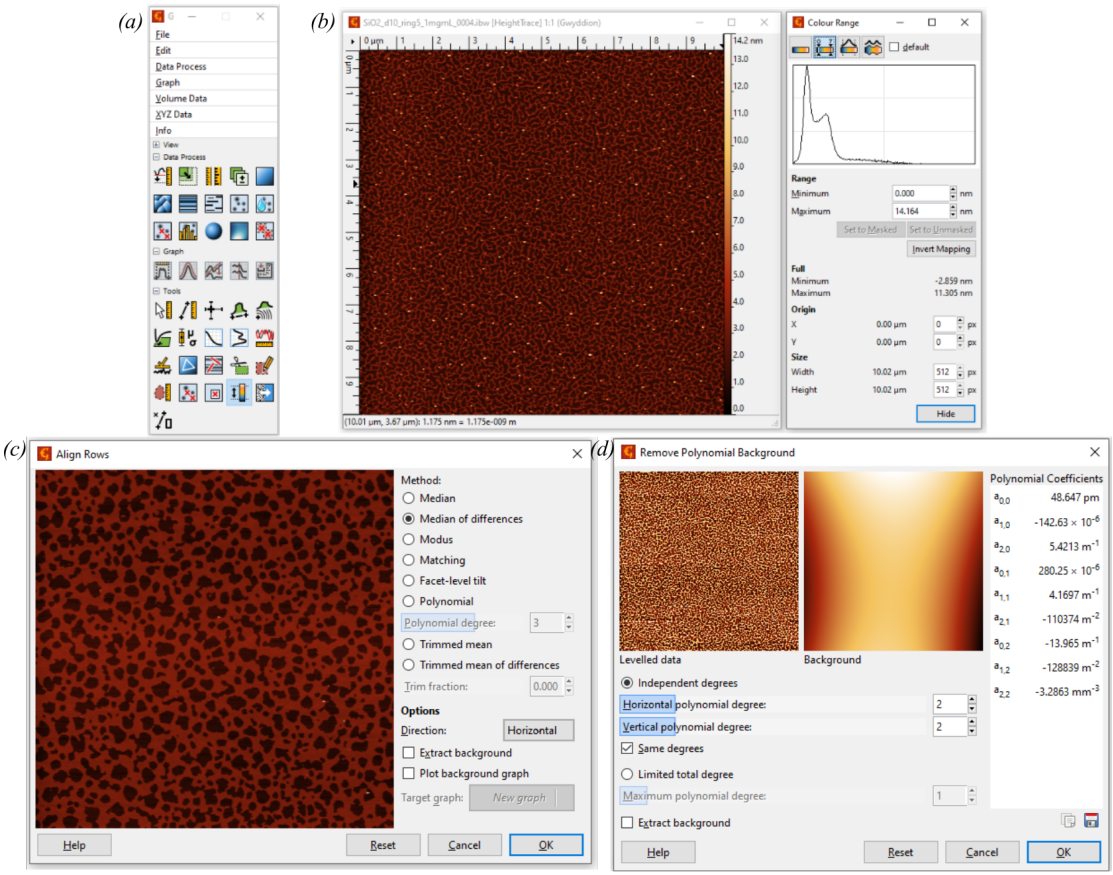

Figure 6.1.1: UI elements of Gwyddion [139] for standard processes utilised during image pre-processing. **(a)** Gwyddion's default toolbar; **(b)** colour range modification window with the image histogram, a plot of pixel counts against grayscale pixel values; **(c)** row alignment tool window with an embedded image preview; **(d)** polynomial background detrending tool window with the resulting image and subtracted background shown.

statistics to rely upon for each. The user may also look to enhance the visibility and place emphasis on key features. Corrections to the contrast by altering the colour range of the image, or encouraging flattening of regions of the image by use of background detrending or explicit levellers, are offered in Gwyddion with a range of degrees of freedom.

Sometimes the user may use the image to extract data along 1D line profiles, such as distance, height and roughness, shown in Figure 6.1.2. Images with features of distinct shifts in height and texture such as those with terraces, films and flakes may want to be presented graphically by the user. The user may also seek to conduct image segmentation. Image segmentation in Gwyddion and other user-centric image processing software offers simple height-based thresholding, shown in Figure 6.1.3. This is often presented to the user as a slider representing the pixel value range of the image, and moving it will highlight regions on the image that are encapsulated by the range. When the user is satisfied with the highlighted region, this region can be used as either an image mask for further processing or to segment the image into a binary

image by means of converting all pixels of value below the chosen threshold to 0 and above it to 1. Creating this image may help the user distinguish two phases within the image, or identify the percentage coverage of each phase.

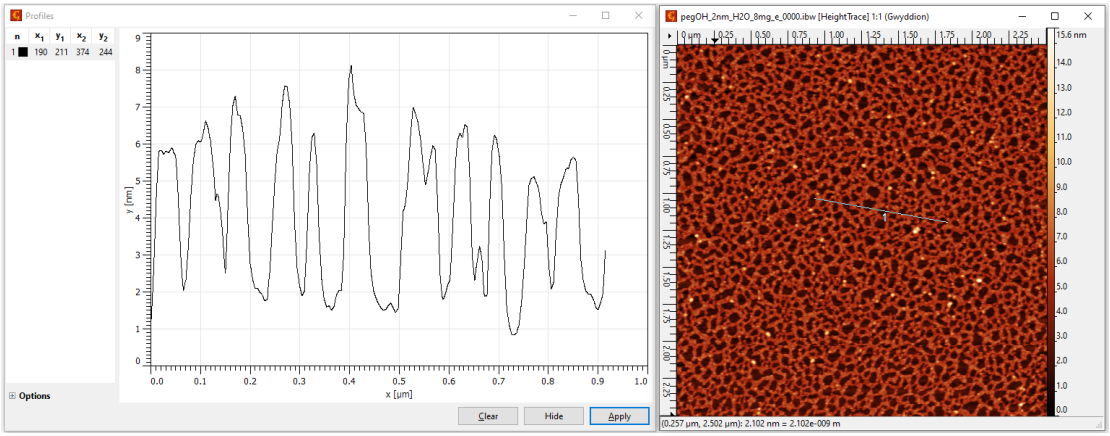

Figure 6.1.2: Gwyddion's 1D line profiling tool used throughout Chapter 4. A line is marked onto the image and a 2D slice is taken and displayed in the graph window.

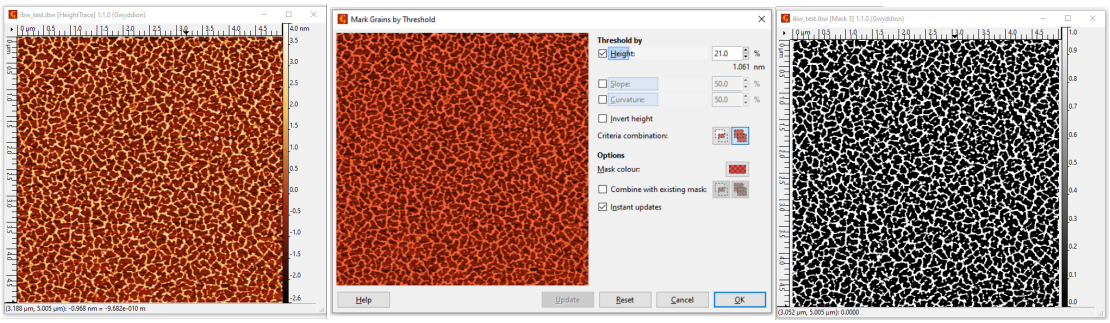

Figure 6.1.3: Gwyddion's manual segmentation by thresholding process as applied to gold nanoparticle dewetting pattern AFM images. **(left)** Pre-processed AFM image; **(centre)** mark by grains tool window, moving the slider labelled Height until the nanoparticles in the preview image are all highlighted, which is saved as an image mask when applied; **(right)** binary image of the regions marked using the "Extract Mask" feature.

All these steps have the potential to introduce user biases. The user will often cycle between the options for filtering and alignment, selecting and applying them with a short time spent on judgement of the results exclusively on a visual level. Kernel-based filters that blur or sharpen the image, though enhancing the images visually, have a tendency to remove data from the image, particularly around sharp changes in pixel values in the image. Colour ranges, particularly non-linear ones, can misrepresent image feature heights or the existence of certain features at all by windowing the data range. The background detrending and levelling algorithm parameters chosen by the user may not be fully optimal on a statistical level. Processing images to yield profiles of certain features creates further bias in the user's approach, placing more focus on denoising and aligning those features. Image segmentation by eye is highly subjective

between users, resulting in potential inconsistencies in inferred statistics between images and users.

A by-eye approach to all these steps is exacerbated by inexperience with the platform, but a good-enough approach by experienced users processing a large number of images in a session can also result in statistically compromised images. Said images introduce corruption into proposed machine learning sets, while contributions of images by different users result in statistical classification by a user as opposed to by image features. Algorithmic image processing, during which the same set of functions is applied in order to every supplied image, aims to remove the majority of user bias.

6.1.3 Contextualising image processing

Although the Monte Carlo approach used in Rabani *et al.*'s model[1] is relatively simple, it is nonetheless an exceptionally powerful and accurate method of simulating "real world" nanoparticle patterns. Given the model's ability to simulate experimental data so well, a key question to address was whether a network trained on simulated data could be used to classify experimental images. This has obvious advantages in terms of bandwidth and quantity of data: it takes seconds to simulate a particular nanoparticle pattern but tens of minutes at a minimum - and hours, or days at worst, if the AFM tip is poorly behaved - to generate an experimental image. If one takes into account the time required to prepare the sample the measurement bandwidth is lowered still further.

Proof of concept for machine learning-based categorisation of SPM images using simulated images exists, but an integration of real experimental data was not involved[244]. The solvent-evaporation experiments explored in Chapter 4 did not focus primarily on reproducing and studying diverse morphologies on uniform substrates, and machine learning demands a high volume of images, so a larger experimental data set was required. Hence the newer data set (2019 - 2021) was combined with a historic data set (2002 - 2009) of AFM images, exhibiting the various morphologies of gold nanoparticle patterns observed, produced by previous members of the Nottingham Nanoscience Group. This unification of real and simulated data necessitates the segmentation of the experimental images to match the final cell states of the simulated images. Mapping the experimental data like this aimed to make the images indistinguishable from simulated data, but comes with numerous challenges. Inherent noise in SPM is not reproduced by simulations, segmentation of nanostructures of this scale requires a strong protocol to minimise the effects of known noise features. Data mining of this historic data set would return a unique training and test set for machine learning, with image processing code written acting as a foundation for re-purposing previously dormant SPM data for exploring new technologies.

Hence this chapter does not consider the visual aspect of images as the result, but instead places more emphasis on statistics returned by a large data set of images. It

is not only impractical to manually and individually process images in the historic data set, but an automated approach to also prevent user bias is preferable, maintaining consistency and integrity in image statistics. An automated approach would involve a script that extracts visual data from the raw scan file, performs a series of image transformations using available image statistics then saves the resulting image in a transferable image file format. This presents some coding obstacles: writing an algorithm that is robust enough to process a variety of images containing nanostructures, with different noise features, to a satisfactory degree.

6.1.4 Inherent noise in SPM

Imaging at the nanoscale puts one's image quality at the mercy of countless sources of noise. The major sources will be from the tip, sample surface, feedback parameters and piezo-scanners. The laser beam reflected partially off the surface, as opposed to entirely off the cantilever, can result in low-frequency undulations across an image. Damage or passengers upon the tip caused by user inexperience, surface contaminants and defects, or tapping mode's intermittent contact with the probed surface can create significant tip artefacts and loss of resolution in the image. Quantisation errors in the electronic conversion of physical observations to a digital calculation, then to a physical response, produce a loss of resolution in the signal. The probe is highly susceptible to vibrations from the environment, with strong vibration events rendering portions of the image unusable, and smaller ones causing salt and pepper noise. Incorrect setting of feedback parameters within the scanning software can result in uncharacteristic sample features[18]. A lot of these noise-producing factors in AFM can be fixed on a short timescale, on the length-scale between scans or scan sessions, within the microscope's scanning software or by physical adjustments. Flaws in the piezo-scanner and associated electronics are non-trivial to prevent, while their resulting noise is similarly non-trivial to remove.

Almost all images in the historic data set were taken with an atomic force microscope in tapping mode in air. A relatively large surface area of side lengths of 5 - 20 microns was used for all scans to get a strong survey of the nanoparticle pattern present. All of these experimental parameters introduce potential noise patterns to the images in the data set, with traceable origins across the SPM process.

Tapping mode images are created by mapping the shift in amplitude of the cantilever made to oscillate close to its resonant frequency. Images are formed using multiple sweeps along the fast scan direction, the effective y axis in all images shown, the tip is incrementally stepped in the slow scan direction, the effective x axis, at the completion of each sweep. The resulting trajectory scans over the probed region in a series of rows, with the atomic force measurement derived from the movement of the tip plotted to pixels along the x and y directions in a raster approach, forming a finalised image. Feedback loops and error analysis algorithms are used to deduce the

extension needed to be induced in the piezoelectric material holder that manages the position of the tip, to maintain tip-sample distance in the effective z axis. The PID controller that manages this performs a short calculation with the signal, quantised by an analogue-to-digital converter (ADC), and then the control value is converted back with a digital-to-analogue converter (DAC) to a voltage for the piezo-scanner.

The strength of this feedback loop is controlled numerically in software with the PID controller, primarily by adjusting the integral gain. Producing images that accurately describe the topography of 1 - 3 nm high nanostructures over micron distances demands a high integral gain and scan speed to maintain sufficient tracking of the patterns. This is known to induce instabilities in the feedback loop[245]. Abrupt inadequacies in the acquisition of height information during the fast scan direction result in rows seemingly tracing the visually correct height features, while appearing at different overall heights to neighbouring rows. This effect is one of two types of noise inherent to every AFM image taken while probing nanostructures, distinguishing it from other forms of noise. Figure 6.1.4 shows the appearance of this noise as it appears on raw AFM images, row-by-row shifts in image contrast while clearly describing the same surface.

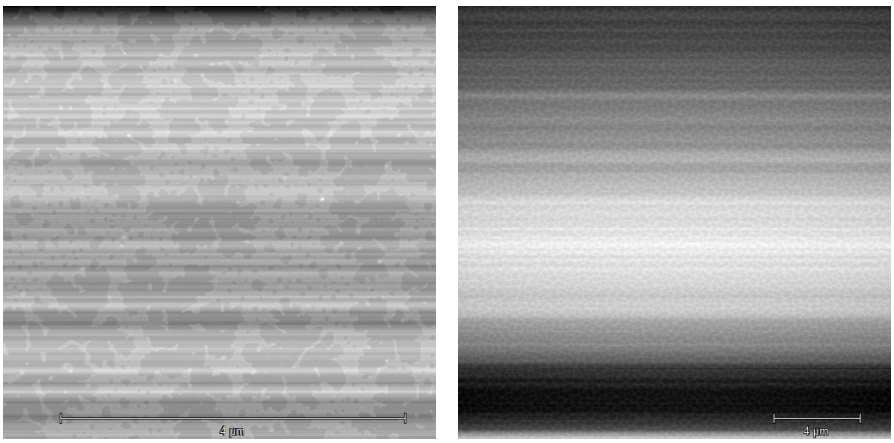

Figure 6.1.4: Raw AFM images with row misalignment.

The second inherent noise source is image curvature. Curvature in a 2D image is understood as a background value added to pixel values as a function of x and y coordinates. AFM piezo-scanners are supported on a mechanical assembly, hence the natural path of the probe is spherical or parabolic. Additionally, piezo-scanners are non-linear devices, responding to driving voltages applied by communication with the DAC in a non-linear trend. This creates a reproducible trend across scans taken in the same position of the piezo-scanner. These two factors result in AFM probes following a curved trajectory, particularly visible in images of the scan size and speed being used for nanostructure probing. While the scanning software, Asylum Research, compensates for this with line-by-line correction, this can have limited effectiveness at faster

scan speeds. Bowing in resulting images often is not clear by visual inspection, particularly on images containing densely-packed nanostructures. Taking a 2D profile to view the z axis data more clearly reveals inherent curvature, demonstrated in Figure 6.1.5. Common solutions to address image background bowing, as well as background tilt if the probe-sample angle is not perpendicular, which results in a planar background, are discussed in this chapter.

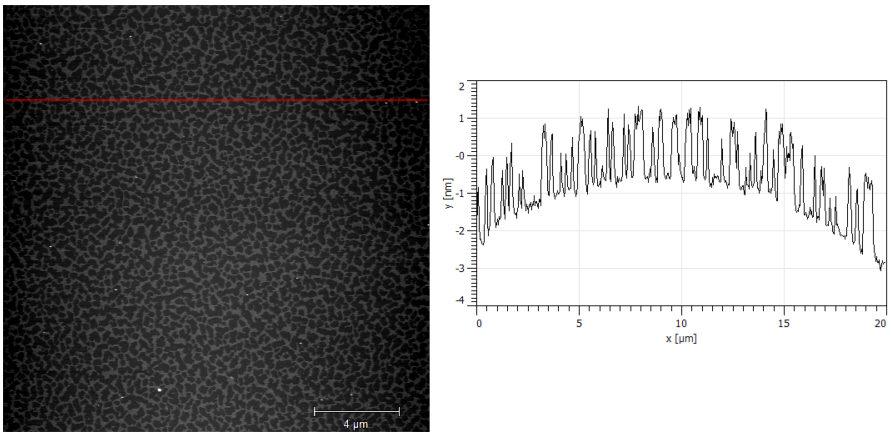

Figure 6.1.5: AFM image with a height profile taken along x axis, showing a distinctive bow across the image.

Both of these inherent sources of noise provide a strong basis for the workflow of image processing software users. The strong correlation between the image statistics, and hence the effectiveness of segmentation, and these two sources renders them the core obstacles of automated image processing.

6.2 Image processing techniques

The majority of image processing experimentation was conducted in the Python coding language within the PyCharm integrated development environment (IDE). Current computational research within the group is conducted within Python, in particular, the Monte Carlo method simulations and convolutional neural network (CNN) scripts. Hence, integration using the same language is preferred. Python offers a variety of common libraries and downloadable packages designed for array manipulation and statistical analysis. NumPy, for numeric data manipulation, and Matplotlib, for graphs and images, are essential for scientific computing, while packages such as Pycroscopy and Pandas serve for more specialised uses. The IDE was chosen due to its simple cloud synchronisation tools and plugins to run different coding languages natively.
Parallel to a user's workflow in Gwyddion, the image processing scripts used all take on a general structure. Python scripts compromise independent algorithms ordered similar to the way a user would sequentially call them. This also meant understanding and then recreating some preexisting functions in Gwyddion and other popular image processing software, then visually and statistically accessing their suitability to the im-

ages within the data set. Some Gwyddion features can not be recreated, particularly those requiring user input such as point triangulation or hand-drawn line-based image levelling algorithms. Also, metadata such as scan size and scan date is only accessible in the original SPM file format.

First, a data file is loaded into the software. The data trace representative of the scanned surface is selected from the loaded file and then pre-processed to remove the aforementioned inherent noise from the image. In this context a segmentation is performed, an image threshold is calculated and binarisation is performed. The image is then screened for confidence in the pre-processing and fitted threshold value, then saved to a universal image format for future usage. This model user workflow is used as a starting framework for proposed Python scripts. Each step is covered below, while saving is covered in Appendix E.1.

6.2.1 Extracting scan data

Data from individual AFM scans are saved as IGOR Pro binary wave (.ibw) files by the Asylum Research scan software. IBW files contain channels of data traces arrays and metadata such as scan parameters set within the scanning software and scan date[246]. In the case of the historic data set, the IBW files only contain 2 channels; a height retrace and phase retrace. The height retrace can be extracted to be manipulated in Python using the Python package Pycroscopy. This returns a 2-dimensional NumPy array, where each value in the array represents a pixel in an image, which can be displayed as a grayscale image. The majority of the historic data set is 512 line scans, resulting in 512 by 512 arrays. The height trace array's values represent pixel intensities which in this case represent relative height across the imaged surface. This concept can be illustrated in Gwyddion's 3D viewer, shown in Figure 6.2.1, with the underlying surface being the darker orange, and deposited gold nanoparticles being the lighter orange.

6.2.2 Normalisation

The loaded data trace array has a simple transformation function applied to all values. The Python package NumPy has known degradation issues when performing calculations with sub-decimal numbers, resulting in quantisation errors. The data trace array assigns values in NumPy based on relative heights, often resulting in negative sub-thousandth values due to the scaling and calibration of the original scan. Normalisation aims to correct this by scaling all data to fall between the range of 0 to 1. A normalisation function is defined that, when supplied a 2-dimensional array, uses the maximum value and minimum value present in the array to offset and rescale all values in the array to fit the range of 0 to 1 using the normalisation formula in equation 6.1 on all values. p_{new} here is a newly normalised pixel value in an array with range p_{min} to p_{max}.

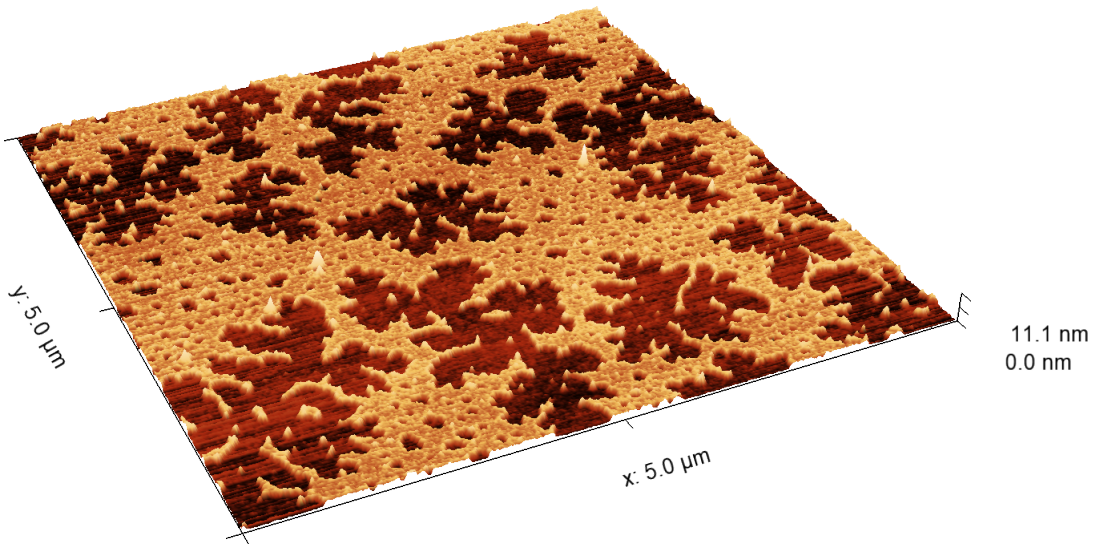

Figure 6.2.1: Pre-processed AFM image displayed in Gwyddion's 3D viewer.

$$p_{new} = \frac{p - p_{min}}{p_{max} - p_{min}} \quad \{6.1\}$$

The function has to have no effect on the statistics or appearance of the array when displayed by figure plotting functions or when saved as an image file, so is recalled after each stage of pre-processing to minimise degradation. The effectiveness of normalisation is reduced significantly by "salt and pepper" noise. Salt and pepper noise appears as black and white pixels dispersed across the grayscale image, with pixel values, by definition, at the minimum and maximum of the range of pixel values present in an image. results in the data range for pixel values being artificially widened. This was later addressed with masking and cropping algorithms.

6.2.3 De-noising representative 2D arrays

Image pre-processing aims to remove inherent noise in SPM from the grayscale image arrays. This requires scripts that transform the array with the context of noise within AFM. It is important the filters chosen do not compromise image statistics. Many processes that may aesthetically improve an image also remove information, for example, low pass filters such as Gaussian blurring. The transformations deployed all use image statistics across the entire array to offset pixel intensity values with an additive approach, as opposed to convolving them with kernel-based filters. The AFM scan pre-processing functions were split into two types, image de-striping and image detrending. Each function is run consecutively on the supplied data trace array, with the normalisation function applied before, in between and after. This order was chosen as detrending algorithms heavily rely on fitting trends to the pixel data, correcting surface incongruities provides a more reliable fit. There was a large amount of experimentation in this stage and the resulting protocols and analysis strategies form the results of such

form the key findings of this chapter.

Image de-striping algorithms attempt to remove streaking and striping noise from images. In the case of AFM images, this is to address the discrepancies in pixel values between each row, discussed in Subsection 6.1.4. The primary method for de-striping while maintaining image integrity is row alignment. During AFM scans, data is collected row by row from either the top or bottom of the set scan area. The path taken horizontally by the cantilever provides important relative information determined by the cantilever's deflection. Aligning rows in an additive manner by offsetting all data in each row by the same offset value is a common way to avoid falsely portraying the cantilever's trajectory. The statistical approach compares a common statistic of each row to neighbouring rows, then increments all pixel values in that row by the numerical difference. These statistics in popular image processing software include mean, median and mode, all easily calculable for all pixels present in individual rows. Offsetting all rows with this approach returns a more visually and statistically congruent image, with overall effectiveness dependent heavily on the data presented. Images containing nanostructures will contain multiple populations of pixel values, one associated with the surface level and then numerous populations of layers of nanostructures. Each population will have their own statistics, while the dominant population of a row will determine the statistic presented to the alignment algorithm. This can result in ineffective row alignment, or even exacerbate the incongruity. Hence row alignment approaches sensitive to nanostructures were explored.

Image detrending algorithms upon row-aligned images aim to remove the curvature in images produced by the equipment. Treating the additive trend across pixels as a three-term function or multiple two-term functions provides a calculable approach to detrending. The derived function or functions that describe the pixel value background can be subtracted from the image's pixel values by a matrix subtraction, then the image is normalised. The effectiveness of detrending is dependent on the preceding row alignment of the image, and the algorithm's ability to fit to the trend of the image data presented. The presence of multiple populations similarly needs to be addressed, fitting algorithms sensitive to the trend experienced by all pixels, as opposed to the data, are preferred. Subsection 6.4.2 describes the initial attempts at writing detrending code, while Subsection 6.4.4 expands upon this with further methods and comparisons.

6.2.4 Image Segmentation

A key aspect of studying nanostructures on surfaces is the ability to identify, characterise and visually distinguish nanostructures from the surface they are deposited onto. Though the user may be able to identify the locations of features, phase shifts and other distinctive physical changes shown in an SPM image, manually or statistically mapping such locations presents numerous problems. It is difficult for the user to physically communicate boundaries between expansive regions to a computer in a fast

and accurate manner. Mapping regions by hand may be sufficient for a small set of images, but the task's length and complexity scales immensely with large data sets and images with more than two phases. Additionally, the user introduces their own biases, a by-eye approach may not correctly identify all regions correctly while mapping the image. A computational approach to partitioning images, or data in general, is preferential for statistical analysis and is widely studied under the term segmentation, grouping pixels in an image with other pixels using statistical and spatial cues.

In the context of images that present two phases, for example, regions where a single layer of nanostructures is deposited and regions absent of nanostructures, showing only bare substrate, a binary image will suffice. A binary image acts as a map of the regions on the image and acts as both an easily transferable description of a region and a visual end product of segmentation. The optimal binary image in this case prescribes all pixels that describe the surface to 0 and all that describe the nanostructure layer to 1, visually a black surface and white nanostructures. Such optimisation is illustrated in Figure 6.2.2, the first set of images shows the use of height-based thresholding as a segmentation method when used upon images from the historic data set, pre-processed by the code. Figure 6.2.2 additionally shows a set of images associated with a ternary image, a segmented image with three distinct phases. Similar to the optimal binary image, the perfect ternary image assigns 0, 0.5 and 1 to the pixels associated with the surface, nanostructure and third layer features respectively. Though not thoroughly explored within the proposed mass-processing code, third layer effects are investigated in a separate code, and segmented using similar methods to the binarisation code.

The majority of simulated images produced by the Rabani *et al.* model contain two phases, the substrate and the nanoparticles. One of the proposed experiments was to map images produced experimentally to identify the regions of the image containing nanoparticles and regions of bare substrate. The goal of this mapping would be to incorporate the historic data set produced by AFM into machine learning code trained on simulated images, requiring one to render images produced experimentally indistinguishable from those produced computationally. The role of the proposed binarisation algorithms is to provide a generic, reliable, optimal segmentation of the now pre-processed images, automated using image statistics.

All segmentation methods deployed in Python relied on height-based thresholding. In the case of binarisation, thresholding involves applying a pre-determined threshold value to an image, which converts every pixel with a value above the threshold value to 1 and below the threshold value to 0. The term height is used as it is assumed the AFM images presented here generally couple pixel values to physical height, like that in Figure 6.2.1. The expectation is, that due to the bimodal distribution of pixel values in surface-nanostructure images, choosing an intermediary value as the threshold value will provide the most optimal labelling of the surface and nanostructures in binary images produced by this method. As mentioned in Subsection 6.1.2, Gwyddion

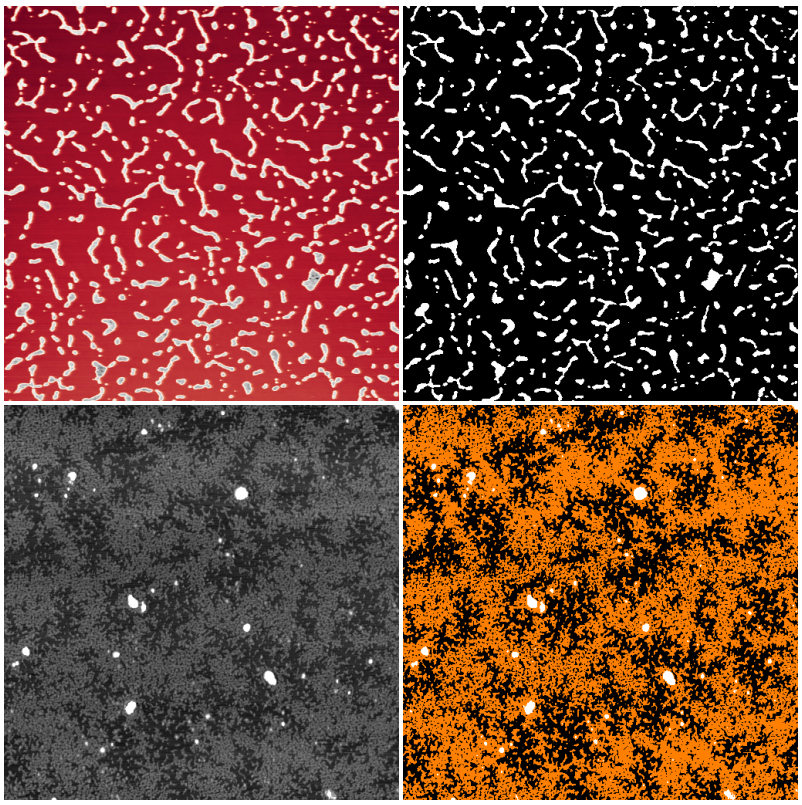

Figure 6.2.2: Pre-processed AFM images next to their respective binary and ternary images segmented by height.

similarly offers thresholding by relative heights and gradient, as well as other segmentation methods such as watershed and edge detection[139]. This includes a manual approach to height-based thresholding, shown in Figure 6.1.3, which relies on the user to select the threshold value using a slider, with the user informed of the end result by an updating preview. The use of image statistics aims to provide a more consistent and unsupervised method, without the biases introduced by this by-eye approach.

The image histogram helps inform the user visually whether the combination of pre-processing and segmentation algorithms is correctly segmenting the image, depicted in Figures 6.1.1(b) in Gwyddion and 6.4.13 in Python. In the case of grayscale images, the image histogram is a graphical representation of a single image that shows the frequency distribution of its residual pixel values. AFM images with two distinct populations after pre-processing will have a clearer bimodal distribution and will be easier to binarise. Similarly, histograms where the two populations are partially or fully convolved are more difficult to binarise. This renders image histograms a useful metric for testing both segmentation and pre-processing effectiveness. Additionally, marking each algorithm's chosen threshold value on the image histogram during testing provides another algorithm evaluation tool.

The two main segmentation methods explored in the Python code were Otsu's thresh-

olding and Gaussian mixture modelling thresholding. Both are two of the simpler and computationally lightweight forms of segmentation, with effectiveness dependent on the shape of the image histogram. Both are discussed in Subsection 6.4.4. Further experimentation with segmentation was conducted using the pre-processed data set by Gordon *et al.*[9] and Farley *et al.*[8] for the purposes of CNN incorporation with the simulated data. K-means and mean-shift clustering, local means and artificial neural network-based segmentation were all deployed to further optimise the process. Pre-processing significantly improved the effectiveness of these methods of segmentation, spurring further investigation into its improvement, using simple segmentation as another metric for the success of each pre-processing method.

6.3 Image screening

6.3.1 Automating screening

When testing new techniques, a handful of diverse images from the entire data set are selected to constitute a testing set to represent the entire data set. Every resulting image in the testing set is visually inspected by the user at multiple stages throughout processing. The user is looking for failings or shortcomings in the algorithms that appear visibly in the images or interpolated from within accompanying graphs. Additionally, the user may observe types of image noise or corruption that render images unworkable, resulting in inevitable failures in any type of processes run on them. These inspection phases give the user a chance to not only check the effectiveness of chosen algorithms but also disqualify unworkable images from the data set. Such a process has been referred to as screening.

When code is run on the whole data set, screening all images visually is impossible. Several attempts when made at automating the screening process. Some simple algorithms to screen out images that fail by corruption, unsuccessful pre-processing or failed segmentation, are deployed as a method of reducing the time users spend visually inspecting returned images. Assessment of image metadata by a simple screening test is discussed in Appendix E.2. The proposed image segmentation regime's effectiveness is heavily influenced by the chosen pre-processing, but some types of noise features may cause unexpected shortcomings within segmentation algorithms. Some SPM images are inherently difficult or impossible to segment within the confines of Python, R or even Gwyddion. Though these failed cases may be fixable on an individual image basis, such as by manually setting the threshold values during simple height segmentation, this significantly adds to the time spent processing data. Introducing visual inspection phases to the process not only increases time spent but reintroduces the previously mentioned user biases. Otherwise, there may be internal problems with the chosen algorithm, so a new algorithm could be written and deployed on the data set. Experimentation with parts of the algorithm is important, but the final algorithm will not likely provide a 100 percent success rate for both pre-processing and segmentation. When current algorithms provide an overwhelming majority success rate, it is no

longer a worthwhile time investment to introduce new code to fix outlier images with the possibility of introducing new outliers within the passing data set. The succeeding machine learning algorithms run using the pre-processed data can adapt to a minor amount of data corruption in the data set, so corruption is instead minimised to within a chosen threshold by running screening algorithms between stages.

Automated screening was conducted using a pass-fail system. Checkpoints using `if` statements were set up between stages, probing statistics about the file being processed in that loop. When an image array fails a check, the algorithm does not continue processing that image and instead the loop restarts and moves to processing the next file. The code returns an error message in the command window informing the user at which checkpoint the image was rejected and the reason why.

6.3.2 Identifying row-based corruption

SPM is an inherently highly sensitive process. Scans take place on a line-by-line basis, changes in surface and tip physics may result in lines devoid of information. Such lines were referred to as null lines and can occur on an individual basis or in groups. These can occur for a variety of reasons, the most common causes include environmental vibrational noise, the AFM user physically nudging the microscope or altering a parameter mid-scan causing the tip to need to readjust trajectory. Rapid shifts in either tip or surface state may result in the decoupling of the tip and surface. Loss in surface contact results in the cantilever oscillating freely above the surface. The scanning software can not distinguish when these corrupting events that result in null lines occur, and as such saves all this erroneous scan data as true probing data. Hence null lines are considered a form of data corruption, with the potential to harshly affect attempts at pre-processing, segmentation and further extraction of statistics. Figure 6.3.1 shows a few examples of images containing them.

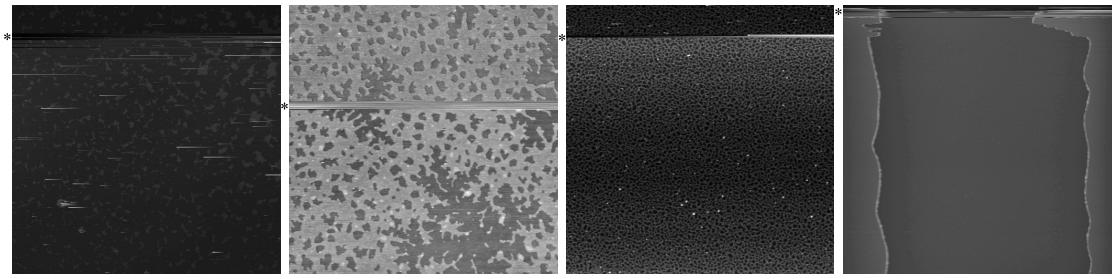

Figure 6.3.1: Pre-processed AFM images showing null lines identified by the screening algorithms, marked with a *.

A screening process was developed to run alongside pre-processing that attempts to identify these null lines within an individual image, then compared the number of null lines identified with an arbitrary confidence limit to either accept or reject the image. A confidence limit was chosen as processing and machine learning could handle small

amounts of corruptions, a single null line would not skew image statistics enough to reject the whole image. Averaging and morphological approaches could phase out the effects of null lines if they occurred in an amount limited by the confidence limit, defined as the maximum percentage of null lines per image. The null line confidence limit was set to 97.5%. An image exhibiting identifiable corruption on over 2.5% of its rows was considered irrecoverable and rejected.

The definition of a null line chosen within the methodology is a horizontal row within the data array that does not fully represent surface data. The scanning software can not distinguish between when it is collecting surface data or null data. This results in said null data being saved within the output file after the scan window is finished. This means the pixels within null lines will have values assigned. The arrangement of these pixel values lends to common types of row corruption which can be tested for using pre-defined functions. The first and most common arrangement to identify is when the row has been assigned the same value within series, often the minimum or maximum value a pixel can take. In the case of a grayscale visual representation of the array, a null line with this corruption appears to be a large black or white horizontal stripe or numerous dashes across the image. The algorithm suggested to identify this arrangement is a simple logic statement that checks every pixel value in a row to see if it takes on the minimum or maximum value. Rows that take on these values exceeding a set degree of error are marked as null lines. This corruption is more much difficult to identify when the corrupt pixels take on an arbitrary value instead of the minimum or maximum possible value. The difficulty comes from identifying this arbitrary value.

Another common arrangement to identify is where a series of pixels take on a slope-like pattern. Similar to the previous arrangement, the grayscale visual representation will display a noticeable stripe across the image, this time however changing from either a lighter or darker tone. The code to identify this arrangement was running an ascending or descending sorting algorithm on each row, then comparing the sorted row to the original data pixel by pixel using a logic statement. If the code recognised the sorted row was similar enough to the original row, it would consider that row a null line. The most common appearance of a null line is a sinusoid, characteristic of a tip-substrate contact event. Identification of this arrangement is done by fitting a sinusoidal model to each row's pixel values, and then comparing the model to the row pixel by pixel. A near-perfect fit of the line data to the model suggests the row is a null line.

It is important to acknowledge the limitations during the implementation of this screening process. Universally among coding languages, functions that compare values in arrays to other values, often by logic statements, are considerably slower than other processes. Simple-to-implement approaches to identify null lines rely on sorting or directly comparing pixel values in each row of the image array. The inherently computationally taxing nature of these processes is amplified over the 512 iterations required to screen entire image arrays for individual null lines. This places a strong limit on the

complexity of the screening process if a logic statement approach is chosen, identifying more complex types of null lines such as slopes and waves was found to double computation time. Additionally, this means identifying partially corrupt null lines, lines with which the event that caused the corruption occurred over a shorter time-frame than that of a single line scan, can similarly be too taxing to identify.

An abundance of null lines within images has a significant effect on proposed image processing. They reduce the effectiveness of the most sensitive techniques of both pre-processing and segmentation. Null lines appear as uncharacteristic scarring or streaking on images. The incongruous data in null lines has an influence on fitting parameters when fitting the background of the row-aligned images when running the background detrender. Some fitting algorithms will attempt to fit a background to the image that caters towards this uncharacteristic data. This results in a background-detrended image with a less confident fit, which is visually noticeable as it creates a wave-like pattern over the image, and is statistically unrepresentative of the imaged surface. Fitting algorithms that were less sensitive to discontinuities were deployed in order to combat this effect.

In segmentation, null lines similarly have both visual and statistical effects. Null lines potentially appear as uncharacteristic white or black streaks on binarised images, this can have consequences when the images are inspected for connected regions. A black streak through a region can be mistaken for a break in connectivity of a region of nanostructure while a white streak can connect two otherwise unconnected regions, affecting the Minkowski metrics. Corrective morphological or machine learning processes were utilised to manage or correct this effect on the segmented images. Higher degrees of null lines of similar values can have significant detrimental effects on the general image statistics. Pixel values of the null lines of similar values appear as a large peak in the image histogram, a rogue population of pixel values that do not characterise the imaged surface. Segmentation algorithms that rely on identifying the statistical midpoint of the two pixel value populations, the pixel value with an equal likelihood to be a member of either population, then using it as the threshold value for binarisation, may shift the calculated value to cater towards this uncharacteristic peak in the image histogram. This weakens the estimate of the surface-nanostructure phase boundary, resulting in misclassification of data in the images. This is even worse when segmenting third layer effect images to three phase or ternary images, segmentation of the third often smaller peak containing the third layer relies on identifying a small population above the nanostructure layer. As null lines often take on arbitrary values within the higher range of allowed pixel values, the algorithm for third layer segmentation may treat a rogue population as the pixels that represent this third layer.

6.3.3 Further screening techniques

The methodology, experimentation and programming of some screening procedures are tied to individual approaches to pre-processing and segmentation. These methods had varying degrees of success, sometimes providing an approach to reject useless images from the data set early within processing, but sometimes weakening the inherent algorithms or requiring user observations. These will be discussed alongside the experimentation with each of these approaches.

6.4 Experimentation and adaptation of script

6.4.1 Tools and principles for testing software

Now that the broad structure of the proposed image processing code has been discussed, it is now necessary to talk about the experimentation that was required to meet the standards required for the proposed further analysis. The role of each stage of the processing algorithm can be filled by various popular or experimental methods developed for and adapted to the data set. Processing algorithms offered in popular image processing software for nanoscience such as Gwyddion and WSxM, or more generic processing tools like ImageJ were recreated in Python for the sake of comparison to proposed methods and usage in an automated workflow. These widely available statistical methods offered an effective starting point for structuring the processing code, and a comparison point for experimentation, as algorithms designed for the data set would be replacing these common conventional approaches.

Some proposed methods coded in Python and R have changeable numeric parameters tied to factors such as sensitivity, degrees of freedom, sampling rate or returned number of data points. Fine-tuning these parameters to the data set takes a lot of trial and error, relying on a combination of visual and statistical analysis. Some key principles for experimenting within the IDE were established. These principles were code implementations across all proposed scripts that aimed to streamline the experimentation and debugging phases.

The first of which was the concept of test sets, a small sample of images that represent the entire data set. These representative sets meant new features of the program could be tested faster, as running processing algorithms on the whole data set is time intensive, while only a handful of images of resulting images would be evaluated by the user, so limiting the number of images being initially processed is preferred.

These test sets were built through visual inspection of the data set, often categorised based on visual predictions on how the raw images would interact with the first conventional processing approaches, and selecting images of different types of dewetting patterns. The first test set was built based on the proposed screening of height-segmented images, at this stage primarily visual inspection of images and their respective image

histograms. Visual inspection checked for frequency of problematic noise patterns identified as having a significant effect on image statistics[8] and wasn't typically addressed by a standardised image processing workflow. An ideal image histogram, for those segmented by height, has two distinct populations, bimodal peaks, with minimal overlap to minimise the degree of misclassification when binarised, as well as a low presence of peaks associated with noise, such as peaks at 0 and 1 in the normalised image, caused by "salt and pepper" noise. The set was split into four categories, these were true positive (TP), false negative (FN), false positive (FP) and true negative (TN). The true positive category encapsulates images where the original scan had very little noise, was fairly uniform and had at least two distinct layers, including those tied to the surface and nanoparticles. The true positive images both provide useful visual information and segment into binary images effectively. The false negatives folder contains similarly useful images, but contain noise features that may cause shortcomings in some conventional processing algorithms. For example, images that fail the final stage of height-based segmentation due to the minor nanoparticle layer or a major third layer effect. False negative images represent a large amount of the actual data set, images that are often worth recovering by developing new processing algorithms. False positive images are fewer in number but provide another challenge for the program, FP images that provide little to no visual information to the user that possibly are not rejected by the code at any stage due to noise features that imitate physical features. False positives should be screened out by means other than the confidence in the segmentation, through other screening algorithms or user intervention. True negative images contain little to no useful visual or statistical information, and hence the user and program were predicted to agree upon this in each case. This first test set was effective for testing simple segmentation methods, but new unique test sets were derived from the data set and shared with the group for testing individual proposed techniques against their conventional counterparts over time. Furthermore, the principle of selecting images for the test set that represent challenges to the proposed algorithms is carried forward.

Visual inspection at every stage of the algorithm as well as the final produced image is a useful procedure while experimenting and debugging the processing script. Saving the returned images at every stage adds additional processing time within the program, as well as time added browsing for the images in the file explorer. Instead, subplots were deployed to provide instantaneous feedback as an array of images and graphs in a temporary window. A rudimentary set of subplots is returned in most cases, containing images before and after certain algorithms, plots of the image histogram, and other plots unique to tested algorithms. This is particularly useful when comparing two or more processes that take the same role within the script, or when changing a single variable or function within a script between runs, as with Figures 6.4.9 to 6.4.11. Additionally, a unique colourmap was chosen for subplots. Red-to-gray (`RdGy`), shown in Figure 6.4.1, was picked over a grayscale or single-colour cold to hot gradient map, such as `afmhot` as it helped in spotting minor fluctuations, particularly background

contrast, and noise features.

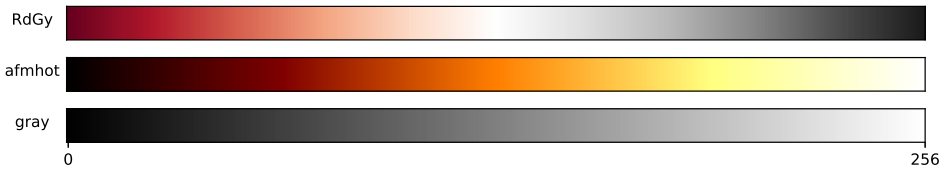

Figure 6.4.1: Colourmaps used throughout scripts.

6.4.2 Initial framework

The first version of the proposed script was aimed at testing Python's capacity to replicate the workflow of a user within Gwyddion. In the case of images of nanostructures aimed to be segmented into binary images, this would be to load a raw AFM file, process the loaded image, and save the resulting binary image. In this version, a raw AFM file, the IBW file from the same root directory as the code, is loaded, converted into an array, pre-processed, segmented, and the resulting binary image is presented to the user. Pre-processing techniques were chosen based on what is commonly used for processing such images in Gwyddion within the cohort. These were row alignment using the median of differences approach, and background detrending using a planar-flattening approach. Segmentation was conducted using a differential and graphical interpolation approach to finding Otsu's threshold. No images were saved in this script, resulting images and subplots were instead displayed in the IDE for code feedback.

Pycroscopy and h5py were shown in combination to translate the IBW file into an HD5 format, then into an array manipulable in Python's NumPy library with zero degradation at an acceptable speed. This translation algorithm was standardised for all future code, with zero functional revisions.

The raw files loaded as arrays were then pre-processed, starting with the initially proposed row alignment method. Unlike other methods of row alignment, by which a single statistic is derived from each row, then all pixel values are incremented or reduced by an offset row by row until that statistic is consistent across all rows, a median of differences approach derives the offset between two neighbouring rows. The algorithm was coded and tested with basic NumPy numeric functions and is outlined in Figure 6.4.2. Starting with the second row, a temporary 512 value array is created that contains the difference between pixel values in the row and the previous row. The median of this array is calculated, returning the statistic used as the offset - the median of differences. This offset is then applied to all values in the row and the process then repeats for all further rows. The resulting aligned array is then normalised to guarantee all values still lie within and fit the 0 to 1 range.

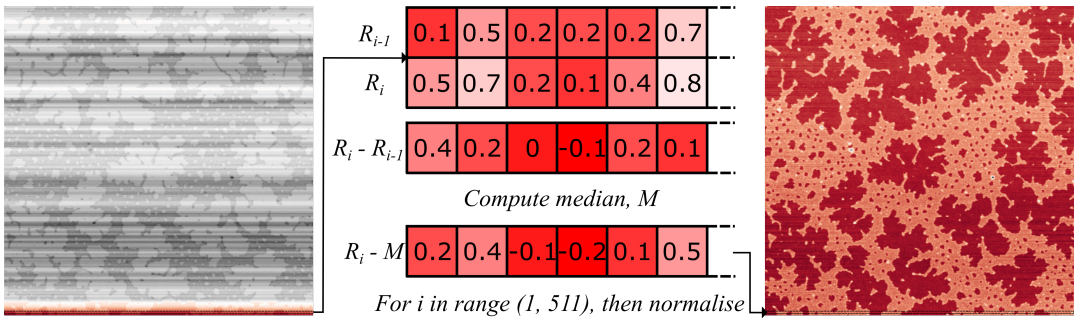

Figure 6.4.2: Diagram illustrating use of median of differences for row alignment of a 512-row image.

Mean or median alignment, two common forms of single statistic row alignment available in software such as Gwyddion, were implemented for qualitative comparison by means of visual and histogram inspection. Figure 6.4.3 compares the three row aligners for four different images that encapsulate multiple common complications with row-by-row correction in images of nanostructures. 6.4.3(a) pre-processes a region containing cellular patterning of continuous feature length, spanning the entire probed area. All three aligners worked effectively, returning near-identical two-population image histograms for all options. The mean aligner's line-by-line offset appears diagonal, as it attempts to correct the image's vertical trend. 6.4.3(b) contains fingering patterns of various sizes, and significant variations in contrast across the surface and nanoparticle pattern layers. Additionally, a third layer, appearing as black dots, spans the top half of the image. The third layer is expected to appear as a small peak at high gray levels in the image histogram. Both median of differences and mean alignment perform similar offsets on the image, however median alignment places emphasis on the third layer and misaligns all rows containing it. This results in suppression of the third peak in the image histogram. Additionally, median alignment misaligns rows where the population of pixels associated with the nanoparticles, exceeds that of the background substrate. The featureless gap between the two contacts in 6.4.3(c) is misaligned by the mean and median aligners, which attempt to equate their respective parameter for rows of bare substrate to rows containing both the surface and contacts. This is especially true for mean alignment, to a degree the image histogram returns four peaks, as opposed to the expected three peaks, one for the bare substrate, and one for each contact. 6.4.3(d) exhibits both a third layer and cellular patterns with two feature lengths. The aligners perform similarly to the pre-processing in (b), with mean alignment most effectively separating the first and second layers, as seen by the gap between the first two peaks in the histogram. A deeper gap between population peaks in the image histogram reduces the number of pixels misclassified as the opposite population when the threshold value is defined between them.

The median of differences approach to row alignment proved to be highly effective. While sometimes outperformed by mean alignment, it makes a strong attempt at all given image types, with no manual parameterisation required, which would be more

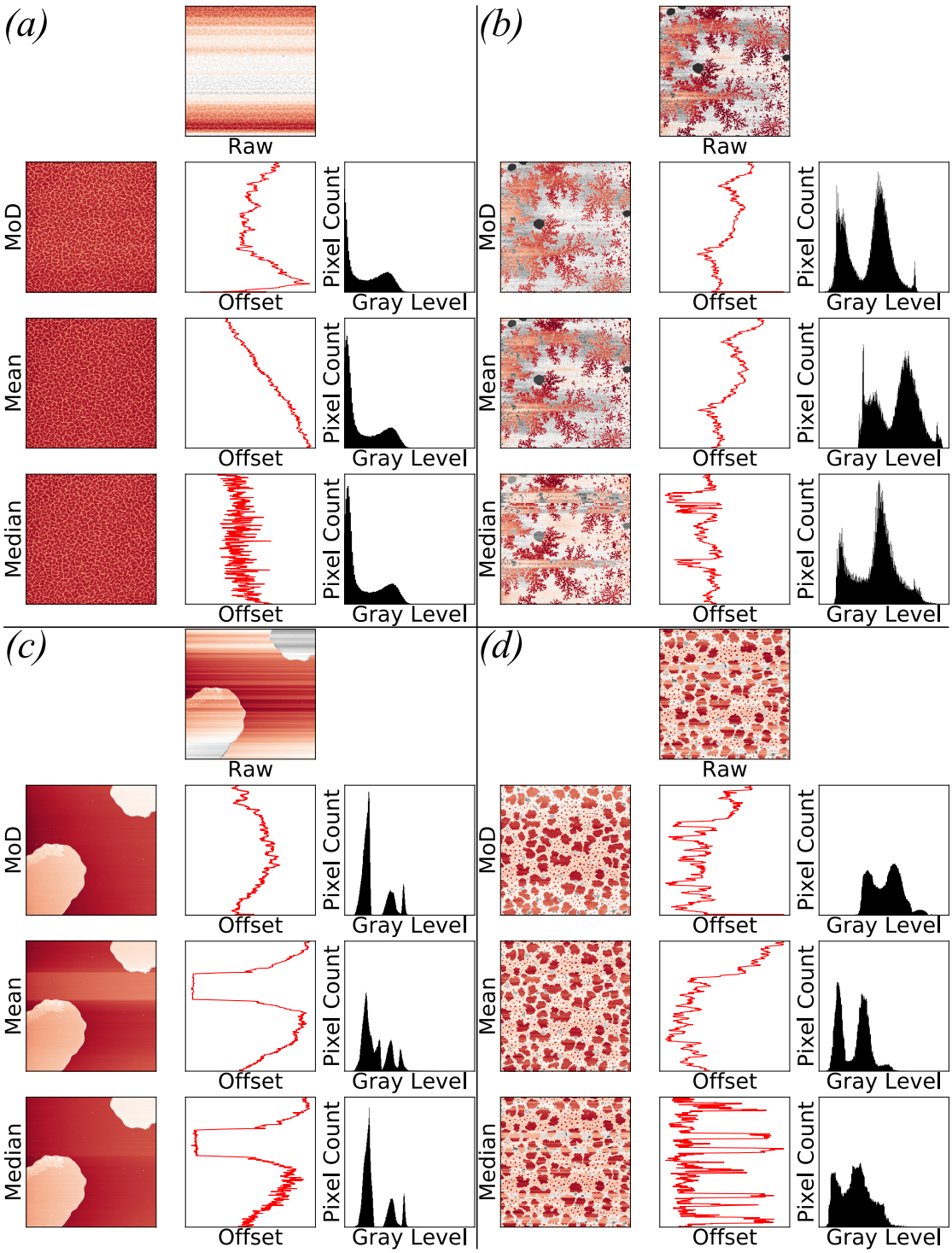

Figure 6.4.3: Testing row-alignment algorithms on AFM images. Each raw image is row-aligned by either median of differences (MoD), equating each row's mean, or equating each row's median. The final row-aligned and planar-flattened image, the graph of relative pixel value correction, or offset, down the image, and the image histogram are provided for each row aligner.

useful in a fully automated mass-processing script. The median of differences approach was found to be much more sensitive to surface features, was less likely to produce uncharacteristic misalignments due to pattern discontinuities or small amounts of noise, returned a more ideal image histogram shape, and provided generally visually stronger results for the first test set. When provided with further test sets, the key feature of median of differences alignment was its higher success rate and sensitivity when aligning multi-phase images with a continuous nanoparticle pattern prominent across the image or with a discontinuity. These test sets, and the final data set, were almost entirely made of two-phase images with a sub-5% coverage third layer. These two phases were continuous in almost every row of the images, feature lengths of nanoparticle patterns were always exceedingly larger than the single pixel length of rows, but exceedingly smaller than the scan size, and there were several cases of the particle-free surface phase being the only phase present over multiple rows. Quantitative analysis on the image histograms in the test set, when combined with subsequent background detrending, showed median of differences alignment minimised the average misclassification rate, as defined in Subsection 6.4.4. Short-term tip interactions had the potential to induce horizontal image curvature across one or more rows, affecting the row-by-row correction described in Figure 6.4.2. Similar to the discontinuities from substrate to adsorbate during median or mean row alignment in 6.4.3(c), this results in an uncharacteristic step across the image after all 3 forms of row alignment, significantly lowering the effectiveness of subsequent background detrending and segmentation. While not disqualifying a median of differences approach, algorithms sensitive to single-line curvature would be tested in future frameworks.

Background detrending was conducted using an iterative process called the planar-flattening approach, shown in Figure 6.4.4. The algorithm begins by returning two arrays of the same size of the image, each representing a slope in the vertical and horizontal directions across the image, with gradients defined by the means of the pixel values in the leftmost and rightmost column, and top and bottom row respectively. These arrays are combined into a third array, representing a pseudo-3D plane describing the generalised slope of the image, this was referred to as the test plane, this test plane was optimised by means of a goodness of fit test. The test plane array is subtracted from the image array in the same manner as a matrix subtraction. The goodness of fit is evaluated by summing the square of all values in the resulting array, the resulting fit factor, effectively a square-sum of the residuals, is saved. Based on this initial test plane, new test planes are created and evaluated using nested loops. A range of different gradients in both the horizontal and vertical directions are applied in combination using these loops. The test plane that returns the lowest fit factor is assumed to be the plane that aligns with the background noise of the image most effectively. This optimal test plane is subtracted as before, returning a planar-flattened image that is normalised and then carried forward within the algorithm.

Background detrending using a planar-flattening approach was favourable when ap-

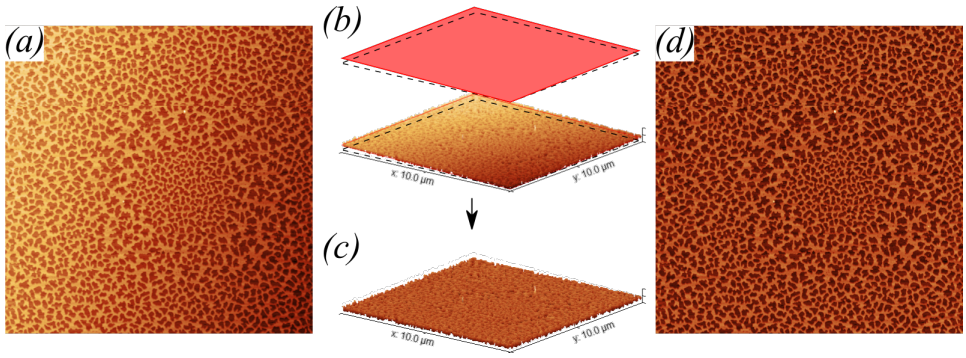

Figure 6.4.4: Diagram illustrating use of planar-flattening approach to image detrending. **(a)** AFM image with rows aligned by median of differences; **(b)** 3D representation of the AFM image, with the derived optimal test plane shown above it; **(c)** 3D representation with test plane subtracted; **(d)** resulting planar-flattened AFM image.

plied to images within the first test set. Though it was effective at removing linear sloping from images, which was particularly common in the first test set, it began to visually fail a large number of images as the test sets expanded. It became clear the limits of this approach when images demonstrated a non-linear trend, significant curvature caused by the equipment. This was particularly clear after segmentation, height-based thresholding fails when too many pixel values associated with the surface were higher than that of the nanoparticles, or pixel values associated with the nanoparticles were lower than that of the surface. Strong curvature that was unaffected by this background detrending approach would result in the effect shown in Figure 6.4.5. The pre-processed image on the left shows bow-like curvature by means of the surface appearing lighter, especially towards the bottom centre, and hence, by the `RdGy` colourmap shown in Figure 6.4.1, considered physically higher for height-based thresholding. This shows an incorrect mapping of the locations of the nanoparticles due to the pixels associated with the nanoparticle layer on the left and right sides falling below the calculated threshold value. This emphasises the importance of the role of the background detrender to mitigate this effect.

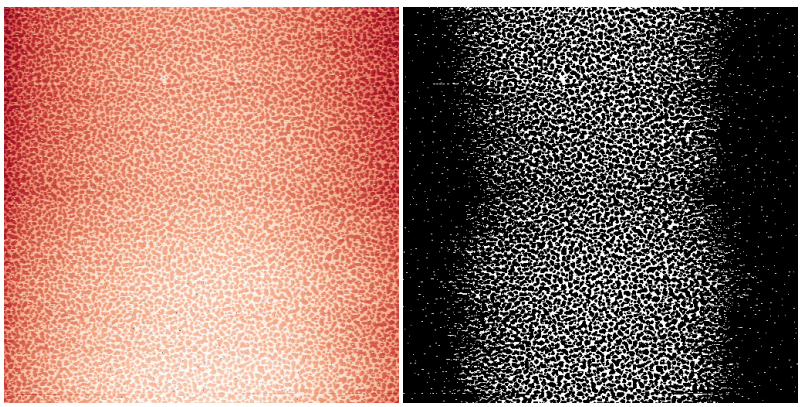

Figure 6.4.5: Median of differences aligned and planar-flattened AFM image with strong curvature before and after height-based thresholding.

Additionally, optimising this approach for a data set entirely consisting of images with a linear slope trend requires calculating the fit factor for more test planes per image. This would mean increasing the number of values in the testing range and the testing range of different gradients in both the horizontal and vertical directions. The iterative nature of the approach combined with a large matrix subtraction scales computation time significantly, tripling the number of gradients tested in both directions increases the computation time nine-fold.

Immediate alternatives to the planar-flattening approach were explored for future scripts, in Subsection 6.4.4. Gwyddion offered a three point levelling tool, by which a user marks three points in the image that are at the same level, and then a plane is computed from them and subtracted from the data. Manually selecting points, or choosing a single set of coordinates for all images, would not scale for large data sets, and introduce potential inaccuracies by incorrectly marking separate layers. Expanding beyond these 1st order approaches to 2nd order upwards was proposed, exploring in-built functions within NumPy to reduce computation time, and critically addressing image curvature.

A simplified application of Otsu's thresholding was deployed as a way to binarise the pre-processed images. This would estimate the threshold value, the pixel value at which the likelihood a pixel of that value is either a member of the nanoparticle or surface phase is equal. First, the cumulative distribution function (CDF) of suitable smoothness is plotted. This begins with creating an array of 1000 evenly spaced potential threshold values between 0 and 1, then producing an array of the same size that determines the percentage of pixel values that fall below each potential threshold. The derivative of this cumulative histogram provides the probability distribution function (PDF). The highly bimodal nature of the images means the PDF commonly returns an image with two peaks along the x-axis, representing two populations of phases, the leftmost peak representing the lower grayscale value pixels tied to the surface phase, and the second rightmost peak representing the higher grayscale value pixels tied to the nanoparticle phase, much like the image histogram. A third small peak tied to the third layer is sometimes visible too. The trough between the first two peaks in the PDF can be estimated to have a pixel value representing equal probability of such pixel being part of either population. This would make for a strong estimate of the optimal threshold value, so an algorithm to interpolate this threshold value was proposed.

A lightweight approach for interpolation was initially chosen. This was to identify the index of the trough by means of SciPy's `find_peaks` function, it can be adapted to find troughs by running the function on the PDF reflected in the y-axis. First a Gaussian-smoothed differential of the CDF was returned, as to limit occurrences of further troughs in the PDF. Then `find_peaks` was run on this PDF, returning multiple indices of troughs that were displayed visually by plotting crosses on this PDF at the identified troughs. The pixel value associated with the index of the first trough along

the PDF was taken to be the threshold value for binarisation. An image plot was displayed as a subplot which had applied a logic statement to the image, assigning all pixels with pixel values below the threshold value 0 and above to 1.

This approximation to Otsu's thresholding proved highly effective on the first test set and served the purpose of understanding the potential ways to communicate multi-phase images to both users and artificial intelligence. The algorithm was not without its problems, it required a very clear bimodal distribution within the PDF, with a substantial separation of pixel values of the surface and nanoparticle populations. This approach also was shown to fail when there was not a visible trough between the two populations in the image histogram, the `find_peaks` function fails to find a local minimum.

Though the Gaussian-smoothing approach was useful for mitigating the effects of noise on the bimodal distribution's clarity within the test set, finding a universal smoothing parameter, σ, that provided a clear bimodal distribution for the entire data set was going to prove near impossible. Additionally, another source of trial and error was the prominence factor in the `find_peaks` function was difficult to set universally by means of the high variance in the sharpest of the two main peaks. There was an immediate attempt to remedy both of these problems by the addition of some further steps in data preparation before differentiating, smoothing and running the `find_peaks` function on the PDF.

The proposal was to crop the data both presented in the PDF and what is presented to `find_peaks`. The presence of noise, particularly salt and pepper noise, results in the data range for pixel values being artificially widened. This was particularly obvious in the CDFs, which often had two large plateaus at 0% and 100%. A short algorithm that identifies the starting and ending indices of the interval which shows the phase shift. The smoothed PDF is calculated for this interval alone, making it easier to standardise the parameters, as the bimodal distribution occupies the majority of the PDF. Secondly, `find_peaks` was run on this distribution to identify the indices of the bimodal peaks, before identifying the troughs. The algorithm was then run to find the trough between these two peaks, limiting `find_peaks` to application on the reflected PDF between the indices calculated in its first application. This further improved confidence in the location of the threshold value, without the user needing to view the subplotted graph of the PDF.

Despite these adaptations and improvements, with further increases in success rate caused by future changes to the pre-processing algorithms, the method by definition was not statistically rigorous. Farley *et al.*, using the historic data pre-processed using the final script that concluded this work, showed a U-Net segmentation outperformed Otsu's thresholding of two-phase images visually, even when artificial noise was added[8]. More global threshold approaches were explored to replace this application of Otsu's

thresholding in Subsection 6.4.4, as well as exploration of a more localised approach to segmentation with FlexMix in Subsection 6.4.5.

6.4.3 Adaptation for mass processing

The natural progression for the code was the ability to find all IBW files within a local folder, and save subplots and processed images based upon those IBW files to a separate folder, without any user input. This move to automation on a directory scale entailed a few steps. The script included a loop through the initial framework for image processing, with an iteration for each IBW file found in the directory chosen within a UI, stating whether each image passes or fails, then saving resulting plots and images passed on each case, without breaking out of the loop due to common errors. Each component will be discussed individually, but the flowchart shown in Figure 6.4.6 is the culmination of all these elements.

Screening proposed in Section 6.3 was introduced at this stage. Python's own errors that would return an error message in the Python console would often terminate the script, this meant an error caused by a single image would cause the loop to cancel and fail to process further images on the list. As these errors were often individualised, break-out conditions that would restart or bypass sections of the `for` loop were implemented, this took the form of the screening process. These cases are reported within the console, as well as further user communication, discussed in Appendix E.3.

Noted at this stage was the effect of null lines, the script's main processing algorithms could not distinguish null lines from rows that characterised the surface. The proposed null line checker from Subsection 6.3.2 was integrated into the row aligner, as the row-by-row inspection nature of both algorithms could be consolidated for the sake of efficiency. After conducting row-alignment, the percentage of null lines detected would be compared to an increased confidence limit, 5%, and the whole image would be rejected accordingly. The limit was considered to be low, but identifiable null lines with the current algorithm was considered to beget a larger amount of undetectable corruption.

The script would not attempt to return a binary image of an array in the loop if no clear threshold value was obtained, found at this point by identifying a trough between the bimodal peaks with the `find_peaks` function. The function's current capacity to identify Otsu's threshold was acting as a screening process. Previously covered improvements to the implementation of Otsu's thresholding naturally improved its efficiency as a screening process, particularly reducing the number of false negative cases of no clear threshold value being available.

Using a `for` loop that encapsulates the entire processing code that acts upon every queried image became the basis for all other future scripts. This approach did have

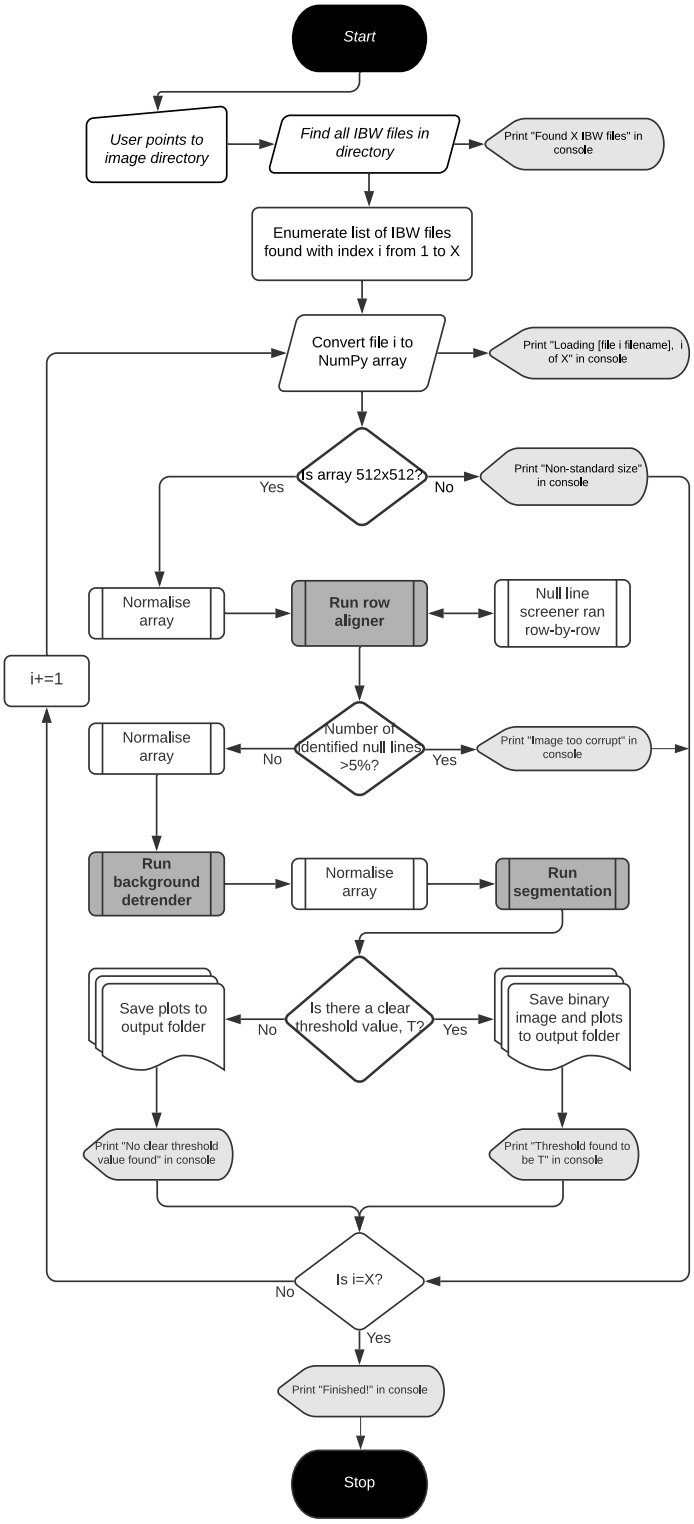

Figure 6.4.6: Flowchart showing framework of image processing code used for directory processing.

limits, the loop would be liable to crash after roughly 200 loops due to a lack of assignable computer memory. Any test sets larger than 200 images were either split or the loop was modified to begin at a later index in order to avoid this.

6.4.4 Further exploration of processing tools within Python

The three highlighted key processes shown in Figure 6.4.6 were written to be modular, and hence easily interchangeable with new potentially more effective techniques. The row aligner module was not going to be addressed further within Python, but the background detrender and segmentation modules were in need of either enhancement or replacement to meet the standards required for further analysis.

At this stage, the subplots produced by looping the script through images in a test set took the appearance of Figure 6.4.7. This displays an AFM file with a similar issue to that shown in Figure 6.4.5, the general trend of the image is second order curvature that can not be removed with the planar flattening approach. The planar flatten approach is shown to remove the vertical trend, but not the curved horizontal trend This shows the importance of tackling unique trends in all directions, so some approaches were developed that took into account trends in each direction individually. The second image on the bottom row displays the unscaled PDF of the pre-processed image, with crosses marking the locations of the peaks and troughs found using the `find_peaks` function. The found trough, the red or second cross, does not lie within a clear trough, resulting in a failed segmentation that bypasses screening. Pre-processing that resulted in two clearly separated bimodal peaks on the PDF returned segmentation with the highest confidence.

The background detrender so far had only been a 1st order line fit approach. The planar-flattening approach would estimate a flat plane that fit the image's global noise trend most effectively. The expansion of this to 2nd order and beyond was a necessity, illustrated by Figure 6.4.5, it was clear not all background trends were linear. Fitting to surface curvature using high order polynomials brings a new problem, called over-fitting. The background detrender's role is to accurately detect the uncharacteristic trend caused by the scanning process, and subtract that trend to leave behind the best estimate of the appearance of the substrate-nanoparticle assembly. It is assumed this trend is far broader than the local data, small raised regions upon the surface where nanoparticle reside. The use of polynomials to help define this trend is highly efficient and sensitive to the background trend. However, a higher order polynomial's higher sensitivity has the potential to fit a trend to the local data, effectively treating characteristic nanoparticle data as the uncharacteristic background trend. This causes detrending to remove height data from the image, making the heights of nanoparticle data much more similar to that of surface data and sometimes adding uncharacteristic features to the image in the form of peaks and troughs, weakening future analysis and particularly segmentation. Hence it stresses the importance of choosing a sensible

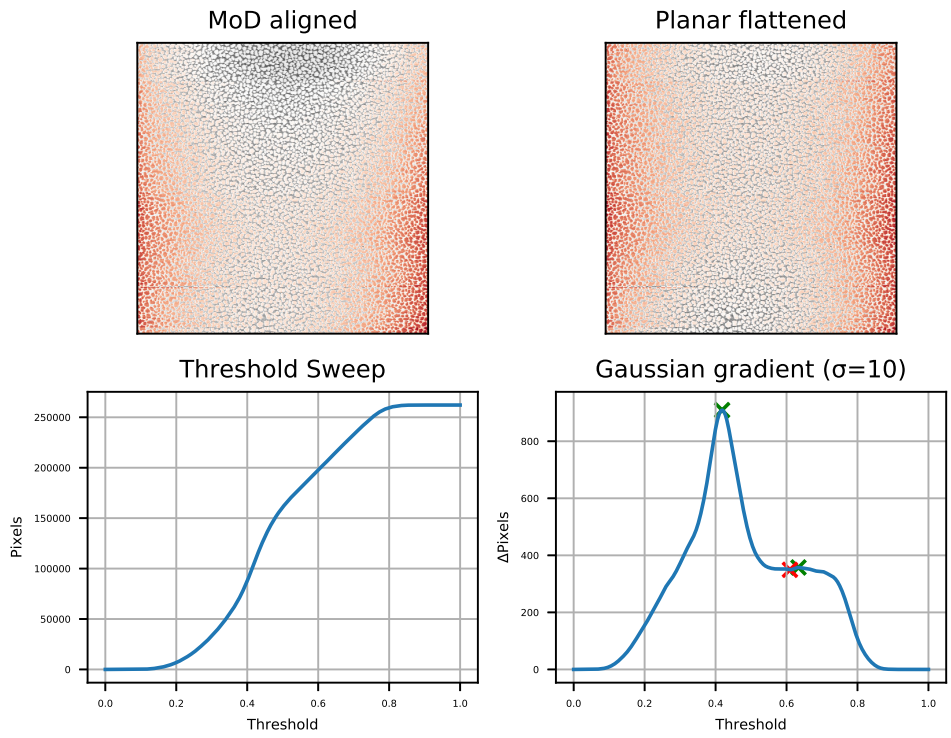

Figure 6.4.7: Subplots produced by a bowed image in the test set of the mass-processing script.

range of orders to test, though a higher order polynomial may return a lower fit factor within the code, this may be a misleading case of over-fitting. Visual inspection can help at this phase to help set this range, particularly by studying the returned background trend as its own image.

Figure 6.4.8 graphically demonstrates what happens during over-fitting. A slice of a real AFM image with submonolayer coverage of gold nanoparticles with a consistent height of 3 nm is displayed as a 2D profile. A straight line does not accurately describe this trend, resulting in an under-fit, while too many degrees of freedom result in a periodic fit to the data, a line representing over-fit. The middle ground fits the curvature of the trend, the desired fitting created by limiting the order of polynomials in the background detrender.

Three experimental approaches to background detrending were explored in Python, all ran from the same directory-processing script on the same test set using a UI to choose which was inserted into the algorithm. The first was referred to as the "generalised" approach, a generalised fit to the image using NumPy's `polyfit` function upon the mean trend in the vertical and horizontal directions across the image. This generalised polynomial background approach uses independent degrees of freedom in

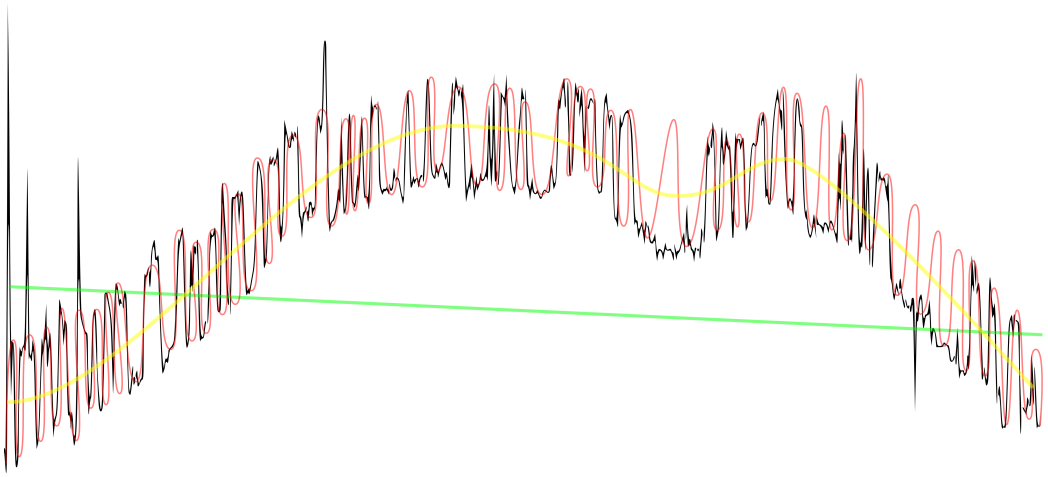

Figure 6.4.8: Profile of an AFM image of nanoparticles of uniform heights before detrending. Three coloured lines show three potential extremes for the detrending algorithm's fitter; (green) an under-fit as a linear function, (yellow) a perfect polynomial fitted to the trend of the data, and (red) an over-fit where the polynomial fits to the data.

the vertical and horizontal direction, each direction is generalised by means of each column averaged to form a 1D array in the x-direction, and each row is averaged to form a 1D array in the y-direction. The `polyfit` function is provided with a range of different orders of polynomial, with the range set to take into account the compromise between fit accuracy and over-fitting. The range was set to 1 to 4, as beyond 4 characteristic over-fitting was observed for images in the test set. The fits in each direction are converted into a 2D meshgrid, combined into a 2D trend, and, similar to the planar-flattening approach, the fit factors are calculated in an iterative manner until an optimal combination of orders in each direction is calculated. The script using this approach returns a wide array of subplots within the IDE and saves the plots and final binary image as PNGs.

Figure 6.4.9 shows the resulting subplots, using the same raw image as that in Figure 6.4.7. The second row shows the `polyfit` approach in sequence, with the polynomial describing the mean of the horizontal and vertical directions displayed as individual, then combined, as a 2D plane. The plane subtraction shows the result of detrending the median of difference aligned using this combined fit, returning the detrended and normalised image. The bottom-right unscaled PDF graph compared to that in Figure 6.4.7 shows how significantly successful background detrending separates the bimodal peaks. This returns a height-thresholded image, with far more confidence in the segmentation.

As a way to address shifts in trend local to individual rows, that result in a streaking effect particularly at the left and right edges, a local application of `polyfit` was con-

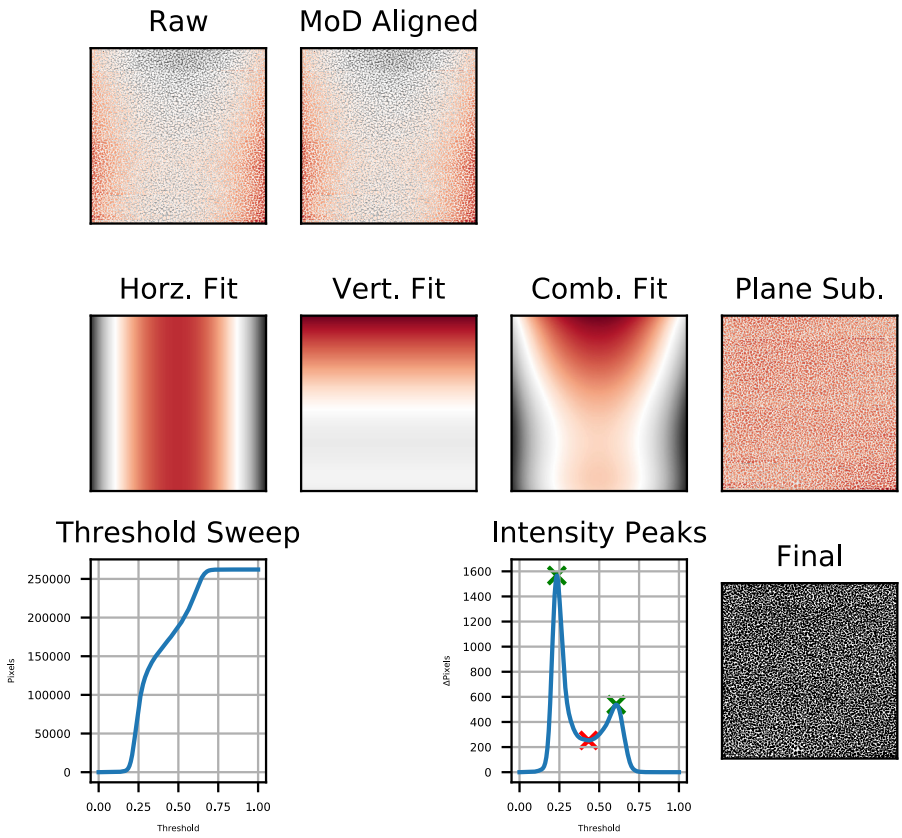

Figure 6.4.9: Subplots produced within Python of the mean-generalised global `polyfit` method.

sidered. The script would supply an order n, fitting a unique nth degree polynomial to every row and column. Figure 6.4.10's second row shows the process, the horizontal fit (Horz. Fit) image displays 512 line-fits of each row of the median of differences aligned image with $n = 3$. This is similarly calculated for the vertical direction (Vert. Fit) and then combined into a third matrix. There was a consideration that the vertical trend was over-augmenting the horizontal trend, resulting in uncharacteristic peaks in the detrended image, so a convolution filter was applied to the image as a way to smooth out the peaks. A high strength (standard deviation on all axes $\sigma = 5$) application of `ndimage`'s Gaussian filter was applied to the 2D array. This uses a kernel, a small matrix, which performs a convolution on the image, this centres the kernel on a pixel and recalculates the pixel's value by adding all the neighbours' pixel values, with those values scaled by the values in the kernel. The kernel for a Gaussian filter will take the appearance of a 2D Gaussian centred upon the centre of the kernel, providing more weighting to the nearest neighbours. The result when applied to all pixels in the array is a blurred image, this turns the combined fit into the blurred trend (Blur. Fit) in Figure 6.4.10. The unscaled PDF subplot in the case displays a third population, a broadening feature on the right side of the second peak. Though the found trend takes a similar appearance to the trend in Figure 6.4.9, the fit is not strong enough to detrend the curvature in the bottom left and right of the image, resulting in an

uncharacteristic population visible on the PDF, and a binary image that does not distinguish the nanoparticle phase from the surface phase at these locations.

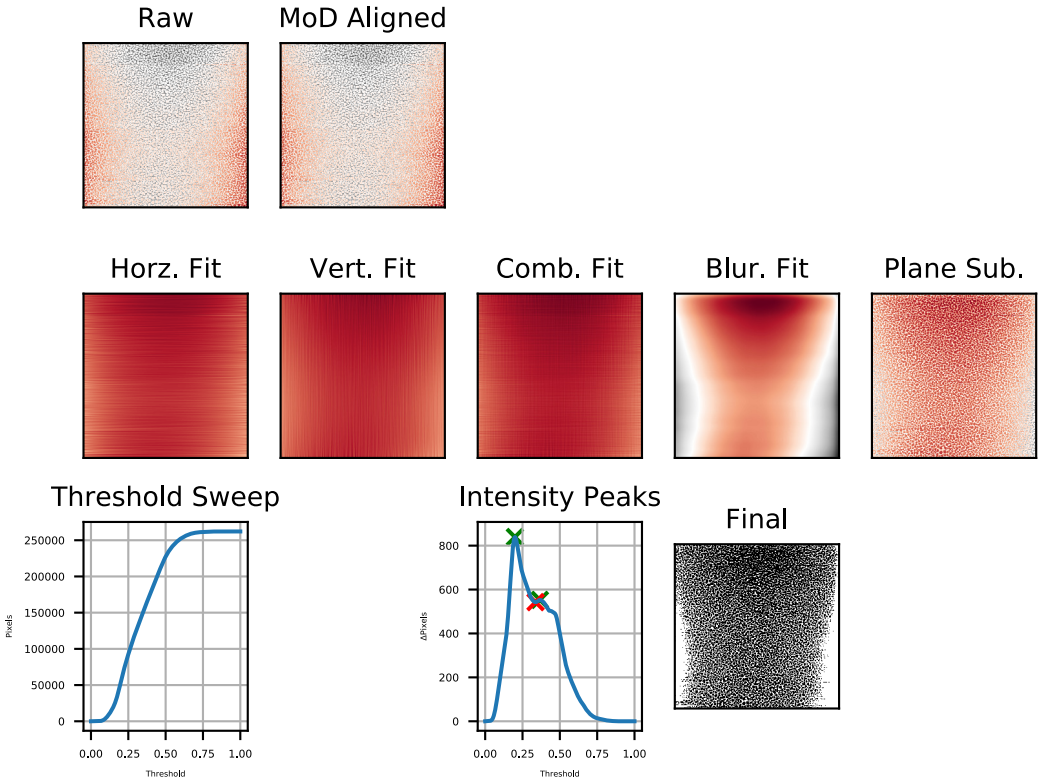

Figure 6.4.10: Subplots produced within Python of the local Gaussian filtered `polyfit` method.

In a similar vein to the second approach, the idea of local weighting using a kernel was applied in the third experimental approach within Python. Each row and column was filtered using a 1D Gaussian kernel in their perpendicular direction, resulting in each row being weighted with data from neighbouring rows, but not by data within the row, with the same being true for the columns. Figure 6.4.11's first row shows the result (labelled Blurred) of this 1D filter. The individual rows and columns in this new local-weighting array were fitted with nth order polynomials and compiled into a new array to describe the trend (Comb. Fit in Figure 6.4.10). The bottom row shows a common issue with the script in its current state, resulting in no second peak being found by the `find_peaks` function. Some uncharacteristic noise introduced by the detrender has caused the PDF to shift towards the left, and due to the standardised smoothing of the PDF has returned the second bimodal peak as a broadening feature of the first peak. This shows the importance of cropping the CDF before calculating the derivative, a feature not yet implemented at the time. The result is an incorrectly segmented image, displaying zero features.

All three methods were able to identify the general trend within the image, but the

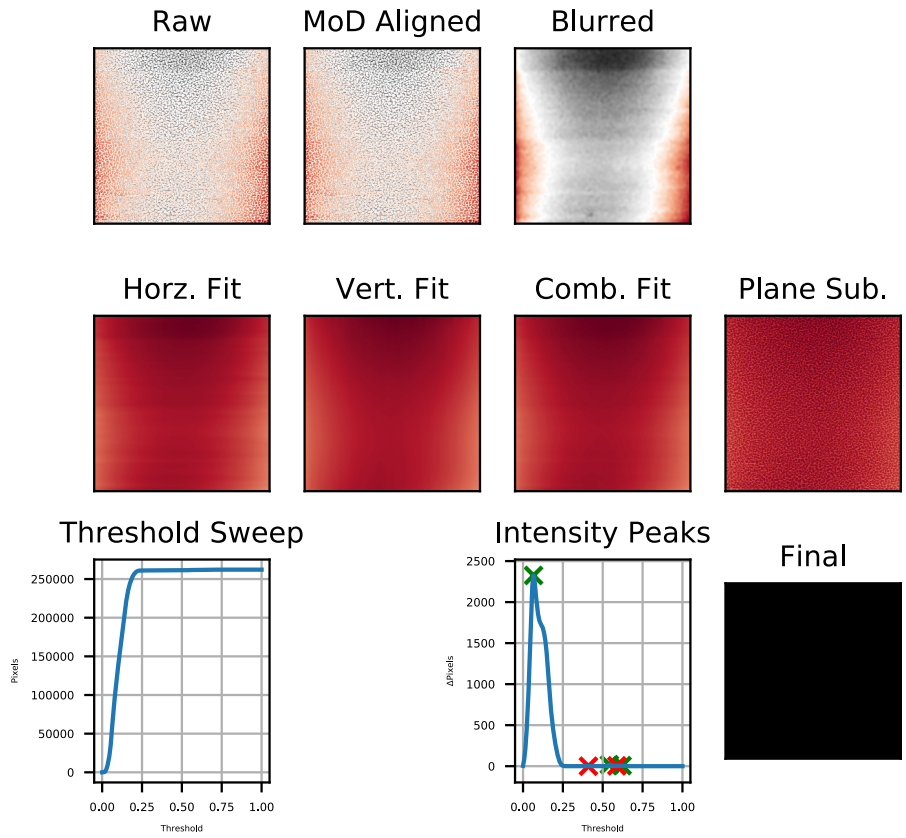

Figure 6.4.11: Subplots produced within Python of the 1D Gaussian filtered local `polyfit` method.

mean-generalised global `polyfit` method was shown to outperform the planar flattening approach and the other two experiment approaches. Though this method was not susceptible to local deviations, such as row-by-row shifts in trend, the proposed segmentation, those demonstrated by Farley *et al.*, heavily diminished local and other subtle fluctuations. This rendered the priorities of the local fitters less significant. Additional flaws in the local fitters included the necessary use of a traditional low-pass filter, which contradicts the original goal of not compromising image statistics. Plus the shifts in trend do not occur within columns, as they only occur in the direction of the cantilever, a fitting approach that found a general trend in the vertical direction and local trends along each row was briefly considered, but the effectiveness at removing local trends by segmentation demonstrated made it less of a priority. Though the generalised approach was the largest improvement over the planar-flattening approach, replacing it until further notice, there was still a goal of seeking a more versatile background detrender within the coding space.

The next priority was to address new methods of segmentation, based upon the image histogram. On Figure 6.4.7's PDF, the first and third crosses are the found peaks and the second cross is the found trough, all estimated by `find_peaks`. Though this particular image's PDF exhibited a much more prominent trough when using the

mean-generalised `polyfit` background detrender, shown in Figure 6.4.9, some images are inherently more difficult to infer the midpoint from the image statistics, even with optimal pre-processing. Though a broad overlap between the bimodal peaks can suggest overlap between the pixel values associated with the surface and nanoparticle phases, identifying and separating the two Gaussian-like distributions of pixel values by modelling can help provide an accurate height threshold.

At this stage, the aforementioned improvements to the `find_peaks` (FP) algorithm were implemented, as well as integrated into a few new experimental approaches. The first was the deployment of a simple image mask to address the effects of uncharacteristic salt and pepper noise and null lines on segmentation and normalisation. The effects of it on normalisation are addressed in Subsection 6.2.2, but this form of noise would often introduce difficulties during the analysis phase. Relevant features on graphs like the image histogram would appear much smaller when the entire pixel value range is plotted, affecting image histogram binning and curve fitting. A masking function would identify the range of pixel values encapsulating 99.5% of the image data, centred on the mean using standard deviation, then masks all pixel values outside this range to take on the value on the bound of the range it falls outside of. The masked array is then normalised. Figure 6.4.12 shows the identification of pixels outside of this range, showing these pixels are often associated with uncharacteristic image streaking or tall debris. The array is not saved as an image, as the masking method is considered to add uncharacteristic data to the image for algorithmic purposes, a compromise to reduce degradation while performing statistical processes.

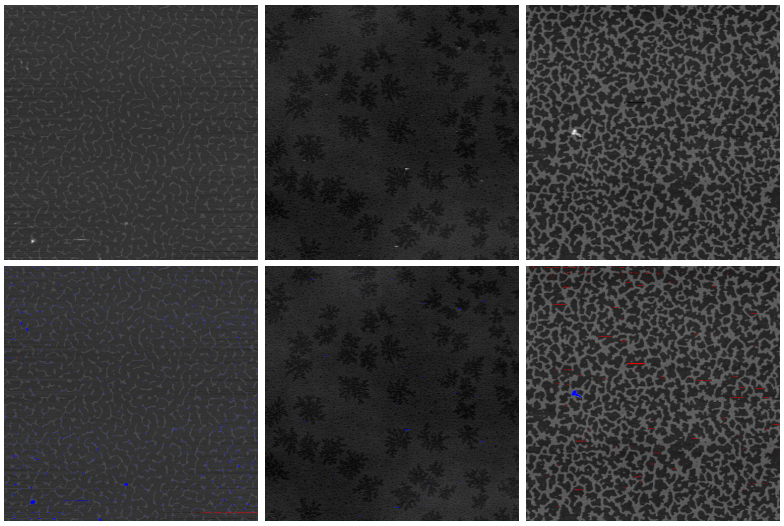

Figure 6.4.12: Three pre-processed AFM images demonstrating the use of the masking algorithm to identify salt and pepper noise. Red pixels were identified as having pixel values below the 99.5% range for the whole image, centred on the mean, while blue pixels were identified as having pixel values above the range.

Further to the goals of this masking approach, truncation of the image histogram was found to be beneficial for biasing fitting algorithms towards the transition between surface and nanoparticle phases. The method to accomplish this became known as

cropping, as the starting and ending indices were defined by an algorithm that effectively cropped the flat regions of the CDF. Cut-off indices for each end of the CDF were calculated using a short function. The function would query in sets of five values along the CDF function, when the variance of the last five values went over a predefined value, the function defined that index as the point at which the CDF was considered no longer effectively flat. The function would run from both ends of the CDF, returning two indices that would define the start and end of where the bimodal peaks appeared in the image histogram, the cut-off indices. This approach to cropping the CDF successfully truncates the image histogram to the statistical region of interest for segmentation.

A new test set was assembled, in collaboration with Farley *et al.*, for testing image segmentation methods. Farley *et al.* curated a test set of pre-processed images that previously interacted poorly with U-Net segmentation[8]. This was expanded to reflect the diversity within the historic data set, featuring images from the previous FN set of a range of dewetting pattern types and correlation lengths.

The two new segmentation methods relied on fitting two Gaussian curves, assumed to fit to the nanoparticle and surface phases, to the image histogram of a provided pre-processed image, then using the intercepts of the individual Gaussian curves as the threshold value. The first script was calling `curve_fit` from `scipy.optimize`, when supplied with a function that defines the sum of two Gaussians with their own unique and unknown coefficients, and the bin centres and frequencies of the image histogram, returns optimised coefficients of the function. The `curve_fit` (CF) algorithm was chosen to use the least-squares approach, similar to that of the planar-flattening and mean-generalised global `polyfit` background detrender, as the optimisation method. This function, as well as individual components, could then be plotted as PDFs for the sake of visual inspection, otherwise, the binary image is saved using the threshold value, defined as where the likelihoods are equal. The index at which the components intercept, where this is true, is calculated by means of finding the index of the minimum value of an array of the modulus of the difference between the two components, bounded between the indices of the peaks. The boundary between the two peaks is chosen to prevent the algorithm from defining effectively flat portions of the component Gaussians as the point of interception.

The second new script used `GaussianMixture` from `sklearn.mixture`. Scikit-learn is a machine learning and statistical modelling library that offers a Gaussian mixture model (GMM) clustering algorithm that can fit the provided image data, as opposed to the image histogram's returned data points, to a provided number of Gaussians, in this case, 2. As with CF, the script fits a mixture model consisting of two Gaussian distributions with unknown parameters. The mixture-of-Gaussians model is fitted using an implementation of the expectation-maximisation (EM) algorithm, an iterative approach to estimating local maximum likelihoods. The individual PDFs and thresh-

old values can be extracted from the returned model using two tests on the model, `test_proba` and `score_samples` return the posterior probabilities and weighted logarithmic probabilities respectively of each component of the model. The threshold value is calculated in the same manner as the CF algorithm, using the peaks as a boundary condition for finding the point at which the likelihoods of each individual PDF are equal, and the binary image is saved.

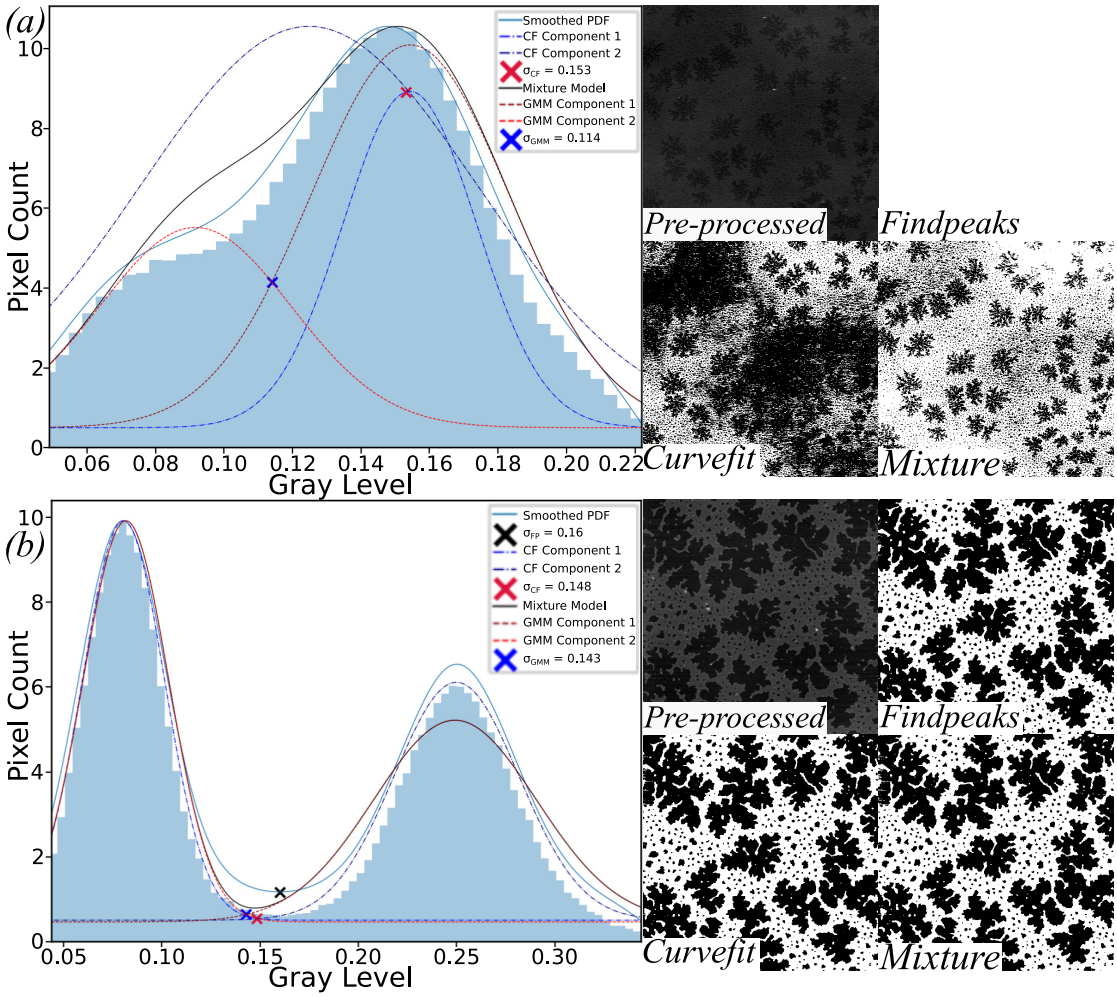

Figure 6.4.13: Plots displaying different approaches to peak-fitting for height-based thresholding over the image histogram with three different methods, and their resulting binary images. Two different AFM images of gold nanoparticles from the test set segmented using 3 different Python scripts.

Figures 6.4.13 and 6.4.14 show the segmentation of four different images in the test set, pre-processed using the median of differences row aligner, and the newly implemented mean-generalised global `polyfit` method for background detrending. Each new curve-fitting method was presented in the same figure overlaid on the image histogram windowed onto the bimodal peaks via the cut-off indices, which was saved locally along with each binary image produced by each proposed segmentation method.

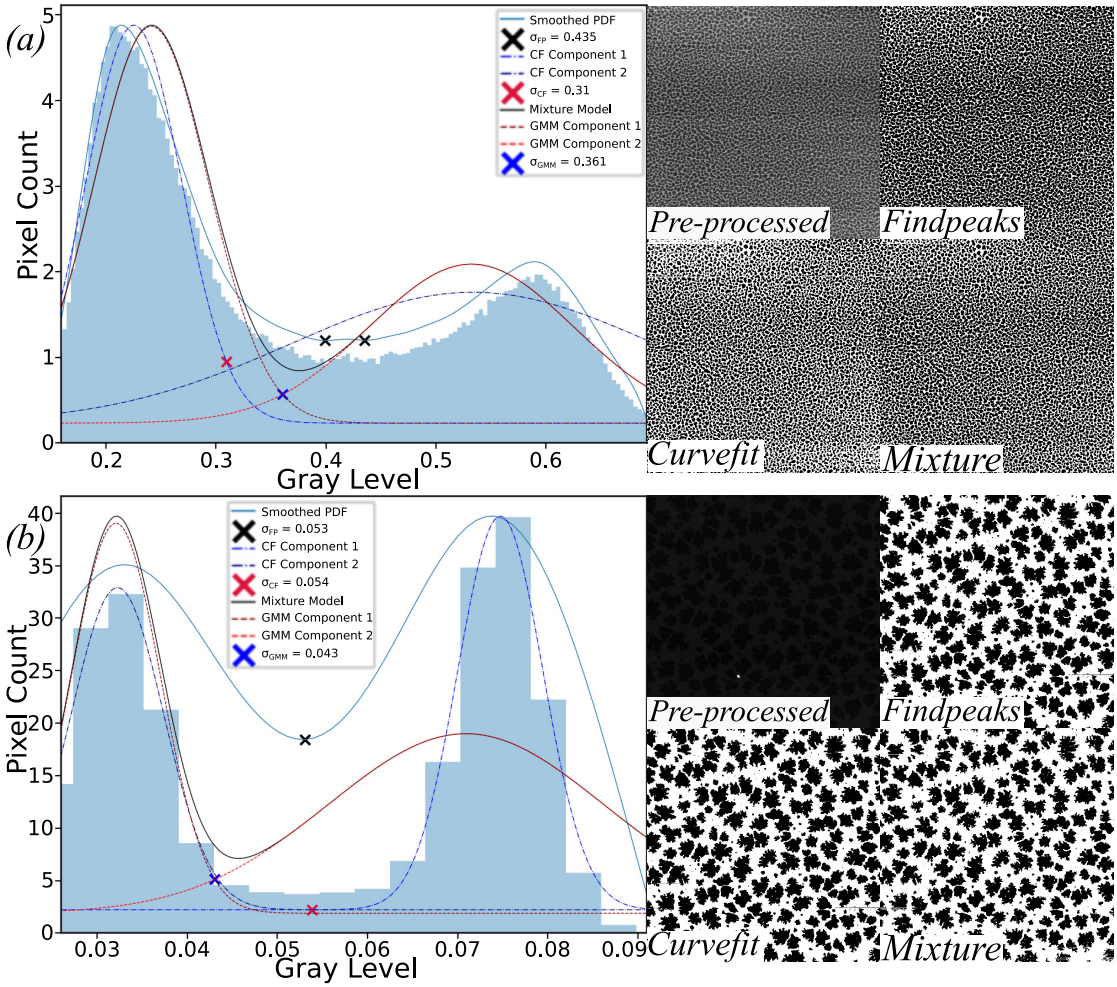

Figure 6.4.14: Further plots displaying 3 different approaches to peak-fitting for height-based thresholding.

The binning of the image histograms was consistent between images. The curves produced by each algorithm are labelled, alongside the coordinate used to determine the threshold value, σ_{FP}, σ_{CF} & σ_{GMM} are the determined threshold value of their respective methods.

6.4.13(a) shows the failure of the trough-finding approach, the appearance of the histogram does not present a trough on the smoothed PDF. translating to there being no turning point in the CDF. The surface phase has substantial physical fluctuations in height that are not detrended by the software, this combined with the intermittent formation of fingering patterns proves a challenging image to segment. The CF method misidentifies the broadening feature, instead considering the first peak the primary peak and the second peak the broadening feature of the image histogram. This may be due to the least-squares approach prioritising the non-Gaussian distribution of the first peak. The GMM method displays the most effective fit compared to the other methods when visually inspected, providing the strongest estimate of the two

bimodal peaks. The GMM peaks do not heavily bias towards fitting to the positions of the modes in the image histogram, as it fits to the data instead of the histogram, and demonstrates the high misclassification rate of the image. The misclassification rate is defined by the area enclosed by the point of intersection of the curves, what is being defined as the threshold value, and the segment curves on the opposite side of this point from their mode, and the x axis, a triangle-like region. These segments of the curve mark the pixel values that are misclassified as part of the other class by segmentation using this threshold value, hence a larger enclosed area means more pixels are considered misclassified. This is strongly related to the parameters of the model, and the appearance of the image histogram.

6.4.13(b) shows a successful segmentation attempt by all methods. This is aided by the clear Gaussian bimodal peaks representing the nanoparticle and surface phases, displayed within the image histogram. The fingering patterns are much larger and visually distinct in this image, present in all rows of the image. The pre-processing appears to be successful, but some minor streaking across the image is visible. CF method has the lowest misclassification rate among the modelling approaches, yet the FP approach provides the best segmentation upon visual inspection. Some of the surface phase in the top left of the binary images segmented by the CF and GMM methods display small white streaks, where segmentation has misclassified the surface as nanoparticles. The GMM method, similar to all other images presented in the figure, does not fit to the height or position of the modes of the Gaussian peaks of the image histogram, or significantly to the spread of the second peak. This is partially due to the model fitting directly to the image data, instead of the binned image data of the image histogram.

6.4.14(a)'s image displays a dense, continuous nanoparticle network, a fairly common image type in the historic data set. The horizontal scar towards the top of the image does not appear to significantly affect segmentation, but FP classifies the scar as surface, while CF and GMM classify it as nanoparticles. The image histogram has significantly more bins, as the pixel values of the bimodal peaks occupy more of the normalised space after masking. FP identifies multiple troughs in the smoothed PDF, due to some fluctuations between the bimodal peaks being misidentified as a third peak, the script takes into account this occurrence and only treats the final index of the FP algorithm for calculation of the threshold value. The GMM and CF approaches assign a Gaussian model to a non-Gaussian second peak, fitting a wide Gaussian and returning weaker, though in this case still adequate, segmentations. Between the binary images, one can observe the nanoparticle network phase coarsening as the assigned threshold value approaches the first peak.

6.4.14(b) has a very low number of bins on the cropped image histogram, bin width was kept constant across all image histograms, and in this case, the histogram was cropped to be between 0.02 and 0.09, despite the image's pixel values being nor-

malised to be between 0 and 1. This appears to work in the favour of both the CF and FP approaches, with both identifying similar and visually-successful threshold values. CF benefits from the low number of bins, as the model fits the coordinates of the bin centres and frequencies in the cropped region. This is due to the peaks in the histogram appearing more Gaussian due to the binning. GMM still provides an effective segmentation, with only a few streaks and scars classified differently to CF and FP.

Multiple lessons were drawn from visual inspection of the returned statistics of segmentation of these four images, and the rest of the test set. The presented modelling approaches to segmentation made multiple assumptions about the data presented. The first assumption was the pixel value data of an image is bimodal. This bimodal demand was not a significant source of issues in the nanostructure images in the test set, but across the whole historic data set there was a potential case of one of the two populations presenting an auxiliary peak that was larger than that of the other phase, such as an image sparsely populated with islands but with large fluctuations in the surface roughness, the model could misidentify the auxiliary peak as the other phase. The second assumption was that all data presented should be part of the fitted model. The algorithms both use an iterative process to fit the model to the data but do not bias towards the regions of high gradient or the turning points across each iteration. Background noise between the two peaks and third layer effects result in the artificial broadening of the PDFs, causing their intersection point and hence threshold value to shift. Lastly, the models assume the two populations take the form of a mixture of two Gaussians. Fitting the PDFs to the population when its associated peak appears non-Gaussian in the image histogram resulted in further artificial broadening and a higher misclassification rate.

The nature of FP makes it difficult to statistically evaluate, as no misclassification rate is returned, though when successful often visually out-performed the binary images of CF and GMM. FP was found to be highly sensitive to the shape of the image histogram, particularly with the addition of the cropping and masking tools. There were still cases of FP not returning a segmented image. This was due to a lack of significant separation between the two populations in select images, resulting in no index for the trough and hence no threshold value.

The GMM method is the most statistically sensitive approach of those tested, considering nearly all 512^2 data points. The test set suggests failures to fit a suitable model when the separation between populations was low, resulting in low confidence thresholding. The `sklearn` implementation of this approach did not meet the necessary standards for nanostructure image segmentation in its current version.

The tested modelling approaches could not confidently fill the role of the segmentation algorithm for mass-processing. Further optimisation such as biasing towards peaks or fitting different distributions could provide a more accurate threshold value, but

all methods tested still had the inherent limits of height-based thresholding with a single value. Adaptive segmentation, assigning pixels to the surface or nanoparticle phase based on a different statistical measure, was proposed and explored on a small scale in Python and R, but segmentation was the primary focus of Farley *et al.*, with proposed advanced segmentation methods. The position of this processing software in the workflow made both optimisation of the two core pre-processing algorithms and adaptation of script for mass-processing the focal point.

6.4.5 Integrating R code functions

The R coding language offers expansive tools for statisticians and data miners, while providing simpler and more efficient routes to image processing methods possible in Python. A plugin within the PyCharm IDE allowed for the running of R code and R markdown scripts, while the `RPy` function allowed for seamless integration of R script into Python script. `RPy` meant image processing available in R code could potentially replace the three image processing modules built in Python, while maintaining the saving, loading, and plotting capability of Python.

A more rigorous application of Otsu's thresholding was performed within R. This begins by considering the bimodal nature of the image histogram, regarding the surface phase as the background (b) and the nanoparticle phase as the foreground (f). Nobuyuki Otsu showed that minimising the within-class variance, σ_W, is the same as maximising the between-class variance, σ_B, in the case of a bimodal image histogram. The maximum separation between each population would correspond to maximised σ_B, and provide the optimal threshold for binarisation. The equation for deriving this is

$$\begin{aligned}
\text{Within Class Variance: } \sigma_W^2 &= W_b\sigma_b + W_f\sigma_f^2 \\
\text{Between Class Variance: } \sigma_B^2 &= \sigma^2 - \sigma_W^2 \\
&= W_b(\mu_b - \mu)^2 + W_f(\mu_f - \mu)^2 \\
&= W_bW_f(\mu_b - \mu_f)^2 \text{ (where } \mu = W_b\mu_b + W_f\mu_f)
\end{aligned}$$

where W_b and W_f are the weightings of the modal peaks of the background and foreground respectively, the ratio of the number of pixels in a population to that of the whole image, and μ_b and μ_f are the mean pixel value of the background and foreground phases respectively. By considering all potential 256 grayscale channel pixel values, the value returning the maximum value of σ_B returns Otsu's threshold[247].

When implemented with the test set used during image segmentation, it was found this application of Otsu's thresholding could replace the graphical approaches developed in Python, though both relied on the same statistics, this version was regarded as more statistically rigorous and outperformed the segmentation methods developed in Python. The algorithm for Otsu's threshold was defined as a function within the R

script, and could be applied to grayscale image data of any size. It was hence proposed as a potential row aligner, as with most row aligners returned a single statistic about a row's pixel data that could be equalised across all rows by a simple offset applied to each row. This was tested within an R markdown to some mild success, but when the test set expanded by use of `RPy`, two issues emerged. It became clear this aligning approach was very susceptible to noise patterns across rows, unlike with a 512 x 512 array, where noise was often mitigated by two large populations, the nanoparticles and surface, for a 512 x 1 array often a noise feature could be misrepresented as one of the populations for the bimodal demand. There was an attempt to mitigate this by using neighbouring rows, so to use a 512 x 3 array, to derive Otsu's threshold, but another more significant issue occurred when attempting to run this algorithm over a loop. The constant communication with R over 512 iterations was causing severe memory leaks in the IDE, there was not a simple solution to this, and hence the testing of usage of R as an aligner tool was discontinued.
R has a library for fitting quadratic spline and orthogonal polynomial-based regression models, with general framework for implementation in a background detrending algorithm. As before, the normalised residuals of the returned fit is the effective detrended image. Both the assignment of maximum knots in the spline and highest order of polynomials within the linear model function control the degrees of freedom in the curve fitting. Degrees of freedom were maintained the same in both the vertical and horizontal directions across the images. The same test set was used to test these two methods alongside two row aligners, the aforementioned Otsu's threshold method and median of differences, for degrees of freedom in a suitable range of 1 to 4, to avoid under and over-fitting. A visual and statistical inspection phase took place for the resulting pre-processed images from the four potential routes.

Figure 6.4.15 shows part of the test set results, with the pre-detrended images at the top. As discussed, the Otsu's threshold-based row aligner was highly susceptible to single high features in all but (c), where no such features were present, where the aligner performed only slightly better than the median of differences approach. The detrending performed by the two R detrending algorithms were visually similar at the same degree in most cases, with misclassification rate, discussed in Subsection 6.4.4, during segmentation being the determining factor in performance. The polynomial-detrended images were returning a lower misclassification rate, and unlike spline-detrended images were not visually over-fitting for degrees of freedom below 4.

Figure 6.4.15(d) shows a non-nanostructure AFM image from within the historic data set, of two metallic contacts placed as macroscopic markers upon the clean silicon surface. Though the image was part of the test set yet not part of the final pre-processed data set, consideration of the algorithms' effect on large isolated features was a short study into the versatility of the tools and a clear visual example over-fitting. In the first and third columns of (d), the effects of median of differences alignment followed by spline and polynomial detrending respectively, display a clear introduction of wave-

like features in the region between the two contacts. This is particularly visible in the spline-based detrending of the maximum degrees of freedom tested. The curve fitting algorithm has prioritised describing the edge of the contacts, known to be 24 nm high with a 10 nm ridge, and the local dark halo caused by a tip event. For detrended images from all degrees of fitting, pixels on the top of the contact were found to have lower intensity than those on the surface, resulting in a highly uncharacteristic binary image during height-based segmentation, of a seemingly simple image. This highlights the necessity for a continuous nanostructure and multi-population presence, both structures and the surface, across the whole image.

Another prospective image segmentation in R was tested, the use of `flexmix` to derive a mixture regression model that described the surface and nanoparticle phases. FlexMix provides a general framework for assigning finite unweighted data points to a finite number of clusters[248,249]. An image of two clusters, defining the surface phase and nanoparticle phase, could be used to return a binary image. This method uses an iterative approach, first assigning the data points, each being the xy coordinates and intensity of each pixel, to the number of classes provided to a first approximation, then using an expectation-maximisation (EM) algorithm, class assignments are repeated until a pre-defined likeliness threshold is met. The EM approach allows for an adaptive segmentation approach, sensitive to local fluctuations in intensity, described by Figure 6.4.16. FlexMix considers the local most likely pixel members of each phase, as if locally calculating the image histogram, and uses that to help assign other neighbouring pixels. The adaptive segmentation approach using `flexmix` under-performed compared to the single-value thresholding approach of Otsu's thresholding within R. The spatial sensitivity of the adaptive segmentation would often cause fitting to large noise features, resulting in regions of binary images having uncharacteristic white regions where no nanoparticles were present. The algorithm would also often take 50-300 iterations to converge, or fail to converge at all, returning no binary image. This added significant computing time and a fail rate higher than that of the FP method. Convergence could be reached on individual images within the test set by altering the algorithm's parameters for each image, but the goals of mass-processing made this impractical. Although theoretically, this algorithm provides the desired flexibility, experimentation shows it does not meet the standards or consistency required for mass-processing nanoparticle images yet. Improvements to `flexmix`'s code could make it an effective tool in the future.

The appeal of R was the ease of integration within the Python IDE. R code uses different indexing, packages and syntax to Python, meaning interpreting commands from both Python and R in the same script requires the use of additional tools. The `RPy` function allowed the execution of R code in Python in the form of string packets forwarded to a concurrent instance of an R console, that compiled the string and returned data to the Python console. The resulting image arrays were parsed to the rest of the script, similar to any other modular image processing tool previously developed in

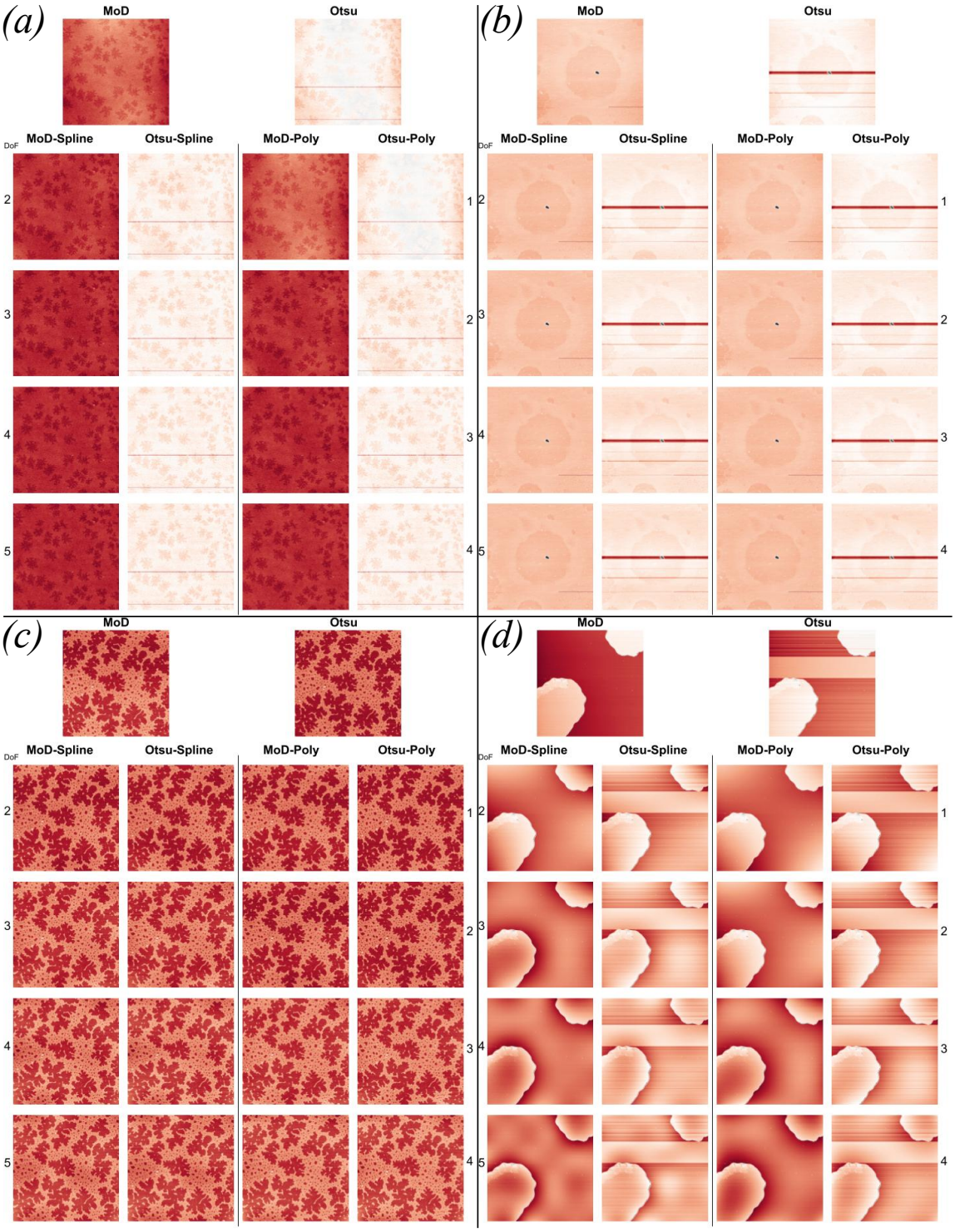

Figure 6.4.15: Results of median of differences (MoD) and Otsu's threshold-based row alignment, top row of two images, followed by subsequent spline and polynomial detrending for different degrees of freedom within R for four different AFM images in the test set.

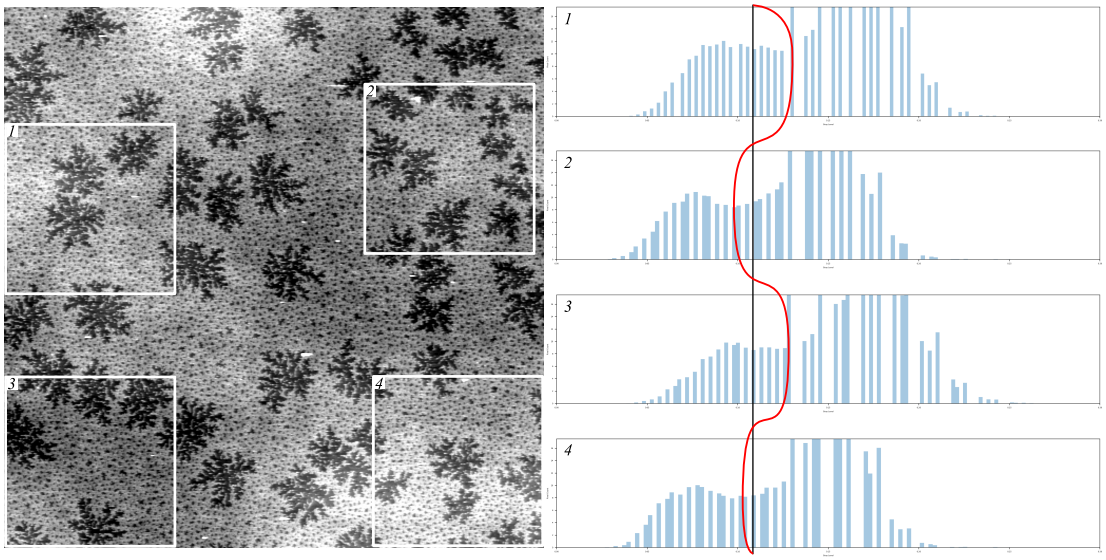

Figure 6.4.16: Image histograms of four different regions on a surface, the straight black line shows the threshold value calculated by height-based threshold, while the curved red line shows the adaptive segmentation approach of `flexmix`.

Python. Remote execution has been shown to have some limitations, such as memory leaks with more strenuous usage such as with the proposed Otsu's aligner, otherwise, the potential image processing tools within R could be considered as readily available as the tools in Python.

After visual and statistical inspection of all images in the test set detrended within R, the polynomial background detrender with two degrees of freedom in both the x and y directions was settled upon as the optimal parameters for the image of nanostructures of the most interest. Similar to other detrending algorithms, over-fitting to large regions of uninterrupted surface or nanoparticle phase on nanostructure images is still a common occurrence. This method could still replace the current background detrending approach in the finalised pre-processing script. Despite its strong statistical basis, the current version of `flexmix` was not considered alongside the segmentation methods proposed by Farley *et al.* The tool is not suited for a data set of images with such high diversity in noise features and nanoparticle feature lengths.

6.4.6 Pre-processing data queries

With the processing algorithms in their final states, a final feature was written that allowed for direct user requests of specific images via a CSV of file names. This was motivated by the work of Farley *et al.*, who, using nanoparticle images from the historic data set pre-processed using Gwyddion, had recorded visual descriptions, including the original file name, nanoparticle pattern category and noise features, in a spreadsheet with the purpose of testing segmentation methods. It was proposed that all images described in the spreadsheet be pre-processed by the Python script.

The data querying algorithm used a dataframe manipulation library, `pandas`, to parse the spreadsheet in Python, which first saved the column of file names to an array of strings. Over a loop, each file name string in term was, using the `os` module which could search all directories and subdirectories, searched for within an external storage device which contained the historic data, returning the full path of all IBW files that matched the file name. Similar to the directory screening code, each match is pre-processed, row-aligned by median of differences and background detrended by a polynomial fit, and the resulting images were saved as PNGs in a designated folder.

6.5 Summary

The resulting script adapted for usage with the historic data set is attached in Appendix C and described by the flowchart in Figure 6.5.1. A folder of pre-processed images based on requested file names in the historic data set was forwarded to Farley *et al.* and Gordon *et al.* for use in published work[8,9]. Farley *et al.* provided a spreadsheet of requested AFM images of known pattern types with visual descriptions, the raw AFM file name column of the sheet was used to query the external storage device which contained all the historic data, with any found files being pre-processed and saved to a secondary external storage device as generic image files. Farley *et al.* segmented the resulting images via a U-Net[8], followed by Gordon *et al.*'s post-processing script[9] to further denoise the now binary images. The images, now indistinguishable from those produced by Monte Carlo methods, were incorporated in Gordon *et al.*'s test set for a convolutional neural network, previously trained on simulated data provided by the Rabani *et al.* model.[9]

Some resulting images from that over 1000 image set are shown in Figure 6.5.2. The chosen row aligner and background detrender were the optimal choices from among those tested, the median of differences row aligner developed in Python, and the polynomial background detrender developed in R. Though there are still cases of pre-processed images that presented both inherent noise, the combination minimised the misclassification rate, defined by each image histogram, to a satisfactory degree across all images. This meant segmentation methods chosen by the groups in receipt were highly effective at distinguishing the surface and nanoparticle phases with minimal information loss. Some tip event-induced noise, be it partially or across the entire slow scan direction, would require denoising on an individual image basis. Tackling individualised image noise is beyond the scope of mass processing, and the introduction of minor corruption into the machine learning is negligible.

Nanostructure images can have a majority of their noise removed by two statistical steps, that are both modular in nature. Each method tested for both steps had its own individual merits, and could supplant the final ones chosen for the nanoparticle image historic data set when using other nanostructure images, providing the ability

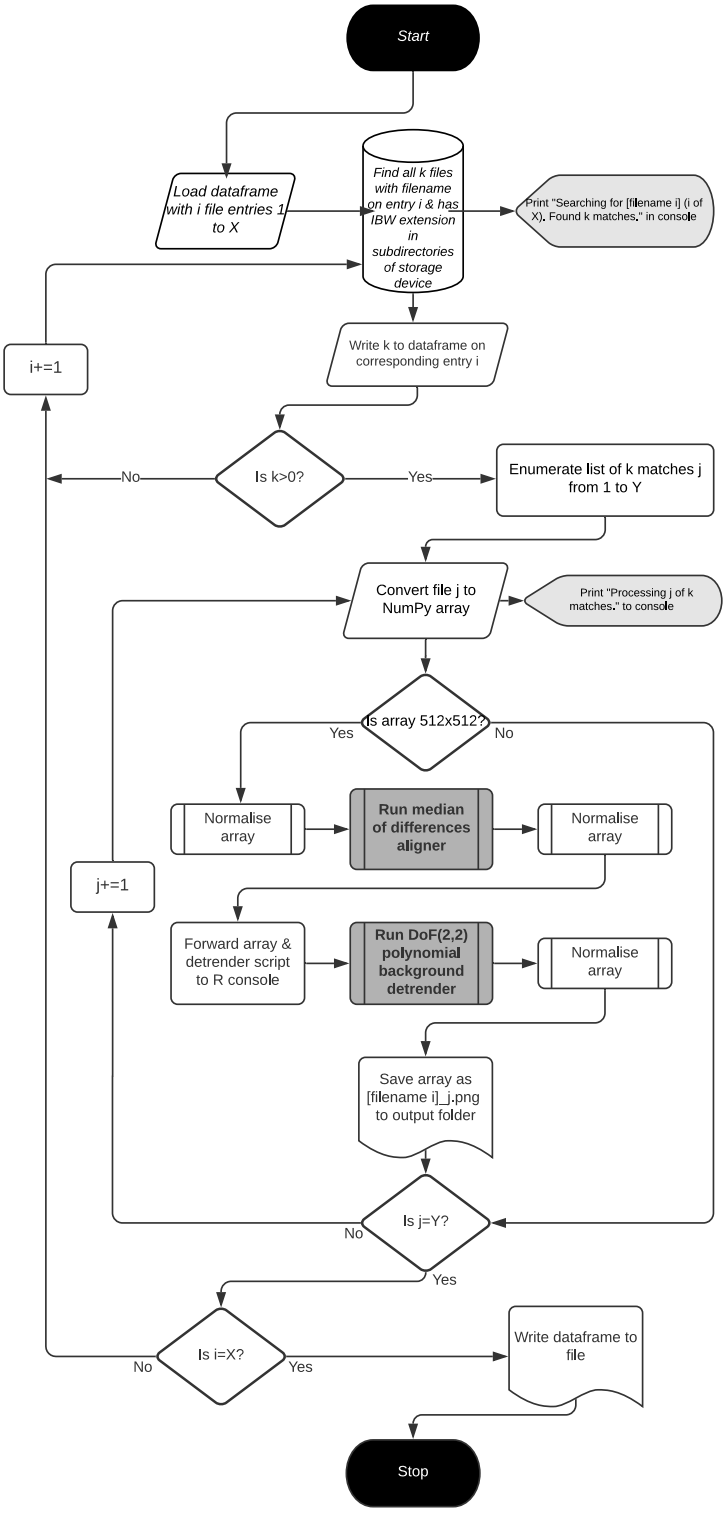

Figure 6.5.1: Flowchart showing framework of image mass pre-processing code used for data queries involving the historic data set of gold nanoparticle AFM images.

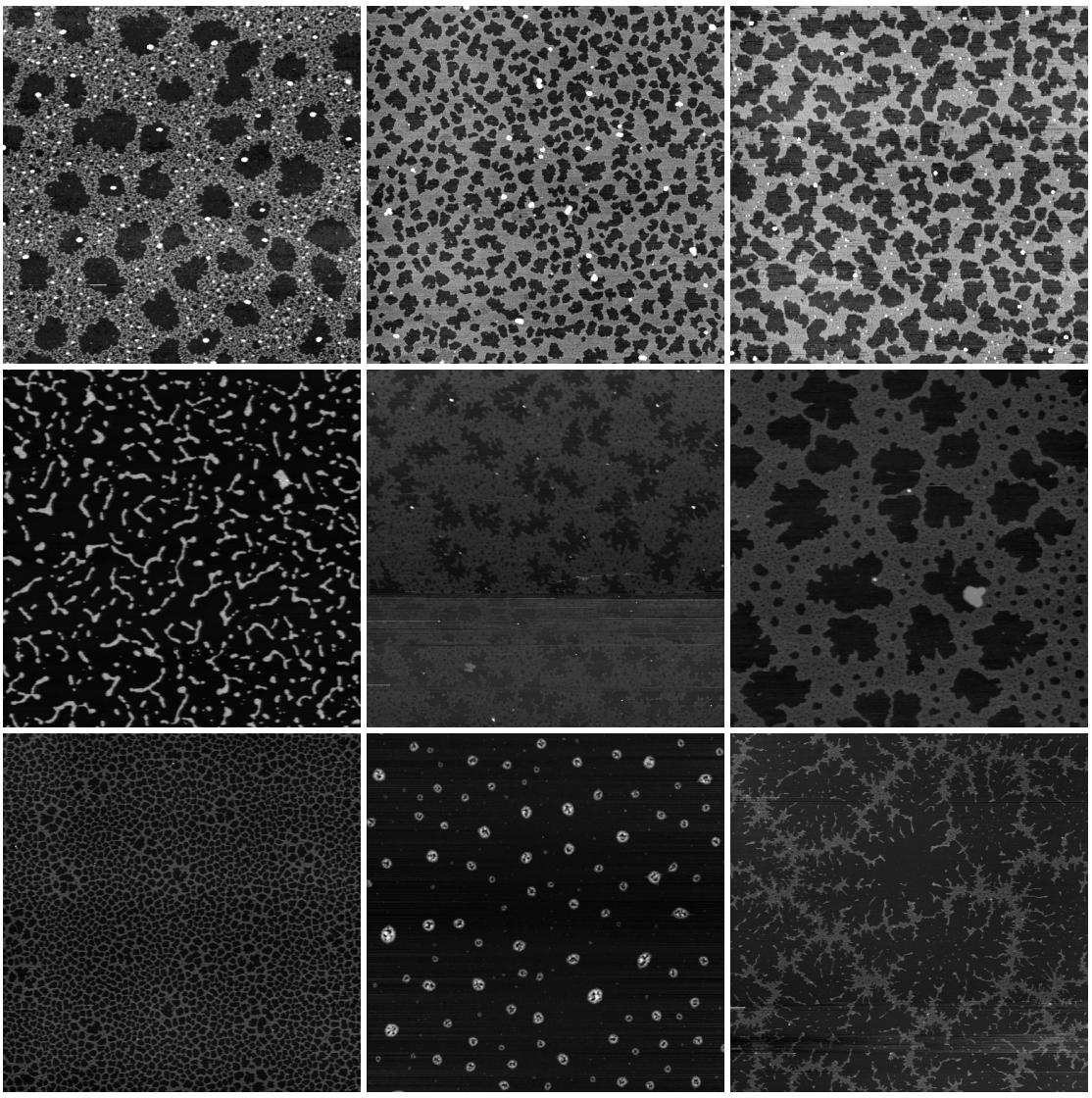

Figure 6.5.2: Images pre-processed by the finalised code in Figure 6.5.1.

to adapt to the data set provided. The screening tools detect corruption common enough amongst SPM for use across all AFM images. Similarly, the background detrenders all had multiple parameters provided by the user, such as degrees of freedom or EM threshold, all further lending to the flexibility of the tools for implementation of mass-processing other data sets of nanostructure images.

The adaptation to multi-population images quickly led to their necessity. The code was much more effective at pre-processing images with non-periodic nanostructures with sub-monolayer coverage across all rows. Large nanostructures with flat regions that occupied more than 10% of the image would frequently be over-fitted by polynomial-based detrenders, while overwhelming majority row coverage of either the surface or nanoparticle phase could result in major discontinuities produced by the single-statistic

row aligners. While median of differences row alignment was shown to minimise the frequency of induced row-by-row discontinuities, this was the major compromise for producing image pre-processing software that was sensitive to nanostructures while not compromising image statistics.

There were some avenues left unexplored. Multiple images in the historic data set exhibited third layer effects, with all images both pre-processed and containing a third layer noted within the dataframe. Segmentation to isolate the third layer of all was relatively simple and consistent using Otsu's threshold, followed by a morphological opening operation to split some observed clusters. The third layer could then be regarded as particles, and could be used for point particle modelling and analysis. The FFT solving tools developed in Subsection 3.3.5 could be deployed on processed nanoparticle images.

A large historic data set of seven years' worth of raw nanoparticle AFM images was data-mined over ten years later. Images were utilised in modern machine learning analysis by mass-processing software tailored towards the data presented, all while developing and evaluating multiple pre-processing tools for the versatile treatment of other data sets of nanostructure images. Visually-simple images presented complex statistics, leading to a broad exploration of image processing and data science techniques across multiple programming languages.

7 Depositions of Photoactive Molecular Dyads

An inevitable and exciting part of nanoscience is being the first to study and report on new materials through the unique lenses provided by the field. The new organic material, in this case, was synthesised, purified and characterised entirely within the Champness Group at the University of Birmingham. Molecular dyads formed of naphthalene diimide (NDI) and phenothiazine (PTZ) were investigated due to their capacity for mimicking photosynthetic solar energy transduction, leading to the consideration of further study within the Nottingham Nanoscience Group and Nanoscale and Microscale Research Centre. Systematic study of the dyads focusing on concentration, deposition techniques, substrate and sample preparation formed the basis of newer research. Scanning probe experiments, conducted and proposed, involving the material provided a short project, acting as a learning tool for surface preparation and experimental design under ambient conditions. The lessons play a major role in future dewetting experiments, particularly in terms of solvent behaviour at the microscale.

7.1 Background

Research into artificial photosynthesis aims to recreate the biological process for converting solar radiation into store-able energy at high efficiency and low cost through synthetic means. Products of photocatalytic water and carbon dioxide splitting act as fuel, allowing for the chemical storage of solar energy. Photoelectrochemical cells (PECs) based on semiconductors (most notably TiO_2) contain modules for light harvesting, water oxidation and proton reduction, all necessary for creating these fuels, hence mimicking natural photosynthesis. Photovoltaic cells (PVs) take a similar role, instead converting solar energy directly to electrical energy as opposed to chemical energy in fuel.[250–253]

Molecular dyads are consistently suggested as a future role player within both these cells[250,254,255]. Photoinduced electron transfer (PET) across a covalently linked electron donor-acceptor complex is of great interest for applications in artificial photosynthesis. Chromophore-catalyst dyad molecules anchored onto semiconductor surfaces take the role of a photo-anode within a PEC while donor-acceptor dyads replace the role of bulk heterojunctions (BHJ) within PVs[251,256]. Donor-acceptor dyad molecules circumvent the physical fine-tuning of complex BHJ interactions in PVs, allowing this fine-tuning to occur more meticulously on the synthesis side[257]. Designing dyad molecules for these roles means experimentation with the donor-bridge-acceptor systems (DBAs), various studies have been conducted with a focus on each component within this system.[258–260]

The work by Pearce *et al.*[261] on dyads constituent of naphthalene diimide (NDI) and phenothiazine (PTZ) bridged by a phenyl spacer[262] within the domestic School of Chemistry acts as a precursor to this project. Polycyclic aromatic hydrocarbon diimide

derivatives as an electron acceptor and phenothiazine as an electron donor are not new concepts, but little previous study into the dyad exists. NDI was chosen due to previous success changing its redox properties through thionation, while PTZ is a well-studied donor in analogous systems investigating PET[258–260,263]. The in-depth electrochemical characterisation of the dyad and its thionated derivatives in the study demonstrate observable variations in parameters important for applications within artificial photosynthesis. The acceptor moiety offers a systematic approach to tuning the DBA through thionation with Lawesson's reagent, shown in Figure 7.2.1. It was shown increasing degrees of thionation of the NDI moiety reduced the HOMO-LUMO energy gap. A decrease in energy gap size has been shown to affect the light harvesting capacity of the dyads and increase the output voltage within PVs utilising dyad molecules[257]. This previous study of naphthalene diimide phenyl-phenothiazine dyads (NDP) offers a foundation for conceptualised scanning probe measurements during this project.

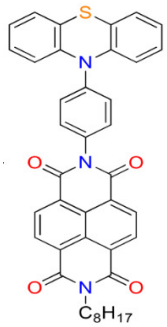

Figure 7.1.1: Chemical structure of naphthalene diimide phenyl-phenothiazine, referred to as NDP or $NDIS_0$-PTZ throughout the literature.

The bridge between the donor and acceptor moieties has been shown to significantly affect the charge transfer time. Chosen donor and acceptor moieties also have an effect due to their impact on crystal packing, for example, the alkyl chain on NDI in NDP affects the dyad's planarity and hence photovoltaic performance. Electron transfer time has been studied using a combination of nano and picosecond region transient absorption spectroscopy and time resolved and steady state fluorescence spectroscopy on dyads using various bridges. The phenyl spacer within NDP lies on a plane perpendicular to the rest of the dyad molecule, affecting charge transfer properties twofold.[251,258,264]

Fluorescence and other spectra in the referenced material were commonly recorded from solution. The project's goal, however, is measurements *in situ* on a substrate alongside SPM. Collecting superimposed light spectra consisting of spectra for each NDP species with varying degrees of thionation is possible, though SPM could measure light emission from single dyad molecules or speculatively individual bonds[261,265]. Studies into tip-induced luminescence, electroluminescence, from single molecules re-

ported LED-like behaviour governed by a voltage drop between the molecule and substrate. In these cases, STM tip-molecule junctions induce light emission when the voltage drop at the junction exceeds the voltage drop between the molecule and substrate, allowing scanning tunnelling microscopy light emission (STM-LE) spectra to be recorded[266,267]. Recent atomic force microscopy advancements allow for potential viewing of molecular orbitals and variations in charge density under ultra high vacuum conditions. This could be compared to density functional theory calculations previously taken of NDP, adapted for substrate-deposited NDP or light-stimulated NDP.[261,268,269]

Experimental design of the systematic study of NDP upon surfaces was highly influenced by concurrent investigations of the influence of the substrate on the fluorescence of adsorbed organic molecules[265,270,271]. PTCDI, PTCDA, TCPP and free-base phthalocyanine upon hexagonal boron nitride (hBN) were studied and offered a potential source of analogies to NDP. The works concluded with hypothesised resonant and non-resonant effects[272–275] on the spectra, commonly red-shifted[270], predicted and calculated by time-dependent modelling. A non-resonant interaction induces a direct shift in molecular energy levels due to substrate adsorption[270,271]. This includes by a change in molecular conformation, the case of the investigation of TCPP by Korolkov *et al.*[265] arising by van der Waals interactions, through the presence of permanent dipoles or other mechanisms. Fluorescence spectra and time-dependent modelling upon PTCDA-hBN showed the presence of dielectric hBN substrate leads to reduction of the HOMO-LUMO gap and weakening of the electron-hole interaction[271]. Compared to a PTCDA molecule in a gas phase, these red-shifting sources are independent of shifts due to the presence of a permanent dipole, attributed to PTCDA's high symmetry and planar appearance, and negligible distortion upon the substrate.[271]

Red-shifts in monolayer coverage of these molecules do not discount the resonant and non-resonant effects induced by neighbouring molecules, informed primarily by SPM images. The works place a significant emphasis on monolayer coverage and often the periodic appearance of the organic molecules upon the surface. The systematic increase in red-shift was strongly correlated to the refractive index of the surface, while neighbouring molecules' contribution to the increase was much less, typically by an order of magnitude.

These findings informed the early experimental design of systematic study with NDP. The chromatic shifts observed in preceding work[265,270,271] were highly dependent on substrate, leading to considerations of all readily available substrates for deposition. SiO_2/Si(100), SiO_2/Si(111), hBN/Si, HOPG, gold on mica, and black phosphorus were all considered. Still, silicon and exfoliated hBN upon silicon were the most suitable, due to ease of spin-casting and visibility upon them.

Significant demand is placed on sub-monolayer coverage for both fluorescence measurements and proposed tip-molecule interactions. The majority of experiments focused

on preparing samples of different deposition techniques, substrates, solvents and concentrations, with the goal of sub-monolayer of NDP upon the substrate. This came with some challenges in ambient conditions, first, it was unwise to consider NDP as a 2D molecule while considering its morphology as an adsorbate. The deposited appearance of perylene derivatives PTCDI and PTCDA does not help deduce this, due to the arrangement of NDP in 3D space. Unlike naphthalene diimide (NDI) or perylene diimide (PDI), the PTZ moiety modifies the hypothetical crystal packing in multiple ways, demonstrated theoretically in Figure 7.1.2. Figure 7.1.2(a) and (b) shows NDP's molecular structure before, when loaded from ChemDraw, and after a molecular mechanics-based geometry optimisation script was run upon NDP in gas phase. The script, run in Avogadro, utilised a universal force field at 300K. Consideration of local forces causes the phenyl spacer to become perpendicular and PTZ to buckle due to the presence of sulphur. This results in lower affinity for π-π stacking among neighbouring molecules compared to the discussed perylene derivatives. Combined with the reduction in symmetry, the result is slipped stacking of molecules, with PTZ positioned adjacent to neighbouring NDI, asserted by previous single crystal x-ray diffraction results[261] shown in Figure 7.1.2(c).

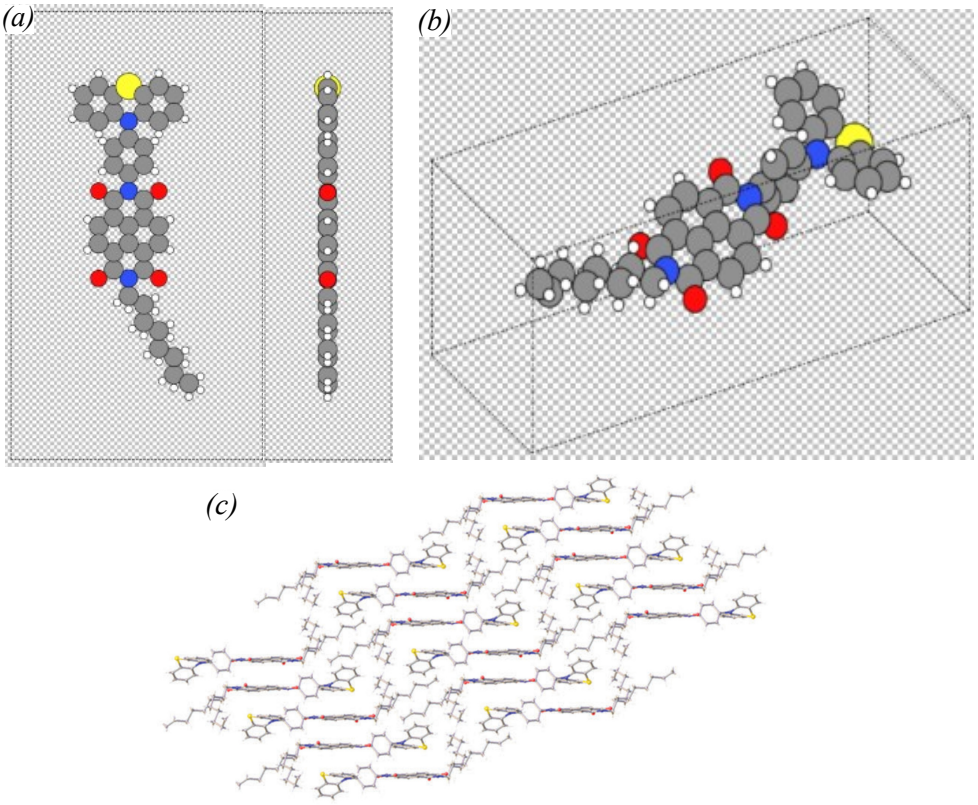

Figure 7.1.2: Informed predictions of NDP bulk crystal arrangement. **(a)** 2D arrangement NDP displayed in Atomic Simulations Environment (ASE) in Python from two different angles. **(b)** Predicted 3D arrangement of NDP in ASE after a 3D geometry optimisation script in Avogadro. **(c)** Predicted packing arrangement attained from single crystal x-ray diffraction data by Pearce *et al.*[261].

7.2 Synthesis and sample preparation

One of the project's initial goals was to acquire familiarity with the synthesis, purification and characterisation of NDP in the domestic School of Chemistry. This would involve synthesis of the molecular dyad starting from its constituent moieties, and purifying the resulting crude reaction mixture to acquire the solid non-thionated product. This was done while consistently characterising the products at different stages, by a combination of thin-layer chromatography (TLC), nuclear magnetic resonance (NMR) spectroscopy, time of flight mass spectrometry (ToFMS) and visual inspection, and comparing the results to that of pure or hypothetical product.

NDP is a 1:1 dyad synthesisable from 2 reagents that form its moieties and phenyl spacer. The dashed box in Figure 7.2.1 encloses the reaction required for synthesis. Naphthalene monoimide (NMI) and 4-aminophenyl-phenothiazine (Ph-PTZ) are made to covalently bond by substitution, giving water as a byproduct. The conditions for this reaction were met using a low pressure line fed to a multi-neck flask inside a conductive heat sheath rested on a magnetic heat plate. The weighed dry reagents, NMI, an excess of Ph-PTZ, and imidazole were heated to 130 °C with a target pressure set to 2.2 mbar for 8 hours. The resulting crude reaction mixture was washed out of the flask within an ultrasonic bath using a combination of chloroform and hydrochloric acid.

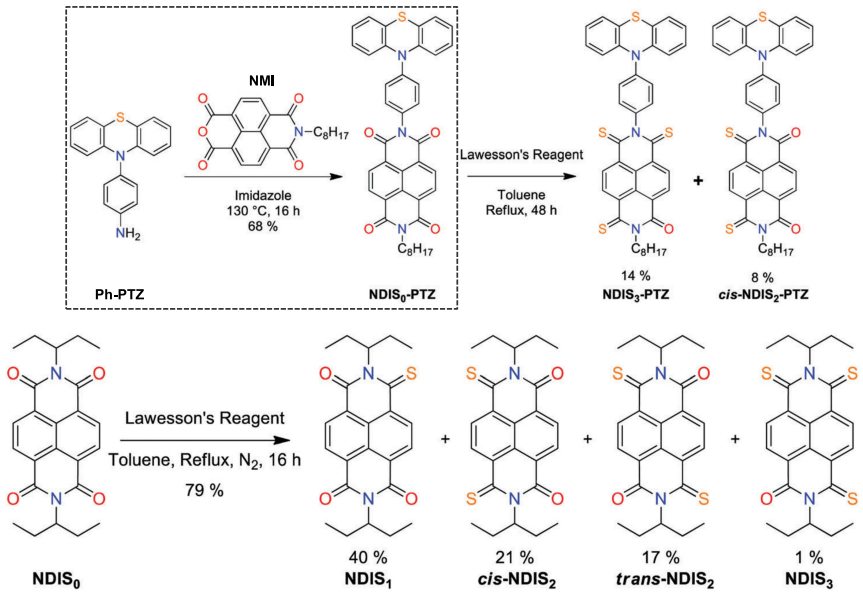

Figure 7.2.1: Chemical reactions for formation of NDP (labelled $NDIS_0$-PTZ here) and its thionated derivatives.

The crude reaction mixture is made to settle within a separator funnel. The mixture separates into a majority-product section at the bottom and a majority-solvent section at the top. The bottom part is collected in a beaker, and the rest is disposed of. This process continues multiple times to separate more solvent from the solid mixture,

including washes of water, and brine, and then finally magnesium sulphate is added as a desiccant to remove the water. The resulting hydrated solid magnesium sulphate is filtered out using filter paper and the reaction mixture is carried forward, taking some aside for characterisation.

Thin-layer chromatography (TLC) in acetone of both the reaction mixture and pure product dissolved in chloroform reveals the reaction mixture contains the pure product and some impurities. These impurities are expected to be imidazole, unreacted reagents and $(NMI)_2$. The impure mixture was also characterised using MALDI time of flight mass spectrometry (ToFMS), using DCTB as the matrix. Figure 7.2.2(a) displays a high intensity negative ion peak, and smaller peaks for low abundance carbon isotopes, centred on the molecular mass of NDP confirm its presence in the mixture. The molecular mass (M_r) embedded is slightly off due to lack of calibration.

Excess solvent was removed using a rotary evaporator, and the resulting impure solid was dissolved in clean chloroform. The impurities were then removed using a chromatography column. The solution splits into bands through the silica-chloroform solution, and the solution collected from each band as it reaches the valve on the column was tested with TLC against the pure product. The band with the TLC comparable to the pure product was put through the rotary evaporator to acquire the pure product.

Once again, the product was characterised; first by eye, as the solid is expected to be a blue powder and colourless in solution, and secondly using nuclear magnetic resonance (NMR) spectra from solution. The NMR spectrum can be compared to a simulated spectrum generated from NDP's chemical structure and hence, proton locations on the dyad. The structure was successfully verified using proton NMR, compared to the estimated chemical shifts in ChemDraw, the spectra are shown in 7.2.2(b).

Depositions in ambient conditions were all performed on a wafer from a precut sheet of Si(100) with a pregrown native 90 nm thick SiO_2 layer, where individual tiles were cut to 10 mm x 10 mm x 400 µm. The cut silicon wafers were solvent cleaned using the standard method from Subsection 2.5.2. Hexagonal boron nitride (hBN) was deposited onto a small portion of a similarly prepared Si(111) wafer, with a 4 - 25 4-25 µm thick SiO_2 layer, using the exfoliation method described in Subsection 2.5.3.

All NDP was deposited from solution onto the silicon wafer in two ways, with results compared. The solution for both was prepared by dissolving weighed NDP in toluene. Toluene is a non-polar solvent volatile enough to dewet from the silicon at room temperature. NDP-toluene solutions formed a colourless solution that remained stable at room temperature for three months, by which time, visible insoluble blue crystals had aggregated and no longer dissolved in solution. Concentrations in the range of 0.7 g/l to 4.6 g/l were tested. The minimum of the range reflects the lowest concentration at which deposited crystals were visible with the MFP-3D camera, while the maximum

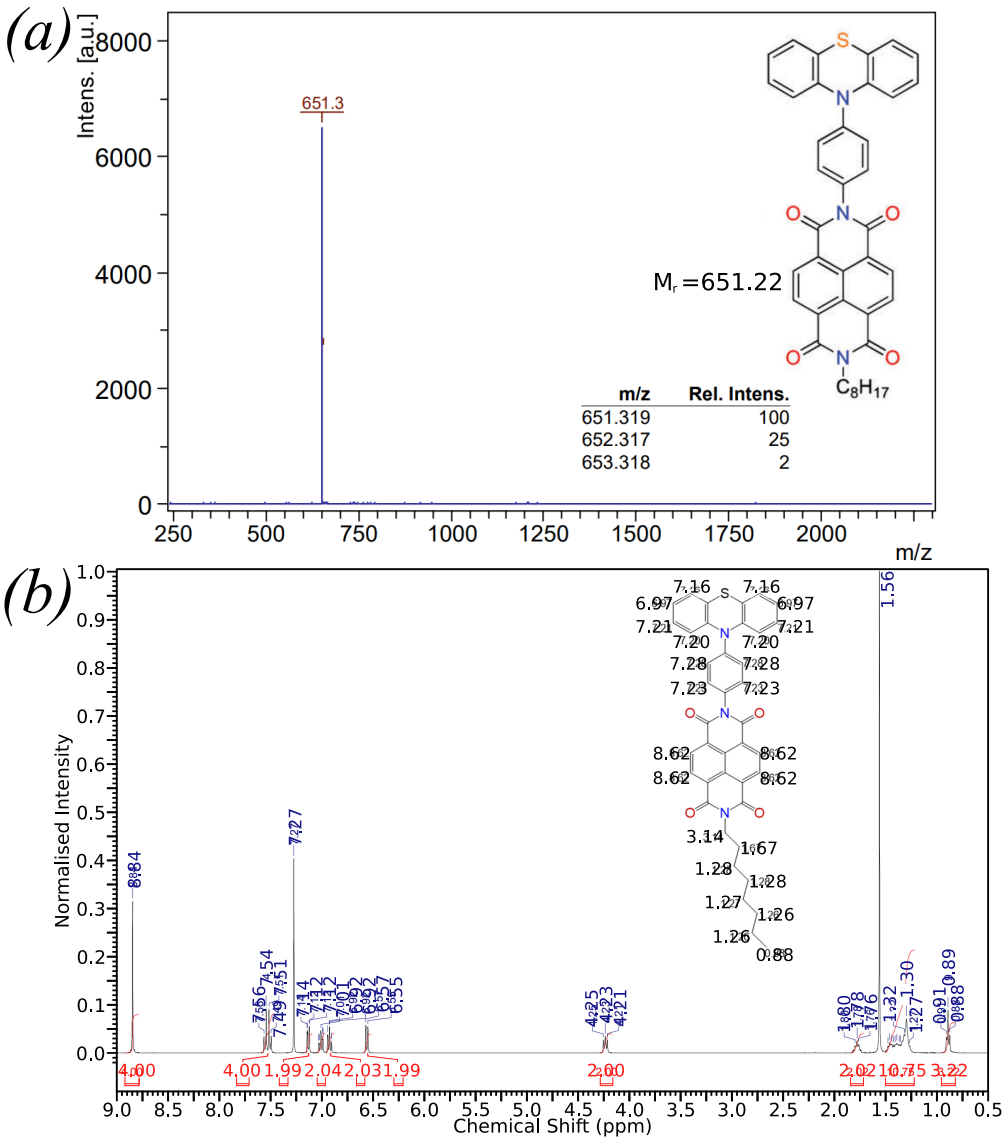

Figure 7.2.2: Characterisation spectra produced during the synthesis of NDP. **(a)** MALDI time of flight mass spectrum of negative ions within an NDP crude reaction mixture in chloroform using a DCTB matrix, with a relative intensity peak table embedded. **(b)** Proton nuclear magnetic resonance spectrum of purified NDP in chloroform, with the predicted chemical shifts of protons calculated in ChemDraw embedded.

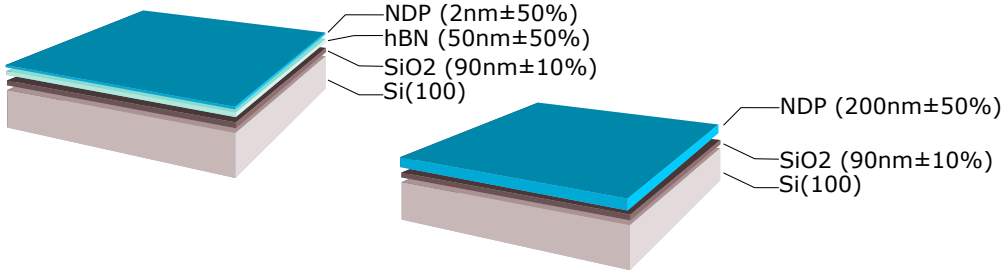

Figure 7.2.3: 3D surface arrangements of NDP samples prepared for AFM, including observed layer heights.

concentration in the range marks the point of saturation.

The first, and in theory, most simple approach to deposition was a dip coating method. The individual cut wafers were dipped perpendicularly, held by tweezers into the solution, then removed and held flat to let the toluene leave the surface. The immersion times were between 10 and 100 seconds, with a withdrawal time for all wafers of half a second. This was conducted for all concentrations of NDP-toluene solution in the aforementioned range, after which the surface was optimally immediately probed with an optical microscope and AFM. Figures 7.3.1(a-c) and 7.3.3(a-b) all utilised this approach.

Demand for thin films without visible drying lines introduced the use of a spin-coater. NDP-toluene solution was pipetted onto vacuum-held, clean, 1 x 1 cm^2 wafers of silicon or hBN-layered silicon until the meniscus entirely filled the surface, then spun up to 2.5 krpm at 1 krpm/s with a 10 second dwell time. The resulting surface was optimally immediately probed with an optical microscope and AFM.

Early stages of systematic study of solution-deposited NDP on silicon wafers placed significant emphasis on preventative measures for impurity-induced aggregation. AFM scan sizes for the initial sample were often of the order of 10s of microns, with aggregated NDP deposits measuring as high as 300 nm. Discrete profiling of NDP aggregates in this configuration also meant the tip was inherently highly susceptible to surface debris. The growth of high-quality thin films without contaminants meant changes to sample preparation. This included changing the solvent from ACS to HPLC-grade toluene, and changes to the cleaning method. While the solvent cleaning method from Subsection 2.5.2 became standard procedure for newly cut wafers, subsequent plasma cleaning was also added to the workflow for non-hBN-layered silicon. Plasma removes all traces of organic matter while leaving no residue. The cut, solvent-cleaned wafers are etched in 25/75% oxygen/argon plasma in a plasma oven at vacuum pressure for 15 minutes. NDP in HPLC-grade toluene was then accordingly deposited with different methods and different concentrations onto each plasma-cleaned wafer.

The prepared samples could generally be described as those in Figure 7.2.3. All AFM measurements were taken with the Asylum Research MFP-3D system.

7.3 NDP on SiO_2/Si(100) and hBN/Si(111)

Figure 7.3.1 shows the various morphologies among tested deposition methods and concentrations upon native oxide-terminated silicon. Despite significant diversity among these AFM images, there is some observable conformity. The deposited NDP takes on two simultaneous phases, relatively large ribbon-like nanocrystals that self-assemble and aggregate upon the surface, and uniform thickness monolayers that are grain-like towards the edges, with holes throughout, and have no clear overlapping grains.

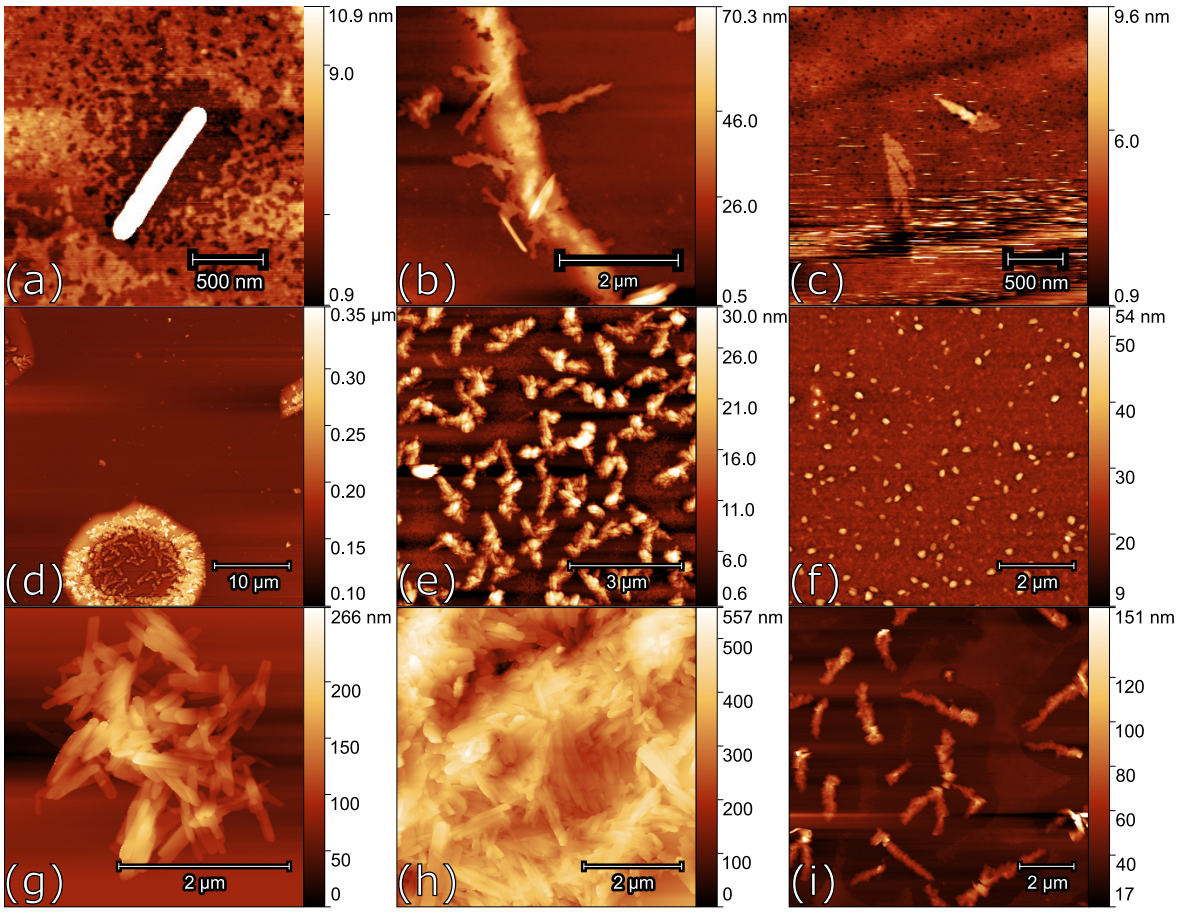

Figure 7.3.1: Tapping mode AFM images of naphthalene diimide phenyl-phenothiazine deposited from toluene solution on 1 x 1 cm^2 SiO_2/Si(100). **(a)** 100s dip-coat in 0.73 g/l; **(b)** 10s dip-coat in 4.63 g/l; **(c)** 70s dip-coat in 0.73 g/l; **(d)** 1.97 g/l spin-cast; **(e)** 1.50 g/l spin-cast; **(f)** 4.60 g/l spin-cast; **(g)** 15 hour submersion in 0.87 g/l; **(h)** 15 hour submersion in 1.50 g/l; **(i)** 1.97 g/l spin-cast.

Grains provided up to 98% monolayer coverage, of highly uniform thickness 3.0±0.2 nm. There were often holes in the monolayer, like those in (c), derived from the limited intrinsic degrees of freedom caused by the shape of the nanocrystalline grains. The monolayer phase was often disrupted by a denuded perimeter around the ribbon phase aggregates, visible in (e) and (i).

The ribbon phase, most visible as an individual ribbon in 7.3.1(a), or aggregates in 7.3.1(g), appears consistently on the silicon surface. During dip coating, the ribbons arrange heavily upon the drying lines, like that in (b), that are often thick enough to be visible to the naked eye. The shape is not a uniform 3D cylinder, the individual ribbons in (g), the product of soaking the silicon wafer in a 0.87 g/l concentration NDP-toluene solution overnight, had an average length of 554±200 nm along their major axes, 78±30 nm on the minor axes, and were 14.8±2.0 nm thick. The result is ribbons that preferentially lie flat upon the surface. The sizes of all images of NDP on SiO_2/Si(100) exhibiting a clear ribbon-like phase are plotted in Figure 7.3.2. There

was little observed correlation between the concentration of NDP in toluene and the observed spread in ribbon sizes and major-to-minor axis ratios across the chosen concentration range. Preparation by overnight submersion returned a more consistent spread in axis ratio, as well as larger maximum ribbon sizes and average axis ratios, than those prepared by spin-coating.

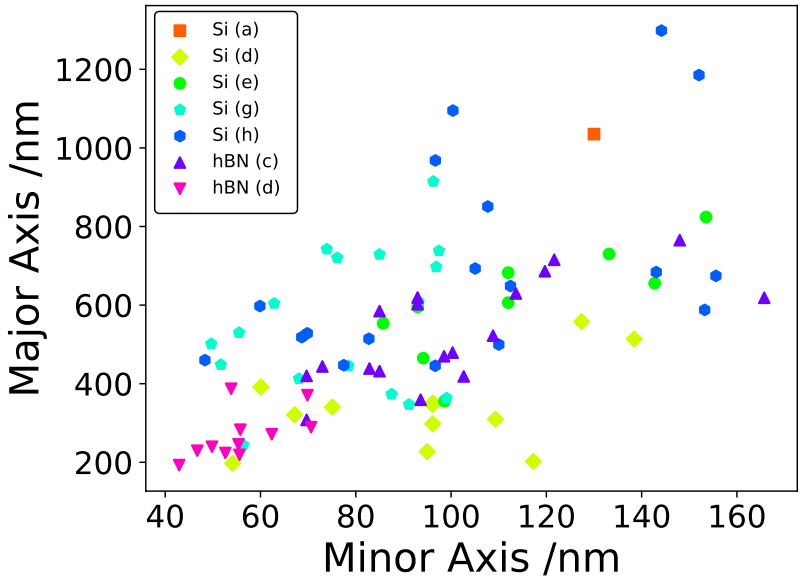

	Substrate	Concentration /g/l	Deposition Method	Mean Major Axis /nm	Mean Minor Axis /nm	Mean Ratio	Ratio Spread /%	Thickness /nm
■	SiO_2	0.73	100s submersion	1035	130	7.96	-	54.1±0.9
◆	SiO_2	1.97	Spin-cast	338	94	3.74	31.8	42.1±19.0
●	SiO_2	1.50	Spin-cast	608	114	5.37	16.0	15.3±2.3
⬟	SiO_2	0.87	15hr submersion	554	78	7.33	30.9	14.8±1.9
⬢	SiO_2	1.50	15hr submersion	705	105	7.04	30.6	40.7±16.0
▲	hBN	1.50	Spin-cast	529	101	5.29	17.4	2.3±0.2
▼	hBN	1.50	Spin-cast	268	56	4.80	17.8	1.9±0.3

Figure 7.3.2: Size distribution of long crystalline phases of substrate-deposited NDP as observed in Figures 7.3.1 and 7.3.3.

Though the grains that form the monolayer are isotropic, in some cases, the ribbons have an orientation dependence on that of neighbouring ribbons during aggregation. 7.3.1(d), (e) and (i) exhibit dendrite-like aggregates, with widths on the same scale as the observed lengths of the ribbons. This implies formation by lateral stacking of parallel major axis to major axis ribbons to form a branching superstructure upon to 3 µm long. Similar superstructures observed for perylene crystals[276,277] are explained by spatial and chemical inhibition of crystal growth. This is in agreement with spatial inhibition during self-organisation observed in the enclosed droplet in Figure 7.3.1(d).

A saturated solution was also investigated, by which NDP was added to toluene until it no longer fully dissolved into the resulting clear solution. 7.3.1(f) shows the saturated

4.6 g/l NDP in toluene solution, spin-casted onto the silicon substrate and probed with AFM. What resembles an intermediate phase between the ribbon and monolayer phases is present. The second layered phase has a slighter lower average height of 2 nm, compared to the 3 nm monolayer phase, but is compromised of more distinctive ribbon shapes that protrude upon the surface. The more distinctive ribbon aggregates in the image have a thickness greater than 10 nm and take on a more oval appearance. The oval-shaped aggregates are formed of parallel ribbons, but with a lower average major axis length of 240±30 nm compared to other depositions. These aggregates are potentially short-term aggregation of NDP left suspended post-saturation.

Observing two simultaneous phases of NDP necessitates discussing what potentially separates the two phases. Similar molecules exhibit crystallisation into sub-micrometre scale crystals that easily precipitate from solution. Aggregation of perylene diimide (PDI) crystals in solution, often at the liquid-air boundary[276], have a similar appearance to the ribbon phase observed for NDP. Given their formation at drying lines, ribbon-like NDP crystals may be imperfect crystal fragments, aggregating at similar rates in solution. It is assumed the slipped π-π stacking in NDP powder observed by Pearce *et al.*[261], shown in 7.1.2(c), also occurs in the observed surface-bound phases. The direction of stacking, however, is unknown and may be the distinguishing factor for the two phases. Slipped π-π stacking in the direction of the major axis of ribbons was observed for PTCDI-C_8[278] while dialkyl-PDI exhibiting superstructures similar to those in 7.3.1(d), (e) and (i), caused by kinetic inhibition[277] similarly observed slipped π-π stacking in the direction of the major axis. The grain-like phase constituting the monolayer may be observations of π stacking in the direction of the substrate plane.[279]

Hexagonal boron nitride, discussed in Subsection 2.5.3, was the second considered substrate. Its wide usage in preceding work[265,270,271] was due to its inert nature, both maximising van der Waals interactions with the planar molecules and minimising fluorescent quenching. The high symmetry axis of the substrate could resolve hypothetical difficulties with the parallel arrangement of the naphthalene or perylene group to the surface, caused by NDP's phenyl spacer, maximising potential ordering during monolayer coverage. This additionally facilitated future investigations of the correlation between morphology and optical properties.

Deposited hBN flakes were typically between 10 and 90 nm high and 10 to 30 µm across. Figure 7.3.3(c) shows a low dispersion of a secondary phase on top of the monolayer phase, with an average major axis length 529±30 nm, but with an average thickness of 2.3±0.2 nm, more similar to that of the first monolayer phase. The size distributions for (c) and (d) are plotted alongside those for silicon in Figure 7.3.2. The average major-to-minor axis ratio and percentage spread are consistent for both concentrations. The first monolayer still adsorbed tightly to the surface, with a 2-3 nm height throughout, which could be mechanically removed with a closer contact tip in contact mode AFM. AFM images of the SiO_2 substrate surrounding the hBN

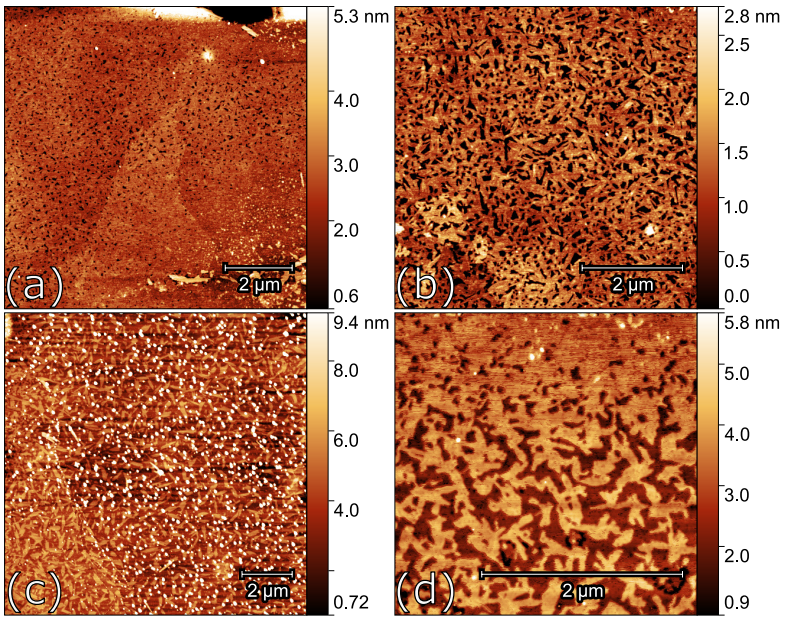

Figure 7.3.3: Tapping mode AFM images of naphthalene diimide phenyl-phenothiazine deposited from toluene solution on flakes of hexagonal boron nitride on 1 x 1 cm^2 SiO_2/Si(111) by spin-casting. **(a-b)** 10s dip-coat in 0.73 g/l; **(c)** 0.73 g/l spin-cast; **(d)** 1.97 g/l spin-cast.

flakes displayed the characteristic ribbon phase, the lack of a ribbon-like phase upon hBN may be due to variance in absorption energy. The NDP-hBN surface had the properties to grow a second layer, previous STM experiments upon crystalline perylene derivatives on hBN[271,280] assert a molecular arrangement, and π stacking, parallel to the substrate plane. The surface energy of the grain-like monolayer phase of NDP upon SiO_2 layer does not afford the growth of a second layer, instead favouring aggregation independent of the surface, similar to that in solution.

7.4 Conclusions on molecular dyad assemblies

Numerous surface morphologies of naphthalene diimide phenyl-phenothiazine by adsorption on two different surfaces are observed via AFM. Deposited naphthalene diimide phenyl-phenothiazine exhibited two unique phases, and microscale superstructures were observed in the higher concentration range. Dissolved NDP formed a highly stable thin film layer upon both substrates, with a second layer forming on high affinity hexagonal boron nitride. The instability of NDP in toluene solution brings into question the proportion of self-assembly of the ribbon aggregate phase manifests during dewetting, yet the absence of the phase on hBN, as well as previously observed self-assembly at liquid-air boundary[276], suggests the rapid formation of ribbons independent of the surface during evaporation of the solvent. The AFM images were consistent with other deposition studies of nanocrystals in related families of polycyclic aromatic hydrocarbons within the Group and wider field, hence the NDI moiety plays the leading role in the physical appearance.

Though the far-from-equilibrium morphologies of NDP nanocrystals were evaluated, the true molecular arrangement in each phase remains unknown. Molecular resolution imaging via SPM and x-ray measurements or other synchrotron approaches[281] upon NDP could shed light on interplanar separation, unit cell, and molecular axis with respect to the substrate. UV-visible spectrum fluorescence measurements from deposited NDP, particularly layered NDP nanocrystals of different thicknesses to investigate transfer properties[282] could be complemented by proposed sub-molecular single photon collection via STM-LE. This would entail a proposed experimental setup with optical access, previously conceived using combinations of mirrors, lenses, photodiodes and optical fibre-based STM tips *in situ*. Such a setup could allow for the simultaneous collection of topographical and electronic characterisation supplemented by electroluminescence data collected from the tunnel junction, photon maps, emission, local density of states and photon yield spectra, density of state maps, the second-order correlation function and luminescence time response as part of the investigation of NDP[283]. Such experiments would include the thionated derivatives of NDP, known to be red-shifted by the sulphur substitutions on the NDI moiety.[261]

UHV experiments were continued elsewhere, due to low stability of NDP in solvent, alongside changes in scope. Though questions are left unanswered, the study of NDP helped inform upon the natural microscale to high-end nanoscale dewetting behaviour of molecules dispersed in solution. This formed the early foundations for gold nanoparticle dewetting study, which utilised similar spin-casting and substrate preparation procedures. Presently, a pathway from synthesis to early ambient surface characterisation was demonstrated for a new material, as well as considerations for further steps in a full surface investigation of NDP.

8 Conclusions

8.1 Summary of Findings

The goal of chapter 4 was to expand both the parameter space in studies of passivated gold nanoparticle dewetting patterns from thin film, and explore rigorous applications of statistics to common nanostructure observables and data processing when measuring with contemporary imaging techniques. The roles of the concentration of gold nanoparticles in solution, local wettability gradients induced by large particulates and the underlying surface roughness and chemistry were visually and statistically discussed. Despite being a fairly simple deposition experiment, the parameter space is exceedingly wide, and yet to be fully explored. Increasing the concentration of the octanethiol-functionalised gold nanoparticles in toluene solution and increasing the roughness of the underlying surface slowed the dewetting process. The spin-casting of higher concentrations stabilised the resulting thin film on the thermally-oxidised Si(111) substrate, which in turn was likely nucleated by Maragoni convection and spinodal dewetting. The increased roughness on top of small uniform heterogeneous regions, grown on a very local level with a charged probe, acted to reduce the evaporation rate of solvent. These factors resulted in cellular dewetting patterns with an increased average distance between neighbouring cell centres, as derived from Fourier analysis and Voronoi tessellation mapping.

Fabricated surface heterogeneities provide an expansive domain for experimentation with directed self-organisation of nanoparticles, while enhancing our fundamental understanding of the physics at play in a dewetting thin film. AFM study of co-deposited and tip-induced heterogeneities suggest the features that rupture the film, such as tall aggregates, induce a strong local wettability gradient centred upon them during morphological evolution of the dewetting thin film, significantly diminishing the effects of other surface heterogeneities. As the film thins further, the gradient competes with the limiting factors in final pattern formation, resulting in strong transitions in pattern type and correlation length along the wettability gradient, as observed by Fourier analysis on residual gold nanoparticles and the underlying surface.

Monte Carlo method-based simulations continue to provide an unmatched simulation of far-from-equilibrium gold nanoparticle dewetting. The Rabani *et al.* model, and new modifications, effectively supported experimental observations, as well as the testing of analytical software. Use of test sets of optimised simulated AFM images allowed for expansive trials of a new software toolbox for Minkowski morphometry, Fourier analysis, and Voronoi tessellation, during prolonged absence from a laboratory setting. The performance of the Minkowski morphometry and Fourier analysis applications on simulated data was compared with previously unexplored principal component analysis. Clustering between the principal components of statistics extracted from images of nanostructure assemblies by these methods offered a promising alternative mechanism

whereby different image classes may be distinguished. PCA showed Minkowski metrics exhibiting stronger clustering than Fourier analysis, and hence, was a stronger candidate for automated dewetting pattern classification. Fourier analysis found success in evaluating the decay of "liquid" states and subsequent coarsening, closely tracking the evolving Monte Carlo model in reciprocal space for numerous resulting dewetting pattern types. Fourier analysis and Voronoi tessellations successfully extracted the same correlation lengths from the dewetting patterns' cellular geometry during the systematic concentration study.

X-ray measurements upon endofullerenes adsorbed to a metal surface suggested adsorption modified the electrostatic potential within the C_{60} cage. This in turn modified the position of the encapsulated molecules, H_2O and HF, relative to the Ag(111) surface, calculated using the coherent position and coherent fraction data from NIXSW measurements. Direct determination of the position of caged molecules is complicated by bonding geometry between the fullerene and silver surface, reconciled with Argand diagram analysis with experimental data, further molecular modelling, SPM and LEED.[58]

Data-mining was highly fruitful, providing a foundational data set for the development of published machine learning research into the categorisation and segmentation of AFM images of gold nanoparticles dewetting patterns[8,9], and future relationship mining with the Rabani *et al.* model. Row alignment followed by background detrending removed the majority of the inherent noise in SPM. A combination of median of differences-based row-alignment and polynomial background detrending minimised information loss and corruption when pre-processing raw multi-phase nanostructure AFM data for machine learning applications. Segmentation code, supplemented by Farley's U-net model segmentation and Gordon's denoising autoencoder, rendered AFM images from the historic data set near-indistinguishable from those produced by the Rabani *et al.* model, seamlessly integrating the simulated and real historic data.

A pathway from synthesis to early ambient surface characterisation of a new crystalline molecular dyad is presented in Chapter 7. Naphthalene diimide phenyl-phenothiazine (NDP) deposition experiments under ambient conditions were invaluable in establishing the workflow for AuNP experiments. Surface morphologies observed in AFM were visually consistent with other deposition studies of nanocrystals on silicon and hexagonal boron nitride in related families of polycyclic aromatic hydrocarbons within the group and wider field, suggesting the naphthalene diimide moiety plays the leading role in the physical appearance of the surface-bound dyad.

Current and newly explored statistical approaches to self-organised nanostructure study are highly transferable. Fourier analysis code is written to be compatible with common systems exhibiting periodic ordering. Mass image processing software is easily applied to common formats of data banks of SPM data, and the primary pre-processing and

segmentation algorithms are highly modular.

8.2 Further work

Avenues for further study of filled and empty fullerenes with x-ray measurements and SPM are discussed in Section 5.4. Work begins to address substrate-deposited buckminsterfullerene in Chapter 4 and Appendix D in two very different studies. Atomic resolution upon species-encapsulating C_{60} is necessary for single-point AFM force spectroscopy, which would accompany NIXSW measurements[58]. C_{60}-AuNP co-depositions returned unique and highly complex patterning. While providing visual evidence of coalescence phenomena by the favourability of clear distinctive boundaries between pattern types, images were too complex to assign further meaningful statistics. More rigorous experiments would require the fixing of the positions of similar particles on the substrate before or during deposition. This could be supplemented by new genetic algorithms by means of modifications to the Rabani *et al.* model to include stalagmite-like heterogeneities with wettability gradients centred around them.

More confident applications of PCA to utilise Minkowski morphometry as a classification method would require reevaluating how to impose scale-invariance on the Minkowski metrics. Fourier analysis could not identify any individual correlations across the whole parameter range between input parameters in the Rabani *et al.* model and the appearance of the PSD of a final stable frame of simulated dewetting. A far larger data set consisting of either all pattern morphologies or a single morphology after any coarsening has occurred, combined with the PCA, could provide more answers. Testing of presented open-source tools for Fourier analysis on similar periodic systems, such as polymers, polymer blends and biomaterials, could also be considered. This could also include point particle modelling and analysis of third layer effects identified in new and data-mined dewetting pattern AFM data.

Scanning probe lithography by AFM tip-induced oxidation provided a source of highly localised deviations in surface roughness and surface chemistry. Despite controlling the humidity and scan speed, and performing all chemical etching in the same batch, it was still challenging to control the roughness of the newly formed oxide layer. It is difficult to control the true tip apex-substrate separation, and the tip condition would change varying degrees throughout the invasive oxidation process. This would also require either a means of modifying the transient roughness value derived from the PSD such to be comparative value between samples, or a standardised set of AFM parameters and resolution limits for measuring roughness. If these are achieved, an extension of the parameter space into higher roughness or smoothness and the effects upon dewetting patterns could be of great benefit, particularly alongside a move to fabricate nanodevices, potentially evaluated with electrical transport.

Further steps in the study of naphthalene diimide phenyl-phenothiazine are discussed

in Section 7.4. Additionally, different deposition methods, substrates, solvents, and the degrees of thionation proposed in the original work, would help characterise the effects of each crystal growth mode. Electrospray deposition of NDP into UHV for STM experiments was planned, with a future pathway to STM-LE.

References

[1] E. Rabani, D. R. Reichman, P. L. Geissler, and L. E. Brus, "Drying-mediated self-assembly of nanoparticles," *Nature*, vol. 426, no. 6964, pp. 271–274, 2003.

[2] G. Binnig and H. Rohrer, "Scanning tunneling microscopy," *Surface Science*, vol. 126, pp. 236–244, 3 1983.

[3] G. Binnig, C. F. Quate, and C. Gerber, "Atomic Force Microscope," *Physical Review Letters*, vol. 56, pp. 930–933, 3 1986.

[4] B. W. Batterman, "Effect of Dynamical Diffraction in X-Ray Fluorescence Scattering," *Physical Review*, vol. 133, pp. A759–A764, 2 1964.

[5] O. Gordon, P. D'Hondt, L. Knijff, S. E. Freeney, F. Junqueira, P. Moriarty, and I. Swart, "Scanning tunneling state recognition with multi-class neural network ensembles," *Review of Scientific Instruments*, vol. 90, p. 103704, 10 2019.

[6] O. M. Gordon, F. L. Q. Junqueira, and P. J. Moriarty, "Embedding human heuristics in machine-learning-enabled probe microscopy," *Machine Learning: Science and Technology*, vol. 1, p. 015001, 2 2020.

[7] O. Gordon and P. Moriarty, "Machine learning at the (sub) atomic scale: next generation scanning probe microscopy," *Machine Learning: Science and Technology*, 2020.

[8] S. Farley, J. E. A. Hodgkinson, O. M. Gordon, J. Turner, A. Soltoggio, P. J. Moriarty, and E. Hunsicker, "Improving the segmentation of scanning probe microscope images using convolutional neural networks," *Machine Learning: Science and Technology*, vol. 2, p. 015015, 12 2020.

[9] O. M. Gordon, J. E. Hodgkinson, S. M. Farley, E. L. Hunsicker, and P. J. Moriarty, "Automated Searching and Identification of Self-Organized Nanostructures," *Nano Letters*, vol. 20, pp. 7688–7693, 10 2020.

[10] C. P. Martin, M. O. Blunt, E. Vaujour, A. Fahmi, A. D'Aléo, L. De Cola, F. Vögtle, and P. Moriarty, "Chapter 1 Self-Organised Nanoparticle Assemblies: A Panoply of Patterns," pp. 1–20, 2008.

[11] A. Stannard, "Dewetting-mediated pattern formation in nanoparticle assemblies," *Journal of Physics: Condensed Matter*, vol. 23, p. 83001, 2 2011.

[12] D. W. Pohl, "Dynamic piezoelectric translation devices," *Review of Scientific Instruments*, vol. 58, pp. 54–57, 1 1987.

[13] C. N. Woodburn, A. W. McKinnon, D. A. Roberts, M. E. Taylor, and M. E. Welland, "A one-dimensional piezoelectric-driven inertial micropositioner with vertical capabilities," *Measurement Science and Technology*, vol. 4, pp. 535–537, 4 1993.

[14] M. Li, R. Lv, S. Huang, Y. Dai, Z. Zeng, L. Wang, and B. Ren, "Electrochemical fabrication of silver tips for tip-enhanced Raman spectroscopy assisted by a machine vision system," *Journal of Raman Spectroscopy*, vol. 47, no. 7, pp. 808–

812, 2016.

[15] M. Rezeq, J. Pitters, and R. Wolkow, "Tungsten nanotip fabrication by spatially controlled field-assisted reaction with nitrogen," *The Journal of chemical physics*, vol. 124, no. 20, p. 204716, 2006.

[16] A. Technologies, "High and Ultra-High Vacuum for Science Research."

[17] M. Audi, "Pumping mechanism for different gases in ion pumps with different configurations," in *AIP Conference Proceedings*, vol. 171, pp. 358–365, AIP, 1988.

[18] J. Stirling, I. Lekkas, A. Sweetman, P. Djuranovic, Q. Guo, B. Pauw, J. Granwehr, R. Lévy, and P. Moriarty, "Critical Assessment of the Evidence for Striped Nanoparticles," *PLOS ONE*, vol. 9, p. e108482, 11 2014.

[19] J. Stirling, "Control theory for scanning probe microscopy revisited," *Beilstein Journal of Nanotechnology*, vol. 5, pp. 337–345, 3 2014.

[20] L. Gross, F. Mohn, N. Moll, P. Liljeroth, and G. Meyer, "The chemical structure of a molecule resolved by atomic force microscopy," *Science*, vol. 325, no. 5944, pp. 1110–1114, 2009.

[21] O. Sahin, C. F. Quate, O. Solgaard, and A. Atalar, "Resonant harmonic response in tapping-mode atomic force microscopy," *Physical Review B*, vol. 69, p. 165416, 4 2004.

[22] T. R. Albrecht, P. Grütter, D. Horne, and D. Rugar, "Frequency modulation detection using high-Qcantilevers for enhanced force microscope sensitivity," *Journal of Applied Physics*, vol. 69, pp. 668–673, 1 1991.

[23] R. Wiesendanger, *Scanning Probe Microscopy and Spectroscopy*. Cambridge University Press, 9 1994.

[24] F. J. Giessibl and B. M. Trafas, "Piezoresistive cantilevers utilized for scanning tunneling and scanning force microscope in ultrahigh vacuum," *Review of Scientific Instruments*, vol. 65, pp. 1923–1929, 6 1994.

[25] S. An, M.-h. Hong, J. Kim, S. Kwon, K. Lee, M. Lee, and W. Jhe, "Quartz tuning fork-based frequency modulation atomic force spectroscopy and microscopy with all digital phase-locked loop," *Review of Scientific Instruments*, vol. 83, p. 113705, 11 2012.

[26] S. Magonov, "Visualization of polymers at surfaces and interfaces with atomic force microscopy," in *Handbook of Surfaces and Interfaces of Materials*, pp. 393–430, Elsevier, 2001.

[27] M. Nonnenmacher, M. P. O'Boyle, and H. K. Wickramasinghe, "Kelvin probe force microscopy," *Applied Physics Letters*, vol. 58, pp. 2921–2923, 6 1991.

[28] A. Gil, J. Colchero, J. G mez Herrero, and A. M. Bar, "Electrostatic force gradient signal: resolution enhancement in electrostatic force microscopy and improved Kelvin probe microscopy," *Nanotechnology*, vol. 14, pp. 332–340, 2 2003.

[29] F. J. Giessibl, "Advances in atomic force microscopy," *Reviews of Modern Physics*, vol. 75, pp. 949–983, 7 2003.

[30] K. Okamoto, K. Yoshimoto, Y. Sugawara, and S. Morita, "KPFM imaging of Si(111)5 root 3 x 5 root 3-Sb surface for atom distinction using NC-AFM," *Applied Surface Science*, vol. 210, pp. 128–133, 3 2003.

[31] J. Tersoff and D. R. Hamann, "Theory of the scanning tunneling microscope," *Physical Review B*, vol. 31, pp. 805–813, 1 1985.

[32] C. J. Chen, *Introduction to Scanning Tunneling Microscopy*. Oxford University Press, 9 2007.

[33] R. Wiesendanger and W. Roland, *Scanning probe microscopy and spectroscopy: methods and applications*. Cambridge university press, 1994.

[34] J. Bardeen, "Tunnelling from a Many-Particle Point of View," *Physical Review Letters*, vol. 6, pp. 57–59, 1 1961.

[35] C. J. Chen, "Theory of scanning tunneling spectroscopy," *Journal of Vacuum Science & Technology A: Vacuum, Surfaces, and Films*, vol. 6, pp. 319–322, 3 1988.

[36] L. Gross, N. Moll, F. Mohn, A. Curioni, G. Meyer, F. Hanke, and M. Persson, "High-Resolution Molecular Orbital Imaging Using a p-Wave STM Tip," *Physical Review Letters*, vol. 107, p. 086101, 8 2011.

[37] A. Sweetman, S. Jarvis, R. Danza, and P. Moriarty, "Effect of the tip state during qPlus noncontact atomic force microscopy of Si (100) at 5 K: Probing the probe," *Beilstein journal of nanotechnology*, vol. 3, p. 25, 2012.

[38] M. Schunack, *Scanning Tunneling Microscopy Studies of Organic Molecules on Metal Surfaces*. PhD thesis, University of Aarhus, 2002.

[39] E. Fitzer, K.-H. Kochling, H. P. Boehm, and H. Marsh, "Recommended terminology for the description of carbon as a solid (IUPAC Recommendations 1995)," *Pure and Applied Chemistry*, vol. 67, pp. 473–506, 1 1995.

[40] E. Cisternas, F. Stavale, M. Flores, C. A. Achete, and P. Vargas, "First-principles calculation and scanning tunneling microscopy study of highly oriented pyrolytic graphite (0001)," *Physical Review B - Condensed Matter and Materials Physics*, vol. 79, 5 2009.

[41] A. Ramstad, G. Brocks, and P. J. Kelly, "Theoretical study of the Si(100) surface reconstruction," *Physical Review B*, vol. 51, pp. 15–1995, 1994.

[42] L. Kantorovich and C. Hobbs, "Probing the Si(001) surface with a Si tip: An ab initio study," *Physical Review B*, vol. 73, p. 245420, 6 2006.

[43] M. V. Gomoyunova and I. I. Pronin, "Photoelectron spectroscopy of atomic core levels on the silicon surface: A review," *Technical Physics*, vol. 49, pp. 1249–1279, 10 2004.

[44] D. Bauza, "Thermal oxidation of silicon and Si-SiO2 interface morphology, structure and localized states," in *Handbook of Surfaces and Interfaces of Materials*,

pp. 115–216, Elsevier, 2001.

[45] R. Doering and Y. Nishi, eds., *Handbook of Semiconductor Manufacturing Technology*. CRC Press, 12 2017.

[46] K. Watanabe, T. Taniguchi, and H. Kanda, "Direct-bandgap properties and evidence for ultraviolet lasing of hexagonal boron nitride single crystal," *Nature Materials*, vol. 3, pp. 404–409, 6 2004.

[47] C. R. Dean, A. F. Young, I. Meric, C. Lee, L. Wang, S. Sorgenfrei, K. Watanabe, T. Taniguchi, P. Kim, K. L. Shepard, and J. Hone, "Boron nitride substrates for high-quality graphene electronics," *Nature Nanotechnology*, vol. 5, pp. 722–726, 10 2010.

[48] M. Yankowitz, J. Xue, D. Cormode, J. D. Sanchez-Yamagishi, K. Watanabe, T. Taniguchi, P. Jarillo-Herrero, P. Jacquod, and B. J. LeRoy, "Emergence of superlattice Dirac points in graphene on hexagonal boron nitride," *Nature Physics*, vol. 8, pp. 382–386, 5 2012.

[49] H. W. Kroto, J. R. Heath, S. C. O'Brien, R. F. Curl, and R. E. Smalley, "C60: Buckminsterfullerene," *Nature*, vol. 318, pp. 162–163, 11 1985.

[50] F. A. Stevie and C. L. Donley, "Introduction to x-ray photoelectron spectroscopy," *Journal of Vacuum Science & Technology A: Vacuum, Surfaces, and Films*, vol. 38, 12 2020.

[51] D. P. Woodruff and D. A. Duncan, "X-ray standing wave studies of molecular adsorption: why coherent fractions matter," *New Journal of Physics*, vol. 22, p. 113012, 11 2020.

[52] R. G. Jones, A. S. Y. Chan, M. G. Roper, M. P. Skegg, I. G. Shuttleworth, C. J. Fisher, G. J. Jackson, J. J. Lee, D. P. Woodruff, N. K. Singh, and B. C. C. Cowie, "X-ray standing waves at surfaces," *Journal of Physics: Condensed Matter*, vol. 14, pp. 4059–4074, 4 2002.

[53] D. P. Woodruff, "Surface structure determination using x-ray standing waves," *Reports on Progress in Physics*, vol. 68, pp. 743–798, 4 2005.

[54] D. P. Woodruff, B. C. C. Cowie, and A. R. H. F. Ettema, "Surface structure determination using X-ray standing waves: a simple view," *Journal of Physics: Condensed Matter*, vol. 6, pp. 10633–10645, 12 1994.

[55] J. Zegenhagen, "Surface structure determination with X-ray standing waves," *Surface Science Reports*, vol. 18, pp. 202–271, 10 1993.

[56] J. Zegenhagen, "X-ray standing waves technique: Fourier imaging active sites," *Japanese Journal of Applied Physics*, vol. 58, p. 110502, 11 2019.

[57] F. C. Bocquet, G. Mercurio, M. Franke, G. van Straaten, S. W. S. Soubatch, C. Kumpf, and F. S. Tautz, "Torricelli: A software to determine atomic spatial distributions from normal incidence x-ray standing wave data," *Computer Physics Communications*, vol. 235, pp. 502–513, 2 2019.

[58] S. P. Jarvis, H. Sang, F. Junqueira, O. Gordon, J. E. A. Hodgkinson, A. Saywell,

P. Rahe, S. Mamone, S. Taylor, A. Sweetman, J. Leaf, D. A. Duncan, T.-L. Lee, P. K. Thakur, G. Hoffman, R. J. Whitby, M. H. Levitt, G. Held, L. Kantorovich, P. Moriarty, and R. G. Jones, "Chemical shielding of H2O and HF encapsulated inside a C60 cage," *Communications Chemistry*, vol. 4, p. 135, 12 2021.

[59] J. Israelachvili, *Intermolecular and Surface Forces*. Elsevier, 2011.

[60] B. Derjaguin and N. Churaev, "Structural component of disjoining pressure," *Journal of Colloid and Interface Science*, vol. 49, pp. 249–255, 11 1974.

[61] G. Reiter, "Dewetting of thin polymer films," *Physical Review Letters*, vol. 68, pp. 75–78, 1 1992.

[62] A. Sharma and G. Reiter, "Instability of Thin Polymer Films on Coated Substrates: Rupture, Dewetting, and Drop Formation," *Journal of Colloid and Interface Science*, vol. 178, pp. 383–399, 3 1996.

[63] R. Seemann, S. Herminghaus, and K. Jacobs, "Dewetting Patterns and Molecular Forces: A Reconciliation," *Physical Review Letters*, vol. 86, pp. 5534–5537, 6 2001.

[64] K. Jain, A. J. Schultz, and J. R. Errington, "Construction of the interface potential from a series of canonical ensemble simulations," *The Journal of Chemical Physics*, vol. 151, p. 044103, 7 2019.

[65] J. R. Henderson, "Statistical mechanics of the disjoining pressure of a planar film," *Physical Review E*, vol. 72, p. 051602, 11 2005.

[66] I. Borgia, B. Brunetti, I. Mariani, A. Sgamellotti, F. Cariati, P. Fermo, M. Mellini, C. Viti, and G. Padeletti, "Heterogeneous distribution of metal nanocrystals in glazes of historical pottery," *Applied Surface Science*, vol. 185, pp. 206–216, 1 2002.

[67] E. Bontempi, P. Colombi, L. Depero, L. Cartechini, F. Presciutti, B. Brunetti, and A. Sgamellotti, "Glancing-incidence X-ray diffraction of Ag nanoparticles in gold lustre decoration of Italian Renaissance pottery," *Applied Physics A*, vol. 83, pp. 543–546, 6 2006.

[68] M. Faraday, "X. The Bakerian Lecture. —Experimental relations of gold (and other metals) to light," *Philosophical Transactions of the Royal Society of London*, vol. 147, pp. 145–181, 12 1857.

[69] R. B. Schasfoort, *Handbook of Surface Plasmon Resonance*. Cambridge: Royal Society of Chemistry, 2008.

[70] L. H. Dubois, B. R. Zegarski, and R. G. Nuzzo, "Molecular ordering of organosulfur compounds on Au(111) and Au(100): Adsorption from solution and in ultrahigh vacuum," *The Journal of Chemical Physics*, vol. 98, pp. 678–688, 1 1993.

[71] F. Schreiber, A. Eberhardt, T. Y. B. Leung, P. Schwartz, S. M. Wetterer, D. J. Lavrich, L. Berman, P. Fenter, P. Eisenberger, and G. Scoles, "Adsorption mechanisms, structures, and growth regimes of an archetypal self-assembling system:

Decanethiol on Au(111)," *Physical Review B*, vol. 57, pp. 12476–12481, 5 1998.

[72] G. Frens, "Controlled Nucleation for the Regulation of the Particle Size in Monodisperse Gold Suspensions," *Nature Physical Science*, vol. 241, pp. 20–22, 1 1973.

[73] C. A. Mirkin, "Programming the Assembly of Two- and Three-Dimensional Architectures with DNA and Nanoscale Inorganic Building Blocks ,," *Inorganic Chemistry*, vol. 39, pp. 2258–2272, 5 2000.

[74] R. P. Andres, J. D. Bielefeld, J. I. Henderson, D. B. Janes, V. R. Kolagunta, C. P. Kubiak, W. J. Mahoney, and R. G. Osifchin, "Self-Assembly of a Two-Dimensional Superlattice of Molecularly Linked Metal Clusters," *Science*, vol. 273, pp. 1690–1693, 9 1996.

[75] E. Verrelli, D. Tsoukalas, K. Giannakopoulos, D. Kouvatsos, P. Normand, and D. Ioannou, "Nickel nanoparticle deposition at room temperature for memory applications," *Microelectronic Engineering*, vol. 84, pp. 1994–1997, 9 2007.

[76] M. O. Blunt, M. Šuvakov, F. Pulizzi, C. P. Martin, E. Pauliac-Vaujour, A. Stannard, A. W. Rushforth, B. Tadić, and P. Moriarty, "Charge Transport in Cellular Nanoparticle Networks: Meandering through Nanoscale Mazes," *Nano Letters*, vol. 7, pp. 855–860, 4 2007.

[77] A. A. Middleton and N. S. Wingreen, "Collective transport in arrays of small metallic dots," *Physical Review Letters*, vol. 71, pp. 3198–3201, 11 1993.

[78] R. Parthasarathy, X.-M. Lin, and H. M. Jaeger, "Electronic Transport in Metal Nanocrystal Arrays: The Effect of Structural Disorder on Scaling Behavior," *Physical Review Letters*, vol. 87, p. 186807, 10 2001.

[79] R. Parthasarathy, X.-M. Lin, K. Elteto, T. F. Rosenbaum, and H. M. Jaeger, "Percolating through Networks of Random Thresholds: Finite Temperature Electron Tunneling in Metal Nanocrystal Arrays," *Physical Review Letters*, vol. 92, p. 076801, 2 2004.

[80] P. Moriarty, "Nanofluids on solid substrates," *Journal of Physics: Condensed Matter*, vol. 21, p. 260302, 10 2009.

[81] D. Brutin and V. Starov, "Recent advances in droplet wetting and evaporation," *Chemical Society Reviews*, vol. 47, no. 2, pp. 558–585, 2018.

[82] D. Zang, S. Tarafdar, Y. Y. Tarasevich, M. Dutta Choudhury, and T. Dutta, "Evaporation of a Droplet: From physics to applications," *Physics Reports*, vol. 804, pp. 1–56, 4 2019.

[83] F. Giorgiutti-Dauphiné and L. Pauchard, "Drying drops," *The European Physical Journal E*, vol. 41, p. 32, 3 2018.

[84] R. D. Deegan, O. Bakajin, T. F. Dupont, G. Huber, S. R. Nagel, and T. A. Witten, "Capillary flow as the cause of ring stains from dried liquid drops," *Nature*, vol. 389, pp. 827–829, 10 1997.

[85] R. D. Deegan, "Pattern formation in drying drops," *Physical Review E*, vol. 61,

pp. 475–485, 1 2000.

[86] E. Pauliac-Vaujour and P. Moriarty, "Meniscus-Mediated Organization of Colloidal Nanoparticles," *The Journal of Physical Chemistry C*, vol. 111, pp. 16255–16260, 11 2007.

[87] T. J. Woehl and T. Prozorov, "The Mechanisms for Nanoparticle Surface Diffusion and Chain Self-Assembly Determined from Real-Time Nanoscale Kinetics in Liquid," *The Journal of Physical Chemistry C*, vol. 119, pp. 21261–21269, 9 2015.

[88] S. Ilday, G. Makey, G. B. Akguc, Yavuz, O. Tokel, I. Pavlov, O. Gülseren, and F. Ilday, "Rich complex behaviour of self-assembled nanoparticles far from equilibrium," *Nature Communications*, vol. 8, p. 14942, 4 2017.

[89] G. Cabra, M. Di Ventra, and M. Galperin, "Local-noise spectroscopy for nonequilibrium systems," *Physical Review B*, vol. 98, p. 235432, 12 2018.

[90] L. Costa, G. Li-Destri, N. H. Thomson, O. Konovalov, and D. Pontoni, "Real Space Imaging of Nanoparticle Assembly at Liquid–Liquid Interfaces with Nanoscale Resolution," *Nano Letters*, vol. 16, pp. 5463–5468, 9 2016.

[91] H. Alhummiany, S. Jarvis, R. A. J. Woolley, A. Stannard, M. Blunt, and P. Moriarty, "Dewetting of Au nanoparticle assemblies," *Journal of Materials Chemistry*, vol. 21, no. 42, p. 16983, 2011.

[92] G. Ge and L. Brus, "Evidence for spinodal phase separation in two-dimensional nanocrystal self-assembly," *Journal of Physical Chemistry B*, vol. 104, pp. 9574–9575, 10 2000.

[93] M. O. Blunt, C. P. Martin, M. Ahola-Tuomi, E. Pauliac-Vaujour, P. Sharp, P. Nativo, M. Brust, and P. J. Moriarty, "Coerced mechanical coarsening of nanoparticle assemblies," *Nature Nanotechnology*, vol. 2, pp. 167–170, 3 2007.

[94] M. O. Blunt, C. P. Martin, M. Ahola-Tuomi, E. Pauliac-Vaujour, P. Sharp, P. Nativo, M. Brust, and P. J. Moriarty, "Coerced mechanical coarsening of nanoparticle assemblies," *Nature Nanotechnology*, vol. 2, pp. 167–170, 2 2007.

[95] A. Stannard, C. P. Martin, E. Pauliac-Vaujour, P. Moriarty, and U. Thiele, "Dual-scale pattern formation in nanoparticle assemblies," *The Journal of Physical Chemistry C*, vol. 112, no. 39, pp. 15195–15203, 2008.

[96] P. Moriarty, M. D. R. Taylor, and M. Brust, "Nanostructured Cellular Networks," *Physical Review Letters*, vol. 89, p. 248303, 11 2002.

[97] C. P. Martin, M. O. Blunt, and P. Moriarty, "Nanoparticle Networks on Silicon: Self-Organized or Disorganized?," *Nano Letters*, vol. 4, pp. 2389–2392, 12 2004.

[98] M. Maillard, L. Motte, and M.-P. Pileni, "Rings and Hexagons Made of Nanocrystals," *Advanced Materials*, vol. 13, pp. 200–204, 2 2001.

[99] C. Stowell and B. A. Korgel, "Self-Assembled Honeycomb Networks of Gold Nanocrystals," *Nano Letters*, vol. 1, pp. 595–600, 11 2001.

[100] E. Pauliac-Vaujour, A. Stannard, C. P. Martin, M. O. Blunt, I. Notingher, P. J.

Moriarty, I. Vancea, and U. Thiele, "Fingering Instabilities in Dewetting Nanofluids," *Physical Review Letters*, vol. 100, p. 176102, 4 2008.

[101] G. Yosef and E. Rabani, "Self-Assembly of Nanoparticles into Rings: A Lattice-Gas Model," *The Journal of Physical Chemistry B*, vol. 110, pp. 20965–20972, 10 2006.

[102] U. Thiele, I. Vancea, A. J. Archer, M. J. Robbins, L. Frastia, A. Stannard, E. Pauliac-Vaujour, C. P. Martin, M. O. Blunt, and P. J. Moriarty, "Modelling approaches to the dewetting of evaporating thin films of nanoparticle suspensions," *Journal of Physics: Condensed Matter*, vol. 21, p. 264016, 7 2009.

[103] P. C. Ohara and W. M. Gelbart, "Interplay between Hole Instability and Nanoparticle Array Formation in Ultrathin Liquid Films," *Langmuir*, vol. 14, pp. 3418–3424, 6 1998.

[104] J. Xu, J. Xia, and Z. Lin, "Evaporation-induced self-assembly of nanoparticles from a sphere-on-flat geometry," *Angewandte Chemie - International Edition*, vol. 46, no. 11, pp. 1860–1863, 2007.

[105] L. Frastia, A. J. Archer, and U. Thiele, "Dynamical Model for the Formation of Patterned Deposits at Receding Contact Lines," *Physical Review Letters*, vol. 106, p. 077801, 2 2011.

[106] A. Stannard, H. Alhummiany, E. Pauliac-Vaujour, J. S. Sharp, P. Moriarty, and U. Thiele, "Directing the Formation of Nanostructured Rings via Local Oxidation," *Langmuir*, vol. 26, pp. 13892–13896, 9 2010.

[107] T. Caro, "The Adaptive Significance of Coloration in Mammals," *BioScience*, vol. 55, no. 2, pp. 125–136, 2005.

[108] A. Turing, "The chemical basis of morphogenesis," *Philosophical Transactions of the Royal Society of London. Series B, Biological Sciences*, vol. 237, pp. 37–72, 8 1952.

[109] J. Bischof, D. Scherer, S. Herminghaus, and P. Leiderer, "Dewetting Modes of Thin Metallic Films: Nucleation of Holes and Spinodal Dewetting," *Physical Review Letters*, vol. 77, pp. 1536–1539, 8 1996.

[110] R. Xie, A. Karim, J. F. Douglas, C. C. Han, and R. A. Weiss, "Spinodal Dewetting of Thin Polymer Films," *Physical Review Letters*, vol. 81, pp. 1251–1254, 8 1998.

[111] S. Herminghaus, K. Jacobs, K. Mecke, J. Bischof, A. Fery, M. Ibn-Elhaj, and S. Schlagowski, "Spinodal Dewetting in Liquid Crystal and Liquid Metal Films," *Science*, vol. 282, pp. 916–919, 10 1998.

[112] E. Ruckenstein and R. K. Jain, "Spontaneous rupture of thin liquid films," *Journal of the Chemical Society, Faraday Transactions 2*, vol. 70, p. 132, 1974.

[113] M. O. Blunt, *Far from equilibrium nanoparticle assemblies: Patterns, transport and dynamics*. PhD thesis, 2006.

[114] U. Thiele, M. Mertig, and W. Pompe, "Dewetting of an Evaporating Thin

Liquid Film: Heterogeneous Nucleation and Surface Instability," *Physical Review Letters*, vol. 80, pp. 2869–2872, 3 1998.

[115] M. Maillard, L. Motte, A. T. Ngo, and M. P. Pileni, "Rings and Hexagons Made of Nanocrystals: A Marangoni Effect," *The Journal of Physical Chemistry B*, vol. 104, pp. 11871–11877, 12 2000.

[116] H. Bénard, "Les tourbillons cellulaires dans une nappe liquide. Première partie: description générale des phénomènes," *Revue Générale des Sciences pures et appliquées*, vol. 11, pp. 1261–1271, 1900.

[117] M. J. BLOCK, "Surface Tension as the Cause of Bénard Cells and Surface Deformation in a Liquid Film," *Nature*, vol. 178, pp. 650–651, 9 1956.

[118] J. R. A. Pearson, "On convection cells induced by surface tension," *Journal of Fluid Mechanics*, vol. 4, pp. 489–500, 9 1958.

[119] V. Arcoleo and V. Liveri, "AFM investigation of gold nanoparticles synthesized in water/AOT/n-heptane microemulsions," *Chemical Physics Letters*, vol. 258, pp. 223–227, 8 1996.

[120] C. Kunstmann-Olsen, D. Belić, and M. Brust, "Monitoring pattern formation in drying and wetting dispersions of gold nanoparticles by ESEM," *Faraday Discussions*, vol. 181, pp. 281–298, 2015.

[121] K. Bhattacharjee, K. Biswas, and B. L. V. Prasad, "Unraveling the Role of Excess Ligand in Nanoparticle Pattern Formation from an Evaporatively Dewetting Nanofluid Droplet," *The Journal of Physical Chemistry C*, vol. 124, pp. 23446–23453, 10 2020.

[122] J. Bico, U. Thiele, and D. Quéré, "Wetting of textured surfaces," *Colloids and Surfaces A: Physicochemical and Engineering Aspects*, vol. 206, pp. 41–46, 7 2002.

[123] I. Vancea, U. Thiele, E. Pauliac-Vaujour, A. Stannard, C. P. Martin, M. O. Blunt, and P. J. Moriarty, "Front instabilities in evaporatively dewetting nanofluids," *Physical Review E*, vol. 78, p. 041601, 10 2008.

[124] T. P. Bigioni, X.-M. Lin, T. T. Nguyen, E. I. Corwin, T. A. Witten, and H. M. Jaeger, "Kinetically driven self assembly of highly ordered nanoparticle monolayers," *Nature Materials*, vol. 5, pp. 265–270, 4 2006.

[125] L. V. Govor, G. Reiter, G. H. Bauer, and J. Parisi, "Formation of low-dimensional close-packed arrays of nanoparticles in a dewetting water layer," *Physical Review E*, vol. 76, p. 041609, 10 2007.

[126] R. Konnur, K. Kargupta, and A. Sharma, "Instability and morphology of thin liquid films on chemically heterogeneous substrates," *Physical Review Letters*, vol. 84, pp. 931–934, 1 2000.

[127] M. Geoghegan, "Wetting at polymer surfaces and interfaces," *Progress in Polymer Science*, vol. 28, pp. 261–302, 2 2003.

[128] I. Torchinsky, N. Amdursky, A. Inberg, and G. Rosenman, "Electron-induced

adhesion and patterning of gold nanoparticles," *Applied Physics Letters*, vol. 96, p. 093106, 3 2010.

[129] M. Kolíbal, M. Konečný, F. Ligmajer, D. Škoda, T. Vystavěl, J. Zlámal, P. Varga, and T. Šikola, "Guided Assembly of Gold Colloidal Nanoparticles on Silicon Substrates Prepatterned by Charged Particle Beams," *ACS Nano*, vol. 6, pp. 10098–10106, 11 2012.

[130] L. Zhang, H.-Y. Si, and H.-L. Zhang, "Highly ordered fluorescent rings by "breath figures" on patterned substrates using polymer-free CdSe quantum dots," *Journal of Materials Chemistry*, vol. 18, no. 23, p. 2660, 2008.

[131] B. P. Khanal and E. R. Zubarev, "Rings of Nanorods," *Angewandte Chemie International Edition*, vol. 46, pp. 2195–2198, 3 2007.

[132] C. P. Martin, M. O. Blunt, E. Pauliac-Vaujour, A. Stannard, P. Moriarty, I. Vancea, and U. Thiele, "Controlling Pattern Formation in Nanoparticle Assemblies via Directed Solvent Dewetting," *Physical Review Letters*, vol. 99, p. 116103, 9 2007.

[133] J. Xu, J. Xia, S. W. Hong, Z. Lin, F. Qiu, and Y. Yang, "Self-Assembly of Gradient Concentric Rings via Solvent Evaporation from a Capillary Bridge," *Physical Review Letters*, vol. 96, p. 066104, 2 2006.

[134] J. Huang, F. Kim, A. R. Tao, S. Connor, and P. Yang, "Spontaneous formation of nanoparticle stripe patterns through dewetting," 2005.

[135] X. M. Lin, H. M. Jaeger, C. M. Sorensen, and K. J. Klabunde, "Formation of Long-Range-Ordered Nanocrystal Superlattices on Silicon Nitride Substrates," *The Journal of Physical Chemistry B*, vol. 105, pp. 3353–3357, 5 2001.

[136] D. E. Haas and D. P. Birnie, "Evaluation of thermocapillary driving forces in the development of striations during the spin coating process," *Journal of Materials Science*, vol. 37, no. 10, pp. 2109–2116, 2002.

[137] K. Tanaka, A. Takahara, and T. Kajiyama, "Film Thickness Dependence of the Surface Structure of Immiscible Polystyrene/Poly(methyl methacrylate) Blends," *Macromolecules*, vol. 29, pp. 3232–3239, 1 1996.

[138] P. C. Jukes, S. Y. Heriot, J. S. Sharp, and R. A. L. Jones, "Time-Resolved Light Scattering Studies of Phase Separation in Thin Film Semiconducting Polymer Blends during Spin-Coating," *Macromolecules*, vol. 38, pp. 2030–2032, 3 2005.

[139] D. Nečas and P. Klapetek, "Gwyddion: an open-source software for {SPM} data analysis," *Open Physics*, vol. 10, pp. 181–188, 1 2012.

[140] I. Horcas, R. Fernández, J. M. Gómez-Rodríguez, J. Colchero, J. Gómez-Herrero, and A. M. Baro, "WSXM: A software for scanning probe microscopy and a tool for nanotechnology," *Review of Scientific Instruments*, vol. 78, p. 013705, 1 2007.

[141] C. A. Schneider, W. S. Rasband, and K. W. Eliceiri, "NIH Image to ImageJ: 25 years of image analysis," *Nature Methods 2012 9:7*, vol. 9, pp. 671–675, 6

2012.

[142] S. G. Brush, "History of the Lenz-Ising Model," *Reviews of Modern Physics*, vol. 39, pp. 883–893, 10 1967.

[143] L. Onsager, "Crystal Statistics. I. A Two-Dimensional Model with an Order-Disorder Transition," *Physical Review*, vol. 65, pp. 117–149, 2 1944.

[144] N. Metropolis, A. W. Rosenbluth, M. N. Rosenbluth, A. H. Teller, and E. Teller, "Equation of State Calculations by Fast Computing Machines," *The Journal of Chemical Physics*, vol. 21, pp. 1087–1092, 6 1953.

[145] W. K. Hastings, "Monte Carlo sampling methods using Markov chains and their applications," *Biometrika*, vol. 57, pp. 97–109, 4 1970.

[146] R. M. Tromp, R. J. Hamers, and J. E. Demuth, "Si(001) Dimer Structure Observed with Scanning Tunneling Microscopy," *Physical Review Letters*, vol. 55, pp. 1303–1306, 9 1985.

[147] D. Weaire and N. Rivier, "Soap, cells and statistics—random patterns in two dimensions," *Contemporary Physics*, vol. 25, pp. 59–99, 1 1984.

[148] S. Kumar and S. K. Kurtz, "Properties of a two-dimensional Poisson-Voronoi tesselation: A Monte-Carlo study," *Materials Characterization*, vol. 31, pp. 55–68, 7 1993.

[149] K. R. Mecke, "Morphological characterization of patterns in reaction-diffusion systems," *Physical Review E*, vol. 53, pp. 4794–4800, 5 1996.

[150] K. R. Mecke and V. Sofonea, "Morphology of spinodal decomposition," *Physical Review E*, vol. 56, pp. R3761–R3764, 10 1997.

[151] W. K. Pratt, *Digital Image Processing (2nd Ed.)*. USA: John Wiley & Sons, Inc., 1991.

[152] P. Siepmann, C. P. Martin, I. Vancea, P. J. Moriarty, and N. Krasnogor, "A genetic algorithm approach to probing the evolution of self-organized nanostructured systems," *Nano letters*, vol. 7, no. 7, pp. 1985–1990, 2007.

[153] J. N. O'Shea, M. A. Phillips, M. D. Taylor, P. Moriarty, M. Brust, and V. R. Dhanak, "Colloidal particle foams: Templates for Au nanowire networks?," *Applied Physics Letters*, vol. 81, pp. 5039–5041, 12 2002.

[154] P. Müller-Buschbaum, J. S. Gutmann, C. Lorenz-Haas, O. Wunnicke, M. Stamm, and W. Petry, "Dewetting of Thin Diblock Copolymer Films: Spinodal Dewetting Kinetics," *Macromolecules*, vol. 35, pp. 2017–2023, 3 2002.

[155] A. M. Higgins and R. A. L. Jones, "Anisotropic spinodal dewetting as a route to self-assembly of patterned surfaces," *Nature*, vol. 404, pp. 476–478, 3 2000.

[156] F. Frehill, K. H. G. Schulte, C. P. Martin, L. Wang, S. Patel, J. A. Purton, J. G. Vos, and P. Moriarty, "Iron Wheels on Silicon: Wetting Behavior and Electronic Structure of Adsorbed Organostannoxane Clusters," *Langmuir*, vol. 20, pp. 6421–6429, 7 2004.

[157] C. Shannon, "Communication in the Presence of Noise," *Proceedings of the*

IRE, vol. 37, pp. 10–21, 1 1949.

[158] K. M. M. Prabhu, *Window Functions and Their Applications in Signal Processing*. CRC Press, 9 2018.

[159] J. M. Elson and J. M. Bennett, "Calculation of the power spectral density from surface profile data," *Applied Optics*, vol. 34, p. 201, 1 1995.

[160] L. I. Smith, "A tutorial on principal components analysis," 2002.

[161] I. T. Jolliffe and J. E. Jackson, "A User's Guide to Principal Components.," *The Statistician*, vol. 42, no. 1, p. 76, 1993.

[162] I. T. Jolliffe, *Principal Component Analysis*. Springer Series in Statistics, New York: Springer-Verlag, 2002.

[163] I. T. Jolliffe and J. Cadima, "Principal component analysis: a review and recent developments," *Philosophical Transactions of the Royal Society A: Mathematical, Physical and Engineering Sciences*, vol. 374, p. 20150202, 4 2016.

[164] A. Chowdhury, E. Kautz, B. Yener, and D. Lewis, "Image driven machine learning methods for microstructure recognition," *Computational Materials Science*, vol. 123, pp. 176–187, 10 2016.

[165] M. Pierpaoli, M. Ficek, P. Jakóbczyk, J. Karczewski, and R. Bogdanowicz, "Self-assembly of vertically orientated graphene nanostructures: Multivariate characterisation by Minkowski functionals and fractal geometry," *Acta Materialia*, vol. 214, p. 116989, 8 2021.

[166] S. Talu, M. Bramowicz, S. Kulesza, A. Ghaderi, V. Dalouji, S. Solaymani, M. F. Kenari, and M. Ghoranneviss, "Fractal features and surface micromorphology of diamond nanocrystals," *Journal of Microscopy*, vol. 264, pp. 143–152, 11 2016.

[167] I. Levchenko, J. Fang, K. K. Ostrikov, L. Lorello, and M. Keidar, "Morphological Characterization of Graphene Flake Networks Using Minkowski Functionals," *Graphene*, vol. 05, no. 01, pp. 25–34, 2016.

[168] Z. Farkas, A. Urmos, and A. Nemcsics, "Results of Principal Component Analyses on a Database of Gallium Arsenide-based Zero Dimensional Nanostructures," in *2021 IEEE 4th International Conference and Workshop Óbuda on Electrical and Power Engineering (CANDO-EPE)*, pp. 55–58, IEEE, 11 2021.

[169] T. D. Jacobs, T. Junge, and L. Pastewka, "Quantitative characterization of surface topography using spectral analysis," 2017.

[170] M. U. Rahman, Y. Xi, H. Li, F. Chen, D. Liu, and J. Wei, "Dynamics and Structure Formation of Confined Polymer Thin Films Supported on Solid Substrates," *Polymers*, vol. 13, p. 1621, 5 2021.

[171] J. E. Hodgkinson, "DeweFFT." https://github.com/j-ea-hodgkinson/DeweFFTting, 2021.

[172] G. Ge and L. E. Brus, "Fast Surface Diffusion of Large Disk-Shaped Nanocrystal Aggregates," *Nano Letters*, vol. 1, pp. 219–222, 4 2001.

[173] "Ostwald, W. Z.," *Phys. Chem.*, no. 37, p. 385, 1901.

[174] Y. Yamamato, N. Yoshi, H. Shiigi, and T. Nagaoka, "Electrical properties of a nanoparticle-networked film," *Solid State Ionics*, vol. 177, pp. 2325–2328, 10 2006.

[175] B. A. Korgel and D. Fitzmaurice, "Condensation of Ordered Nanocrystal Thin Films," *Physical Review Letters*, vol. 80, pp. 3531–3534, 4 1998.

[176] H. Tanaka, "Viscoelastic phase separation," *Journal of Physics: Condensed Matter*, vol. 12, pp. R207–R264, 4 2000.

[177] A. Hens, K. Mondal, G. Biswas, and D. Bandyopadhyay, "Pathways from disordered to ordered nanostructures from defect guided dewetting of ultrathin bilayers," *Journal of Colloid and Interface Science*, vol. 465, pp. 128–139, 3 2016.

[178] A. Vrij and J. T. G. Overbeek, "Rupture of thin liquid films due to spontaneous fluctuations in thickness," *Journal of the American Chemical Society*, vol. 90, pp. 3074–3078, 6 1968.

[179] M. Brinkmann, S. Graff, and F. Biscarini, "Mechanism of nonrandom pattern formation of polar-conjugated molecules in a partial wetting regime," *Physical Review B*, vol. 66, p. 165430, 10 2002.

[180] V. Lavrentiev, H. Abe, S. Yamamoto, H. Naramoto, and K. Narumi, "Isolation of Co nanoparticles by C60 molecules in co-deposited film," *Materials Letters*, vol. 57, pp. 4093–4097, 8 2003.

[181] U. Makhmanov, O. Ismailova, A. Kokhkharov, E. Zakhidov, and S. Bakhramov, "Features of self-aggregation of C 60 molecules in toluene prepared by different methods," *Physics Letters A*, vol. 380, pp. 2081–2084, 5 2016.

[182] W. H. Evers, B. D. Nijs, L. Filion, S. Castillo, M. Dijkstra, and D. Vanmaekelbergh, "Entropy-Driven Formation of Binary Semiconductor-Nanocrystal Superlattices," *Nano Letters*, vol. 10, pp. 4235–4241, 10 2010.

[183] S. J. Khan, F. Pierce, C. M. Sorensen, and A. Chakrabarti, "Self-Assembly of Ligated Gold Nanoparticles: Phenomenological Modeling and Computer Simulations," *Langmuir*, vol. 25, pp. 13861–13868, 12 2009.

[184] K. Jiang and P. Pinchuk, "Temperature and size-dependent Hamaker constants for metal nanoparticles," *Nanotechnology*, vol. 27, p. 345710, 8 2016.

[185] A. Guha and A. Mukherjee, "Calculation of Structural Forces and Jump Limit Between Two Fullerene Surfaces in Various Liquids," *International Journal of Chemical Sciences*, vol. 8, no. 1, pp. 157–175, 2010.

[186] Y. I. Prylutskyy, S. S. Durov, L. A. Bulavin, I. I. Adamenko, K. O. Moroz, A. Graja, A. Bogucki, and P. Scharf, "Structure, Vibrational, and Calorical Properties of Fullerene C60 in Toluene Solution," *Fullerene Science and Technology*, vol. 9, pp. 167–174, 4 2001.

[187] P. Müller-Buschbaum, E. Bauer, O. Wunnicke, and M. Stamm, "The control of thin film morphology by the interplay of dewetting, phase separation and mi-

crophase separation," *Journal of Physics: Condensed Matter*, vol. 17, pp. S363–S386, 3 2005.

[188] A. Sharma, R. Konnur, and K. Kargupta, "Thin liquid films on chemically heterogeneous substrates: self-organization, dynamics and patterns in systems displaying a secondary minimum," *Physica A: Statistical Mechanics and its Applications*, vol. 318, pp. 262–278, 2 2003.

[189] L. L. Sohn and R. L. Willett, "Fabrication of nanostructures using atomic-force-microscope-based lithography," *Applied Physics Letters*, vol. 67, pp. 1552–1554, 9 1995.

[190] R. D. Piner, J. Zhu, F. Xu, S. Hong, and C. A. Mirkin, ""Dip-Pen" Nanolithography," *Science*, vol. 283, pp. 661–663, 1 1999.

[191] J. A. Dagata, J. Schneir, H. H. Harary, C. J. Evans, M. T. Postek, and J. Bennett, "Modification of hydrogen-passivated silicon by a scanning tunneling microscope operating in air," *Applied Physics Letters*, vol. 56, pp. 2001–2003, 5 1990.

[192] G. S. Higashi, Y. J. Chabal, G. W. Trucks, and K. Raghavachari, "Ideal hydrogen termination of the Si (111) surface," *Applied Physics Letters*, vol. 56, pp. 656–658, 2 1990.

[193] J. A. Hayton, E. Pauliac-Vaujour, and P. J. Moriarty, "Anisotropic Assembly of Colloidal Nanoparticles: Exploiting Substrate Crystallinity," *Nano*, vol. 02, pp. 361–365, 12 2007.

[194] V. A. Burrows, Y. J. Chabal, G. S. Higashi, K. Raghavachari, and S. B. Christman, "Infrared spectroscopy of Si(111) surfaces after HF treatment: Hydrogen termination and surface morphology," *Applied Physics Letters*, vol. 53, pp. 998–1000, 9 1988.

[195] G. S. Higashi, R. S. Becker, Y. J. Chabal, and A. J. Becker, "Comparison of Si(111) surfaces prepared using aqueous solutions of NH 4 F versus HF," *Applied Physics Letters*, vol. 58, pp. 1656–1658, 4 1991.

[196] D. Gräf, M. Grundner, and R. Schulz, "Reaction of water with hydrofluoric acid treated silicon(111) and (100) surfaces," *Journal of Vacuum Science & Technology A: Vacuum, Surfaces, and Films*, vol. 7, pp. 808–813, 5 1989.

[197] X. Xie, H. Chung, C. Sow, and A. Wee, "Nanoscale materials patterning and engineering by atomic force microscopy nanolithography," *Materials Science and Engineering: R: Reports*, vol. 54, pp. 1–48, 11 2006.

[198] A. E. Gordon, "Mechanisms of surface anodization produced by scanning probe microscopes," *Journal of Vacuum Science & Technology B: Microelectronics and Nanometer Structures*, vol. 13, p. 2805, 11 1995.

[199] A. A. Tseng, A. Notargiacomo, and T. P. Chen, "Nanofabrication by scanning probe microscope lithography: A review," *Journal of Vacuum Science & Technology B: Microelectronics and Nanometer Structures*, vol. 23, no. 3, p. 877, 2005.

[200] R. Garcia, M. Calleja, and H. Rohrer, "Patterning of silicon surfaces with non-contact atomic force microscopy: Field-induced formation of nanometer-size water bridges," *Journal of Applied Physics*, vol. 86, pp. 1898–1903, 8 1999.

[201] P. Avouris, T. Hertel, and R. Martel, "Atomic force microscope tip-induced local oxidation of silicon: kinetics, mechanism, and nanofabrication," *Applied Physics Letters*, vol. 71, pp. 285–287, 7 1997.

[202] U. Thiele, "Open questions and promising new fields in dewetting," *The European Physical Journal E - Soft Matter*, vol. 12, pp. 409–416, 11 2003.

[203] K. Kurotobi and Y. Murata, "A Single Molecule of Water Encapsulated in Fullerene C60," *Science*, vol. 333, pp. 613–616, 7 2011.

[204] H. Shinohara, "Endohedral metallofullerenes," *Reports on Progress in Physics*, vol. 63, pp. 843–892, 6 2000.

[205] Y. Kubozono, Y. Takabayashi, S. Kashino, M. Kondo, T. Wakahara, T. Akasaka, K. Kobayashi, S. Nagase, S. Emura, and K. Yamamoto, "Structure of La2@C80 studied by La K-edge XAFS," *Chemical Physics Letters*, vol. 335, pp. 163–169, 2 2001.

[206] E. Nishibori, M. Takata, M. Sakata, and H. Shinohara, "Structural studies of endohedral metallofullerenes by synchrotron radiation powder diffraction," *Journal of Synchrotron Radiation*, vol. 5, pp. 977–979, 5 1998.

[207] X. Xu and H. S. Kang, "Ferromagnetic and half-metallic behaviors of fullerene-cobalt polymer chains," *The Journal of Chemical Physics*, vol. 128, p. 074707, 2 2008.

[208] H. Macpherson, S. Cornes, S. Zhou, and K. Porfyrakis, "A porphyrin-centred fullerene tetramer containing an N@C 60 substituent," *Royal Society Open Science*, vol. 5, p. 180338, 7 2018.

[209] E. G. Gillan, C. Yeretzian, K. S. Min, M. M. Alvarez, R. L. Whetten, and R. B. Kaner, "Endohedral rare-earth fullerene complexes," *The Journal of Physical Chemistry*, vol. 96, pp. 6869–6871, 8 1992.

[210] T. Akasaka and S. Nagase, eds., *Endofullerenes*, vol. 3 of *Developments in Fullerene Science*. Dordrecht: Springer Netherlands, 2002.

[211] M. Murata, Y. Murata, and K. Komatsu, "Synthesis and Properties of Endohedral C 60 Encapsulating Molecular Hydrogen," *Journal of the American Chemical Society*, vol. 128, pp. 8024–8033, 6 2006.

[212] A. Krachmalnicoff, M. H. Levitt, and R. J. Whitby, "An optimised scalable synthesis of H 2 O@C 60 and a new synthesis of H 2 @C 60," *Chem. Commun.*, vol. 50, no. 86, pp. 13037–13040, 2014.

[213] B. Meier, S. Mamone, M. Concistrè, J. Alonso-Valdesueiro, A. Krachmalnicoff, R. J. Whitby, and M. H. Levitt, "Electrical detection of ortho–para conversion in fullerene-encapsulated water," *Nature Communications*, vol. 6, p. 8112, 11 2015.

[214] A. Krachmalnicoff, R. Bounds, S. Mamone, S. Alom, M. Concistrè, B. Meier, K. Kouřil, M. E. Light, M. R. Johnson, S. Rols, A. J. Horsewill, A. Shugai, U. Nagel, T. Rõõm, M. Carravetta, M. H. Levitt, and R. J. Whitby, "The dipolar endofullerene HF@C60," *Nature Chemistry*, vol. 8, pp. 953–957, 10 2016.

[215] C. Beduz, M. Carravetta, J. Y.-C. Chen, M. Concistre, M. Denning, M. Frunzi, A. J. Horsewill, O. G. Johannessen, R. Lawler, X. Lei, M. H. Levitt, Y. Li, S. Mamone, Y. Murata, U. Nagel, T. Nishida, J. Ollivier, S. Rols, T. Room, R. Sarkar, N. J. Turro, and Y. Yang, "Quantum rotation of ortho and para-water encapsulated in a fullerene cage," *Proceedings of the National Academy of Sciences*, vol. 109, pp. 12894–12898, 8 2012.

[216] P. A. Brühwiler, A. J. Maxwell, A. Nilsson, N. Mårtensson, and O. Gunnarsson, "Auger and photoelectron study of the Hubbard U in C60 , K3C60 , and K6C 60," *Physical Review B*, vol. 48, pp. 18296–18299, 12 1993.

[217] A. J. Gibson, R. H. Temperton, K. Handrup, and J. N. O'Shea, "Resonant core spectroscopies of the charge transfer interactions between C60 and the surfaces of Au(111), Ag(111), Cu(111) and Pt(111)," *Surface Science*, vol. 657, pp. 69–78, 3 2017.

[218] J. A. Gardener, G. A. Briggs, and M. R. Castell, "Scanning tunneling microscopy studies of C60 monolayers on Au(111)," *Physical Review B - Condensed Matter and Materials Physics*, vol. 80, p. 235434, 12 2009.

[219] P. Moriarty, A. W. Dunn, Y. R. Ma, M. D. Upward, and P. H. Beton, "Investigation and manipulation of C60 on a Si surface using a scanning tunneling microscope," *Fullerene Science and Technology*, vol. 5, no. 4, pp. 769–780, 1997.

[220] M. J. Humphry, P. H. Beton, D. L. Keeling, R. H. J. Fawcett, P. Moriarty, M. J. Butcher, P. R. Birkett, D. R. M. Walton, R. Taylor, and H. W. Kroto, "Lateral translation of covalently bound fullerenes," *Journal of Physics: Condensed Matter*, vol. 18, pp. S1837–S1846, 8 2006.

[221] S. Szuba, R. Czajka, A. Kasuya, A. Wawro, and H. Rafii-Tabar, "Observation of C60 film formation on a highly oriented pyrolitic graphite substrate via scanning tunnelling microscopy," *Applied Surface Science*, vol. 144-145, pp. 648–652, 1999.

[222] P. J. Moriarty, "Fullerene adsorption on semiconductor surfaces," *Surface Science Reports*, vol. 65, pp. 175–227, 7 2010.

[223] R. S. Ruoff and A. P. Hickman, "Van der Waals binding to fullerenes to a graphite plane," *The Journal of Physical Chemistry*, vol. 97, pp. 2494–2496, 3 1993.

[224] L. A. Girifalco, "Molecular properties of fullerene in the gas and solid phases," *The Journal of Physical Chemistry*, vol. 96, pp. 858–861, 1 1992.

[225] J. M. Pacheco and J. P. Prates Ramalho, "First-Principles Determination of the Dispersion Interaction between Fullerenes and Their Intermolecular Potential,"

Physical Review Letters, vol. 79, pp. 3873–3876, 11 1997.

[226] J. P. Doye, D. J. Wales, W. Branz, and F. Calvo, "Modeling the structure of clusters of C60 molecules," *Physical Review B - Condensed Matter and Materials Physics*, vol. 64, pp. 2354091–23540911, 11 2001.

[227] C. Chiutu, A. M. Sweetman, A. J. Lakin, A. Stannard, S. Jarvis, L. Kantorovich, J. L. Dunn, and P. Moriarty, "Precise orientation of a single C 60 molecule on the tip of a scanning probe microscope," *Physical Review Letters*, vol. 108, p. 268302, 6 2012.

[228] L. A. Girifalco, "Interaction potential for carbon (C60) molecules," *The Journal of Physical Chemistry*, vol. 95, pp. 5370–5371, 7 1991.

[229] H. I. Li, K. Pussi, K. J. Hanna, L. L. Wang, D. D. Johnson, H. P. Cheng, H. Shin, S. Curtarolo, W. Moritz, J. A. Smerdon, R. McGrath, and R. D. Diehl, "Surface Geometry of C60 on Ag(111)," *Physical Review Letters*, vol. 103, p. 056101, 7 2009.

[230] K. Pussi, H. I. Li, H. Shin, L. N. Serkovic Loli, A. K. Shukla, J. Ledieu, V. Fournée, L. L. Wang, S. Y. Su, K. E. Marino, M. V. Snyder, and R. D. Diehl, "Elucidating the dynamical equilibrium of C60 molecules on Ag(111)," *Physical Review B - Condensed Matter and Materials Physics*, vol. 86, p. 205406, 11 2012.

[231] B. Lesiak, L. Kövér, J. Tóth, J. Zemek, P. Jiricek, A. Kromka, and N. Rangam, "C sp2/sp3 hybridisations in carbon nanomaterials – XPS and (X)AES study," *Applied Surface Science*, vol. 452, pp. 223–231, 9 2018.

[232] A. J. Maxwell, P. A. Brühwiler, A. Nilsson, N. Mårtensson, and P. Rudolf, "Photoemission, autoionization, and x-ray-absorption spectroscopy of ultrathin-film C60 on Au(110)," *Physical Review B*, vol. 49, pp. 10717–10725, 4 1994.

[233] C. J. Satterley, L. M. A. Perdigão, A. Saywell, G. Magnano, A. Rienzo, L. C. Mayor, V. R. Dhanak, P. H. Beton, and J. N. O'Shea, "Electrospray deposition of fullerenes in ultra-high vacuum: in situ scanning tunneling microscopy and photoemission spectroscopy," *Nanotechnology*, vol. 18, p. 455304, 11 2007.

[234] A. V. Naumkin, A. Kraut-Vass, S. W. Gaarenstroom, and C. J. Powell, "NIST X-ray Photoelectron Spectroscopy Database," 2012.

[235] S. M. Gatica, H. I. Li, R. A. Trasca, M. W. Cole, and R. D. Diehl, "Xe adsorption on a C60 monolayer on Ag(111)," *Physical Review B*, vol. 77, p. 045414, 1 2008.

[236] J.-R. Huo, J. Wang, H.-Y. Yang, and C.-Z. He, "Ag (111) surface for ambient electrolysis of nitrogen to ammonia," *Journal of Molecular Modeling*, vol. 27, p. 38, 2 2021.

[237] T. Fransson, Y. Harada, N. Kosugi, N. A. Besley, B. Winter, J. J. Rehr, L. G. M. Pettersson, and A. Nilsson, "X-ray and Electron Spectroscopy of Water," *Chemical Reviews*, vol. 116, pp. 7551–7569, 7 2016.

[238] L. Tjeng, R. Hesper, A. Heessels, A. Heeres, H. Jonkman, and G. Sawatzky,

"Development of the electronic structure in a K-doped C60 monolayer on a Ag(1 1 1) surface," *Solid State Communications*, vol. 103, pp. 31–35, 7 1997.

[239] W. L. Yang, V. Brouet, X. J. Zhou, H. J. Choi, S. G. Louie, M. L. Cohen, S. A. Kellar, P. V. Bogdanov, A. Lanzara, A. Goldoni, F. Parmigiani, Z. Hussain, and Z.-X. Shen, "Band Structure and Fermi Surface of Electron-Doped C 60 Monolayers," *Science*, vol. 300, pp. 303–307, 4 2003.

[240] D. P. Woodruff, "Surface structure determination using x-ray standing waves," *Reports on Progress in Physics*, vol. 68, pp. 743–798, 3 2005.

[241] D. Woodruff, "Normal incidence X-ray standing wave determination of adsorbate structures," *Progress in Surface Science*, vol. 57, pp. 1–60, 1 1998.

[242] E. I. Altman and R. J. Colton, "Determination of the orientation of C60 adsorbed on Au(111) and Ag(111)," *Physical Review B*, vol. 48, pp. 18244–18249, 12 1993.

[243] W. W. Pai, H. T. Jeng, C. M. Cheng, C. H. Lin, X. Xiao, A. Zhao, X. Zhang, G. Xu, X. Q. Shi, M. A. Van Hove, C. S. Hsue, and K. D. Tsuei, "Optimal electron doping of a C60 monolayer on Cu(111) via interface reconstruction," *Physical Review Letters*, vol. 104, p. 036103, 1 2010.

[244] L. Burzawa, S. Liu, and E. W. Carlson, "Classifying surface probe images in strongly correlated electronic systems via machine learning," *Physical Review Materials*, vol. 3, p. 033805, 3 2019.

[245] O. Payton, A. R. Champneys, M. E. Homer, L. Picco, and M. J. Miles, "Feedback-induced instability in tapping mode atomic force microscopy: Theory and experiment," *Proceedings of the Royal Society A: Mathematical, Physical and Engineering Sciences*, vol. 467, pp. 1801–1822, 6 2011.

[246] "SPM Software User Guide Software User Guide Including beta (complete, reviewed) chapters,"

[247] N. Otsu, "Threshold Selection Method from Gray-Level Histograms," *IEEE Trans Syst Man Cybern*, vol. SMC-9, no. 1, pp. 62–66, 1979.

[248] F. Leisch, "FlexMix: A general framework for finite mixture models and latent class regression in R," *Journal of Statistical Software*, vol. 11, pp. 1–18, 2004.

[249] A. P. Dempster, N. M. Laird, and D. B. Rubin, "Maximum Likelihood from Incomplete Data Via the EM Algorithm," *Journal of the Royal Statistical Society: Series B (Methodological)*, vol. 39, pp. 1–22, 9 1977.

[250] J. R. Durrant, S. A. Haque, and E. Palomares, "Photochemical energy conversion: from molecular dyads to solar cells," *Chemical Communications*, pp. 3279–3289, 8 2006.

[251] S. Berardi, S. Drouet, L. Francàs, C. Gimbert-Suriñach, M. Guttentag, C. Richmond, T. Stoll, and A. Llobet, "Molecular artificial photosynthesis," *Chemical Society Reviews*, vol. 43, pp. 7501–7519, 10 2014.

[252] L. Duan, L. Tong, Y. Xu, and L. Sun, "Visible light-driven water oxidation—from

molecular catalysts to photoelectrochemical cells," *Energy & Environmental Science*, vol. 4, pp. 3296–3313, 8 2011.

[253] J. W. Youngblood, S. H. A. Lee, Y. Kobayashi, E. A. Hernandez-Pagan, P. G. Hoertz, T. A. Moore, A. L. Moore, D. Gust, and T. E. Mallouk, "Photoassisted overall water splitting in a visible light-absorbing dye-sensitized photoelectrochemical cell," *Journal of the American Chemical Society*, vol. 131, pp. 926–927, 1 2009.

[254] P. Farràs and F. Cucinotta, "Recent advances in artificial photosynthetic systems at Newcastle University," *Comptes Rendus Chimie*, vol. 20, pp. 272–282, 3 2017.

[255] J. Roncali, "Single Material Solar Cells: the Next Frontier for Organic Photovoltaics?," *Advanced Energy Materials*, vol. 1, pp. 147–160, 3 2011.

[256] A. Cravino, S. Roquet, P. Leriche, O. Alévêque, P. Frère, and J. Roncali, "A star-shaped triphenylamine π-conjugated system with internal charge-transfer as donor material for hetero-junction solar cells," *Chemical Communications*, pp. 1416–1418, 3 2006.

[257] Y. Lin, Y. Li, and X. Zhan, "Small molecule semiconductors for high-efficiency organic photovoltaics," *Chemical Society Reviews*, vol. 41, pp. 4245–4272, 5 2012.

[258] D. W. Cho, M. Fujitsuka, A. Sugimoto, U. C. Yoon, P. S. Mariano, and M. Tetsuro, "Photoinduced Electron Transfer Processes in 1,8-Naphthalimide-Linker-Phenothiazine Dyads," *Journal of Physical Chemistry B*, vol. 110, pp. 11062–11068, 6 2006.

[259] M. Zuffo, S. Ladame, F. Doria, and M. Freccero, "Tuneable coumarin-NDI dyads as G-quadruplex specific light-up probes," *Sensors and Actuators B: Chemical*, vol. 245, pp. 780–788, 6 2017.

[260] F. Chaignon, F. Buchet, E. Blart, M. Falkenström, L. Hammarström, and F. Odobel, "Photoinduced electron transfer in ruthenium(II) trisbipyridine complexes connected to a naphthalenebisimide via an oligo(phenyleneethynylene) spacer," *New Journal of Chemistry*, vol. 33, pp. 408–416, 2 2009.

[261] N. Pearce, E. S. Davies, R. Horvath, C. R. Pfeiffer, X.-Z. Sun, W. Lewis, J. McMaster, M. W. George, and N. R. Champness, "Thionated naphthalene diimides: tuneable chromophores for applications in photoactive dyads," *Physical Chemistry Chemical Physics*, vol. 20, no. 2, pp. 752–764, 2018.

[262] A. Aviram and M. A. Ratner, "Molecular rectifiers," *Chemical Physics Letters*, vol. 29, pp. 277–283, 11 1974.

[263] E. A. Weiss, M. J. Ahrens, L. E. Sinks, A. V. Gusev, M. A. Ratner, and M. R. Wasielewski, "Making a Molecular Wire: Charge and Spin Transport through para-Phenylene Oligomers," *Journal of the American Chemical Society*, vol. 126, pp. 5577–5584, 5 2004.

[264] J. F. Martinez, N. T. L. Porte, and M. R. Wasielewski, "Electron Transfer from Photoexcited Naphthalene Diimide Radical Anion to Electrocatalytically

Active Re(bpy)(CO)3Cl in a Molecular Triad," *Journal of Physical Chemistry C*, vol. 122, pp. 2608–2617, 2 2018.

[265] V. V. Korolkov, S. A. Svatek, A. Summerfield, J. Kerfoot, L. Yang, T. Taniguchi, K. Watanabe, N. R. Champness, N. A. Besley, and P. H. Beton, "van der Waals-Induced Chromatic Shifts in Hydrogen-Bonded Two-Dimensional Porphyrin Arrays on Boron Nitride," *ACS Nano*, vol. 9, pp. 10347–10355, 9 2015.

[266] B. Doppagne, M. C. Chong, E. Lorchat, S. Berciaud, M. Romeo, H. Bulou, A. Boeglin, F. Scheurer, and G. Schull, "Vibronic Spectroscopy with Submolecular Resolution from STM-Induced Electroluminescence," *Physical Review Letters*, vol. 118, p. 127401, 3 2017.

[267] G. Reecht, F. Scheurer, V. Speisser, Y. J. Dappe, F. Mathevet, and G. Schull, "Electroluminescence of a Polythiophene Molecular Wire Suspended between a Metallic Surface and the Tip of a Scanning Tunneling Microscope," *Physical Review Letters*, vol. 112, p. 047403, 1 2014.

[268] A. M. Sweetman, S. P. Jarvis, H. Sang, I. Lekkas, P. Rahe, Y. Wang, J. Wang, N. Champness, L. Kantorovich, and P. Moriarty, "Mapping the force field of a hydrogen-bonded assembly," *Nature Communications*, vol. 5, p. 3931, 9 2014.

[269] A. Sweetman, M. A. Rashid, S. P. Jarvis, J. L. Dunn, P. Rahe, and P. Moriarty, "Visualizing the orientational dependence of an intermolecular potential," *Nature Communications*, vol. 7, p. 10621, 4 2016.

[270] M. Alkhamisi, V. V. Korolkov, A. S. Nizovtsev, J. Kerfoot, T. Taniguchi, K. Watanabe, N. A. Besley, E. Besley, and P. H. Beton, "The growth and fluorescence of phthalocyanine monolayers, thin films and multilayers on hexagonal boron nitride," *Chemical Communications*, vol. 54, no. 85, pp. 12021–12024, 2018.

[271] J. Kerfoot, V. V. Korolkov, A. S. Nizovtsev, R. Jones, T. Taniguchi, K. Watanabe, I. Lesanovsky, B. Olmos, N. A. Besley, E. Besley, and P. H. Beton, "Substrate-induced shifts and screening in the fluorescence spectra of supramolecular adsorbed organic monolayers," *Journal of Chemical Physics*, vol. 149, no. 5, p. 54701, 2018.

[272] M. Kasha, H. R. Rawls, and M. Ashraf El-Bayoumi, "The exciton model in molecular spectroscopy," *Pure and Applied Chemistry*, vol. 11, pp. 371–392, 1 1965.

[273] A. Davydov, "The theory of molecular excitons," *Uspekhi Fizicheskih Nauk*, vol. 82, no. 3, pp. 393–448, 1964.

[274] M. Müller, A. Paulheim, A. Eisfeld, and M. Sokolowski, "Finite size line broadening and superradiance of optical transitions in two dimensional long-range ordered molecular aggregates," *The Journal of Chemical Physics*, vol. 139, p. 044302, 7 2013.

[275] S. M. Vlaming and A. Eisfeld, "Tunable superradiance in porphyrin chains on insulating surfaces," *Journal of Physics D: Applied Physics*, vol. 47, p. 305301,

7 2014.

[276] Y.-J. Kim, Y. Lee, K. Park, C. W. Ahn, H.-T. Jung, and H.-J. Jeon, "Hierarchical Self-Assembly of Perylene Diimide (PDI) Crystals," *The Journal of Physical Chemistry Letters*, vol. 11, pp. 3934–3940, 5 2020.

[277] L. Bu, E. Pentzer, F. A. Bokel, T. Emrick, and R. C. Hayward, "Growth of Polythiophene/Perylene Tetracarboxydiimide Donor/Acceptor Shish-Kebab Nanostructures by Coupled Crystal Modification," *ACS Nano*, vol. 6, pp. 10924–10929, 12 2012.

[278] A. L. Briseno, S. C. B. Mannsfeld, C. Reese, J. M. Hancock, Y. Xiong, S. A. Jenekhe, Z. Bao, and Y. Xia, "Perylene Diimide Nanowires and Their Use in Fabricating Field-Effect Transistors and Complementary Inverters," *Nano Letters*, vol. 7, pp. 2847–2853, 9 2007.

[279] R. J. Chesterfield, J. C. McKeen, C. R. Newman, P. C. Ewbank, D. A. da Silva Filho, J.-L. Brédas, L. L. Miller, K. R. Mann, and C. D. Frisbie, "Organic Thin Film Transistors Based on N -Alkyl Perylene Diimides: Charge Transport Kinetics as a Function of Gate Voltage and Temperature," *The Journal of Physical Chemistry B*, vol. 108, pp. 19281–19292, 12 2004.

[280] J. Kerfoot, V. V. Korolkov, S. A. Svatek, M. Alkhamisi, T. Taniguchi, K. Watanabe, P. W. Parkinson, and P. H. Beton, "Two-Dimensional Diffusion of Excitons in a Perylene Diimide Monolayer Quenched by a Fullerene Heterojunction," *The Journal of Physical Chemistry C*, vol. 123, pp. 12249–12254, 5 2019.

[281] E. A. Muller, B. Pollard, H. A. Bechtel, P. van Blerkom, and M. B. Raschke, "Infrared vibrational nanocrystallography and nanoimaging," *Science Advances*, vol. 2, 10 2016.

[282] F. Würthner, "Perylene bisimide dyes as versatile building blocks for functional supramolecular architectures," *Chem. Commun.*, no. 14, pp. 1564–1579, 2004.

[283] K. Kuhnke, C. Große, P. Merino, and K. Kern, "Atomic-Scale Imaging and Spectroscopy of Electroluminescence at Molecular Interfaces," *Chemical Reviews*, vol. 117, pp. 5174–5222, 3 2017.

[284] H. Liu, Z. Lin, L. V. Zhigilei, and P. Reinke, "Fractal Structures in Fullerene Layers: Simulation of the Growth Process," *The Journal of Physical Chemistry C*, vol. 112, pp. 4687–4695, 3 2008.

[285] H. Liu and P. Reinke, "C60 thin film growth on graphite: Coexistence of spherical and fractal-dendritic islands," *The Journal of Chemical Physics*, vol. 124, 4 2006.

[286] H. Shin, S. E. O'Donnell, P. Reinke, N. Ferralis, A. K. Schmid, H. I. Li, A. D. Novaco, L. W. Bruch, and R. D. Diehl, "Floating two-dimensional solid monolayer of C60 on graphite," *Physical Review B - Condensed Matter and Materials Physics*, vol. 82, p. 235427, 12 2010.

[287] J. L. Wragg, J. E. Chamberlain, H. W. White, W. Krätschmer, and D. R. Huffman, "Scanning tunnelling microscopy of solid C60/C70," *Nature*, vol. 348, pp. 623–624, 12 1990.

List of Figures

List of Tables

List of Symbols & Nomenclature

Abbreviations

AI	Artificial Intelligence
ML	Machine Learning
SPM	Scanning Probe Microscopy
AFM	Atomic Force Microscopy
STM	Scanning Tunnelling Microscopy
UHV	Ultra-High Vacuum
UI	User Interface
PID	Proportional-Integral-Derivative
vdW	van der Waals
NC	Non-Contact
FM	Frequency Modulation
AM	Amplitude Modulation
KPFM	Kelvin Probe Force Microscopy
CPD	Contact Potential Difference
LDOS	Local Density Of States
VB	Valence Band
CB	Conduction Band
K-cell	Knudsen cell
VT-STM	Variable Temperature Scanning Tunnelling Microscope
LT-STM	Low Temperature Scanning Tunnelling Microscope
HOPG	Highly Oriented Pyrolytic Graphite
DFT	Density Functional Theory
hBN	Hexagonal Boron Nitride

RPES Resonant Photoemission Spectroscopy

XPS X-ray Photoelectron Spectroscopy

LEED Low Energy Electron Diffraction

NIXSW Normal Incident X-ray Standing Wave

CCD Charge-Coupled Device

HPLC High-Performance Liquid Chromatography

rpm Revolutions Per Minute

PCA Principal Component Analysis

CNN Convolutional Neural Network

FFT Fast Fourier Transform

PSD Power Spectral Density

RMS Root Mean Square

LOWESS Locally Weighted Scatterplot Smoothing

NDI Naphthalene Diimide

PTZ Phenothiazine

PEC Photoelectrochemical Cell

PV Photovoltaic Cell

PET Photoinduced Electron Transfer

BHJ Bulk Heterojunctions

DBA Donor-Bridge-Acceptor

HOMO Highest Occupied Molecular Orbital

LUMO Lowest Unoccupied Molecular Orbital

NDP Naphthalene Diimide Phenyl-phenothiazine

LED Light-Emitting Diode

STM-LE Scanning Tunnelling Microscopy Light Emission

PTCDI Perylene-3,4,9,10-Tetracarboxylic-3,4,9,10-Diimide

PTCDA Perylene-3,4,9,10-Tetracarboxylic-3,4,9,10-Dianhydride

TCPP 5,10,15,20-Tetrakis(4-Carboxylphenyl)Porphyrin

NDI Naphthalene Diimide

PDI Perylene Diimide

TD-DFT Time Dependent Density Functional Theory

ASE Atomic Simulations Environment

NMI Naphthalene Monoimide

Ph-PTZ 4-Aminophenyl-Phenothiazine

TLC Thin-Layer Chromatography

MALDI ToFMS Matrix-assisted laser desorption/ionisation time of flight mass spectroscopy

DCTB Trans-2-[3-(4-Tert-Butylphenyl)-2-Methyl-2-Propenylidene]Malononitrile

NMR Nuclear Magnetic Resonance

SiO_2/Si(hkl) Thermally oxidised silicon dioxide on silicon of Miller indices hkl

ACS American Chemical Society

HPLC High-Performance Liquid Chromatography

UV Ultraviolet

AuNP Gold Nanoparticles

TEM Transmission Electron Microscopy

ADC Analog-to-Digital Converter

DAC Digital-to-Analog Converter

IDE Integrated Development Environment

IBW IGOR-Pro Binary Wave

PNG Portable Network Graphic

CSV	Comma-Separated Values
HD5	Hierarchical Data format 5
TP	True Positive
TN	True Negative
FP	False Positive
FN	False Negative
CDF	Cumulative Distribution Function
PDF	Probability Distribution Function
FP	Find Peaks
CF	Curve Fit
GMM	Gaussian Mixture Model
EM	Expectation-Maximisation
MoD	Median of Differences

Scanning Probe Microscopy

xy	Axes parallel to the surface
z	Axis perpendicular to the surface
$\delta h(t)$	Time dependent controller output at time t
E	Error term
τ	Dummy integration variable
K_p	Proportional gain
K_i	Integral gain
K_d	Derivative gain
σ	Equilibrium position
E_{bond}	Bonding energy
κ	Characteristic inverse decay length

Q	Quality factor
Δf	Resonant frequency shift
ΔA	Amplitude shift
$\Delta\phi$	Phase shift
V_0	Barrier height
z_t	Barrier width
E	Energy of electronic wavefunction
ψ	Wavefunction of decay
k	Wave number
μ	Inverse decay length
$A - F$	Tunnelling coefficients
I	Tunnel current
$f(E)$	Fermi function
E_t	Tip energy level
E_s	Surface energy level
E_F	Fermi energy
M_{ts}	Tunnelling matrix
ψ_t	Tip wavefunction
ψ_s	Surface wavefunction
r_0	Centre of spherical tip
R	Radius of curvature of spherical tip
Ω_t	Volume of spherical tip
c_t	Normalisation term
$T(E)$	Transmission coefficient
ϕ	Workfunction
E_{vac}	Vacuum energy

e	Charge of the electron (1.60 x 10^{-19} coulombs)
V	Applied tunnel junction bias
Å	Angstrom (0.1 nanometres)

Normal-Incidence X-ray Standing Waves

E_0	Energy of the incident beam
n	Mode of oscillation
λ	Wavelength of oscillation
d_{hkl}	Lattice constant
θ	Angle between plane and beam
z	Normal distance from the crystal
I	Standing wave intensity
E_{hkl}	Energy of the reflected beam
R	Standing wave reflectivity
P_c	Coherent position
F_c	Coherent fraction

Thin Film Dewetting

$\phi(h_z)$	Free energy per unit area of two surfaces as a function of surface separation h_z
Π	Disjoining pressure
F	Free energy of mixing
ϕ	Binary mixture composition
T_c	Critical temperature at the spinodal stable-unstable phase boundary
ϕ_c	Critical composition at the spinodal stable-unstable phase boundary
γ	Interfacial tension

M_a	Marangoni number
B	Variation in interfacial tension with temperature
h_z	Film thickness
ρ	Liquid density
ν	Liquid dynamic viscosity
κ	Liquid thermal diffusivity
α	Periodicity of convective movement

Monte Carlo Modelling

i	Index of a grid site
j	Index of a neighbouring grid site
L	Size of the system along each dimension
E	Total energy of the system
ΔE	Energy change due to (proposed) change of state
$\pm J$	Energetic favourability
σ	Spin of an Ising model system
P	Probability of a given system state
C	Starting nanoparticle concentration
μ	Chemical potential
MR	Nanoparticle mobility ratio
ϵ_l	Liquid-liquid interaction energy
ϵ_n	Nanoparticle-nanoparticle interaction energy
ϵ_{nl}	Nanoparticle-liquid interaction energy
T	Temperature of the system

T_c	Critical temperature of the system
k_B	Boltzmann constant
$\Delta\mu_f$	Fractional change in chemical potential at the critical vapour fraction
ν	Vapour fraction
ν_s	Critical vapour fraction
σ	Sharpness of shift in chemical potential at the critical vapour fraction
ϵ_{sl}	Surface-liquid interaction energy
ϵ_{sn}	Surface-nanoparticle interaction energy

Statistical Analysis

$p(n)$	Probability of finding a Voronoi cell of n sides
$\bar{n}$	Mean sidedness of Voronoi cells
μ_2	Variance in Voronoi cell sidedness
S	System entropy
S_v	vth elementary symmetric function
R_i	ith principal radius of curvature
dS	$(d-1)$th surface element
A	Area
P	Perimeter
χ	Euler characteristic
$\tilde{A}$	Scale-invariant area
$\tilde{P}$	Scale-invariant perimeter
$\tilde{\chi}$	Scale-invariant Euler characteristic
N_0	Number of particles

N_1	Number of holes
N	Larger number between the number of particles or holes
L	Physical length of the image
$\bar{A}_p$	Average particle area
q	(Peak) wave vector
h_{rms}	Root mean square roughness
Δq	Shift in peak wave vector
$\Delta\%h_{rms}$	Percentage change in root mean square roughness
$Cov(x, y)$	Covariance between variable x and y
A	Hamaker constant
PCX	Xth principal component
M^T	Transpose of matrix M
M_r	Molecular mass

Image Segmentation

p_{new}	Normalised pixel value
p	Original pixel value
p_{min}	Minimum pixel value in image
p_{max}	Maximum pixel value in image
σ	Standard deviation
σ_X	Threshold value of segmentation method X
σ_W	Within class variance

σ_B	Between class variance
W_b	Weighting of background modal peak
μ_b	Mean of background modal peak
W_f	Weighting of foreground modal peak
μ_f	Mean of foreground modal peak

A FFT-based coarsening analysis script

```
# Fast Fourier Transform Power Spectral Density code adapted to look at
# different runs of Monte Carlo simulations of gold nanoparticle dewetting
# from the Farley test set to plot the shift in peak of the PSD via
# coarsening. Also returns a gif of how the radially averaged 1D FFT spectra
# change with the simulation on request.

import os
import numpy as np
import matplotlib.pyplot as plt
from scipy import fftpack
import re
import pylab as py
import imageio

# From the folder structure, select the type of pattern and the run number,
# edit these accordingly
selected_type = 3 # 0'Cellular', 1'Fingering', 2'Holes', 3'Islands',
# 4'Labyrinthine', 5'Worm-like'
selected_run = 2
remove_liquid = 1 # Make it so the liquid isn't present by making liquid
# states = substrate states for the FFT
save_movie = 0 # Save a gif of the coarsening, saving the subplots to a
# movie folder
image_size = 20 # Provide the image size in microns


sim_plot = 0 # Used for plotting some PSDs on the same graph, for figure
# production

# Change the 4 frames if necessary, the current frames chosen happen to be
# quintessential phases
# The default frames for (type,run) are as follows, graph_in is the starting
# index for the plot (to avoid leakage)
# Fingering 2 (1,2): 420, 2920,3820, 5500, 3:230
# Islands 2 (3,2): 140, 240, 1080, 1500, 8:230
# Worm-like 2 (5,2): 140, 520, 720, 1000, 8
if selected_type == 1:
    selected_frames = [420, 2920, 3820, 5500]
    graph_in = 3
elif selected_type == 3:
    selected_frames = [140,240,1080,1500]
```

```
    graph_in = 8
elif selected_type == 5:
    selected_frames = [140, 520, 720, 1000]
    graph_in = 8

height = 0 # Dummy starting variable for tracking PSD peak height

psd1D_sim_plot = np.zeros((len(selected_frames), 362)) # 362 is the number
# of values in the x array for the sim plot
i=-1 # Counter for the simultaneous plot

# Sets the thickness and sizes of elements in the plotsFFT_Frame_crop.py
line = 0.7
marker = 3

# Find the chosen folder
type = ['Cellular', 'Fingering', 'Holes', 'Islands', 'Labyrinthine',
        'Worm_like']
type_dir = r'Frame_Data/' + type[selected_type] + '/' + str(selected_run)\
           + '/'

# Define a function that converts PNGs to grayscale arrays
def rgb2gray(rgb):
    return np.dot(rgb[...,:3], [0.299, 0.587, 0.144])

# Define a function that calculates the radially averaged profile of a 2D
# power spectrum
def radial_profile2(data, center=None, binning=2):
    y, x = np.indices((data.shape)) # first determine radii of all pixels

    if not center:
        center = np.array([(x.max() - x.min()) / 2.0, (x.max() - x.min())
                           / 2.0])

    r = np.sqrt((x - center[0]) ** 2 + (y - center[1]) ** 2)

    # radius of the image.
    r_max = np.max(r)
    bin_no = np.rint(r_max/binning).astype(int)
    ring_brightness, radius = np.histogram(r, weights=data, bins=bin_no)
    return ring_brightness
```

```
# Define a function that sets an image numpy array's values to be between 0
# and 1
def normalise(array):
    norm_array = (array-np.min(array))\
                            / (np.max(array)-np.min(array))
    return norm_array

# Look into the folder for all images that are PNGs
files = os.listdir(type_dir)
files_png = [i for i in files if i.endswith('.png')]

# Write a file name RegEx that all file names take to extract the data from
# the file name
re_input = re.compile('outfile_C(?P<C>\d+)_'
                      'kT(?P<kT>\d+)_MR1_mu0(?P<mu0>\d+)_'
                      'muf15_vus75_sig01_L1024_m(?P<m>\d+)_'
                      'IC.png')

print('Sorting files ...')
# Sort images in order of monte carlo steps, m
steps = list([])  # Make an empty array for sorting
for j in files_png:
    image_name = j
    match = re_input.match(image_name)
    m = match.group('m')
    steps.append(int(m))

steps_sort = np.argsort(steps)

print('Calculating power spectra ...')
# In the calculated order, start the loop
for index in steps_sort:
    # Load the image location
    image_name = files_png[index]
    image_loc = type_dir + image_name

    # Use the RegEx to find the value of m from the file name
    match = re_input.match(image_name)
    m = match.group('m')

    # Load the image from location then convert it to grayscale then
    # normalise
    image = plt.imread(image_loc)
```

```
image_gray = normalise(rgb2gray(image))

# Convert the array such that the liquid isn't presence, if requested
if remove_liquid == 1:
    image_gray[image_gray > 0.9] = 0 # Sets the liquid layer to 0
    image_gray = (image_gray > 0.5).astype(int) # Sets the nanoparticle
    # layer to 1

# Take the 2D Fourier transform of the image.
F1 = fftpack.fft2(image_gray)

# Now shift the quadrants around so that low spatial frequencies are in
# the center of the 2D fourier transformed image.
F2 = fftpack.fftshift(F1)

# Calculate a 2D power spectrum
psd2D = np.abs(F2) ** 2

# Calculate the radially averaged 1D power spectrum
psd1D = radial_profile2(psd2D)

# Save the spectrum's peak index
height = np.append(height, np.max([psd1D[5:255]]))

# Calculate the x-axis in per-micron
x, y = image_gray.shape
# Use Pythagoras to work out the furthest radius on the image for the
# sake of cropping
horz = np.linspace(0, np.sqrt((x / 2) ** 2 + (y / 2) ** 2), 362)\
       / image_size

# Plot the 1D power spectrum in a log plot
py.figure(1)
py.clf()
py.semilogy(horz[:255], psd1D[:255], label='FFT', lw=line)
py.xlabel('Wavevector /$\u03BCm^{-1}$')
py.ylabel('Power Spectrum')
# py.legend(loc="best", fontsize='xx-small')

# Save both the figure and grayscale image to the results folder
# res/frame/
fig_sav_loc = r'res/frame/' + type[selected_type] + '_'\
              + str(selected_run) + '_1DFFT_m' + m + '.png'
```

```
    img_sav_loc = r'res/frame/' + type[selected_type] + '_'\
                  + str(selected_run) + '_IMG_l' + str(remove_liquid)\
                  + '_m' + m + '.png'
    py.savefig(fig_sav_loc, dpi=300)
    py.imsave(img_sav_loc, image_gray, dpi=300, cmap=py.cm.gray)

    print(m)

    # Save the spectrum at the selected frames
    if sim_plot == 1 and int(m) in selected_frames:
        i+=1
        print('Appending...')
        psd1D_sim_plot[i] = psd1D
        # py.figure(3)

    # Make and save subplots for the gif
    if save_movie == 1:
        py.figure(2)
        py.clf()
        py.subplot(1, 2, 1)
        py.imshow(image_gray, cmap=py.cm.gray)
        py.xticks([])
        py.yticks([])
        py.title('m = ' + m)
        py.subplot(1, 2, 2)
        py.semilogy(horz[:255], psd1D[:255], label='FFT', lw=line)
        py.ylim([1e6, 1e11])
        py.xlabel('Wavevector / $\u03BCm^{-1}$')
        # py.ylabel('Power Spectrum')
        sub_sav_loc = r'res/frame/movie/' + type[selected_type] + '_' +\
                      str(selected_run) + '_SUB_l' + str(remove_liquid) +\
                      '_m' + m + '.png'
        py.savefig(sub_sav_loc, dpi=300)

if sim_plot == 1:

    # Plot the simultaneous plot of the selected frames
    py.figure(3)
    py.clf()
    i = 0

    # Use green triangle, red square, blue circle, purple diamond for the
    # plot
```

```
    markers_to_use = ['g^', 'rs', 'bo', 'md']
    lines_to_use = ['g','r','b','m']

    for m in selected_frames:
        psd1D = psd1D_sim_plot[i]
        label = str(m) + ' Steps'
        f=(image_size / 1024)
        py.semilogy(f*horz[graph_in:255:2], psd1D[graph_in:255:2],
                    lines_to_use[i], lw=line)
        py.semilogy(f*horz[graph_in:255:2], psd1D[graph_in:255:2],
                    markers_to_use[i], ms=1, label=label, lw=line)
        i+=1

    py.xlabel('Wavevector /pixels$^{-1}$')
    py.ylabel('Intensity (a.u.)')
    py.yticks([])
    py.legend()

    # Save the plot to an appropriate location
    sub_sav_loc = r'res/frame/paper/' + type[selected_type] + '_' +\
                  str(selected_run) + '_SUB_I' + str(
        remove_liquid) + '_m' + str(m) + '.png'
    sub_sav_loc_eps = r'res/frame/paper/' + type[selected_type] + '_' +\
                      str(selected_run) + '_SUB_I' + str(
        remove_liquid) + '_m' + str(m) + '.svg'
    py.savefig(sub_sav_loc, dpi=300)
    py.savefig(sub_sav_loc_eps, dpi=300, format='svg')

# Makes the gif by stitching together the subplots of the simulation and the
# PSD
if save_movie == 1:
    print('Saving gif ...')
    images = []
    for index in steps_sort:
        m = steps[index]
        sub_sav_loc = r'res/frame/movie/' + type[selected_type] + '_' +\
                      str(selected_run) + '_SUB_I' + str(
            remove_liquid) + '_m' + str(m) + '.png'
        images.append(imageio.imread(sub_sav_loc))
    gif_sav_loc = img_sav_loc = r'res/frame/gif/' + type[selected_type] +\
                                '_' + str(selected_run) + '_GIF_I' +\
                                str(remove_liquid) + '_m' + str(m) + '.gif'
    imageio.mimsave(gif_sav_loc, images, duration=0.5)
```

```
print('Done!')

# Use the saved height indices of the PSD to fit to a power law

# Function to calculate the power-law with constants a and b
def power_law(x, a, b):
    return a*np.power(x, b)

# Modify these parameters accordingly until the established exponential
# graph fits the data
a_fit = 1e9
b_fit = 0.25

py.figure(4)
py.plot(np.arange(60, 1520, 20), height[1:], 'rx')
py.plot(np.arange(60, 1520, 20), power_law(np.arange(60, 1520, 20), a_fit,
                                           b_fit))
py.show()
```

B Sectional Fourier analysis script

```
# Code that takes in a singular image, and can return the radially averaged
# 1D FFT spectrum of two squares of the same size.
# Used mainly for oxide layer images.

# Import the usual suspects
import numpy as np
import matplotlib.pyplot as plt
from scipy import fftpack
import pylab as py
from skimage.filters import window


def rgb2gray(rgb):  # Define a function that converts PNGs to grayscale
    # arrays
    return np.dot(rgb[...,:3], [0.299, 0.587, 0.144])


def normalise(array):  # Set an image numpy array's values to be between 0
    # and 1
    norm_array = (array-np.min(array))\
                            / (np.max(array)-np.min(array))
    return norm_array


def radial_profile2(data, center=None, binning=1): # Radial profile
    # calculator
    y, x = np.indices((data.shape))  # first determine radii of all pixels

    if not center:
        center = np.array([(x.max() - x.min()) / 2.0, (x.max() - x.min()) /
                           2.0])

    r = np.sqrt((x - center[0]) ** 2 + (y - center[1]) ** 2)

    # radius of the image.
    r_max = np.max(r)
    bin_no = np.rint(r_max/binning).astype(int)

    ring_brightness , radius = np.histogram(r, weights=data, bins=bin_no)
    # plt.plot(radius[1:], ring_brightness)
    # plt.show()
```

```
    return ring_brightness

def SpectralFFT(array):  # Calculate the radially averaged 1D FFT spectrum
    # Take the fourier transform of the image.
    F1 = fftpack.fft2(array)

    # Now shift the quadrants around so that low spatial frequencies are in
    # the center of the 2D fourier transformed image.
    F2 = fftpack.fftshift(F1)

    # Calculate a 2D power spectrum
    psd2D = np.abs(F2) ** 2

    # Calculate the radially averaged 1D power spectrum
    spectra = radial_profile2(psd2D)

    return spectra


# def hann_SpectralFFT(array):  # Calculate the radially averaged 1D FFT
# spectrum of a Hann windowed image
#     wimage_gray = array * window('hann', array.shape)
#     windowed_array_spectrum = SpectralFFT(wimage_gray)
#     return windowed_array_spectrum

nudes = 0  # set to 1 if you are in Oxide Data/Nudes
img_name = '2a_0.75_5x5_hs'  # Take a file name from Oxide Data, or Oxide
# Data/Nudes if nudes = 1
file_name = img_name + '.png'


run_no = 10  # appends a number to image, useful tool for when you don't
# want to overwrite old data
image_size = 7  # provide the whole image size in microns
# Black is square 1, put it on the tip-oxidised region #
# Orange is square 2, put it on the air-oxidised region #
look_good = 1  # change to 1 when you're happy with the square locations,
# otherwise just displays the square locations
square_1_origin = [150,388] # Modify these coordinates
square_2_origin = [100,0]
square_size = 82  # size of square in pixels, must be the same size for
# comparable results
```

```
# Make the parameters for use in drawing
ox1 = square_1_origin [0]
oy1 = square_1_origin [1]
rx1 = square_size
ry1 = square_size
c_x1 = [ox1, ox1+rx1, ox1+rx1, ox1, ox1]  # make a set of coordinates to
# draw the rectangle on the image
c_y1 = [oy1, oy1, oy1+ry1, oy1+ry1, oy1]

ox2 = square_2_origin [0]
oy2 = square_2_origin [1]
rx2 = square_size
ry2 = square_size
c_x2 = [ox2, ox2+rx2, ox2+rx2, ox2, ox2]  # make a set of coordinates to
# draw the rectangle on the image
c_y2 = [oy2, oy2, oy2+ry2, oy2 + ry2, oy2]


# Find the image directory
if nudes == 1:
    image_loc = 'Oxide_Data/Nudes/' + file_name
else:
    image_loc = 'Oxide_Data/' + file_name
# Load the image, then grayscale and normalise the pixel values
image = plt.imread(image_loc)
image_gray = normalise(rgb2gray(image))
# Returns the image shape, used sometimes
x, y = image_gray.shape

# Plot the image with the 2 squares drawn on it
py.figure(1)
py.clf()
py.imshow(image_gray, cmap=py.cm.Greys)
py.plot(c_y1, c_x1, 'black', ms=10)
py.plot(oy1, ox1, 'kx', ms=10)
py.plot(c_y2, c_x2, 'tab:orange', ms=10)
py.plot(oy2, ox2, 'kx', ms=10)
fig_sav_loc = 'res/oxide/comparesquares/' + img_name + 'locns_' +\
              str(run_no) + '.png'
py.savefig( fig_sav_loc , dpi=300)
py.show()
```

```
# Crop to the squares
crop_square1_array = image_gray[ox1:ox1+rx1, oy1:oy1+ry1]
crop_square2_array = image_gray[ox2:ox2+rx2, oy2:oy2+ry2]

# Display the returned cropped region
py.figure(2)
py.clf()
py.subplot(1, 2, 1)
py.imshow(crop_square1_array, cmap=py.cm.Greys)
py.subplot(1, 2, 2)
py.imshow(crop_square2_array, cmap=py.cm.Greys)
py.show()

# Quits out here if you're just testing square locations look_good=0
if look_good == 0:
    exit

# Save the raw 2D FFT of the images
# Square 1
F1 = fftpack.fft2( crop_square1_array )
F2 = fftpack.fftshift (F1)
cm_2d = np.abs(F2) ** 2
s1_sav_loc = 'res/oxide/comparesquares/' + img_name + '_square1_' +\
             str(run_no) + '.png'
py.imsave( s1_sav_loc , np.log(cm_2d), dpi=300, cmap='rainbow')

# Square 2
F1 = fftpack.fft2( crop_square2_array )
F2 = fftpack.fftshift (F1)
cm2_2d = np.abs(F2) ** 2
s2_sav_loc = 'res/oxide/comparesquares/' + img_name + 'square2_' +\
             str(run_no) + '.png'
py.imsave( s2_sav_loc , np.log(cm2_2d), dpi=300, cmap='rainbow')


# Solve for the 1D power spectra
psd1D_1 = SpectralFFT(crop_square1_array)
psd1D_2 = SpectralFFT(crop_square2_array)

# Calculate the wavevector to plot on the x-axis, using the provided image
# size
ratio = square_size / x
horz_1 = np.linspace(0, np.sqrt(( square_size / 2) ** 2 + ( square_size / 2)
```

```
                                        ** 2), len(psd1D_1)) / (image_size * ratio *
                                                1000)
horz_2 = np.linspace(0, np.sqrt((square_size / 2) ** 2 + (square_size / 2)
                                        ** 2), len(psd1D_2)) / (image_size * ratio *
                                                1000)

# Display the 1D radially averaged FFT of the 2 squares on the same graph
py.figure(3)
py.clf()
py.rcParams['font.size'] = '17'
region1 = int(np.floor(len(psd1D_1)/np.sqrt(2)))  # Use the ratio between
# the diagonal and side length to remove cusp
region2 = int(np.floor(len(psd1D_2)/np.sqrt(2)))  # ' '
py.semilogy(horz_1[1:region1:1], psd1D_1[1:region1:1], 'ko',
            label='FFT Region 1', ms=5)
py.semilogy(horz_2[2:region2:1], psd1D_2[2:region2:1], 's', color='orange',
            label='FFT Region 2', ms=5)
py.yticks([])
py.ylabel('Intensity (a.u.)', fontsize=22)
py.xlabel('Wave vector ($nm^{-1}$)', fontsize=22)
# py.legend(loc="best", fontsize='xx-small')
fig_sav_loc = 'res/oxide/comparesquares/' + img_name + 'plot_' +\
              str(run_no)+ '.svg'
py.savefig(fig_sav_loc, dpi=300)
fig_sav_loc = 'res/oxide/comparesquares/' + img_name + 'plot_' +\
              str(run_no) + '.png'
py.savefig(fig_sav_loc, dpi=300)
py.show()

# Display the wave vector of the peak intensity and their separation in per
# micron
print('Black Square peak is ' + str(horz_1[np.argmax(psd1D_1[1:])+1]))
print('Orange Square peak is ' + str(horz_2[np.argmax(psd1D_2[1:])+1]))
print('Delta = ' + str(horz_1[np.argmax(psd1D_1[1:])]-horz_2[np.argmax
(psd1D_2[1:])]))

# Calculate and display the area under the 1D radially averaged FFT ie the
# rms roughness squared
area1 = np.trapz(psd1D_1[1:region1], x=horz_1[1:region1:1])
area2 = np.trapz(psd1D_2[1:region2], x=horz_2[1:region2:1])

print('Area under Oxide PSD is ' + str(area1))
print('Area under Silicon PSD is ' + str(area2))
```

C Image pre-processing script

```
# Finalised pre-processing code with just the median of difference row
# aligner and R-based polynomial background detrender modules inserted,
# takes in any file structure from an external storage device,
# finds every ibw file, and preprocesses them into locally-saved png
# files. Also creates a csv file of all found ibw file name instances (
# useful for finding duplicate file names)

import pycroscopy as scope
import matplotlib.pyplot as plt
import h5py
import numpy as np
import os
import pandas as pd
import glob
from rpy2 import robjects as ro


def preprocess(ibw_name, ibw_path):
    # Create an object capable of translating .ibw files
    TranslateObj = scope.io.translators.IgorIBWTranslator(max_mem_mb=1024)

    # Translate the requisite file
    Output = TranslateObj.translate(
        file_path =ibw_path, verbose=False)

    print(Output)

    # Opening this file to read in sections as a numpy array
    # Read_Path = Output
    h5_File = h5py.File(Output, mode='r')

    data_Trace = h5_File['Measurement_000/Channel_000/Raw_Data']

    data_Trace_Array = np.array(data_Trace[:])

    # Identify the size of the data trace array
    if data_Trace_Array.shape[0] == 65536:
        row_num = 256
    elif data_Trace_Array.shape[0] == 262144:
        row_num = 512
    elif data_Trace_Array.shape[0] == 1048576:
```

```
    row_num = 1024
else:
    row_num = 0
    norm_data_Trace_Array = 0

h5_File.close()
os.remove(Output)

# Define a function that sets an image numpy array's values (pixel
# intensities) to be between 0 and 1
def normalise(array):
    norm_array = (array - np.min(array)) \
                 / (np.max(array) - np.min(array))
    return norm_array

if row_num > 0:
    shaped_data_Trace_Array = np.reshape(data_Trace_Array,
                                         (row_num, row_num))
    aligned_med_data_Trace_Array  = normalise(shaped_data_Trace_Array)


    # Next step is to apply median difference to rows #
    # Create a function to take two adjacent rows and return the
    # alignment required to move the second row in line with the first


    def line_align (row1, row2):
        diff = row1 - row2
        bins = np.linspace(np.min(diff), np.max(diff), 1000)
        binned_indices = np.digitize(diff, bins, right=True)
        np.sort(binned_indices)
        median_index = np.median(binned_indices)
        return bins[int(median_index)]


    for i in range(1, row_num):
        row_iless1 = aligned_med_data_Trace_Array[i - 1, :]
        row_i = aligned_med_data_Trace_Array[i, :]
        Offset = line_align(row_iless1, row_i)
        aligned_med_data_Trace_Array[i, :] =\
            aligned_med_data_Trace_Array[i, :] + Offset

    aligned_med_data_Trace_Array = normalise(
```

```
        aligned_med_data_Trace_Array)

    # Next step is polynomial detrending #
    # In R Code apply a polynomial detrending algorithm to the image
    # array

    polystring = '''
      row_num<-dim(alignim)[1]
      # Turning image1 into a dataframe of columns x, y and intensity
      im1data<-data.frame(as.vector(alignim))
      names(im1data)<-"intensity"
      im1data$x<-rep(1:row_num,row_num)
      # 1st step of poly detrend
      im1data$y<-as.vector(t(matrix(rep(1:row_num,row_num),
      row_num,row_num)))
      im4mod3<-lm(intensity~poly(x,df)*poly(y,df),data=im1data)
      im1data$lmresid<-(im4mod3$residuals -min(im4mod3$residuals))
      # 2nd step of poly detrend
      /(max(im4mod3$residuals)-min(im4mod3$residuals))


      poly_dt<-(matrix(im1data$lmresid,row_num,row_num))
    '''

    data_matrix = ro.r.matrix(aligned_med_data_Trace_Array, nrow=row_num
                              , ncol=row_num)
    ro.r.assign("r_data_matrix", data_matrix)
    ro.r("alignim <- r_data_matrix")

    poly_dt_data_Trace_Array = ro.r( polystring )
    norm_data_Trace_Array = normalise( poly_dt_data_Trace_Array )



    # Where to save the resulting files, all appended with the file name
    # and method number
    sav_loc = r'res2/' + ibw_name + '.png'

    # Save the raw ibw and processed images
    plt.imsave(sav_loc, norm_data_Trace_Array, origin='lower',
               cmap='gray')

return norm_data_Trace_Array
```

```
## Below few lines used for targeting unique folders, commented out when
# looking at whole USBs
import tkinter
from tkinter import filedialog
# root = tkinter.Tk()
# root.withdraw()
# dirname = filedialog.askdirectory(parent=root, initialdir ="/",
#                                   title ='Please select a directory')

dirname = 'D:/USB 3'
usb_num = 3 # Change this to reflect the USB number for the ibw location

Data = pd.read_csv('ManualImageClassificationsV2_4.csv', sep=',')

FileNames = Data['Predicted ibw file name']

ro.numpy2ri.activate()  # Converts all R-objects entering the python
# variable space into numpy-able formats
# Define a degree of freedom to be used in polynomial detrender
Df = 2
# Assign DoF to a variable in R space
DoF = ro.r.matrix(Df)
ro.r.assign("df", DoF)

for k in range(0, FileNames.size):
    if k not in [363, 364, 374, 391, 395, 531, 561, 765]:
        # Some corrupted file numbers that break the loop
        print('Searching for image ', k + 1, ' of ', FileNames.size)
        locate = dirname + '/**/' + FileNames[k]
        matches = glob.glob(locate, recursive =True)
        print('~~~ ' + str(len(matches)) + ' found')
        if len(matches) > 0:
            col_name = 'Ibw matches ' + str(usb_num)
            new_col = pd.Series(Data[col_name][k]+len(matches), name=
            col_name, index=[k])
            Data.update(new_col)
            for j in range(0, len(matches)):
                file_name = FileNames[k].replace('.ibw', '') + '_' + \
                            str(usb_num) + '_' + str(j)
                preprocess(file_name, matches[j])  # Run code commented out
                # to just count the number of found images
```

```
# Run this in console to save changes to the csv if doesn't reach end
Data.to_csv('ManualImageClassificationsV2_4.csv', index=False)
```

D Fullerene deposition on HOPG for SPM

Fullerenes were deposited into UHV onto HOPG using the sublimation cell from Figure 2.4.1 into the low-temperature scanning tunnelling microscope's (LT-STM) preparation chamber. A 1 x 1 cm HOPG sample was cleaved using sellotape, entered into the UHV chamber via the loadlock, then degassed at 600 °C for three hours, then left to cool to room temperature to avoid desorption events during the sublimation of C_{60} onto the freshly-cleaved and degassed HOPG. 99% C_{60} powder was sublimed at 400 °C onto the HOPG at a glancing angle exposure to the sublimation cell from Figure 2.4.1 for two hours at room temperature. The sample was withdrawn from UHV and probed with the Cypher AFM. A second attempt with an exposure time of one hour on a subsequently cleaved and degassed HOPG sample followed.

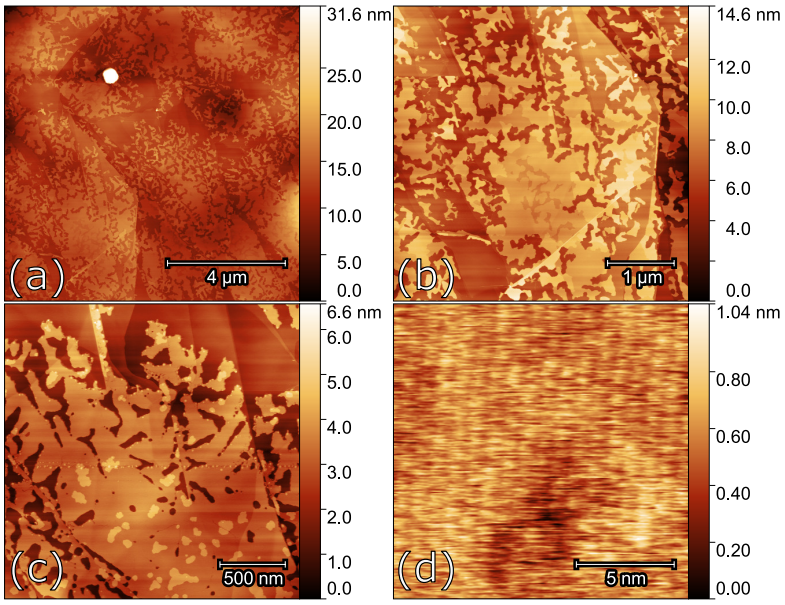

Figure D.0.1: Ambient conditions AFM images of cleaved and degassed HOPG exposed to a C_{60} sublimation cell for two hours in UHV conditions, then withdrawn from UHV. **(a)** 10^2, **(b)** 4.4^2, **(c)** 2.25^2 micron scans in first harmonic tapping mode; **(d)** 15 x 15 nm^2 scan in third harmonic FM mode.

Figure D.0.1 shows the typical structure of a C_{60} film. The fractal-like geometry of the first layer is attributed to diffusion-limited aggregation, by which particles undergoing a random walk accrete to form an aggregate by individually approaching it from a distance, and sticking to a point-like aggregation centre or to particles that have already accreted[284]. Initial adsorption is often spurred by the quenching of surface defects induced during heating, with further fullerenes coalescing due to diffusion, resulting in a "fractal" growth pattern[285,286]. The second and third layers form mainly towards the centre of the more expansive regions of the first layer, where the binding energy exceeds that of adsorbed monolayer.[221]

The first layer's average height was 1.9±0.3 nm, with heights up to 3.2 nm for the small islands atop the layer. C_{60} multilayer regions occurred in a fairly high abundance, of the observed maximum 60% coverage of C_{60} upon the HOPG, 70% had a secondary layer or more. While the first three images in Figure D.0.1 were taken in the amplitude modulation (AM) mode tuned to the cantilever's first harmonic from across a variety of locations on the HOPG surface, the last image was taken in frequency modulation (FM) mode tuned to the cantilever's third harmonic upon a C_{60} monolayer, as a means to achieve molecular resolution. The fullerenes self-assemble as a close-packed monolayer film in a hexagonal lattice at low coverage[286], with an observed molecular separation of 1.00±0.04 nm for the first layer. This value is in agreement with existing C_{60}-HOPG SPM data.[221,286,287]

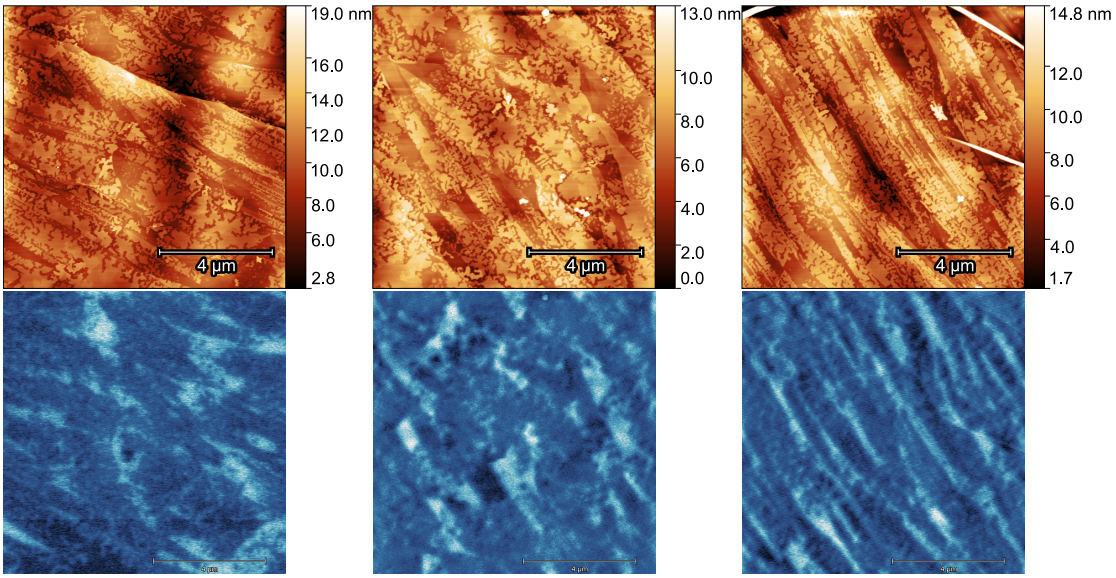

Figure D.0.2: 10 x 10 µm^2 AM-AFM scans of multi-layer coverage of C_{60} on HOPG (two hour deposition), with their respective 3 V KPFM images below.

Kelvin probe force microscopy was also used to investigate the fullerene samples, shown in Figure D.0.2. This was done to evaluate the relative electrostatic force response of fullerene deposits compared to HOPG, in preparation for KPFM on mixed depositions of filled and unfilled C_{60} molecules, as a continuation from endofullerene research in Chapter 5. KPFM was performed with a conductive Cr/Pt tip with a 50 nm height above the surface and a 3 V tip bias. The height retraces and potential retraces clearly track the same surface, with the brightest regions in the KPFM scan correlating to the most expansive nude HOPG regions of highest relative work function, and the darkest regions correlating with regions of expansive C_{60} layers of lowest relative work function. Though the effective CPD image distinguishes the C_{60} from HOPG, the resolution of KPFM was limited, often making distinguishing the two surface phases difficult at lower scan sizes, while there was also an observed height dependence on larger scans due to an abundance of defects and terraces in HOPG.

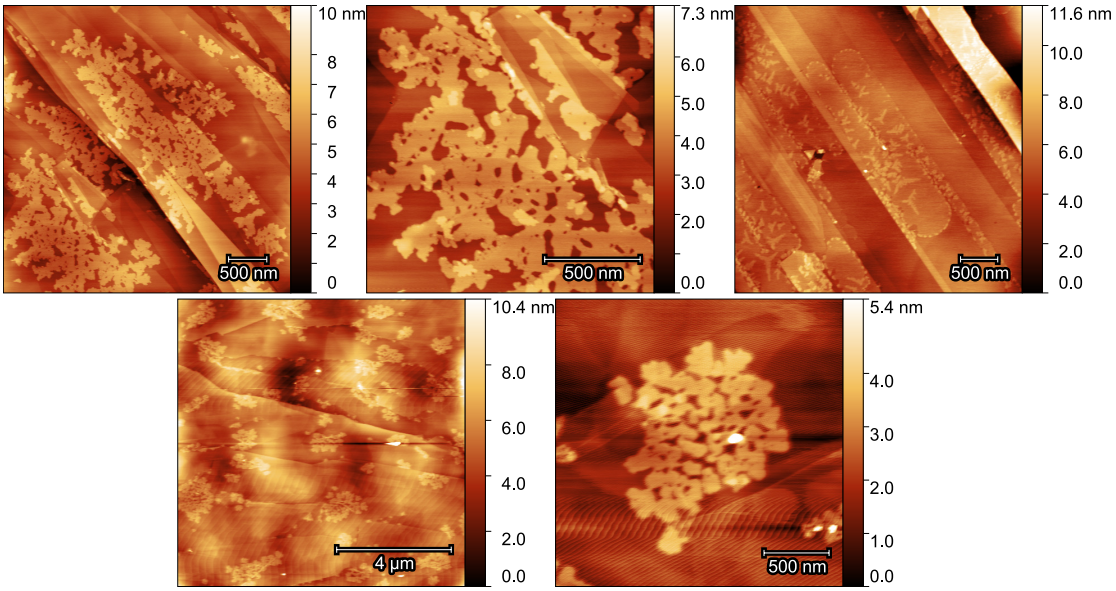

Figure D.0.3: AFM images of cleaved and degassed HOPG exposed to a C_{60} sublimation cell for one hour in UHV conditions. (From left to right, first row then second row) 3.8^2, 1.5^2, 3.9^2 µm scans in tapping mode.

The deposition time was halved for a subsequent deposition, with the resulting surfaces shown in Figure D.0.3. Average C_{60} coverage was observed to be 13%, with relatively nascent "fractal" and cluster-like forms with heights consistent with the first experiment across the surface. While single-molecule resolution KPFM measurements were further pursued in UHV conditions within the Group, C_{60} is utilised as a dewetting mediator in Subsection 4.3.1.

E Supplementary technical material for Chapter 6

E.1 Saving

The final stage of any image processing code is converting and saving the processed arrays locally as a file. The 512 by 512 array is effectively a bitmap. Every individual pixel represents data about the surface, so a lossless, transferable and generic storage method was chosen. Each array is saved as a portable network graphic (.png) file, such that when opened in any image viewing software, it displays a grayscale image perfectly representative of the saved array. Unlike using a plain text format such as a text (.txt) or comma-separated values (.csv) file, this allows for quick visual inspection of resulting images by the user from outside an IDE. The main downside to this storage method is the large file size, this makes transferring large directories of results slower and adds an additional step to all further processing in which image files need to be re-converted back into arrays in a more computationally taxing manner than plain text files would require.

Saved files were named and labelled appropriately, the PNG files were given the same name as the source IBW files. This allows for easy querying during further analysis, keeping naming consistent with databases relating to the data set. Depending on the code and the objectives of the further analysis, the images before and then after the proposed segmentation were saved into a folder of results, labelled with useful extensions. It was not uncommon that images in the data set shared the same IBW file name. As the IBW files are in their own folder structure, this was not a problem until the PNG files of the same names were saved into a single results folder. This was fixed during querying, checking every occurrence of the same name of IBW file and putting an extension of a number on the end of the saved PNG file to distinguish between re-occurrences.

While developing mass-processing code, Subsection 6.4.3, displaying figures and resulting images within the IDE was no longer effective for visual inspection. It was becoming necessary to be able to visually inspect results without rerunning the script or opening the IDE, especially when larger test sets were being used. The script was updated to save arrays and figures as PNGs at the end of each loop. The saved figure included subplots of the median of differences-aligned array, planar-flattened array, CDF and PDF with peaks and trough marked if found, Figure 6.4.7, and a binary image using the threshold value provided by the trough location if found, via the Otsu's thresholding method. The naming scheme for these files was the filename of the IBW file, with "fig" and "thres" appended to the figure and binary image filenames respectively, and all saved in an individual output folder within the probed directory.

While querying the entire historic data set, during Subsection 6.4.6, name redundancy at this stage was becoming a greater issue, as the visual description would only match

one of the returned images. This was resolved in a few ways, the first was enumerating PNG file names with multiple matches with the provided file name to prevent new matches from overwriting and deleting each other. The number of matches associated with each file name was saved to an array and written to a new column in the spreadsheet using `pandas`. These two methods of flagging redundancies still required a manual inspection of the redundant images to choose which image reflected the visual description.

E.2 Screening image and array metadata

Another screening measure is confirming the loaded data from the IBW file is not only the height retrace but also a 2-dimensional 512 by 512 pixel array when loaded. The SPM software provided three options when collecting the used historic scan data that could lead to these parameters not being the same throughout the data set. The user may have set a different resolution to either produce sharper images or reduce scan times. The pre-processing and segmentation were set up for resolutions different from 512 by 512, but further processing and extraction of statistics done by succeeding parties required identical resolutions, and the overwhelming majority of images were 512 by 512 arrays. Another case is that the user may have preemptively ended a scan and saved a partial image, resulting in less than 512 rows in the image. The resulting rectangular images are incompatible with the deployed and future code, so they are hence rejected. Both are checked between loading and pre-processing by simply counting the number of cells in the loaded array and rejecting the image if it does not contain 262144, 512^2, cells. Finally, during the SPM scanning session, the software allows reconfiguration of the data collection channels, changing the data or order of channels where the data is stored. The algorithm that extracts the height retrace from the HD5 file format of the loaded IBW file assumes the height retrace is stored in the first channel. The screening algorithm for this occurrence is another simple check between the loading and pre-processing stages, if the name of the first channel in the IBW file's metadata is not height retrace, the image is rejected.

E.3 Console messages

Transparency was also a useful quality for scripts to have during this stage. Messages for users printed to the console were triggered by the script. These informative updates took numerous forms, providing instant feedback to the user. They would display the progress through the script, such as how many images of those provided had been processed and when the code had started and finished. Custom error messages associated with the aforementioned break-out conditions would be displayed when the image within the current loop failed to meet the screening standards. This included displaying how many null lines the current null line checker identified and whether that many would result in a pass or fail. The script also printed a threshold value obtained by the Otsu's thresholding and, if so, the threshold value found. After all

loops are finished, a success rate showing how many images of those found in the directory made it to the end of the loop and was saved as a segmented binary image. This rate could be recorded, for example, when trying to refine Otsu's thresholding or other segmentation methods, as a metric for the success of the current combination of processing algorithms.